MHD FLOWS IN THE SOLAR ATMOSPHERE

Luca Del Zanna

A Thesis Submitted for the Degree of PhD
at the
University of St Andrews

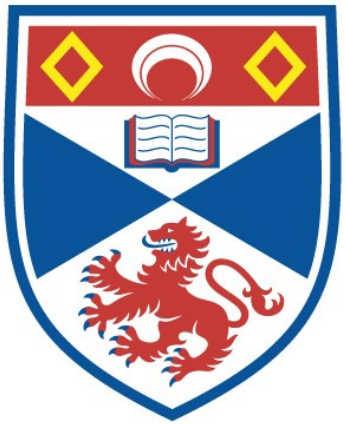

1997

MHD Flows in the Solar Atmosphere

Luca Del Zanna

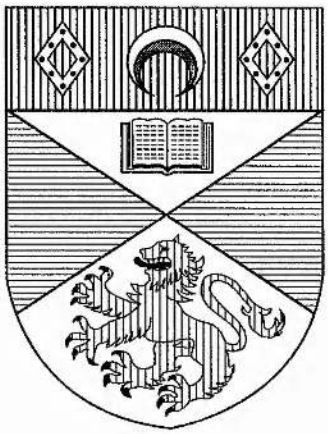

Thesis submitted for the degree of Doctor of Philosophy
of the University of St. Andrews

9 July 1997

TH C350

Abstract

In this thesis, different aspects of the physics of flows in the solar atmosphere are examined. These are described by means of the set of (ideal) magnetohydrodynamics (MHD) and throughout the thesis there is a progressive refinement in the mathematical methods to solve these equations.

First, an analysis of symmetric MHD equilibria is presented and the difficulties that are found in solving the steady equations, both analytically and numerically, are discussed in detail. A novel method to find *exact* solutions in the incompressible case is presented and families of solutions are given in different geometries.

Then, attention is turned to flows in coronal magnetic structures, namely quiescent prominences (closed fieldlines) and polar plumes (open fieldlines), and MHD models for these structures are developed by following two different methods: for the former a semi-analytic approach while for the latter a linearisation through a low β assumption.

In the prominence model, the effects of a subsonic flow along the fieldlines supporting the structure are studied and the results are compared both with a previous static model and with the observed flow speeds.

For the plume model, flows are supposed to be transonic along the open fieldlines and their behaviour is studied for different distributions of temperature, density and magnetic flux. However, here the main goal is to demonstrate that coronal plumes are essentially magnetic features and some results of the model are compared with observations.

Finally, a time dependent MHD code in spherical coordinates is presented. The aim is to study the interaction of the solar wind with the large scale coronal magnetic structures and the propagation of MHD waves. As a test in 1-D, simulations of the dynamic response of a spherically symmetric extended corona to changes at the outer pressure are studied, following a previous analytic work.

Declarations

I, Luca Del Zanna, hereby certify that this thesis, which is approximately 50,000 words in length, has been written by me, that it is the record of work carried out by me and that it has not been submitted in any previous application for a higher degree.

Date: 9/7/97.. Signature of candidate: ..

I was admitted as a research student in October 1994 and as a candidate for the degree of Ph.D. in October 1995; the higher study for which this is a record was carried out in the University of St. Andrews between 1994 and 1997.

Date: 9/7/97.. Signature of candidate: .

I hereby certify that the candidate has fulfilled the conditions of the Resolution and Regulations appropriate to the Degree of Ph.D. in the University of St. Andrews and that the candidate is qualified to submit this thesis in application to that degree.

Date: 9/7/97.. Signature of supervisor: .. ...

In submitting this thesis to the University of St. Andrews I understand that I am giving permission for it to be made available for use in accordance with the regulations of the University Library for the time being in force, subject to any copyright vested in the work not being affected thereby. I also understand that the title and abstract will be published, and that a copy of the work may be made and supplied to any *bona fide* library or research worker.

Date: 9/7/97.. Signature of candidate:

To my wife Giulia

Acknowledgements

Being an Italian, the idea of spending three years of my life in a place that is sadly known for its wet weather and its notorious cuisine (haggis being considered the most delicious dish!), probably more than for the magnificent scenarios of the Highlands or the picturesque castles, did not sound particularly attractive to me when my former supervisor, Prof. Claudio Chiuderi, first proposed it. However, in spite of my initial fears, the period here in St. Andrews turned out to be an exciting experience and I would like to thank all the people who contributed to make it so.

First of all my dearest wife Giulia, to whom this thesis is dedicated, for her patience in bearing the periods of separation and for the great time we had together when she came with me up here, during my second year. Then my parents, without whom nothing of all this would have been possible. Very special thanks are due to my supervisor, Dr. Alan Hood, whose devotion and enthusiasm are really incomparable. I would also wish to thank all the people in the Solar Theory Group, which I found a stimulating environment indeed to work in, and in particular Profs. Eric Priest and Bernie Roberts, who initiated me to the fascinating subject of solar physics.

Last, but certainly not least, I would like to thank all the friends who helped me to enjoy the stay in this small town: Gonçalo, Kostantin, Giovanna, Maria, Nicola, Alex, Susana, César, Maurizio, Gabriele, Alessandra, Roberta, Ilaria, Martha, Luzia and Kumar, César and Beatriz, Valera and Natasha, Partha, Jack, Cheryl, Jason, Nick, Miguel and many, many others.

Contents

Chapter 1

Preliminaries of solar physics

1.1 Introduction

The study of the Sun plays a fundamental role in astrophysics. Although its properties are remarkably ordinary among the other stars (absolute magnitude 4.8, spectral type G2, age of 4.5 billion years, mass of 2×10^{33} g and radius $\approx 7 \times 10^5$ km), its proximity to the Earth makes it a unique object.

Despite the fact that the Sun has been studied for thousands of years, due to its central role not only in astrophysics but, above all, for the very existence of life on Earth, it was only in the sixties that solar astronomers began to realize the importance of Sun's magnetic fields and their interactions with the solar plasma. This has led to the birth of a new branch in theoretical astrophysics known as *solar magnetohydrodynamics*. The Solar Theory Group of the University of St. Andrews, led by Profs. E. Priest and B. Roberts, is certainly one of the world leading groups in the study of this fascinating subject.

Traditionally, solar phenomena have been divided into two classes: quiet and active. The *quiet Sun* is viewed as a static, spherically symmetric ball of plasma, whose properties depend on a first approximation on radial distance from the centre and whose magnetic field is neglected. The *active Sun* consists of transient, sometimes periodical, phenomena like sunspots, loops, prominences and flares, which are super-imposed on the quiet Sun and, in all cases, owe their existence to the presence of the magnetic field.

Another important aspect, although it is usually neglected in most theoretical models of MHD equilibria, is the presence of flows in these magnetic structures. Since the magnetic field is usually the dominant force in the atmospheric layers of the Sun, motion of plasma

across the fieldlines is completely controlled by the field itself, which probably simply evolves slowly through a series of stationary, mainly force free states. But along the fieldlines the plasma is observed to be in continual motion, rather than static. These flows can be either impulsive, usually directed outwards with speeds of the order of some tens of km s^{-1} along curved magnetic fields and eventually falling back to the surface (surges, spicules, jets), or quasi-steady, like siphon flows (driven by a pressure deficit) in coronal loops and arcades, Evershed flows around sunspots, persistent coronal downflows and others.

In the present thesis attention will be devoted to the MHD modelling of such steady flows in the solar atmosphere, in particular in the corona. A review of observations and mathematical models of these kinds of flows inside magnetic structures will be given in Chapter 3, while some observational properties of the coronal environment and its structures relevant to the aims of this thesis are summarised in the next section.

A very special stationary flow is obviously the solar wind. This is a continuous outflow of solar plasma into interplanetary space and appears to escape from the large scale (unipolar) open field regions, called coronal holes, and also along their fine scale structures, namely macrospicules and plumes. The properties and basic modelling of the solar wind and its interaction with the large scale coronal field are reviewed in Sects. 1.3 and 1.4.

Finally, the basics of plasma physics and its fluid description (magnetohydrodynamics), with the derivation of the corresponding mathematical equations, will be discussed in Sect. 1.5, whereas an outline of the work presented in this thesis may be found in Sect. 1.6. Throughout this thesis, cgs Gaussian units will be used, although most of the distances will be expressed in km and the velocities in km s^{-1}.

1.2 The corona

The corona is the outer layer of the solar atmosphere (beyond 3 000 km of height above the photosphere) and its existence has been known for many centuries. In visible light the corona emits thanks to the scattering of photospheric light coming up from below, both off electrons (the K-corona) and off dust (the F-corona). However, due to the dominant photospheric emission, the faint white light emission from the corona was visible only during total eclipses or, after 1930, with the aid of a coronograph.

The corona is composed by an extremely rare plasma (average number density of

$\approx 10^8\,\mathrm{cm}^{-3}$, to be compared with photospheric values seven orders of magnitude higher), whose density is monotonically decreasing outwards. However, its most amazing characteristic is certainly the extremely high temperature ($T \simeq 2 \times 10^6$ K), somewhat 500 times hotter than the top of the photosphere, where the temperature minimum (4300 K) is reached, and the coronal heating mechanism is still one of the most puzzling open questions in solar physics.

This very hot coronal plasma is mainly composed of totally ionised hydrogen atoms, that is free protons and electrons; the heavier elements, due to the extremely high temperature, may loose many of their electrons. Radiation is emitted from the corona by these heavier ionised elements in spectral lines in the extreme ultra-violet (EUV) part of the spectrum and in soft X-rays, where the corona emits thermally. The first X-ray images were taken in the seventies, by the Skylab satellite, and revealed a truly new Sun: regions of low emission, situated at the poles but often sneaking their way towards the equator (*coronal holes*), and regions of greater emission stretching outwards up to 10 solar radii (*coronal streamers*), as it may be seen in the composite image from the EIT and UVCS instrument aboard on SOHO (Fig. 1.1).
On a smaller scale, the corona appears to be made up by myriads of *coronal loops* and intense small features called *X-ray bright points*. Inside coronal holes, elongated structures (*coronal plumes*) extend radially outwards.

All these features are intrinsically magnetic in nature: coronal holes correspond to the large scale, unipolar, open fieldlines regions from which the solar wind is free to escape, streamers contain a denser plasma, basically static, trapped inside large magnetic closed arcades, loops are clearly the result of curved magnetic flux tubes emerging from the below photosphere, bright points appear to be connected to small magnetic bipoles and plumes track the radial open fieldlines and appear to be rooted in photospheric magnetic flux concentrations. Another very special class of coronal objects is that of *prominences*. These are huge, elongated curtains of chromospheric material (they are visible in Hα), hundreds of times cooler and denser than the surrounding atmosphere, which are suspended at heights of 50 000 km in the corona, clearly by some kind of magnetic support against gravity.

A description of the solar structures of greater interest for the aims of this thesis, namely quiescent prominences and polar plumes, is given below. Coronal holes and streamers, and their interaction with the solar wind, will be discussed in Sect. 1.4, while some

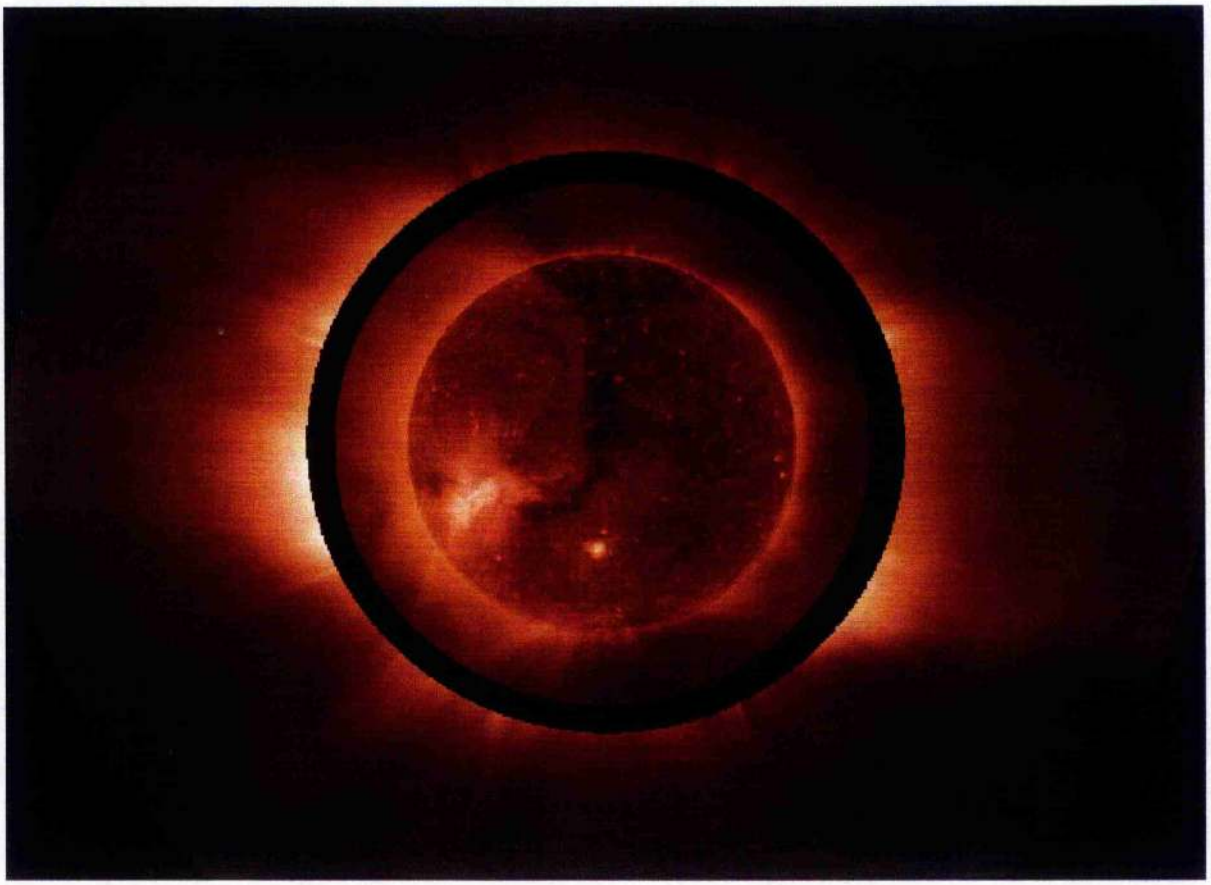

Figure 1.1: The solar corona as it appears in ultraviolet light emitted by ionized oxygen atoms (region outside black circle), and the disk of the Sun in light emitted by ionized iron atoms at temperatures near two million degrees Celsius (region inside circle). This composite image taken by two instruments (UVCS, outer region and EIT, inner region) aboard the SOHO spacecraft shows clearly the coronal holes (dark areas) at the poles and across the disk of the Sun, where the highest speed solar wind originates, and the streamers of denser and slower plasma. Taken from the SOHO gallery (http://sohowww.nascom.nasa.gov/gallery/).

properties of coronal loops will be given in Chapter 3. However, for an excellent general introduction to the Sun and its amazing features, the interested reader should certainly refer to Priest (1982) and to the references therein.

1.2.1 Quiescent prominences

Prominences are usually classified in two distinct types: *active* and *quiescent*. Active prominences are located in active regions and are highly dynamical structures. Their life times are only of minutes or hours and they possess magnetic fields and temperatures which can be much higher of those of quiescent prominences. However, here only quiescent prominences will be considered.

A quiescent prominence is an exceedingly stable structure and may last for many months. It begins its life as a relatively small *active region filament* (the prominences are called traditionally filaments when seen on the disk where, in Hα, they appear as dark, thin, meandering ribbons) in a *filament channel* situated along the polarity inversion line of the underlying magnetic field, thus dividing two regions of uniform but opposite polarity. As the active region disperses, the prominence grows thicker and longer and during this process it migrates slowly towards the nearest pole. Eventually, a quiescent prominence disappears by either slowly dispersing and breaking up, or erupting, or flowing down to the chromosphere.

As said above, a quiescent prominence is a huge, almost vertical sheet of dense, cool plasma surrounded by a hotter and rarer coronal environment. Typical physical properties are reviewed in Table 1.1.

	Minimum	Average	Maximum
Length	60 000 km	200 000 km	600 000 km
Height	15 000 km	50 000 km	100 000 km
Width	4 000 km	6 000 km	15 000 km
Density (n_e)	10^{10} cm^{-3}	10^{11} cm^{-3}	5×10^{11} cm^{-3}
Temperature (T_e)	5 000 K	7 000 K	8 000 K
Magnetic field	–	5-10 G	40 G

Table 1.1: Typical values for quiescent prominences (from Priest 1982).

The magnetic field is aligned with the prominence at its birth in the filament channel,

as it is clear also from the *fibrils* which tend to be all parallel on either side. Later the magnetic field is seen to form an increasing higher angle (15–25 degrees) with the axis of the prominence, and the presence of this perpendicular component might be the possible cause for a progressive raising of the structure from the chromosphere and its support against gravity (see Chapter 4 for the mathematical models of magnetic support). Finally, during the eruption phase, the magnetic field appears to be highly twisted inside the prominence and its excessive twist might be the very cause for the instability and subsequent eruption.

Concerning the structure of a quiescent prominence, usually it is connected to the lower chromosphere through a series of *feet*, more or less regularly spaced and located above supergranular cell boundaries, which are joined by huge arches (see Fig. 1.2). The fine structure of a prominence is in form of vertical *threads*, of average length 5 000 km and diameter 300 km or less, in which a slow downflow (a few km s^{-1}, much less than the free fall speed) is usually observed. For a discussion of flows in and around prominences and for the possible mechanisms of mass replenishment, the reader is again referred to Chapter 4, whereas for further informations on prominences in general, the two books by Tandberg-Hanssen (1974) and Priest (1989) are recommended.

1.2.2 Polar plumes

Solar coronal plumes were first observed in white light eclipse photographs as long, faint rays of enhanced density (3 – 5 times denser than the background) located inside coronal holes (e.g. Van de Hulst 1950; Saito 1965; Koutchmy 1977). In extreme ultraviolet (EUV) spectroheliograms they appear as shorter spikes near the polar limb (Bohlin et al. 1975; Ahmad & Withbroe 1977; Widing & Feldman 1992; Walker et al. 1993) and they show lifetimes of several hours or even days. Recently, diffuse Mg IX plume like structures have been observed inside low latitude coronal holes undergoing limb passage (Wang & Sheeley 1995a), thus suggesting that coronal plumes are common features of all coronal hole regions and not only in the polar caps (therefore the term *coronal* plume should be preferred to *polar* plume, although the latter is more commonly used). Plumes have been also identified in soft X-ray images (Ahmad & Webb 1978) and possibly even as weak radio sources (Gopalswamy et al. 1992). More recently, white light observations by the *Spartan* spacecraft coronagraph have been used to identify plumes up to a height of 5 solar radii (Fisher & Guhathakurta 1995), whereas the LASCO coronographs aboard the SOHO spacecraft have tracked plumes out to at least 15 solar radii.

Figure 1.2: A picture taken in Hα at the solar limb, showing a huge prominence with a very well defined structure. The feet and arches are clearly visible. This is a black and white negative picture, with brighter features being darker. Note also the presence of a curved filament (here white) on the disk (courtesy of Meudon observatory).

Characteristic values of coronal plumes, as seen at the solar limb, are widths of $6-7\times 10^4$ km, number densities in the range $10^8-10^9\,\mathrm{cm}^{-3}$ and temperatures around 10^6 K (Mg IX lines, where plume intensities peak, form around 9.5×10^5 K). The outflow velocity is unknown, but it should not be larger than, say, $10\,\mathrm{km\,s}^{-1}$ at the base of the plume, where plumes are observed to be roughly in hydrostatic equilibrium (e.g. Ahmad & Withbroe 1977). However, preliminary results from SOHO observations seem to show substantial velocities at rather low heights ($\approx$100 km s^{-1} at 2 solar radii; G. Poletto, private communication) thus suggesting that the bulk of the solar wind acceleration might actually occur at lower heights than previously thought.

With regard to the magnetic field, SOHO/MDI high resolution magnetograms show that at the base of plumes strong field concentrations (up to almost 200 G) are often present (see Fig. 1.3), but it is not clear whether less intense bipoles are also present near their base (see Chapter 5 for a discussion of the relationships between plumes and magnetic flux concentrations).

1.3 The solar wind

Without any doubt, the most important of all kinds of flows in the solar atmosphere is the continuous plasma outflow escaping from the open field regions of the sun and expanding outwards into the interplanetary space, known as the *solar wind.*

The study of the solar wind is an immense subject and it unifies together different areas in modern space research, due to its relevance for solar physics, geophysics, plasma physics, astronomy and particle physics. In the light of this fundamental and interdisciplinary role, it may be difficult to recall that the very existence of this quasi-stationary outflow of solar material through interplanetary space, as well as its hydrodynamical description, was an object of a serious debate until the advent, in the early 1960s, of the first *in situ* measurements of the plasma parameters, which put these controversies to an end by confirming the existence of a supersonic flow reaching the Earth.

The man who first pointed out the necessity of the presence of a supersonic wind and proposed the hydrodynamic model for a stationary, radial expansion of the solar corona was Eugene Parker in his celebrated paper (Parker 1958). The fact that a previously unknown, fundamental process such as the solar wind, was predicted before its actual discovery is indeed remarkable and, unfortunately, is a rare event in theoretical astrophysics.

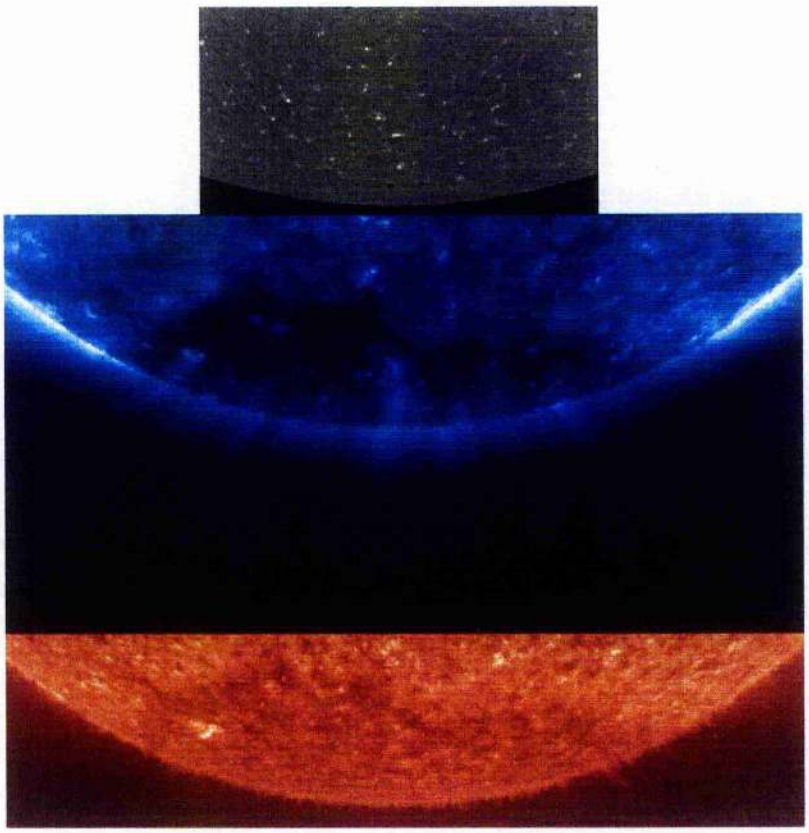

Figure 1.3: Polar plumes as seen at the limb in the southern coronal hole. Note the presence of magnetic flux concentration regions where some of the plumes are rooted. Plumes are visible in high temperature lines (like the iron line shown in the middle picture from EIT, corresponding to a temperature of roughly 10^6 K), but not in transition region lines at lower temperatures (He II, in the bottom picture, with $T = 6 \times 10^4$ K). Taken from the SOHO gallery (http://sohowww.nascom.nasa.gov/gallery/).

1.3.1 General properties

The solar wind is believed to escape from the regions of unipolar and open magnetic field, corresponding to coronal holes. The flow speed increases monotonically from low values near the coronal base, to reach the local sound speed somewhere in the inner corona ($c_s \approx 120$ km s^{-1}) and finally becoming super-Alfvénic beyond the Alfvén radius. Within this radius the magnetic field dominates the plasma dynamics, for example the closed fieldlines in the inner part of helmet streamers prevent the outflow by trapping a basically static plasma, whereas beyond it the magnetic field is carried by the plasma. This leads to the stretching of the dipole-like fieldlines and to the formation of current sheets at the top of helmet streamers. Another consequence is the spiral structure of the interplanetary magnetic field, due to the solar rotation: if there were no rotation the magnetic field would be simply radial at large distances, but its coupling with the plasma forces it to follow the geometrical pattern of the streamlines imposed by the *garden hose effect.*

The solar wind properties at 1 AU (an *Astronomical Unit*, that is the mean Sun-Earth distance: 1 AU $= 1.50 \times 10^{13}$ cm $= 215\, R_\odot$) are summarised in Table 1.3.1. Beyond the Earth orbit, which is reached by the wind in about 5 days, the solar wind is believed to extend out to a boundary with the interstellar medium at 50–100 AU, where a shock slows the flow from supersonic to subsonic speeds.

	Minimum	Average	Maximum
Velocity	200 km s^{-1}	400 km s^{-1}	900 km s^{-1}
Density	0.4 cm^{-3}	6.5 cm^{-3}	10^2 cm^{-3}
Electron temperature	5×10^3 K	2×10^5 K	10^6 K
Proton temperature	3×10^3 K	5×10^4 K	10^6 K
Magnetic field	2×10^{-6} G	6×10^{-5} G	8×10^{-4} G
Alfvén speed	30 km s^{-1}	60 km s^{-1}	150 km s^{-1}

Table 1.2: Properties of the solar wind at 1 AU (from Priest 1982).

The data in Table 1.3.1 refers to the region around the Earth orbit, that is in the solar equatorial region, where the streamers and the neutral sheet are usually located, and show that the solar wind is far from uniform. On the contrary, it consists of a series of persistent *high speed streams.* The structure of a typical stream, as first observed by Mariner II in

1962, shows a rapid rise in the flow speed (typically from 300–400 to 700–800 km s^{-1}) followed by a slower decline, over an average period of 5 days. A similar profile is observed for the proton temperature, while the electron temperature remains nearly constant. The density and magnetic field rise sharply in the leading edge of the stream and possess lower values within the bulk of the stream.

High speed streams are the most uniform part in the solar wind and they are recurrent with the period of the solar rotation (27 days), lasting between 1 and 18 solar rotations. This may be an evidence for their association with coronal holes, when one of them extends to the equatorial region (for a monograph on this subject, see Zirker 1977). Recent results from the Ulysses spacecraft (Goldstein et al. 1996), which has an orbit almost perpendicular to the ecliptic plane, show that outside the equatorial belt the solar wind is highly uniform (on a large scale), with a typical velocity of ≈ 800 km s^{-1}, thus confirming that the high speed component of the solar wind is indeed generated from open field, unipolar regions.

On smaller scales, both spatial and temporal, the solar wind becomes more and more irregular. Magnetic field fluctuations are continually present and consist mainly of Alfvén waves propagating outwards and possibly generated by super-granulation. These were first observed by Mariner V and identified through the relation

$$\mathbf{b} = \pm\sqrt{4\pi\rho}\mathbf{v}, \tag{1.1}$$

where $\mathbf{b}$ and $\mathbf{v}$ are respectively the magnetic and velocity perturbations, by Belcher & Davis (1971). Also, *tangential* and *rotational* discontinuities are very common features in the small scale solar wind. Finally, fast magnetosonic shock waves are usually observed, believed to be in connection with eruptive events at the solar surface that can lead to geomagnetic storms at the Earth's magnetosphere.

1.3.2 The Parker solution

The first theory of the extended solar corona was by Chapman (1957), who considered a static atmosphere whose energetics is controlled by thermal conduction alone. For a spherically symmetric atmosphere the energy equation simply reads

$$\nabla \cdot (\kappa \nabla T) = \frac{1}{r^2}\frac{\mathrm{d}}{\mathrm{d}r}\left(r^2 \kappa \frac{\mathrm{d}T}{\mathrm{d}r}\right) = 0, \tag{1.2}$$

where the coefficient of thermal conduction is $\kappa = \kappa_0 T^{5/2}$ (for typical coronal values $\kappa_0 \simeq 8 \times 10^{-7}$ cgs units). Under the boundary condition that the temperature must

approach zero at large distances from the Sun, Eq. (1.2) may be integrated to give

$$T(r) = T_0 \left(\frac{R_\odot}{r}\right)^{2/7}. \tag{1.3}$$

Taking $T_0 = 10^6$ K at the Sun, Eq. (1.3) gives a value of $T \simeq 10^5$ K at 1 AU, suggesting correctly that the Earth is surrounded by a very hot plasma. Furthermore, from the equation of hydrostatic equilibrium, which reduces simply to the balance between the pressure gradient against gravity

$$\frac{\mathrm{d}p}{\mathrm{d}r} = -\frac{GM_\odot}{r^2}\rho, \tag{1.4}$$

and by using the equation of state $p = 2(k_B/m_p)\rho T$, Chapman was able to deduce the pressure as

$$p(r) = p_0 \exp\left\{\frac{7}{5}\frac{GM_\odot m_p}{2k_B T_0 R_\odot}\left[\left(\frac{R_\odot}{r}\right)^{5/7} - 1\right]\right\}, \tag{1.5}$$

and the numerical electron density ($n_e = \rho/m_p$) as

$$n_e(r) = n_{e0}\left(\frac{r}{R_\odot}\right)^{2/7} \exp\left\{\frac{7}{5}\frac{GM_\odot m_p}{2k_B T_0 R_\odot}\left[\left(\frac{R_\odot}{r}\right)^{5/7} - 1\right]\right\}. \tag{1.6}$$

It is easily seen that at large distances $r \gg R_\odot$ the model fails to give reasonable results, as the pressure tends to a constant whose value is unacceptably large (10^{-5} dyne cm^{-2}, while the interstellar medium pressure should be about 7 orders of magnitude smaller) and the density diverges ($n_e \simeq 10^2 - 10^3$ at 1 AU).

These inconsistencies were solved by Parker (1958) in his truly classic paper by suggesting that the corona cannot be in static equilibrium, since it is not confined by a strong pressure *lid*, and instead must be continuously expanding outwards. Parker modelled this steady, radial expansion and found a class of solutions with the desired property of a vanishing pressure at infinity. However, his ideas were not widely accepted at that time. In 1960 Chamberlain produced a paper in which Parker's model was attacked violently (Chamberlain 1960) and, curiously, he retained his antagonist position even after the solar wind was actually observed by the satellites Lunik III and Venus I in 1959 and later studied in detail by Mariner II in 1962.

Chamberlain sustained that the transonic solution (see below) is too particular and unlikely to occur in nature, while *breezes* (outflows which are always subsonic and with a vanishing velocity at infinity) are to be considered the natural solutions (see Chapter 6 for a numerical proof of how wrong Chamberlain was!). This opposition had the positive effect

of the production of a series of papers by Parker (1960a, 1960b, 1961) in which he clarifies in more detail the mathematical subtleties of his hydrodynamic model. The notion of the solutions topology, with the classification of the solutions according to their position in the phase plane with respect to a critical point, and the extension of the treatment from isothermal to polytropic with an arbitrary γ appear in the cited series of papers.

Consider then a spherically symmetric corona in steady motion. Equation (1.4) is replaced by the Euler momentum equation

$$\rho v \frac{\mathrm{d}v}{\mathrm{d}r} = -\frac{\mathrm{d}p}{\mathrm{d}r} - \frac{GM_\odot}{r^2}\rho, \tag{1.7}$$

where the velocity of the expansion is assumed to be purely radial (rotation is neglected). To this equation, the mass conservation equation must be added

$$\frac{1}{r^2}\frac{\mathrm{d}}{\mathrm{d}r}(r^2\rho v) = 0. \tag{1.8}$$

For an isothermal atmosphere ($T = \text{const}$), the density ρ can be eliminated through the equation of state and the two fluid equations yield

$$\left(v - \frac{v_c^2}{v}\right)\frac{\mathrm{d}v}{\mathrm{d}r} = \frac{2v_c^2}{r} - \frac{GM_\odot}{r^2}, \tag{1.9}$$

where $v_c = \sqrt{2k_BT/m_p}$ is the *isothermal sound speed*, which is somewhat less than the usual adiabatic sound speed. The critical point occurs when the right hand side vanishes, that is for

$$r_c = \frac{GM_\odot}{2v_c^2} = \frac{GM_\odot m_p}{4k_BT}, \tag{1.10}$$

which is greater that $R_\odot$ when $T < GM_\odot m_p/4k_B$. For coronal temperatures, the position of the critical point scales as

$$\frac{r}{R_\odot} \simeq 5.8 \times \left(\frac{T}{10^6\,\mathrm{K}}\right)^{-1}. \tag{1.11}$$

At this critical radius, also the left hand side of Eq. (1.9) must vanish. This can occur in two ways; either because

$$v^2(r_c) = v_c^2 = 2k_BT/m_p, \tag{1.12}$$

or because

$$\frac{1}{v}\left(\frac{\mathrm{d}v}{\mathrm{d}r}\right)_{r=r_c} = 0. \tag{1.13}$$

Four different classes of single valued solutions are found (see Fig. 1.4):

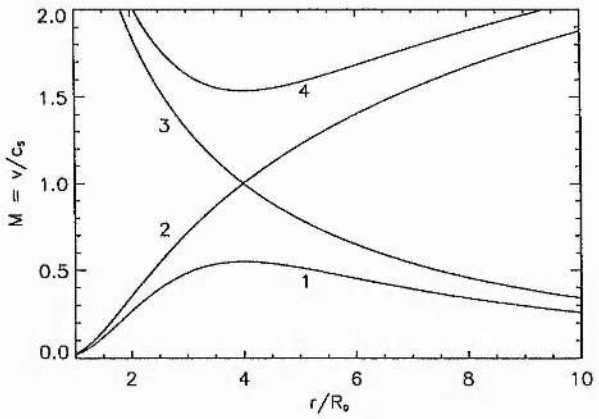

Figure 1.4: The phase plane (M, r). The Mach number v/c_s is shown as a function of the position $r/R_\odot$ for the four possible classes of solutions described in the text. Here the value $r_c = 4.0$ has been chosen for the critical radius.

- *Class 1:* A family where $v(r)$ increases for $R_\odot \leq r \leq r_c$, reaches a maximum value less than v_c at $r = r_c$, satisfying Eq. (1.13), and then decreases with r.
- *Class 2:* A unique solution with $v(r)$ monotonically increasing, crossing the critical point according to Eq. (1.12).
- *Class 3:* A unique solution always decreasing with r, again satisfying Eq. (1.12).
- *Class 4:* A family where $v(r)$ decreases for $R_\odot \leq r \leq r_c$, reaches a minimum value greater than v_c at $r = r_c$, and increases after that.

Each of the solution classes given above fits a different set of boundary conditions at $r = r_0$ and $r \to \infty$. The physical acceptability of these solutions depends upon these boundary conditions. For example, classes 3 and 4 can be ruled out because they have unrealistic large velocities at $r = R_\odot$. The solutions of class 1 and 2 have both the desired property of a small velocity for $r = R_\odot$, but differ greatly for their behaviour at $r \to \infty$. This may be investigated by integrating Eq. (1.9) as

$$\left(\frac{v}{v_c}\right)^2 - 1 - \log\left(\frac{v}{v_c}\right)^2 = 4\left[\log\frac{r}{r_c} + \left(\frac{r}{r_c}\right)^{-1} - 1\right] + C, \tag{1.14}$$

where C is a positive integration constant ($C = 0$ gives the solution of class 2). For solutions belonging to class 1, the term $(v/v_c)^2$ can be neglected at large distances, yielding

the asymptotic behaviour

$$\textit{Class 1:} \quad r \to \infty \Rightarrow v \propto 1/r^2, \tag{1.15}$$

whereas for the unique solution of class 2 is $|-\log(v/v_c)^2|$ that can be neglected, leading to the relation

$$\textit{Class 2:} \quad r \to \infty \Rightarrow v \approx 2v_c\sqrt{\log r}. \tag{1.16}$$

From the continuity equation it is apparent that the solutions of class 1 have the same problem of a constant asymptotic pressure, whereas the solution of class 2 has the desired feature of a vanishing pressure at infinity. The solution of class 2, which correctly describes supersonic velocities of some hundreds km s^{-1} at the Earth's orbit, was called by Parker the *solar wind.*

1.3.3 Additional effects and corrections to the Parker model

The assumption of an isothermal corona may be a good approximation only in the inner corona, where the high temperature is sustained by some (unknown) heating mechanism, but it is certainly a poor approximation at larger heliocentric distances, where conduction must take over and make the temperature decline.

Parker (1960a) proposed a modification to his basic model to account for an isothermal wind in the inner corona and an adiabatic ($\gamma = 5/3$) wind after a certain fixed radius. Another improvement (Parker 1960b) consisted in the assumption of a constant polytropic index γ with an intermediate value in order to simulate somehow the heating effect. Increasing profiles of $v(r)$ are found when $1 \leq \gamma < 3/2$ ($\gamma = 1$ returns the isothermal model). The observed density scale heights in the corona suggest a value of $\gamma = 1.1$. For a polytropic wind, the critical velocity and radius are respectively given by

$$v_c = \sqrt{\frac{2\gamma k_B T}{m_p}}, \qquad r_c = \frac{GM_\odot m_p}{4\gamma k_B T}, \tag{1.17}$$

but this time the temperature T is no longer constant. However, the solutions topology of Fig. 1.4 remains qualitatively unchanged.

The next step was to include a more realistic energy equation, first with thermal conduction alone. In this case, the following integral is found:

$$4\pi\rho v r^2 \left(\frac{1}{2}v^2 + \frac{5}{2}\frac{p}{\rho} - \frac{GM_\odot}{r}\right) - 4\pi r^2 \kappa_0 T^{5/2}\frac{\mathrm{d}T}{\mathrm{d}r} = E_\infty, \tag{1.18}$$

where E_∞ is the energy at infinity. Several solutions have been discovered which traverse the critical point and have a vanishing temperature at infinity, with different temperature asymptotic behaviours (Parker 1964; Whang & Chang 1965; Durney 1971).

Other effects which have been included are the energy exchange between electron and protons (for Coulomb collisions), leading to the *two-fluid* treatment (Sturrock & Hartle 1966, Hartle & Sturrock 1968), in which the proton and electron temperatures have a different decay, with the proton temperature decaying much faster (almost adiabatically) since its conduction coefficient is much less than that for electrons ($\kappa_p = \sqrt{m_e/m_p}\,\kappa_e$). Later, also heat deposition due to dissipation by hydromagnetic waves has been taken into account, with the first quantitative model by Hartle & Barnes (1970).

The presence of the spiral magnetic field has two effects: it modifies the solutions topology (three critical points appear, Weber & Davis 1967) and it makes thermal conduction only effective along the fieldlines. For an excellent monograph on this subject, although now dated, see the book by Hundhaunsen (1972). A more recent review on astrophysical winds and jets, with particular emphasis to the 2-D MHD models, was given by Sauty (1994).

1.4 Interaction of large scale magnetic coronal structures with the solar wind

The main assumption in all the solar wind models presented in the previous section was that of a spherically symmetric coronal expansion. However, this is certainly a poor approximation near the Sun, where the magnetic effects are dominant ($\beta \ll 1$) and the coronal expansion must be influenced by the large scale geometry of the magnetic field structures.

As shown in Sect. 1.2, the inner corona appears to be composed by alternating open and closed field regions, respectively known as coronal holes and helmet streamers. The high speed component of the solar wind escapes from coronal holes (Krieger et al. 1973; Neupert & Pizzo 1974; Wagner 1976; Nolte et al. 1977; Zirker 1977), whereas the low speed component might come from the denser, closed fieldlines regions (either by escaping with the aid of small scale interchange instabilities or simply by sliding along the open fieldlines overlying the helmet streamers).

In order to model these complex interactions between the solar wind plasma and the

coronal magnetic field, a 2-D, self-consistent MHD treatment is needed. An interesting stationary model was proposed by Pneuman & Kopp (1971), who solved iteratively the axisymmetric MHD equations in spherical geometry. Starting from an arbitrary electric current distribution they derive first the magnetic field, then the density, pressure and velocity are found by solving the momentum equation along the fieldlines and imposing that closed loops contain a static plasma. Finally, the back reaction on the magnetic field is calculated by solving the momentum equation across the fieldlines to find the new electric current. This numerical algorithm is iterated until convergence is achieved.

In this work, the temperature is uniform everywhere and a constant density and a dipolar radial component of the magnetic field are assumed at the coronal base. The separation between closed and open fieldlines regions is chosen arbitrarily at the beginning and then modified at each iteration, while the cusp-like shape of the magnetic field at the top of the helmet streamer is imposed *a priori*. A similar approach will be used for a model of coronal plumes (see Chapter 5) under the assumption of a low β plasma. However, only the first order corrections are worked out and these increase monotonically with r when the kinetic pressure varies across the fieldlines. This is possibly the reason why in the Pneuman & Kopp (1971) model the base density and temperature were taken to be uniform: when this condition does not hold, the unbalanced pressure at infinity diverges, causing the iterative method to break down.

For a correct treatment of the non-linear effects, avoiding the complications of the presence of the MHD critical points (see the discussion in Sect. 2.3.3), one has necessarily to turn to a time dependent analysis. Many numerical models have been presented in the literature, but none of them is based on the correct treatment of the boundary conditions at the coronal base. This problem will be discussed in detail in Sect. 7.4, where a sophisticated shock capturing MHD code in spherical geometry, currently under construction, is described.

1.4.1 Coronal hole models

Since the high speed solar wind, which is the regular component of the solar wind, is believed to come from coronal holes, the radial wind models of the previous section should be modified in order to take into account the particular geometry of the coronal hole regions due to the diverging magnetic field.

The first model (Kopp & Holzer 1976) considered a polytropic flow in a *flux tube* with

a varying, but given, cross sectional area $A(r)$. The modified continuity equation reads

$$\frac{1}{A}\frac{\mathrm{d}}{\mathrm{d}r}(A\rho v) = 0, \tag{1.19}$$

which returns Eq. (1.8) for $A(r) = r^2$. By defining the Mach number $M = v/c_s$, where $c_s = \sqrt{\gamma p/\rho}$ is the sound speed, the solar wind equation is found to be

$$\frac{M^2-1}{2M^2}\frac{\mathrm{d}M^2}{\mathrm{d}r} = \frac{1}{2}\left(\frac{\gamma+1}{\gamma-1}\right)\left(1+\frac{\gamma-1}{2}M^2\right)\frac{1}{g}\frac{\mathrm{d}g}{\mathrm{d}r}, \tag{1.20}$$

where

$$g(r) = A(r)^{2(\gamma-1)/(\gamma+1)}\left(E+\frac{GM_\odot}{r}\right), \tag{1.21}$$

and

$$E = \frac{1}{2}v^2 + \frac{\gamma}{\gamma-1}\frac{p}{\rho} - \frac{GM_\odot}{r} \tag{1.22}$$

is the (constant) total energy.

Just as for Parker's solar wind solution, Eq. (1.20) possesses a critical point where $M = 1$ and its right hand side vanishes; moreover, it may be integrated analytically to give $v(r)$ implicitly. However, by selectively choosing the function $A(r)$ it is possible to obtain more than one critical point, and these new points may be either X type or O type in nature, depending on whether $g(r)$ has a minimum or maximum, respectively.

By deriving the function $A(r)$ from observations of coronal holes boundaries (Munro & Jackson 1977), Kopp and Holzer modelled the expansion to be radial at low heights and for large heliocentric distances, while a fast over-radial expansion is assumed to occur near $1.5\,R_\odot$. For high values of this expansion, two extra critical points appear before Parker's X type point (taken to be at $r = 4.5\,R_\odot$), and the wind can become supersonic right after the coronal base. However, after Parker's critical point, the solution begins to approach the classical solar wind solution, hence the presence of a super-radial expansion in the inner corona does not affect at all the velocities at large heliocentric distances.

This model has been later extended by several authors. A different kind of model, based on an expansion of the MHD equations about a spherically symmetric state, was presented by Suess et al. (1977); the resulting hole boundary compares favourably with the above cited observations by Munro and Jackson.

1.5 Characteristics of plasmas and equations of magnetohydrodynamics

The solar atmosphere is, as most of the matter in the whole universe, in the state of *plasma*. A plasma is a fully or partially ionised gas in which the dynamics and the electromagnetic forces interact together in a complex interplay. The fluid motion generates electric currents which create magnetic fields which, in turn, act on the plasma by modifying its dynamics in a truly non-linear way.

For the correct definition of the state of plasma, another condition must be fulfilled: the *collisional* effects, that is the Coulomb scattering between neighbouring charged particles, must be small when compared with the *collective* effects, which are determined by the long range electrodynamic interactions on the plasma as a whole. This property makes a plasma behave in a fundamentally different way from a neutral gas. In the latter, there are no long range interactions but only microscopic, random, binary collisions and these act in a way to keep particles initially close together in a small region, thus allowing for a fluid description. In a plasma, this duty is performed instead by the large number of long range interactions that a particle undergoes simultaneously.

Therefore, plasmas also allow a fluid description. Under certain assumptions, it will then be possible to reduce the system of fluid equations for each species and the Maxwell equations of electrodynamics to a single, self-consistent set of fluid equations, which are known as the *magnetohydrodynamic* (MHD) equations. Here, the MHD equations will be presented and the process of their actual derivation from the kinetic equations will be briefly summarised and discussed. In the last sub-section, attention will be focused on ideal MHD (when all the collisional terms are neglected) and the corresponding equations are those which will be used throughout the thesis.

1.5.1 Physical parameters of plasmas

Consider a fully ionised gas. The first question to answer is on what spatial scale it can be considered as neutral or, in other words, what is the maximum distance beyond which the binary Coulomb collisions become negligible? It may be demonstrated (e.g. Boyd & Sanderson 1969) that the electric potential Φ of a test particle of (positive) charge q inside a plasma is given by

$$\Phi(r) = \frac{q}{r} \exp\left(-\frac{r}{\lambda_D}\right), \tag{1.23}$$

which decays much more rapidly with r (the distance from the test particle) than in void. The quantity λ_D is called the *Debye's shield length*, and its expression is

$$\lambda_D = \left(\frac{k_B T}{4\pi e^2 n}\right)^{1/2}, \tag{1.24}$$

where the temperature T and the number density n are assumed to be the same for protons and electrons. From Eq. (1.23) is clear that for $r > \lambda_D$ the effect of the test particle is completely shielded and the plasma has modified itself in order to reach again the global neutrality state.

The corresponding time scale for this process of charge re-distribution is given by (the inverse of) the so-called plasma frequency:

$$\omega_p = \left(\frac{4\pi e^2 n}{m_e}\right)^{1/2}. \tag{1.25}$$

Note that this time scale coincides with the time taken by an electron travelling with the thermal velocity, v_{th}, to cover a distance λ_D:

$$\lambda_D \omega_p = \left(\frac{k_B T}{m_e}\right)^{1/2} \equiv v_{th}. \tag{1.26}$$

The physical parameters λ_D and ω_p both refer to the collective plasma behaviour. It may be demonstrated that the typical spatial and temporal scales for the collisional effects are of the order of

$$l_c \sim \Lambda \lambda_D \gg \lambda_D, \quad \tau_c \sim \Lambda \omega_p^{-1} \gg \omega_p^{-1}, \tag{1.27}$$

(l_c is the mean free path) where $\Lambda \gg 1$ is the so-called plasma parameter, hence confirming the dominant role of the collective behaviour for a plasma. This plasma parameter is defined as the average number of particles in a Debye's sphere of volume $\sim \lambda_D^3$. By imposing that the potential energy of a particle is much less than its kinetic energy, the result is

$$\frac{e^2}{r} \sim n^{1/3} e^2 \ll k_B T \Rightarrow \Lambda \equiv n \lambda_D^3 \gg 1, \tag{1.28}$$

as expected.

Another important parameter is the equipartition time, that is the time necessary for electrons and protons to exchange their random kinetic energy and to reach a Maxwellian distribution with a common temperature $T = T_e = T_i$. This is found to be

$$\tau_{eq} = \frac{m_i}{m_e} \tau_c. \tag{1.29}$$

The equipartition time for electrons alone (i.e. the time necessary to be able to define an electron temperature T_e) coincides with τ_c, whereas the corresponding value for ions is $\sqrt{m_i/m_e}\tau_c$. Therefore, electrons thermalise first, in a time $\approx \tau_c$, then the ions in a time ≈ 43 times longer and finally the two species thermalise together after a period another ≈ 43 times longer.

Finally, for a (strongly) magnetised plasma the microscopic collisional characteristic parameters have to be modified. The collisional time has to be replaced with the Larmor frequency (for electrons)

$$\omega_L = \frac{eB}{mc} \gg \tau_c^{-1}, \tag{1.30}$$

and the mean free path l_c by the Larmor radius

$$r_L = \omega_L^{-1} v_{th} \ll l_c. \tag{1.31}$$

The net result is that collisional terms in the MHD equations, like the coefficients of thermal and electric conduction, will assume an anisotropic character, because the presence of the magnetic field prevents these effects occurring in directions perpendicular to it.

1.5.2 Derivation of the MHD equations

The first step towards a fluid description of a plasma is the introduction of a *distribution function* for each of the species (protons and electrons for a fully ionised hydrogen gas). In the phase space $(\mathbf{r}, \mathbf{v})$, the average number of particles of species α in a position between $\mathbf{r}$ and $\mathbf{r} + d\mathbf{r}$ and a velocity between $\mathbf{v}$ and $\mathbf{v} + d\mathbf{v}$ is defined to be

$$f_\alpha(\mathbf{r}, \mathbf{v}, t) d^3r\, d^3v \tag{1.32}$$

where the mean is assumed to be over all the possible combinations of microscopic states resulting in the same macroscopic configuration. The fluid element d^3r must be taken much smaller than the characteristic length scale of the system under consideration, but also large enough as to contain a great number of particles. Moreover, this volume should be smaller than Debye's sphere, otherwise all the collisional effects will be lost *a priori*. For charged particles, the kinetic Boltzmann equation for f_α reads

$$\frac{\partial f_\alpha}{\partial t} + \mathbf{v} \cdot \nabla f_\alpha + \frac{q_\alpha}{m_\alpha} \left(\mathbf{E} + \frac{\mathbf{v}}{c} \times \mathbf{B} \right) \cdot \nabla_v f_\alpha = \left(\frac{\partial f_\alpha}{\partial t} \right)_C, \tag{1.33}$$

where the last term takes into account all the collisional effects.

The next step consists in taking the *moments* of this kinetic equation, that is to multiply Eq. (1.33) by progressively increasing powers of $\mathbf{v}$ and then integrate in d^3v. In this way the information regarding the different velocities that different particles have inside the same fluid element are inevitably lost, but this is the price to pay if one wants to simplify the equations. Each of the resulting *transport equations* contains terms with higher order powers of $\mathbf{v}$ (*transport coefficients*). A physical meaning is retained for the zeroth order equation (mass conservation), first order (momentum conservation) and second order (energy conservation). After decomposing the velocity in its *ordered* and *random* components, the set of fluid equations for each species α is found to be:

$$\frac{\partial n_\alpha}{\partial t} + \nabla \cdot (n_\alpha \mathbf{v}_\alpha) = 0, \tag{1.34}$$

$$n_\alpha m_\alpha \frac{\mathrm{d}\mathbf{v}_\alpha}{\mathrm{d}t} = -\nabla P_\alpha - \nabla \cdot \Pi_\alpha + n_\alpha q_\alpha \left(\mathbf{E} + \frac{1}{c} \mathbf{v}_\alpha \times \mathbf{B} \right) + \mathbf{R}_\alpha, \tag{1.35}$$

$$\frac{\mathrm{d}}{\mathrm{d}t} \left(\frac{P_\alpha}{n_\alpha^\gamma} \right) = \frac{1}{c_v n_\alpha^\gamma} \left[-(\Pi_\alpha \cdot \nabla)\mathbf{v}_\alpha - \nabla \cdot \mathbf{h}_\alpha + Q_\alpha \right], \tag{1.36}$$

where $\mathrm{d}/\mathrm{d}t$ is the convective derivative, c_v is the specific heat at constant volume and $\gamma = 5/3$ is the adiabatic index.

If the scalar pressure $P_\alpha = n_\alpha k_B T_\alpha$, which takes into account the flux of random momentum perpendicular to the surface of the fluid element, is considered as an unknown, the transport coefficients are the stress tensor Π_α (which contains the viscous effects, that is the random momentum exchanged tangentially to the fluid element surface), the term $\mathbf{R}_\alpha$ of exchange of momentum due to collisions between particles of different species, the heat current $\mathbf{h}_\alpha$ due to random kinetic energy and the heat Q_α exchanged due to collisions.

The final step in deriving the MHD equations consists of combining together the fluid equations for protons and electrons in order to find a unique set of equations for some global variables (one-fluid equations). First of all, consider length scales of the order of, or greater than, Debye's lenght λ_D, so that $n_e \simeq n_i \simeq n$. Then, since $m_i \gg m_e$ the mass density of the fluid and its momentum correspond both approximately to those of the ion component:

$$\rho \equiv m_i n_i + m_e n_e \simeq m_i n; \quad \rho \mathbf{V} \equiv m_i n_i \mathbf{v}_i + m_e n_e \mathbf{v}_e \simeq m_i n \mathbf{v} \Rightarrow \mathbf{V} \approx \mathbf{v}_i. \tag{1.37}$$

Moreover, the charge and current densities become, respectively:

$$\rho_q \equiv e n_i - e n_e \simeq 0; \quad \mathbf{J} \equiv e n_i \mathbf{v}_i - e n_e \mathbf{v}_e \simeq e n (\mathbf{V} - \mathbf{v}_e). \tag{1.38}$$

Note that the assumptions that the inertia of the plasma is carried by the ions alone is true only in a low frequency regime. If the time scales are of the order of ω_p^{-1} or smaller, then the ions do not have time to respond to the perturbations and the inertia will be carried by the electrons instead. The last condition is that of non-relativistic velocities $V \ll c$, so that the displacement current in the Maxwell's equations may be neglected.

The resulting MHD equations are:

- *Continuity equation*

$$\frac{\partial \rho}{\partial t} + \nabla \cdot (\rho \mathbf{V}) = 0, \tag{1.39}$$

- *Momentum equation*

$$\rho \frac{\mathrm{d}\mathbf{V}}{\mathrm{d}t} = -\nabla P - \nabla \cdot \Pi + \frac{1}{c}\mathbf{J} \times \mathbf{B}, \tag{1.40}$$

  where $P = P_i + P_e$ and $\Pi = \Pi_i + \Pi_e$,

- *Generalised Ohm's law*

$$\mathbf{E} + \frac{1}{c}\mathbf{V} \times \mathbf{B} = \frac{1}{en}\left(\frac{1}{c}\mathbf{J} \times \mathbf{B} - \nabla P_e - \nabla \cdot \Pi_e + \mathbf{R}\right), \tag{1.41}$$

  where $\mathbf{R} = \mathbf{R}_e = -\mathbf{R}_i$ is the electric resistivity term,

- *Energy equation*

$$\frac{\mathrm{d}}{\mathrm{d}t}\left(\frac{P}{\rho^\gamma}\right) = \frac{1}{c_v \rho^\gamma}\left[-(\Pi \cdot \nabla)\mathbf{V} - \nabla \cdot \mathbf{h} + \mathbf{R} \cdot \frac{\mathbf{J}}{en}\right] + \frac{\mathbf{J}}{en} \cdot \nabla\left(\frac{P_e}{\rho^\gamma}\right), \tag{1.42}$$

  valid for pure elastic collisions, for which $Q_i + Q_e = -\mathbf{R} \cdot (\mathbf{v}_i - \mathbf{v}_e) = \mathbf{R} \cdot \mathbf{J}/en$,

- *Maxwell's equations*

$$\nabla \times \mathbf{E} = -\frac{1}{c}\frac{\partial \mathbf{B}}{\partial t}, \quad \nabla \times \mathbf{B} = \frac{4\pi}{c}\mathbf{J}, \quad \nabla \cdot \mathbf{B} = 0. \tag{1.43}$$

In order to close the system, some physical assumptions are needed to express the transport coefficients $\mathbf{R}, \Pi$ and $\mathbf{h}$ in terms of the known quantities. This is possible if the velocity distribution is locally quasi-Maxwellian, that is if the characteristic spatial and temporal scales of the system are much greater than the corresponding collisional scales:

$$1/\nabla \sim l \gg l_c, \qquad 1/\frac{\partial}{\partial t} \sim \tau > \tau_{eq} \gg \tau_c. \tag{1.44}$$

Note that when these two conditions hold, the conditions for the one-fluid approximation are automatically satisfied too, since $l_c \gg \lambda_D$ and $\tau_c \gg \omega_p^{-1}$. For typical coronal values, both these plasma parameters are very small:

$$\lambda_D \simeq 0.69 \left(\frac{T/10^6\,\mathrm{K}}{n/10^8\,\mathrm{cm}^{-3}} \right)^{1/2} \mathrm{cm}; \qquad \omega_p \simeq \left(\frac{n}{10^8\,\mathrm{cm}^{-3}} \right) \times 10^{22}\,\mathrm{rad\ s}^{-1}, \tag{1.45}$$

so that the conditions for the validity of the MHD equations are easily fulfilled and, in general, all the collisional terms will be very small.

Under the conditions of Eqs. (1.44), the following relations have been found (Braginsky 1965):

- The resistivity term is related to the electric current as

$$\frac{\mathbf{R}}{en} = \frac{\mathbf{J}}{\sigma}, \qquad \sigma \approx \sigma_e = \frac{ne^2\tau_c}{m_e} \sim T_e^{3/2}, \tag{1.46}$$

  where σ is the electric conduction coefficient.

- The stress tensor components may be expressed in terms of the derivatives of the macroscopic velocity $\mathbf{V}$ as

$$\Pi_{ij} = -\eta \left(\frac{\partial V_i}{\partial x_j} + \frac{\partial V_j}{\partial x_i} - \frac{2}{3} \nabla \cdot \mathbf{V}\, \delta_{ij} \right), \qquad \eta \approx \eta_i = \frac{n m_i l_c^2}{\tau_c} \sim T_i^{5/2}, \tag{1.47}$$

  where η is the viscosity coefficient.

- The heat flux current is given by

$$\mathbf{h} = -\kappa \nabla T, \qquad \kappa \approx \kappa_e = \frac{n l_c^2}{\tau_c} \sim T_e^{5/2}, \tag{1.48}$$

  where κ is the thermal conduction coefficient.

Finally, when the plasma is strongly magnetised ($\omega_p \tau_c \gg 1$), a preferential direction is introduced by the field. The condition for the characteristic length scale splits into the two expressions

$$1/\nabla_{\|} \sim l_{\|} \gg l_c, \qquad 1/\nabla_{\perp} \sim l_{\perp} \gg r_L, \tag{1.49}$$

where the preferential direction is obviously that of the local magnetic field $\mathbf{B}$. One of the resulting effects is the modification of the transport coefficients. In particular, thermal conduction across the magnetic field is strongly inhibited, since the corresponding coefficient is

$$\kappa_{\perp} = \frac{\kappa_{\|}}{(\omega_L \tau_D)^2} \ll \kappa_{\|}, \tag{1.50}$$

and $\kappa_{\|}$ is the normal thermal conduction coefficient defined in Eq. (1.48).

1.5.3 Ideal MHD

In the remainder of this thesis, all the collisional effects will be considered to be negligible with respect to the ideal terms. The set of ideal MHD equations is usually written by eliminating the electric field and the current density to yield

$$\frac{\partial \rho}{\partial t} + \nabla \cdot (\rho \mathbf{V}) = 0, \tag{1.51}$$

$$\rho \left(\frac{\partial}{\partial t} + \mathbf{V} \cdot \nabla \right) \mathbf{V} = -\nabla P + \frac{1}{4\pi} (\nabla \times \mathbf{B}) \times \mathbf{B}, \tag{1.52}$$

$$\frac{\partial \mathbf{B}}{\partial t} = \nabla \times (\mathbf{V} \times \mathbf{B}), \tag{1.53}$$

$$\left(\frac{\partial}{\partial t} + \mathbf{V} \cdot \nabla \right) \left(\frac{P}{\rho^\gamma} \right) = 0, \tag{1.54}$$

that is a system of eight equations in the eight unknowns ρ, $\mathbf{V}$, $\mathbf{B}$ and P.

The solenoidal relation

$$\nabla \cdot \mathbf{B} = 0 \tag{1.55}$$

may be considered as an initial condition, since if it is satisfied at $t = 0$, the induction equation, Eq. (1.53), guarantees that it will be always fulfilled. Once the equations are solved, the other two divergence-free vectors may be derived from Ohm's and Ampere's equations

$$\mathbf{E} + \frac{1}{c} \mathbf{V} \times \mathbf{B} = 0, \qquad \nabla \times \mathbf{B} = \frac{4\pi}{c} \mathbf{J}, \tag{1.56}$$

and the temperature T from the ideal gas law

$$P = \frac{k_B}{\mu m_p} \rho T, \tag{1.57}$$

where μ is the mean molecular weight ($\mu \simeq 0.6$ in the solar corona).

Throughout the thesis, different forms of the energy equation, rather then just the adiabatic relation, Eq. (1.54), will be assumed. If the index γ is varied from its adiabatic value 5/3 down to the isothermal value $\gamma = 1$, various forms of heating may be simulated. In this case γ is called the polytropic index. Another possibility is to assume an incompressible plasma, $\mathrm{d}\rho/\mathrm{d}t = 0$, for which the energy equation is replaced by

$$\nabla \cdot \mathbf{V} = 0. \tag{1.58}$$

An important dimensionless parameter comes directly from an analysis of the momentum equation. The dynamics of the system may be driven by two different forces: that due

to the gas pressure gradient and that due to the magnetic field. The relative importance of these two kinds of forces is usually expressed through a simple parameter called the plasma β, which is defined as the ratio between the kinetic pressure and the magnetic pressure

$$\beta = \frac{P}{B^2/8\pi}, \tag{1.59}$$

where the magnetic pressure is derived from the Lorentz force term through the vector relation Eq. (A-9). This parameter also corresponds to the ratio of the squares of the two characteristic velocities in an ideal plasma, which are the sonic and Alfvén velocities:

$$c_s = \sqrt{\gamma \frac{P}{\rho}}, \qquad v_A = \frac{B}{\sqrt{4\pi\rho}}, \tag{1.60}$$

corresponding, respectively, to the response of the plasma to pressure or magnetic field perturbations.

For typical coronal values, the plasma β is usually very small and therefore the magnetic field is dominant over the other forces. The three quantities defined above have the approximate values:

$$\beta \simeq 0.35 \left(\frac{n}{10^8\,\mathrm{cm}^{-3}}\right)\left(\frac{T}{10^6\,\mathrm{K}}\right)\left(\frac{B}{1\,\mathrm{G}}\right)^{-2}, \tag{1.61}$$

$$c_s \simeq 166 \left(\frac{T}{10^6\,\mathrm{K}}\right)^{1/2} \mathrm{km\ s}^{-1}, \tag{1.62}$$

$$v_A \simeq 280 \left(\frac{n}{10^8\,\mathrm{cm}^{-3}}\right)^{-1/2}\left(\frac{B}{1\,\mathrm{G}}\right) \mathrm{km\ s}^{-1}, \tag{1.63}$$

where it is worth noticing the rather fast decay of the value of β with the magnetic field strength.

1.6 Outline of the thesis

This thesis is concerned with dynamical MHD equilibria, applied to models for different kinds of flows in the solar atmosphere. In Chapter 2 the mathematical formalism for steady flows in systems with one ignorable coordinate will be presented, discussing in detail the reduced equations and their mathematical nature. A method for finding exact solutions in the incompressible limit will also be shown and applied. In Chapter 3 this formalism will be further developed to the study of steady flows in magnetic structures in the solar atmosphere and different techniques will be presented. These techniques will be then applied in Chapters 4 and 5 where, respectively, MHD models for quiescent

prominences (closed magnetic structures) and polar plumes (open magnetic structures) will be discussed. In Chapter 6, some time dependent simulations will be performed in order to study the reactions of a spherically symmetric, isothermal atmosphere to changes of the conditions at the external boundary. Finally, in Chapter 7, all the results obtained will be summarised and further discussed. Also, future work will be proposed, with particular attention to a 2-D full MHD code which is currently being tested. More specific subject are presented separately in four appendices.

Chapter 2

Symmetric MHD equilibria

2.1 Introduction

The system of equations of ideal magnetohydrodynamics, derived in Sect 1.5, may be used to describe mathematically a wide variety of astrophysical phenomena. Therefore the solution of the MHD equations is of fundamental importance in the research of theoretical astrophysics. Despite the simplifications introduced by neglecting the collisional terms in the equations, the resolution of the *complete* set of ideal MHD still remains a formidable task, which can be tackled only by means of computer simulations. However, in order to make some analytical progress, and thus in order to gain a deeper understanding of the physics of MHD, some simplifying assumptions can be made.

The most obvious choice is certainly to start looking for time independent solutions. This approach is justified whenever the system under consideration evolves in time according to time scales which are larger than the typical length scale divided by the average characteristic velocities, that is the sound and Alfvén speeds. The research for stationary solutions is of primary importance, since they may represent the final configurations to which nature tends. Moreover, once a steady structure has been found it will always be possible to study its stability by perturbing it. That is why analytical solutions to the MHD set of equations are fundamental for any study of either wave propagation or instability evolution.

In spite of the great simplification that the hypothesis $\partial/\partial t = 0$ introduces, the *only* known general solution to the MHD steady equations is the so-called *equipartition solution*

(Chandrasekhar 1956):

$$\rho = \text{const}, \quad P + B^2/8\pi + \rho\Phi = \text{const}, \quad \mathbf{V} = \pm\mathbf{B}/\sqrt{4\pi\rho}, \tag{2.1}$$

where Φ is the potential energy per mass unit of all the conservative external forces acting on the system (e.g. gravity). This particular solution has very strict constraints, namely the plasma has to be incompressible with constant density everywhere, and the velocity must be equal (in modulus) to the local Alfvén speed. On the other hand, there is a complete freedom in the spatial 3-D structure of the magnetic field.

The second step towards the analytic resolution of the ideal MHD equations is usually the assumption of *spatial symmetry* of the system, thus all the physical quantities depend just on two spatial coordinates while the third coordinate is ignorable. The situation in which the physical vectors retain their three components but they depend upon two coordinates is generally indicated with the term 2.5-D.

Symmetric systems allow for drastic simplifications in the structure of the steady MHD equations. It will be shown that the whole set reduces to just two coupled equations: a second order PDE for the *magnetic flux function* A (which gives the geometrical structure of the magnetic field), known either as the *generalised Grad-Shafranov equation* (since it is the generalisation of the equation derived originally for static equilibria of fusion plasmas) or as the *transfield equation* (since it is obtained by projecting the momentum equation across the magnetic fieldlines), and an equation for the density ρ along the magnetic field, known as the *generalised Bernoulli equation.*

The derivation of these two equations and the discussion of their mathematical nature will be done here in a generic system of orthogonal coordinates (x_1, x_2, x_3), under the assumption $\partial/\partial x_3 \equiv 0$. In the ordinary 3-D Euclidean space the most general geometry satisfying the symmetry requirement

$$\frac{\partial g_{ij}}{\partial x_3} = 0, \tag{2.2}$$

where g_{ij} are the covariant components of the metric tensor, is the helical symmetry (see Solov'ev 1967 and Edenstrasser 1980b for different demonstrations), which includes the translational and rotational symmetries as particular cases. The helical system of coordinates is intrinsically curvilinear and non-orthogonal, thus it will not be treated here for simplicity. Anyway, the only difference in the final form of the reduced equations is just an extra term that appears in the transfield equation. Unified treatments in a

generic curvilinear system can be found in Edenstrasser (1980a), for the static case, Agim & Tataronis (1985) and Del Zanna & Chiuderi (1996), for dynamical MHD equilibria, whereas the helical symmetry has been studied first by Morozov & Solov'ev (1963) and later by Tsinganos (1982b), as an extension of his previous study in orthogonal systems (Tsinganos 1981, 1982a).

In the present chapter the problem of symmetric MHD equilibria will be tackled gradually. Section 2.2 deals with static equilibria ($\mathbf{V} = 0$) and the original Grad-Shafranov equation is derived. In Sect. 2.3 the more general dynamical case is studied and the nature of the equations is discussed, as it is affected by the presence of the steady flow. The incompressible case, for which the two equations are no longer coupled and *completely analytical* solutions can be found, will be treated separately in Sect. 2.4. A new method for finding exact solutions for steady, incompressible flows will be presented in Sect. 2.5 and novel classes of solutions will be derived in three different geometries of physical relevance. Finally, Sect. 2.6 contains a brief discussion and the conclusions to the problem of MHD dynamic equilibria.

2.2 Static equilibria

The first, systematic attempts to solve the ideal MHD equations were made in the fifties, within the research of static configurations for thermonuclear fusion of laboratory plasmas. These configurations were often treated as axisymmetric in a toroidal geometry (*tokamaks*).

The introduction of the magnetic flux function (originally called ψ, while here the notation A will be used throughout) is due to Shafranov (1957). It is interesting to note that Shafranov derived his formalism directly from the (incompressible) hydrodynamic theory, simply by replacing the velocity $\mathbf{V}$ with the magnetic field $\mathbf{B}$ and the vorticity $\nabla \times \mathbf{V}$ with the current density $\mathbf{J} \propto \nabla \times \mathbf{B}$. The Grad-Shafranov equation for A, which will be derived here, provides a self-consistent description of the static MHD equilibrium problem and it is possibly the most extensively studied equation in plasma physics.

The formalism of the magnetic flux function will be introduced in the following subsection, while Sect. 2.2.2 will be devoted to the derivation and discussion of the Grad-Shafranov equation.

2.2.1 The magnetic flux function A and its integrals

The equations for static MHD equilibria are easily derived from the ideal MHD set by letting

$$\frac{\partial}{\partial t} \equiv 0, \qquad \mathbf{V} = 0 \tag{2.3}$$

everywhere. Thus the only two equations left are respectively the solenoidal relation and the momentum balance

$$\nabla \cdot \mathbf{B} = 0, \tag{2.4}$$

$$\frac{1}{4\pi}(\nabla \times \mathbf{B}) \times \mathbf{B} - \nabla P = 0, \tag{2.5}$$

where external forces will be here neglected for simplicity. Note that in the static case, in absence of gravity, the density does not appear in the equations and the equilibrium magnetic structure is hence independent on the thermodynamics of the system.

In a generic orthogonal coordinate system (x_1, x_2, x_3), with invariance along the third coordinate

$$\frac{\partial}{\partial x_3} \equiv 0, \tag{2.6}$$

the solenoidal relation Eq. (2.4) reads (see Appendix A for the formulae of vector calculus in an orthogonal coordinate system):

$$\frac{1}{h_1 h_2 h_3}\left[\frac{\partial}{\partial x_1}(h_2 h_3 B_1) + \frac{\partial}{\partial x_2}(h_1 h_3 B_2)\right] = 0. \tag{2.7}$$

Thus the *poloidal* part of the vector $\mathbf{B}$ (i.e. orthogonal to the symmetry direction $\mathbf{e}_3$) may be derived from a single function $A(x_1, x_2)$:

$$B_1 = \frac{1}{h_2 h_3}\frac{\partial A}{\partial x_2}, \qquad B_2 = -\frac{1}{h_1 h_3}\frac{\partial A}{\partial x_1}, \tag{2.8}$$

and the field $\mathbf{B}$ may be written in two equivalent vectorial forms:

$$\mathbf{B} = \nabla \times \left(\frac{A}{h_3}\mathbf{e}_3\right) + B_3\mathbf{e}_3 = \frac{\nabla A}{h_3} \times \mathbf{e}_3 + B_3\mathbf{e}_3. \tag{2.9}$$

From the first expression it is clear that the function A coincides with the third covariant component of the usual vector potential $\mathbf{A}$ ($\mathbf{B} = \nabla \times \mathbf{A}$), whereas the latter readily yields

$$\mathbf{B} \cdot \nabla A = 0. \tag{2.10}$$

This relation is very important, since it means that the fieldlines must lie on the *magnetic surfaces* $A(x_1, x_2) = \text{const}$. Moreover, it is easily demonstrated (e.g. Edenstrasser

1980a) that the function $A(x_1, x_2)$ coincides with the *transverse* flux of $\mathbf{B}$ across the surface $A(x_1, x_2) = \text{const}$, that is the reason why A is known as a flux function. From the second expression in Eq. (2.9) a new set of orthogonal *magnetic coordinates* may be derived: ∇A, being normal to the magnetic surfaces, $\mathbf{e}_3$, the invariance direction, and $\nabla A \times \mathbf{e}_3$, lying on the magnetic surfaces and perpendicular to $\mathbf{e}_3$. The momentum equation (2.5) will be now decomposed in this new coordinate set.

Thanks to the symmetry in x_3, the scalar product of Eq. (2.5) with $\mathbf{e}_3$ yields

$$\mathbf{B} \cdot \nabla(h_3 B_3) = 0, \tag{2.11}$$

hence the quantity $h_3 B_3$ (the third covariant component of $\mathbf{B}$) must be constant on magnetic surfaces, thus

$$B_3 = \frac{I}{h_3}, \tag{2.12}$$

where $I = I(A)$ is a free function of the magnetic flux function. With analogy to the relation between A and $\mathbf{B}$, it may be shown that I is related to the transverse flux of the divergence-less vector $\mathbf{J} = (c/4\pi)\nabla \times \mathbf{B}$. By using the magnetic coordinates the expression for the electric current becomes

$$\mathbf{J} = \frac{c}{4\pi} \frac{\mathrm{d}I}{\mathrm{d}A} \frac{\nabla A}{h_3} \times \mathbf{e}_3 + J_3 \mathbf{e}_3, \tag{2.13}$$

hence also $\mathbf{J}$ lies on the magnetic surfaces $A(x_1, x_2) = \text{const}$ ($\mathbf{J} \cdot \nabla A = 0$).

Before proceeding with the actual derivation of the equation for A, another integral of the system can be obtained by projecting Eq. (2.5) along the magnetic field, that is simply:

$$\mathbf{B} \cdot \nabla P = 0. \tag{2.14}$$

Hence, the pressure itself is another free function of A, $P = P(A)$, and therefore isobaric surfaces actually coincide with magnetic surfaces. This ceases to be true when an external force, like gravity, is present.

2.2.2 The Grad-Shafranov equation

The equation for the magnetic flux function A is derived from the momentum equation by projecting it *across* the fieldlines, that is in the direction ∇A normal to the magnetic surfaces. That is the reason why it is generally referred to as the *transfield* equation, as

it takes into account the momentum balance across different magnetic surfaces. By using Eqs. (2.13) and (2.9), Eq. (2.5) becomes

$$\left(-\frac{4\pi}{c}\frac{J_3}{h_3}+\frac{B_3}{h_3}\frac{\mathrm{d}I}{\mathrm{d}A}+4\pi\frac{\mathrm{d}P}{\mathrm{d}A}\right)\nabla A=0. \tag{2.15}$$

The expression for J_3, from the curl of Eq. (2.9), is

$$\frac{4\pi}{c}J_3=-h_3\nabla\cdot\left(\frac{\nabla A}{h_3^2}\right), \tag{2.16}$$

so that the final form of the transfield equation may be written as

$$\nabla\cdot\left(\frac{\nabla A}{h_3^2}\right)+\frac{I}{h_3^2}\frac{\mathrm{d}I}{\mathrm{d}A}+4\pi\frac{\mathrm{d}P}{\mathrm{d}A}=0. \tag{2.17}$$

This is the Grad-Shafranov equation expressed in a generic orthogonal system, whereas the original equation was derived in cylindrical coordinates ($h_3=r$) under the hypothesis of axisymmetry ($\partial/\partial\phi=0$).

Equation (2.17) is a quasi-linear, second order PDE for the unknown function $A(x_1,x_2)$. Its linearity depends upon the choice for the two arbitrary functions (integrals) $I(A)$ and $P(A)$, to be specified *a priori*. This is the main difficulty in solving Eq. (2.17), since the current flux I and the gas pressure P have to be given as functions of the magnetic geometry before this is known. The linear, second order operator is known as the Shafranov operator and reduces to the usual Laplacian operator in translational symmetry ($h_3=1$). Its general form is

$$\nabla\cdot\left(\frac{\nabla A}{h_3^2}\right)=\frac{1}{h_1h_2h_3}\left[\frac{\partial}{\partial x_1}\left(\frac{h_2}{h_1h_3}\frac{\partial A}{\partial x_1}\right)+\frac{\partial}{\partial x_2}\left(\frac{h_1}{h_2h_3}\frac{\partial A}{\partial x_2}\right)\right], \tag{2.18}$$

and is clearly elliptic in nature.

Once the magnetic flux is found by solving the transfield equation, the magnetic field components are given by Eqs. (2.8) and (2.12). Note that the electric current may be expressed, by combining the relations for $\mathbf{B}$ and $\mathbf{J}$ with the transfield equation, as

$$\frac{4\pi}{c}\mathbf{J}=\frac{\mathrm{d}I}{\mathrm{d}A}\mathbf{B}+4\pi\frac{\mathrm{d}P}{\mathrm{d}A}h_3\mathbf{e}_3, \tag{2.19}$$

from which is apparent that for *force free* fields ($\nabla P=0$) the current is actually parallel to the magnetic field and the relation

$$\nabla\times\mathbf{B}=\alpha\mathbf{B};\qquad \alpha=\alpha(A)=\frac{\mathrm{d}I}{\mathrm{d}A} \tag{2.20}$$

holds for symmetric systems. Constant-α magnetic force free structures are hence found by letting I to be a linear function of A, whereas current-free configurations (potential) require $I=\text{const}$.

2.3 Dynamic equilibria

The more general problem of symmetric, stationary MHD flows will be addressed here. If the study of symmetric static equilibria is very important in the field of laboratory plasma physics, symmetric, MHD dynamic structures are widespread in a great variety of astrophysical situations. These range from stellar or galactic winds and jets (generally in spherical coordinates under the assumption of azimuthal invariance), to various kinds of flows in the solar atmosphere, such as the so-called Evershed flows around sunspots (cylindrical coordinates and again axisymmetry) or siphon flows in coronal arcades or loops (usually treated as Cartesian 2-D structures, hence with translational symmetry along the third direction, or as flux tubes in cylindrical geometry).

Symmetric MHD flows were first considered by Chandrasekhar (1956), who treated the time dependent equations for an axisymmetric, incompressible plasma with a finite electric conductivity. Steady, axisymmetric flows were studied by Woltjer (1959a, 1959b), who extended the formalism of the flux function A to the dynamical case and showed that an incompressible flow can be described by four integrals of A, whereas polytropic, compressible flows require an extra integral. Grad (1960) first identified the Alfvénic singularity in the velocity field for an axisymmetric plasma, but the problem of critical velocities and its implication on the mathematical nature of the generalised transfield equation remained unexplored until the early seventies (Zehrfeld & Green 1972). Finally, relativistic, symmetric MHD flows are treated in Lovelace et al. (1986) and Bogovalov (1994).

In this section the equations for a symmetric, stationary flow will be derived following the formalism introduced for static equilibria in the previous section, therefore the orthogonal coordinate system (x_1, x_2, x_3) and invariance $\partial/\partial x_3 = 0$ will be assumed throughout.

2.3.1 Integrals of the equations

Consider here the ideal MHD equations, presented in Sect. 1.5.3, under the assumption of a stationary flow ($\partial/\partial t \equiv 0$):

$$\nabla \cdot \mathbf{B} = 0, \tag{2.21}$$

$$\nabla \cdot (\rho \mathbf{V}) = 0, \tag{2.22}$$

$$\nabla \times (\mathbf{V} \times \mathbf{B}) = 0, \tag{2.23}$$

$$\rho(\mathbf{V}\cdot\nabla)\mathbf{V} = \frac{1}{4\pi}(\nabla\times\mathbf{B})\times\mathbf{B} - \nabla P - \rho\nabla\Phi, \tag{2.24}$$

where this time the presence of an external, conservative force is allowed in the momentum equation.

Since the solenoidal relation (2.21) is the same as in the static case, all the expressions from Eqs. (2.7) to (2.10) are still valid here. Analogous relations are found for the other divergence-free vector $\rho\mathbf{V}$, thus its poloidal part may be derived from a *stream function* $\tilde{\Psi}$ (proportional to the corresponding mass flux across a stream surface) as

$$4\pi\rho V_1 = \frac{1}{h_2 h_3}\frac{\partial\tilde{\Psi}}{\partial x_2}, \quad 4\pi\rho V_2 = -\frac{1}{h_1 h_3}\frac{\partial\tilde{\Psi}}{\partial x_1}. \tag{2.25}$$

Consider now the induction equation, Eq. (2.23). Its projection along the poloidal directions x_1 and x_2 yields

$$h_3(V_1 B_2 - V_2 B_1) = \text{const.} \tag{2.26}$$

This constant, which is proportional to the component of the electric field along the invariance direction, has always been set to zero in all previous treatments of symmetric equilibria, thus implying parallelism between the poloidal components of the two fields.

The only work in which the general case $E_3 \neq 0$ is considered is a recent paper by Contopoulos (1996), where some self-similar solutions for axisymmetric astrophysical jets are derived. However, three problems appear to arise when $E_3 \neq 0$ is considered. First, the mathematics involved becomes so complicated (the derivation of a single equation for the flux function is not possible) that the analytical approach is no longer convenient. Second, not to have the poloidal velocity parallel to the magnetic field means that the magnetic surfaces are continuously advected towards or from the magnetic axis of the system (at a rate proportional to E_3), which hence must act as a magnetic sink or source, respectively. Third, for symmetries other than the translational one, the quantity $V_1 B_2 - V_2 B_1$ might diverge at some points; for example, in cylindrical axisymmetry ($h_3 = r$) that quantity becomes infinite on the axis $r = 0$.

For all these reasons here the standard assumption $E_3 = 0$ will be adopted. In this case the poloidal components of $\mathbf{B}$ and $\mathbf{v}$ are proportional and the two fields may be written as

$$\mathbf{B} = \frac{\nabla A}{h_3}\times\mathbf{e}_3 + B_3\mathbf{e}_3, \quad \mathbf{V} = \frac{\Psi}{4\pi\rho}\frac{\nabla A}{h_3}\times\mathbf{e}_3 + V_3\mathbf{e}_3, \tag{2.27}$$

where $\Psi = \Psi(A) = \mathrm{d}\tilde{\Psi}/\mathrm{d}A$ is the first integral for symmetric, dynamic equilibria. From these expressions the strong coupling of the fields, due to the steady induction equation for

symmetric systems, becomes apparent, since they both lie on the same surfaces ($\mathbf{B}\cdot\nabla A = \mathbf{V}\cdot\nabla A = 0$). The cross product of the two fields (proportional to the electric field) reads

$$\mathbf{V}\times\mathbf{B} = \left(\frac{V_3}{h_3} - \frac{\Psi}{4\pi\rho}\frac{B_3}{h_3}\right)\nabla A. \tag{2.28}$$

Since this quantity must be necessarily normal to $\mathbf{B}$ (and $\mathbf{V}$), the expression within brackets

$$\frac{V_3}{h_3} - \frac{\Psi}{4\pi\rho}\frac{B_3}{h_3} = \Omega \tag{2.29}$$

must be a function of A, therefore $\Omega = \Omega(A)$ is the second integral (proportional to the derivative of the electric potential in respect with A).

In the particular case of an axisymmetric, non-uniformly rotating system ($\Psi = 0$), for example a magnetised star, Eq. (2.29) reduces to the well known *isorotation law* (Ferraro 1937), for which the angular velocity must be constant on the magnetic surfaces, that is

$$\frac{V_\phi}{r\sin\theta} = \Omega(A). \tag{2.30}$$

Any violation of this law causes the lines of force to be drawn out in the direction of motion, giving rise to a time dependent toroidal component of the field.

Note that Eq. (2.29) yields another interesting relation

$$\mathbf{V} = \frac{\Psi}{4\pi\rho}\mathbf{B} + \Omega h_3 \mathbf{e}_3, \tag{2.31}$$

that means that the velocity is parallel to the magnetic field if, and only if, the free function $\Omega(A)$ is set to zero.

The third integral is obtained by analogy with Eqs. (2.11) and (2.12) for the static case. The third component of the momentum equation, Eq. (2.24), may be written as

$$\mathbf{B}\cdot\nabla(h_3 B_3) - 4\pi\rho\mathbf{V}\cdot\nabla(h_3 V_3) = 0, \tag{2.32}$$

from which is clear that the quantity

$$h_3 B_3 - \Psi h_3 V_3 = I \tag{2.33}$$

must be another free function of A, $I = I(A)$, and when $\Psi = 0$ the static relation is recovered.

Finally, by making use of Eqs. (2.29) and (2.33) it is possible to give the expressions for the vector fields $\mathbf{B}$ and $\mathbf{V}$ in terms of the density ρ, the flux function A and the three

integrals Ψ, Ω and I:

$$\mathbf{B} = \frac{\nabla A}{h_3} \times \mathbf{e}_3 + \frac{1}{h_3} \frac{I + h_3^2 \Omega \Psi}{1 - \Psi^2/4\pi\rho} \mathbf{e}_3, \tag{2.34}$$

$$\mathbf{V} = \frac{\Psi}{4\pi\rho} \frac{\nabla A}{h_3} \times \mathbf{e}_3 + \frac{1}{h_3} \frac{I\Psi/4\pi\rho + h_3^2 \Omega}{1 - \Psi^2/4\pi\rho} \mathbf{e}_3. \tag{2.35}$$

Note the presence of a singularity in the third components of the fields, unless

$$M_A^2 \equiv \frac{\Psi^2}{4\pi\rho} = 1 \Leftrightarrow I + h_3^2 \Omega \Psi = 0, \tag{2.36}$$

where $M_A = |\mathbf{V}_\mathrm{p}|/(|\mathbf{B}_\mathrm{p}|/\sqrt{4\pi\rho})$ indicates the poloidal Alfvénic Mach number. The singularity in the denominators of B_3 and V_3, which will also be found in the equation for A, is a direct consequence of the parallelism between the poloidal components of the two fields and disappears in time dependent simulations, non-symmetric steady systems and in symmetric steady flows with a non-vanishing third component of the electric field, that is a non-zero constant in Eq. (2.26) (Contopoulos 1996).

2.3.2 The generalised Grad-Shafranov and Bernoulli equations

As was done in the static case, consider now the momentum equation. By using the two following expressions

$$(\nabla \times \mathbf{B}) \times \mathbf{B} = -\left\{ \left[\nabla \cdot \left(\frac{\nabla A}{h_3^2} \right) \right] \nabla A + \frac{B_3}{h_3} \nabla (h_3 B_3) \right\}, \tag{2.37}$$

$$(\nabla \times \mathbf{V}) \times \mathbf{V} = -\left\{ \frac{\Psi}{4\pi\rho} \left[\nabla \cdot \left(\frac{\Psi}{4\pi\rho} \frac{\nabla A}{h_3^2} \right) \right] \nabla A + \frac{V_3}{h_3} \nabla (h_3 V_3) \right\}, \tag{2.38}$$

and expanding the term in square brackets in Eq. (2.38), the momentum equation reads

$$\left[\left(1 - \frac{\Psi^2}{4\pi\rho} \right) \nabla \cdot \left(\frac{\nabla A}{h_3^2} \right) - \frac{\Psi}{4\pi\rho} \frac{\mathrm{d}\Psi}{\mathrm{d}A} \frac{|\nabla A|^2}{h_3^2} + \frac{\Psi^2}{4\pi\rho} \frac{\nabla \rho}{\rho} \cdot \frac{\nabla A}{h_3^2} \right] \nabla A +$$

$$\left[\frac{B_3}{h_3} \nabla (h_3 B_3) - 4\pi\rho \frac{V_3}{h_3} \nabla (h_3 V_3) \right] + 4\pi\rho \left\{ \frac{\nabla P}{\rho} + \nabla \left[\frac{1}{2} \left(\frac{\Psi}{4\pi\rho} \right)^2 \frac{|\nabla A|^2}{h_3^2} + \frac{V_3^2}{2} + \Phi \right] \right\} = 0. \tag{2.39}$$

The use of the definitions of the integrals Ω and I, Eqs. (2.29) and (2.33), allows one to write the second term in Eq. (2.39) as

$$\left[\frac{1}{h_3^2} (I + h_3 V_3 \Psi) \left(\frac{\mathrm{d}I}{\mathrm{d}A} + h_3 V_3 \frac{\mathrm{d}\Psi}{\mathrm{d}A} \right) + 4\pi\rho h_3 V_3 \frac{\mathrm{d}\Omega}{\mathrm{d}A} \right] \nabla A - 4\pi\rho \nabla (h_3 V_3 \Omega), \tag{2.40}$$

so that the momentum equation may be finally decomposed in its two *natural* components; along the magnetic field (generalised Bernoulli equation):

$$\mathbf{B} \cdot \left\{ \frac{\nabla P}{\rho} + \nabla \left[\frac{1}{2} \left(\frac{\Psi}{4\pi\rho} \right)^2 \frac{|\nabla A|^2}{h_3^2} + \frac{V_3^2}{2} + \Phi - h_3 V_3 \Omega \right] \right\} = 0, \tag{2.41}$$

and across the magnetic surfaces (generalised Grad-Shafranov or transfield equation):

$$\left(1-\frac{\Psi^2}{4\pi\rho}\right)\nabla\cdot\left(\frac{\nabla A}{h_3^2}\right)-\frac{\Psi}{4\pi\rho}\frac{\mathrm{d}\Psi}{\mathrm{d}A}\frac{|\nabla A|^2}{h_3^2}+\frac{\Psi^2}{4\pi\rho}\frac{\nabla\rho}{\rho}\cdot\frac{\nabla A}{h_3^2}+\frac{1}{h_3^2}\left(I+h_3V_3\Psi\right)\left(\frac{\mathrm{d}I}{\mathrm{d}A}+h_3V_3\frac{\mathrm{d}\Psi}{\mathrm{d}A}\right)$$

$$+4\pi\rho h_3V_3\frac{\mathrm{d}\Omega}{\mathrm{d}A}+4\pi\rho\left\{\frac{\nabla P}{\rho}+\nabla\left[\frac{1}{2}\left(\frac{\Psi}{4\pi\rho}\right)^2\frac{|\nabla A|^2}{h_3^2}+\frac{V_3^2}{2}+\Phi-h_3V_3\Omega\right]\right\}\cdot\frac{\nabla A}{|\nabla A|^2}=0, \tag{2.42}$$

where the expression for V_3 is obtained from Eq. (2.35).

These two non-linear reduced equations, strongly coupled together, describe all the possible symmetric, dynamic MHD equilibria and result directly from the set of stationary, ideal MHD equations under the assumption of one ignorable coordinate ($\partial/\partial x_3\equiv 0$). However, the system is not closed yet and an equation of state connecting P and ρ is required. Here three cases will be examined, namely the barotropic, isothermal and polytropic (adiabatic for $\gamma=5/3$), leaving the special case of incompressible flows for the last two sections.

1. *Barotropic case*:

$$P=P(\rho). \tag{2.43}$$

Suppose that the kinetic pressure is a given function of the density ρ *only*. In this case

$$\frac{\nabla P}{\rho}=\nabla\int\frac{\mathrm{d}P}{\rho}, \tag{2.44}$$

and the terms in graph brackets in Eqs. (2.41) and (2.42) may be considered as the gradient of a single scalar function

$$\int\frac{\mathrm{d}P}{\rho}+\frac{1}{2}\left(\frac{\Psi}{4\pi\rho}\right)^2\frac{|\nabla A|^2}{h_3^2}+\frac{V_3^2}{2}+\Phi-h_3V_3\Omega=E, \tag{2.45}$$

which is the fourth integral of the system, $E=E(A)$, and takes into account the momentum balance along the fieldlines ($\mathbf{B}\cdot\nabla E=0$). In Eq. (2.42) the last term on the left hand side becomes simply

$$4\pi\rho\{\ldots\}\cdot\frac{\nabla A}{|\nabla A|^2}=4\pi\rho\frac{\mathrm{d}E}{\mathrm{d}A}. \tag{2.46}$$

2. *Isothermal case*:

$$\mathbf{V}\cdot\nabla T=0\Rightarrow P=T(A)\rho. \tag{2.47}$$

Under the isothermal assumption, the temperature T (the notation $(k_B/\mu m_p)T \to T$ will be assumed throughout) is a free function itself, as stated in Eq. (2.47). Now, Eq. (2.41) yields

$$T\log\rho + \frac{1}{2}\left(\frac{\Psi}{4\pi\rho}\right)^2 \frac{|\nabla A|^2}{h_3^2} + \frac{V_3^2}{2} + \Phi - h_3 V_3 \Omega = E, \tag{2.48}$$

where again $E = E(A)$. Finally, the relation corresponding to Eq. (2.46) is

$$4\pi\rho\{\ldots\}\cdot\frac{\nabla A}{|\nabla A|^2} = 4\pi\rho\left[\frac{\mathrm{d}E}{\mathrm{d}A} + (1-\log\rho)\frac{\mathrm{d}T}{\mathrm{d}A}\right]. \tag{2.49}$$

3. *Polytropic case* $(1 < \gamma \leq 5/3)$:

$$\mathbf{V}\cdot\nabla(P/\rho^\gamma) = 0 \Rightarrow P = K(A)\rho^\gamma. \tag{2.50}$$

For a polytropic plasma the new free function of A is $K = P/\rho^\gamma$, which is related to the entropy per unit mass in the adiabatic case $\gamma = 5/3$. This time, the relations corresponding to Eqs. (2.48) and (2.49) are respectively

$$\frac{\gamma}{\gamma-1}K\rho^{\gamma-1} + \frac{1}{2}\left(\frac{\Psi}{4\pi\rho}\right)^2 \frac{|\nabla A|^2}{h_3^2} + \frac{V_3^2}{2} + \Phi - h_3 V_3 \Omega = E, \tag{2.51}$$

with $E = E(A)$, and

$$4\pi\rho\{\ldots\}\cdot\frac{\nabla A}{|\nabla A|^2} = 4\pi\rho\left[\frac{\mathrm{d}E}{\mathrm{d}A} - \frac{1}{\gamma-1}\rho^{\gamma-1}\frac{\mathrm{d}K}{\mathrm{d}A}\right]. \tag{2.52}$$

Note that in the barotropic case the total number of integrals of the system is four, whereas there are five free functions of A in the isothermal and polytropic cases.

The choice of a particular equation of state allows one to close the system. The density is derived from the generalised Bernoulli equation (Eqs. (2.45), (2.48) or (2.51)), which is a non-linear, algebraic equation for ρ, and then substituted in the transfield equation (2.42), with the last term on the left-hand side given by one of the three relations listed above. This equation is a quasi-linear, second order PDE for the magnetic flux function $A(x_1, x_2)$, in analogy to the static case. The differences with static equilibria are twofold: first the coupling to the Bernoulli equation through the density, which makes the resolution enormously more complicated, second the mathematical nature of the transfield equation, which is mixed in character and changes according to the flow speed, as will be shown in the next sub-section.

2.3.3 On the mathematical nature of the reduced equations

The strong coupling between the two reduced equations for symmetric, dynamic MHD equilibria not only makes their solution hard, both analytically and numerically, but also affects the mathematical nature of the transfield PDE for A, Eq. (2.42), especially though the term with $\nabla\rho\cdot\nabla A$.

After many tedious calculations (for this sub-section implicit reference is made to Sakurai (1985, 1990) and Tsinganos et al. (1996)), the gradient of the Bernoulli equation, say in the isothermal or polytropic case, reads

$$V_p^2\frac{\nabla|\nabla A|^2}{2|\nabla A|^2}-\frac{V_p^4-(C_s^2+V_A^2)V_p^2+C_s^2V_{Ap}^2}{V_p^2-V_{Ap}^2}\frac{\nabla\rho}{\rho}+\ldots=0, \tag{2.53}$$

where the dots represent lower order terms, unimportant for the study of the nature of the transfield equation. Here $V_p^2=(\Psi/4\pi\rho)^2B_p^2$ is the square of the poloidal velocity, $V_{Ap}^2=B_p^2/4\pi\rho$ ($V_A^2=B^2/4\pi\rho$) is the square of the poloidal (total) Alfvén speed and $C_s^2=\gamma P/\rho$ is the square of the sound speed, which in the isothermal limit $\gamma\to 1$ becomes simply $C_s^2=T(A)$.

By deriving the expression for $\nabla\rho/\rho$ from Eq. (2.53) and then substituting it into Eq. (2.42), the main part of the latter (that is the part containing the second order derivatives) becomes

$$\frac{1}{h_3^2}\left(1-\frac{V_p^2}{V_{Ap}^2}\right)\left[\nabla^2A-q\frac{\nabla|\nabla A|^2\cdot\nabla A}{2|\nabla A|^2}\right]+\ldots=0, \tag{2.54}$$

where

$$q=\frac{V_p^4}{V_p^4-(C_s^2+V_A^2)V_p^2+C_s^2V_{Ap}^2}. \tag{2.55}$$

The presence of the term $1-M_A^2$, $M_A^2=V_p^2/V_{Ap}^2$ from Eq. (2.36), multiplying the second order derivatives means that $M_A^2=1$ is a singular surface for the PDE, therefore a compatibility condition must be imposed on the remaining terms. It has been shown (Heyvaerts & Norman 1989; Sakurai 1990; Sauty & Tsinganos 1994) that not satisfying this Alfvén regularity condition leads to the formation of current sheets with consequent kinks in the fieldlines, due to the discontinuities in the second derivatives of $A(x_1,x_2)$.

Write now Eq. (2.54) as

$$\frac{1}{h_3^2}\left(1-\frac{V_p^2}{V_{Ap}^2}\right)\left[\frac{a}{h_1^2}\frac{\partial^2A}{\partial x_1^2}+\frac{2b}{h_1h_2}\frac{\partial^2A}{\partial x_1\partial x_2}+\frac{c}{h_2^2}\frac{\partial^2A}{\partial x_2^2}\right]+\ldots=0, \tag{2.56}$$

with the coefficients a, b and c given by

$$a = 1 - q\sin^2\eta, \quad b = q\cos\eta\sin\eta, \quad c = 1 - q\cos^2\eta, \tag{2.57}$$

where η is the angle between $\mathbf{B}_p$ and $\mathbf{e}_1$ in the poloidal plane (x_1, x_2).

The sign of the characteristic discriminant of the second order derivatives coefficients determines the mathematical nature of a second order PDE like Eq. (2.56). The discriminant, Δ, is ($b^2 - ac = q - 1$):

$$\Delta = \left[\frac{1}{h_3^2}\left(1 - \frac{V_p^2}{V_{A_p}^2}\right)\right]^2 \frac{(V_p^2 - V_{cp}^2)(C_s^2 + V_A^2)}{(V_p^2 - V_{sp}^2)(V_p^2 - V_{fp}^2)}, \tag{2.58}$$

where the *cusp*, fast and slow poloidal characteristic speeds are respectively given by

$$V_{cp}^2 = \frac{C_s^2 V_{A_p}^2}{C_s^2 + V_A^2}, \quad (V_{f,s})_p^2 = \frac{1}{2}\left[(C_s^2 + V_A^2) \pm \sqrt{(C_s^2 + V_A^2)^2 - 4C_s^2 V_{A_p}^2}\right], \tag{2.59}$$

with $V_{cp}^2 < V_{sp}^2 < V_{fp}^2$.

Depending on the poloidal flow speed, four different regimes are allowed:

$$\begin{aligned}
0 < V_p^2 < V_{cp}^2 &\Rightarrow \Delta < 0\text{: elliptic,}\\
V_{cp}^2 < V_p^2 < V_{sp}^2 &\Rightarrow \Delta > 0\text{: hyperbolic,}\\
V_{sp}^2 < V_p^2 < V_{fp}^2 &\Rightarrow \Delta < 0\text{: elliptic,}\\
V_{fp}^2 < V_p^2 < \infty &\Rightarrow \Delta > 0\text{: hyperbolic.}
\end{aligned}$$

Note that crossing the Alfvénic surface does not affect the nature of the transfield equation.

Whenever $\Delta > 0$ real characteristics exist and at each point (x_1, x_2) the directions of the two curves are

$$\left(\frac{h_2}{h_1}\frac{\mathrm{d}x_2}{\mathrm{d}x_1}\right)_{\pm} = \frac{b \pm \sqrt{b^2 - ac}}{a}. \tag{2.60}$$

It may be shown (Tsinganos et al. 1996), that in each hyperbolic region there is one *limiting characteristic* (e.g. Guderley 1962) to which one of the two families of characteristics tends asymptotically (that is the curves tend to be tangent to it). These limiting characteristics define two new critical surfaces on which additional compatibility conditions must be imposed. Bogovalov (1994, 1996) called these critical surfaces as slow and fast magnetosonic separatrix surfaces and also claimed that boundary conditions should be applied at the fast separatrix surface for a correct solution of the problem. Note that the slow and fast separatrices do *not* coincide with the corresponding surfaces where the discriminant reverses its sign in Eq. (2.58), *unless* the flow is perpendicular to these surfaces.

Another case in which this situation occurs is when the geometry of the magnetic field is known, that is $A(x_1, x_2)$ is given and only the Bernoulli equation needs to be solved, thus yielding the classical critical surfaces. Therefore, the new critical surfaces are due to the non-linear coupling of the two equations and to the back reaction of the plasma on the magnetic structure.

Finally, note that the question of the number of the appropriate boundary conditions required in order to obtain a unique solution to the problem is directly related to the above remarks on critical surfaces and characteristics. For example, consider the case of a stellar wind, starting with a velocity $V_p < V_{sp}$ at the lower boundary, crossing the three critical surfaces and exiting the outer boundary with a velocity $V_p > V_{f_p}$. It is well known that the number of conditions that can be imposed on a boundary corresponds to the number of incoming (entering the domain) characteristic waves, that is four at the inner boundary while all the waves are outgoing (leaving the domain) at the outer boundary. This means that four conditions can be freely chosen on four out of the seven MHD unknowns (corresponding in symmetric MHD flows to ρ, A and the five integrals of A), whereas the remaining three are to be selected by the compatibility conditions on the three critical surfaces. This happens automatically in time dependent calculations (see Sect. 7.4).

Needless to say, the position of these critical surfaces is not known *a priori* and this is one of the main difficulties in the search for either analytical or numerical solutions to the system of stationary MHD equations.

2.4 Analytical approach: incompressible flows

As made clear in the last sub-section, the analytical solution of the ideal MHD equations is, despite the assumptions of stationarity and spatial symmetry, still a hard task. Usually a semi-analytical approach is followed: a *self-similar* behaviour for the flux function is assumed (that is $A(x_1, x_2) \propto f_1(x_1) f_2(x_2)$, where one of the two functions is given) and the two coupled equations are solved numerically. To this class belong works on polytropic, MHD, astrophysical jets from disks in axisymmetry (Bardeen & Berger 1978; Blandford & Payne 1982; Contopoulos & Lovelace 1994; Ferreira & Pelletier 1995) or isothermal flows in a planar, stratified atmosphere with uniform gravity for solar applications (Tsinganos et al. 1993; Del Zanna & Hood 1996a; see Chapter 3 and Chapter 4). A way to avoid

the difficulties related with the coupling of the two equations consists in not specifying any energy equation and in deriving the temperature and the other thermodynamical quantities only *a posteriori*. Examples of this approach are models of non-polytropic, MHD, axisymmetric winds and outflows from a central object (e.g. Trussoni & Tsinganos 1993; Lima & Priest 1993; Sauty & Tsinganos 1994). Again, the solutions found in the cited works are not fully analytical, in the sense that a final numerical integration is required.

In order to find purely analytical solutions, the coupling between the two reduced equations for symmetric equilibria must necessarily be removed by means of some strong assumption. This assumption is to have the density itself as a free function of A:

$$\rho = \rho(A). \tag{2.61}$$

Now, because of the symmetry $\partial/\partial x_3 = 0$, this condition coincides with the relation $\mathbf{V} \cdot \nabla\rho = 0$ thus, thanks to the continuity equation, Eq. (2.22), this is equivalent to the condition of an incompressible flow

$$\nabla \cdot \mathbf{V} = 0, \tag{2.62}$$

hence yielding a full symmetry between the fields $\mathbf{B}$ and $\mathbf{V}$.

It should be clear that Eq. (2.61) must be regarded as a special equation of state and that no other relation linking ρ and P can be imposed (the Bernoulli integral simply becomes an expression for the pressure). However, sometimes this point is overlooked by some authors. For example, in Villata & Tsinganos (1993) and Villata & Ferrari (1994a) the two relations $P = P(\rho)$ and $\rho = \rho(A)$ are assumed together. This means that the pressure itself is a free function of A, but this is impossible in the general dynamical case because of the velocity (and gravity) terms in the Bernoulli equation. Moreover, in Villata & Ferrari (1994b) the discovery of novel exact *non-barotropic* solutions is announced, without specifying that they simply refer to the incompressible case.

Another situation in which the relation $\rho = \rho(A)$ can be freely assumed is when the flow is parallel to the invariance direction, that is $\Psi = 0 \Leftrightarrow \mathbf{V} = h_3\Omega(A)\mathbf{e}_3$, since in this case the continuity equation is automatically satisfied by any form of ρ, exactly as in the static case. However, Eq. (2.62) is more general and it reduces to this last case when $\Psi = 0$.

The reduced equations for symmetric equilibria, Eqs. (2.41) and (2.42), may now be rewritten in the incompressible limit $\rho = \rho(A)$. By taking the density inside the Bernoulli

integral and by rearranging a few terms, the reduced equations become, respectively

$$P+\frac{1}{2}\rho|\mathbf{V}|^2+\rho\Phi-h_3^2\rho\frac{\Omega^2}{s}=\Pi(A), \tag{2.63}$$

$$s\nabla\cdot\left(\frac{\nabla A}{h_3^2}\right)+\frac{1}{2}\frac{\mathrm{d}s}{\mathrm{d}A}\frac{|\nabla A|^2}{h_3^2}+\frac{1}{2h_3^2}\frac{\mathrm{d}}{\mathrm{d}A}\left(\frac{I^2}{s}\right)+\frac{h_3^2}{2}\frac{\mathrm{d}}{\mathrm{d}A}\left(\frac{4\pi\rho\Omega^2}{s}\right)+4\pi\left(\frac{\mathrm{d}\Pi}{\mathrm{d}A}-\Phi\frac{\mathrm{d}\rho}{\mathrm{d}A}\right)=0, \tag{2.64}$$

where $s=s(A)=1-\Psi^2/4\pi\rho=1-M_A^2$. Note that now M_A is itself a free function of A and the poloidal Alfvénic critical surface is actually a magnetic surface. Moreover, Eq. (2.64) is always elliptic, the discriminant of its second order derivatives coefficients being $\Delta=(s/h_3)^2$, hence no problems related with the presence of real characteristics and additional critical surfaces (which were due to the coupling with the Bernoulli equation) arise for incompressible flows.

The structure of Eq. (2.64) is very similar to that for static equilibria, Eq. (2.17), the only substantial difference being the non-linear term with $|\nabla A|^2$. However, it has been shown (Tkalich 1959a, 1959b, 1962; Solov'ev 1961, 1967; Gebhardt & Kiessling 1992) that through a variable transformation it is actually possible to reduce the incompressible case to the static case $\Psi=0$. To this purpose, write Eq. (2.64) as

$$s\nabla\cdot\left(\frac{\nabla A}{h_3^2}\right)+\sqrt{s}\frac{\mathrm{d}\sqrt{s}}{\mathrm{d}A}\frac{|\nabla A|^2}{h_3^2}+\frac{\partial Q}{\partial A}=0, \tag{2.65}$$

where sub-Alfvénic flows are assumed for simplicity, and then define a new flux function $\tilde{A}$ through

$$\frac{\mathrm{d}\tilde{A}}{\mathrm{d}A}=\sqrt{s(A)}. \tag{2.66}$$

It is straightforward to verify that Eq. (2.65) simply becomes

$$\nabla\cdot\left(\frac{\nabla\tilde{A}}{h_3^2}\right)+\frac{\partial\tilde{Q}}{\partial\tilde{A}}=0, \tag{2.67}$$

where $\tilde{Q}(\tilde{A})=Q[A(\tilde{A})]$, which is exactly what one would expect in the limiting case $\Psi=0\Rightarrow s=1$.

2.5 A self-similar method for incompressible equilibria

Completely analytic solutions for MHD dynamic equilibria under the assumption $\rho=\rho(A)$ have been found so far only for unidirectional flows along the invariance coordinate in laboratory structures (Masche & Perrin, 1980; Agim & Tataronis, 1985), or in the more

general incompressible case by linearising Eq. (2.64) through particular choices of the three integrals of A (Tsinganos 1981, 1982a; de Ville & Priest 1989a, 1989b, 1991; Villata & Ferrari 1994b). Such an approach has the advantage that the magnetic flux function $A(x_1, x_2)$ may be expressed in terms of known functions of mathematical physics, but often the resulting solutions are not suitable for physical applications because the shape of the solutions can not be controlled *a priori*. To avoid these difficulties a self-similar, regular nesting of the magnetic surfaces around their axis is imposed in the plane (x_1, x_2):

$$x_1 = \xi f(x_2), \tag{2.68}$$

where f is any regular and limited function of x_2, while ξ is the scale factor characterising the surface, say $\xi = 0$ for the magnetic axis and $\xi = 1$ for the external boundary surface. Since ξ must necessarily be constant on a given magnetic surface, the relation

$$A = A(\xi) \tag{2.69}$$

can be freely assumed. All the integrals of A are now to be considered as functions of ξ. The new expressions for the two vectors are

$$\mathbf{B} = \dot{A}\frac{\nabla\xi}{h_3} \times \mathbf{e}_3 + \frac{1}{h_3}\frac{I\dot{A} + h_3^2\Omega\dot{\Psi}}{s}\mathbf{e}_3, \tag{2.70}$$

$$\mathbf{V} = \frac{\dot{\Psi}}{4\pi\rho}\frac{\nabla\xi}{h_3} \times \mathbf{e}_3 + \frac{1}{h_3}\frac{I\dot{\Psi}/4\pi\rho + h_3^2\Omega\dot{A}}{s}\mathbf{e}_3, \tag{2.71}$$

where the dot indicates the derivative with respect to ξ and

$$s(\xi) = \dot{A}^2 - \dot{\Psi}^2/4\pi\rho = \dot{A}^2(1 - M_A^2), \tag{2.72}$$

whereas the equation for $\xi(x_1, x_2)$ is simply Eq. (2.64) with ξ replacing A everywhere:

$$s\nabla\cdot\left(\frac{\nabla\xi}{h_3^2}\right) + \frac{1}{2}\frac{\mathrm{d}s}{\mathrm{d}\xi}\frac{|\nabla\xi|^2}{h_3^2} + \frac{1}{2h_3^2}\frac{\mathrm{d}}{\mathrm{d}\xi}\left(\frac{I^2}{s}\right) + \frac{h_3^2}{2}\frac{\mathrm{d}}{\mathrm{d}\xi}\left(\frac{4\pi\rho\Omega^2}{s}\right) + 4\pi\left(\frac{\mathrm{d}\Pi}{\mathrm{d}\xi} - \Phi\frac{\mathrm{d}\rho}{\mathrm{d}\xi}\right) = 0. \tag{2.73}$$

The two geometrical coordinates x_1 and x_2 are now replaced by the new set of *magnetic coordinates*, defined as

$$\xi = x_1/f(x_2), \quad X = f(x_2), \tag{2.74}$$

with X having the same dimensions as x_1 thus letting ξ to be a non-dimensional variable. The meaning of these magnetic coordinates is rather simple: given a point P in the (x_1, x_2) plane, ξ determines the magnetic surface containing P while X determines the position

of P along the profile of the surface. At this stage, all the physical and geometrical quantities can be rewritten in terms of ξ and X; proceeding in this way, Eq. (2.73) will be shown to become a second order equation for the unknown function $X(x_2)$ with coefficients depending on ξ and on its integrals. Since the solution for X has to be valid for every ξ, the coefficients of the equation have to be constant. This produces a number of *compatibility conditions* for the functions of ξ, reducing at the same time the original Grad-Shafranov equation to an ordinary, non-linear, differential equation for the function X. Obviously, boundary conditions must be restricted to be consistent with the assumed separation.

This self-similar approach has been introduced for the first time by Bacciotti & Chiuderi (1992) for axisymmetric structures with a field aligned ($\Omega = 0$), incompressible flow and some families of exact solutions have been found. A generalisation of the method for a generic set of orthogonal coordinates is due to Del Zanna & Chiuderi (1996), to which an implicit reference will be assumed for the remainder of the chapter, where novel classes of exact, non-linear solutions in three different geometries are derived. These solutions are presented here in the following sub-sections.

2.5.1 Translational symmetry: flows in a magnetic flux tube with non-circular section

The translational symmetry is the simplest to treat, since the geometrical factor h_3 equals unity. The first consequence is that, from Eqs. (2.70) and (2.71), the third components of the magnetic and velocity fields become functions of A (or ξ) themselves and may replace I and Ω. Moreover, the structure of Eq. (2.73) suggests, in the present symmetry, the definition of the new surface function $\tilde{\Pi}(\xi) = \Pi + 1/8\pi(I^2 + 4\pi\rho\Omega^2)/s$. Thanks to the relation $(I^2 - 4\pi\rho\Omega^2)/s = B_3^2 - 4\pi\rho V_3^2$, the new generalised pressure turns out to be:

$$\tilde{\Pi}(\xi) = P + \frac{1}{8\pi}\left(\frac{\dot{\Psi}^2}{4\pi\rho}|\nabla\xi|^2 + B_3^2\right) + \rho\Phi. \tag{2.75}$$

Therefore, using this new function $\tilde{\Pi}$ instead of Π, the equation to solve reduces to

$$s\nabla^2\xi + \frac{1}{2}\frac{\mathrm{d}s}{\mathrm{d}\xi}|\nabla\xi|^2 + 4\pi\left(\frac{\mathrm{d}\tilde{\Pi}}{\mathrm{d}\xi} - \Phi\frac{\mathrm{d}\rho}{\mathrm{d}\xi}\right) = 0. \tag{2.76}$$

In the present sub-section the method of solution is applied to a case with no external gravitational field ($\Phi = 0$ in Eqs. (2.75) and (2.76)), with magnetic and flow surfaces nested around a straight magnetic axis parallel with the direction of invariance. Let z be

the ignorable coordinate in a cylindrical set of coordinates ($x_1 = r, x_2 = \phi, x_3 = z$). Thus the unknown function $\xi(r, \phi)$ is written as

$$\xi = r/R(\phi). \tag{2.77}$$

The profile of the intersections of the magnetic surfaces with the planes of constant z are given in the form $r = \xi R(\phi)$, for every positive value of ξ ($\xi = 0$ is the magnetic axis). For its geometrical meaning, it is clear that $R(\phi)$ has to be a continuous function, limited within two positive values R_{min} and R_{max}, and periodic with period $2\pi/n$, where n is any natural number.

By using the new coordinates ξ and R, Eq. (2.76) becomes

$$\frac{R''}{R} - \left[2 + \frac{\xi}{2s}\frac{\mathrm{d}s}{\mathrm{d}\xi}\right]\frac{R'^2}{R^2} = \left[4\pi\frac{\xi}{s}\frac{\mathrm{d}\tilde{\Pi}}{\mathrm{d}\xi}\right]R^2 + \left[1 + \frac{\xi}{2s}\frac{\mathrm{d}s}{\mathrm{d}\xi}\right], \tag{2.78}$$

where, following the discussion above, the terms in square brackets must be constant since the profile $R(\phi)$ has to be the same for every value of ξ. The results of these compatibility conditions are

$$s(\xi) = s_0\xi^{2\nu}, \quad \tilde{\Pi}(\xi) = \tilde{\Pi}_0 + \frac{\mu s_0}{8\pi\nu}\xi^{2\nu}, \tag{2.79}$$

where $s_0, \tilde{\Pi}_0, \mu$ and ν are arbitrary constants, with $\nu > 0$ to avoid divergences in Eqs. (2.79) for $\xi \to 0$. The equation for R now becomes

$$\frac{R''}{R} - (\nu + 2)\frac{R'^2}{R^2} = \mu R^2 + (\nu + 1), \tag{2.80}$$

which can be rewritten in the form of a simple first order linear differential equation for R'^2, with the general solution

$$R'^2 = -CR^{2(\nu+2)} + DR^4 - R^2, \tag{2.81}$$

where C is an arbitrary constant, while $D = -\mu/\nu$. A careful examination of Eq. (2.81) would show that both C and D have to be positive in order to have closed magnetic surfaces.

A simple solution of Eq. (2.81) with the right periodicity is easily found by setting $\nu = 1$:

$$R(\phi) = \frac{R_0}{\sqrt{1 - \beta\cos 2\phi}}, \tag{2.82}$$

where $R_0 = \sqrt{2/D}$ and $\beta = \sqrt{1 - 4C/D^2}$, with $C \leq D^2/4$. The profiles $r = \xi R(\phi)$, on the planes $z = \text{const}$, are then ellipses (see Fig. 2.1) with eccentricity $e = \sqrt{2\beta/(\beta+1)}$

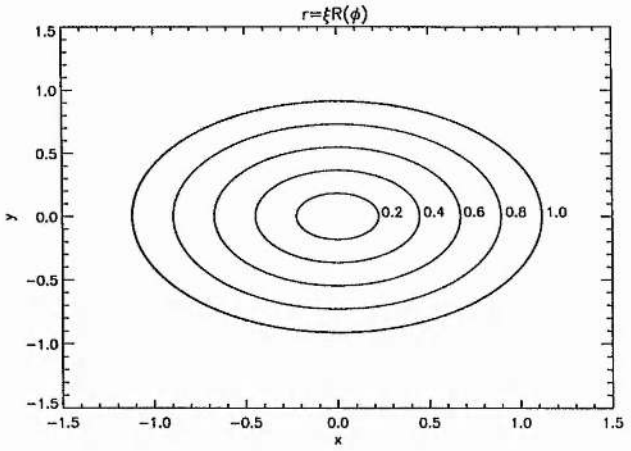

Figure 2.1: Projection of fieldlines in the $x-y$ plane [from Eq. (2.82) with $R_0 = 1, \beta = 0.2$].

and semiaxes $a = \xi R_{max}, b = \xi R_{min}$, where $R_{max} = R_0/\sqrt{1-\beta}, R_{min} = R_0/\sqrt{1+\beta}$. Consequently, the magnetic and flow surfaces are cylinders with elliptical section, nested one inside the other around the z axis. Note that only in the case $\nu = 1$ it is possible to derive a simple analytical form of the function $R(\phi)$; apart from the two cases $\nu = 1/2$ and $\nu = 2$, for which expressions involving elliptical functions can be found, Eq. (2.81) must be solved numerically.

It is now practical to obtain the expressions for the physical quantities involved in the problem. Together with $B_z(\xi)$ and $V_z(\xi)$, other two free surface functions may be chosen in order to satisfy Eq. (2.79) (let $\nu = 1$), for example the density and the Alfvénic Mach number normal to the z axis, namely $\rho = \rho_0 \mathcal{F}(\xi)$ and $M_A = M_A(\xi)$. Thus, the two flux functions $\dot{A}$ and $\dot{\Psi}$ are given by

$$\dot{A} = -A_0 \xi \mathcal{M}(\xi), \quad \dot{\Psi} = -\Psi_0 \xi \sqrt{\mathcal{F}(\xi)} \mathcal{N}(\xi), \tag{2.83}$$

where

$$\mathcal{M}(\xi) = \left| \frac{1 - M_0^2}{1 - M_A^2(\xi)} \right|^{1/2}, \quad \mathcal{N}(\xi) = \frac{M_A(\xi)}{M_0} \mathcal{M}(\xi), \tag{2.84}$$

and $M_0 \equiv M_A(0) = \Psi_0/\sqrt{4\pi\rho_0} A_0$, $s_0 = A_0^2 - \Psi_0^2/4\pi\rho_0 = A_0^2(1 - M_0^2)$. In the limit $M_A = M_0$ the two functions $\mathcal{M}$ and $\mathcal{N}$ equal unity. The magnetic and velocity fields are respectively ($B_0 = A_0/R_0, V_0 = \Psi_0/4\pi\rho_0 R_0$):

$$B_r \equiv \frac{\dot{A}}{r}\frac{\partial \xi}{\partial \phi} = -B_0 \frac{r}{R_0} \beta \sin 2\phi \mathcal{M}(\xi), \tag{2.85}$$

$$B_\phi \equiv -\dot{A}\frac{\partial \xi}{\partial r} = B_0 \frac{r}{R_0}(1 - \beta \cos 2\phi)\mathcal{M}(\xi), \tag{2.86}$$

$$V_r \equiv \frac{\dot{\Psi}}{4\pi\rho}\frac{1}{r}\frac{\partial\xi}{\partial\phi} = -V_0\frac{r}{R_0}\beta\sin 2\phi\frac{\mathcal{N}(\xi)}{\sqrt{\mathcal{F}(\xi)}}, \tag{2.87}$$

$$V_\phi \equiv -\frac{\dot{\Psi}}{4\pi\rho}\frac{\partial\xi}{\partial r} = V_0\frac{r}{R_0}(1-\beta\cos 2\phi)\frac{\mathcal{N}(\xi)}{\sqrt{\mathcal{F}(\xi)}}. \tag{2.88}$$

Note that on the magnetic axis only the z components of the two vectors are non-vanishing. The analytical form of the *total* pressure may be found from Eqs. (2.75) and (2.79); in the simple case $M_\mathrm{A} = \mathrm{const}$ it reads

$$P + \frac{B_z^2}{8\pi} = \tilde{\Pi}_0 - \frac{B_0^2}{4\pi}\xi^2\left(1 - \frac{1-\beta^2}{1-\beta\cos 2\phi}\frac{M_0^2}{2}\right), \tag{2.89}$$

which is a function of ξ only when $M_0 = 0$, as expected. It is interesting to note that the presence of a flow in the $x-y$ plane allows for a larger pressure, while $V_z(\xi)$ does not enter at all in this balance relation. These properties may have a great importance for the study of the stability of steady flows inside magnetic flux tubes and our solution can be used as a non-trivial unperturbed configuration. Moreover, elliptical flows are known to be unstable (Lifschitz & Hameiri 1991) but it is not clear whether the presence of the magnetic field can stabilise them.

Finally, note that this solution may also be found by using the method by Gebhardt & Kiessling (1992) described in the previous section. Choosing a pressure linear in $\tilde{A}$, Eq. (2.67) may be written as

$$\frac{1}{r}\frac{\partial}{\partial r}\left(r\frac{\partial\tilde{A}}{\partial r}\right) + \frac{1}{r^2}\frac{\partial^2\tilde{A}}{\partial\phi^2} = -2\frac{k}{R_0^2}. \tag{2.90}$$

The general solution of this Poisson equation is

$$\tilde{A}(r,\phi) = -\frac{k}{2}\frac{r^2}{R_0^2} + \sum_{n=0}^{+\infty} a_n r^n\cos(n\phi - \phi_n), \tag{2.91}$$

where all the constants a_n and ϕ_n are arbitrary and where all the terms diverging for $r \to 0$ have been rejected. By choosing $a_2 = k\beta/2R_0^2$ and setting all the other constants to zero, the magnetic flux function becomes

$$\tilde{A} = -\frac{k}{2}\left(\frac{r}{R_0}\sqrt{1-\beta\cos 2\phi}\right)^2 = -\frac{k}{2}\xi^2 \Rightarrow \frac{\mathrm{d}\tilde{A}}{\mathrm{d}\xi} = -k\xi, \tag{2.92}$$

and from the relation

$$\frac{\mathrm{d}A}{\mathrm{d}\xi} = \frac{\mathrm{d}\tilde{A}}{\mathrm{d}\xi}\left(\frac{\mathrm{d}\tilde{A}}{\mathrm{d}A}\right)^{-1} = -\frac{k\xi}{\sqrt{1-M_A^2(\xi)}} \tag{2.93}$$

which coincides with the first relation in (2.83) when $k = A_0\sqrt{1-M_0^2}$.

2.5.2 Translational symmetry: plasma in a uniform gravitational field

As a second application of the method of solution, consider now Cartesian coordinates to describe the situation in which there are two mutually orthogonal preferential directions: that of a uniform gravitational field ($\Phi = gz$) and that of invariance ($\partial/\partial y \equiv 0$). This time the separation is chosen as

$$\xi = z/Z(x). \tag{2.94}$$

After some rearranging, Eq. (2.76) reduces to

$$\frac{Z''}{Z} - \left[2 + \frac{\xi}{2s}\frac{\mathrm{d}s}{\mathrm{d}\xi}\right]\frac{Z'^2}{Z^2} = \left[\frac{1}{2\xi s}\frac{\mathrm{d}s}{\mathrm{d}\xi}\right]\frac{1}{Z^2} + \left[\frac{4\pi}{s\xi}\frac{\mathrm{d}\tilde{\Pi}}{\mathrm{d}\xi}\right] + \left[-\frac{4\pi g}{s}\frac{\mathrm{d}\rho}{\mathrm{d}\xi}\right]Z. \tag{2.95}$$

By imposing the constancy of the coefficients within the square brackets, the following compatibility conditions are found:

$$s = s_0, \quad \tilde{\Pi} = \tilde{\Pi}_0 + \frac{\mu s_0}{8\pi}\xi^2, \quad \rho = \rho_0 - \frac{\lambda s_0}{4\pi g}\xi. \tag{2.96}$$

The last condition holds only for $g \neq 0$. With these assumptions, the equation to solve becomes

$$\frac{Z''}{Z} - 2\frac{Z'^2}{Z^2} = \lambda Z + \mu, \tag{2.97}$$

with the first integral

$$Z'^2 = CZ^4 + DZ^3 + EZ^2, \tag{2.98}$$

where C is a new arbitrary constant, while $D = -2\lambda$ and $E = -\mu$.

Assuming $Z \geq 0$ for every x, in order to describe, for example, the atmosphere just above a stellar surface (coincident with $\xi = 0$), three different cases are considered depending on the values of E:

1. $E = 0$. In this case $\tilde{\Pi} \equiv \tilde{\Pi}_0 = \text{const}$ and the solution is (see Fig. 2.2):

$$Z(x) = \frac{Z_0}{1 + \beta x^2}, \tag{2.99}$$

with $Z_0 = D/|C|, \beta = D^2/4|C|, D > 0$ and $C < 0$.

2. $E < 0$. In this case a periodic solution is found (see Fig. 2.3):

$$Z(x) = \frac{Z_0}{1 - \beta\cos\alpha x}, \tag{2.100}$$

where $Z_0 = 2|E|/D, \beta = \sqrt{1 - 4|E||C|/D^2}, \alpha = \sqrt{E}$, with $D > 0$ and $-D^2/4|E| \leq C < 0$.

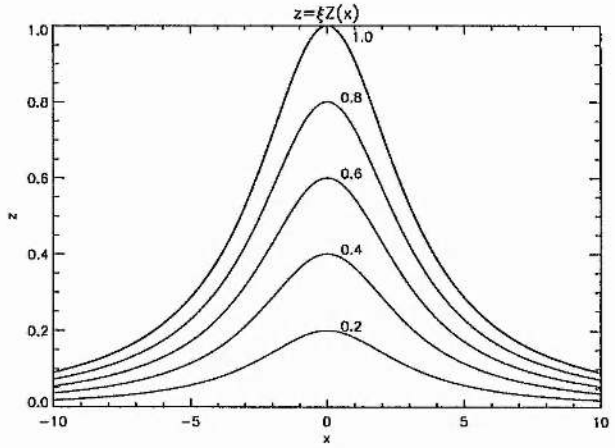

Figure 2.2: Projection of fieldlines in the $x - z$ plane [from Eq. (2.99) with $Z_0 = 1, \beta = 0.1$].

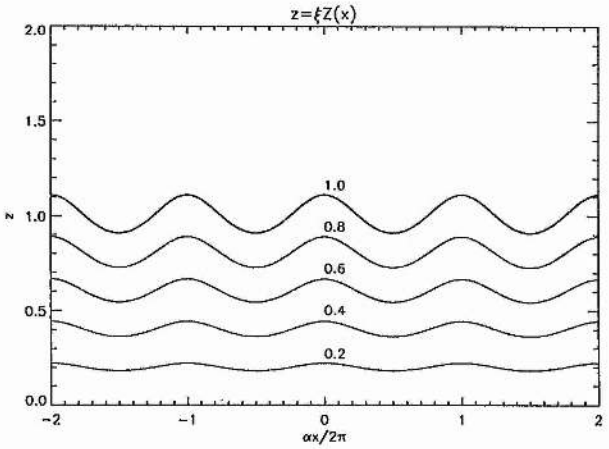

Figure 2.3: Projection of fieldlines in the $x - z$ plane [from Eq. (2.100) with $Z_0 = 1, \beta = 0.1$].

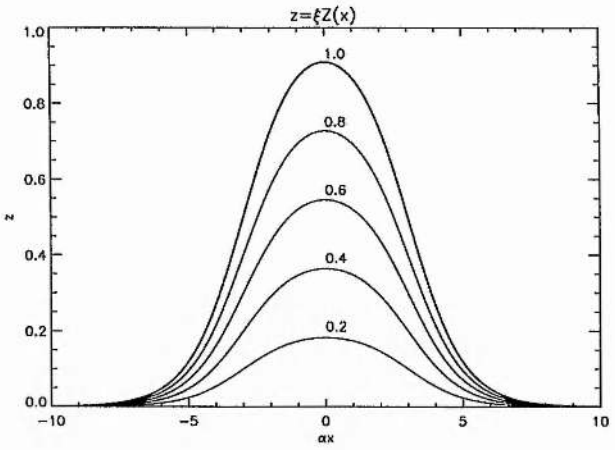

Figure 2.4: Projection of fieldlines in the $x - z$ plane [from Eq. (2.101) with $Z_0 = 1, \beta = 0.1$].

3. $E > 0$. This last case is the only one that allows realistic solutions in the absence of gravity, that is when $D = 0$. Here there are again three different cases:

   (a) $D < 0$; the solution is (see Fig. 2.4):

   $$Z(x) = \frac{Z_0}{1 + \beta \cosh \alpha x}, \tag{2.101}$$

   where $Z_0 = 2E/|D|$, $\alpha = \sqrt{E}$ and $\beta = \sqrt{1 - 4EC/D^2}$, with $C \leq D^2/4E$.

   (b) $D > 0$; the solution is:

   $$Z(x) = \frac{Z_0}{-1 + \beta \cosh \alpha x}, \tag{2.102}$$

   where $Z_0 = 2E/D$, $\alpha = \sqrt{E}$ and $\beta = \sqrt{1 + 4E|C|/D^2}$, with $C < 0$ in order to avoid divergencies ($\beta > 1$).

   (c) $D = 0$; the solution is:

   $$Z(x) = \frac{Z_0}{\cosh \alpha x}, \tag{2.103}$$

   where $Z_0 = \sqrt{E/|C|}$ and $\alpha = \sqrt{E}$, with $C < 0$.

The most interesting case for astrophysical applications is the solution with $E > 0$ and $D < 0$ (Eq. (2.101) and Fig. 2.4), which is also that resembling more closely a magnetic arcade in the solar corona. For sub-Alfvénic flows, as expected in the low β corona, both the density and the total pressure are decreasing functions of height. Define now

$$\rho = \rho_0 \mathcal{F}(\xi), \qquad \dot{A} = -A_0 \mathcal{M}(\xi), \qquad \dot{\Psi} = -\Psi_0 \sqrt{\mathcal{F}(\xi)} \mathcal{N}(\xi), \tag{2.104}$$

where $\mathcal{M}$ and $\mathcal{N}$ retain the same definition as in the previous sub-section, while the density reads (when $g = 0$ the density is still a free function of ξ):

$$\mathcal{F}(\xi) = 1 - \delta\xi, \qquad \delta = \frac{\alpha^2 A_0^2}{4\pi\rho_0 g Z_0}(1 - M_0^2). \tag{2.105}$$

The magnetic and velocity field components are ($B_0 = A_0/Z_0$, $V_0 = \Psi_0/4\pi\rho_0 Z_0$)

$$B_z \equiv -\dot{A}\xi Z'/Z = B_0\alpha z\beta \sinh\alpha x \mathcal{M}(\xi), \tag{2.106}$$

$$B_x \equiv -\dot{A}/Z = B_0(1 + \beta\cosh\alpha x)\mathcal{M}(\xi), \tag{2.107}$$

$$V_z \equiv -\frac{\dot{\Psi}}{4\pi\rho}\xi\frac{Z'}{Z} = V_0\alpha z\beta\sinh\alpha x\frac{\mathcal{N}(\xi)}{\sqrt{\mathcal{F}(\xi)}}, \tag{2.108}$$

$$V_x \equiv -\frac{\dot{\Psi}}{4\pi\rho}\frac{1}{Z} = V_0(1 + \beta\cosh\alpha x)\frac{\mathcal{N}(\xi)}{\sqrt{\mathcal{F}(\xi)}}, \tag{2.109}$$

while the expression for P may be derived from Eqs. (2.75) and (2.96).

2.5.3 The axisymmetric case

As a last application of the self-similar method, consider now the axisymmetric case, in which the magnetic surfaces are nested around the z axis in a cylindrical set of coordinates ($x_1 = z, x_2 = r, x_3 = \phi; h_3 = r$):

$$\xi = r/R(z), \tag{2.110}$$

so that the magnetic magnetic and flow surfaces are given by the relation $r = \xi R(z)$, with $R > 0$, for every positive value of ξ. Equation (2.73) may be written as

$$\frac{R''}{R} - \left[2 + \frac{\xi}{2s}\frac{\mathrm{d}s}{\mathrm{d}\xi}\right]\frac{R'^2}{R^2} =$$

$$\left[\frac{\xi^3}{2s}\frac{\mathrm{d}}{\mathrm{d}\xi}\left(4\pi\rho\frac{\Omega^2}{s}\right)\right]R^4 + \left[4\pi\frac{\xi}{s}\frac{\mathrm{d}\Pi}{\mathrm{d}\xi}\right]R^2 + \left[\frac{1}{2s\xi}\frac{\mathrm{d}}{\mathrm{d}\xi}\left(\frac{I^2}{s}\right)\right] + \left[\frac{1}{2s\xi}\frac{\mathrm{d}s}{\mathrm{d}\xi} - \frac{1}{\xi^2}\right]\frac{1}{R^2}, \tag{2.111}$$

and the compatibility conditions give

$$\rho = \rho_0\mathcal{F}(\xi), \quad s = s_0\xi^2, \quad \Pi = \Pi_0 + \frac{\mu s_0}{8\pi}\xi^2, \quad \Omega = \Omega_0\xi/\sqrt{\mathcal{F}(\xi)}, \quad I = \sqrt{\lambda/2}s_0^2\xi^3, \tag{2.112}$$

where ρ_0, s_0, Π_0, μ and λ are arbitrary constants ($\rho_0 > 0, \lambda \geq 0$) and $\mathcal{F}(\xi)$ is a free function. The two last relations are not the most general, but these forms have been chosen in order to avoid singularities in the physical quantities as $\xi \to 0$. With these choices for the integrals, the equation for R reduces simply to

$$\frac{R''}{R} - 3\frac{R'^2}{R^2} = \mu R^2 + \lambda, \tag{2.113}$$

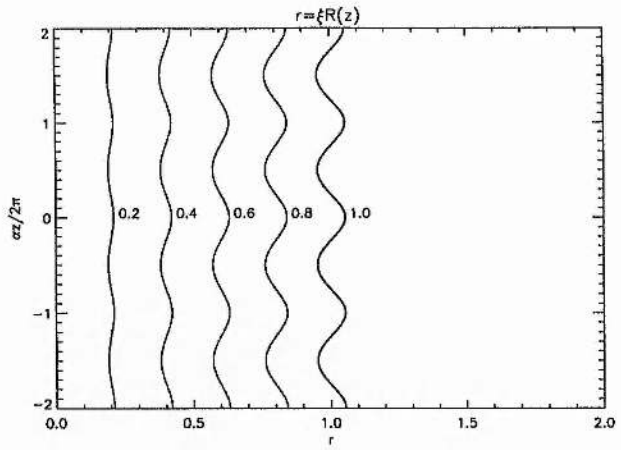

Figure 2.5: Projection of fieldlines in the $r-z$ plane [from Eq. (2.115) with $R_0 = 1, \beta = 0.1$].

with its first integral given by

$$R'^2 = -CR^6 + DR^4 - ER^2, \tag{2.114}$$

where $E = \lambda/2 > 0, D = -\mu$ and C is an integration constant. Equation (2.114) is analogous to the one found in Sect. 2.5.1 in the only analytically integrable case $\nu = 1$. Since $E > 0$, the conditions $D > 0$ and $0 < C \leq D^2/4E$ must be imposed in order to find well behaved solutions. The shape function is then

$$R(z) = \frac{R_0}{\sqrt{1 - \beta \cos \alpha z}}, \tag{2.115}$$

being $R_0 = \sqrt{2E/D}, \beta = \sqrt{1 - 4EC/D^2}, \alpha = 2\sqrt{E}$ (see Fig. 2.5). As previously anticipated, the periodic solution (2.115) is the same found in Bacciotti & Chiuderi (1992), but now $\Omega(\xi) \neq 0$, that is to say that the two vectors $\mathbf{V}$ and $\mathbf{B}$ are not parallel.

The usual choice of $\rho = \rho_0 \mathcal{F}(\xi)$ and $M_A = M_A(\xi)$ as free integrals, together with the assumptions

$$\dot{A} = A_0 \xi \mathcal{M}(\xi), \quad \dot{\Psi} = \Psi_0 \xi \sqrt{\mathcal{F}(\xi)} \mathcal{N}(\xi), \tag{2.116}$$

leads to the following expressions for the magnetic field components ($B_0 = A_0/R_0^2$ and $V_0 = \Psi_0/4\pi\rho_0 R_0^2$):

$$B_z \equiv \frac{\dot{A}}{r}\frac{\partial \xi}{\partial r} = B_0(1 - \beta \cos \alpha z)\mathcal{M}(\xi), \tag{2.117}$$

$$B_r \equiv -\frac{\dot{A}}{r}\frac{\partial \xi}{\partial z} = -B_0 \frac{\alpha}{2} r \beta \sin \alpha z \mathcal{M}(\xi), \tag{2.118}$$

$$B_\phi \equiv \frac{1}{r}\frac{I\dot{A}}{s} + r\frac{\Omega\dot{\Psi}}{s} = B_0 \frac{\alpha}{2} r(1 - \beta \cos \alpha z)\mathcal{M}(\xi) + \frac{\Omega_0 \Psi_0}{s_0} r \mathcal{N}(\xi), \tag{2.119}$$

and for the velocity field components:

$$V_z \equiv \frac{\dot{\Psi}}{4\pi\rho}\frac{\partial\xi}{\partial r} = V_0(1-\beta\cos\alpha z)\frac{\mathcal{N}(\xi)}{\sqrt{\mathcal{F}(\xi)}}, \tag{2.120}$$

$$V_r \equiv -\frac{\dot{\Psi}}{4\pi\rho}\frac{\partial\xi}{\partial z} = -V_0\frac{\alpha}{2}r\beta\sin\alpha z\frac{\mathcal{N}(\xi)}{\sqrt{\mathcal{F}(\xi)}}, \tag{2.121}$$

$$V_\phi \equiv \frac{1}{r}\frac{I\dot{\Psi}}{4\pi\rho s} + r\frac{\Omega\dot{A}}{s} = V_0\frac{\alpha}{2}r(1-\beta\cos\alpha z)\frac{\mathcal{N}(\xi)}{\sqrt{\mathcal{F}(\xi)}} + \frac{A_0\Omega_0}{s_0}r\frac{\mathcal{M}(\xi)}{\sqrt{\mathcal{F}(\xi)}}. \tag{2.122}$$

It is interesting to notice that in the particular case $M_A = M_0$ the choice of the free functions is exactly the same as in Villata & Ferrari (1994b). Therefore, despite the different methods adopted to solve the equations (self-similarity in the present work, linearisation in the other), the same solutions may be derived. In fact, when $M_A = M_0$ these solutions reduce to one of their classes of axisymmetric solutions.

The obvious astrophysical application of this class of solutions is the modelling of the *knotty* jet type structures in the outflows from both protostellar object and extragalactic nuclei. Although the present solution refers to the incompressible case the basic structure of the jet could be modelled in these simple terms. An example of this approach is given in Villata & Ferrari (1995), where the M 87 jet is modelled by matching the synchrotron emissivity that results from their incompressible solutions (taken as proportional to the plasma density times the magnetic field squared) with the observed radio contours.

2.6 Conclusions

In this chapter the problem of stationary, ideal MHD flows has been studied, mostly from a general mathematical point of view, leaving physical applications, in the particular field of solar physics, to the remainder of this thesis.

In order to make some analytical progress in the search for solutions to the set of MHD equations, the hypothesis of spatial symmetry has been introduced, which means that the physical quantities depend only upon two spatial coordinates, while retaining their full 3-D structure. The treatment of symmetric MHD equilibria has been carried out here in a generic set of orthogonal coordinates (x_1, x_2, x_3), under the only assumption $\partial/\partial x_3 = 0$.

By analogy with the static case, a magnetic flux function A has been introduced (which gives the geometry of the poloidal part of the magnetic field) and several integrals of this function have been found. The resulting reduced equations are an algebraic, non-linear equation for the density, which takes into account the momentum balance along

the fieldlines (generalised Bernoulli equation), and a quasi-linear, second order PDE for the magnetic flux function, which takes into account the momentum balance across the magnetic surfaces (generalised Grad-Shafranov equation, or transfield equation).

These two equations are strongly coupled together and this leads to two main difficulties in the search for solutions. First, the impossibility of obtaining an analytical expression for the density from the Bernoulli equation, regardless of the energy equation linking P and ρ, which therefore must be solved numerically. Second, the coupling affects the mathematical nature of the transfield equation, which may become hyperbolic depending on the poloidal flow speed, with consequent presence of real characteristics and critical surfaces, where compatibility conditions have to be imposed, thus limiting the freedom in the choice of the free functions of A. Moreover, the position of these critical surfaces are not known *a priori*, and this makes things harder even from a numerical point of view.

Usually, a semi-analytical approach is followed: a self-similar behaviour for the flux function and for the density is assumed and the equations are reduced to two coupled ordinary differential equations, to be solved numerically. To achieve this, the energy equation is often left unspecified and the thermodynamic behaviour of the system is checked only *a posteriori*, once the solution is known. The only way to avoid this kind of problems is to reduce the energy equation to the simple case of incompressible flows. For symmetric systems this is equivalent to the density being a free function of A, thus decoupling the two reduced equations and leaving the thermodynamics out of the problem (the Bernoulli equation simply becomes an analytic expression for the gas pressure). Moreover, the transfield equation is always elliptic for an incompressible plasma and no additional critical surfaces are present.

After this quite general presentation, a new self-similar method for incompressible, symmetric flows has been presented. This assumes a regular nesting of the magnetic surfaces around the magnetic axis of the system, thus limiting the analytic research to physically well behaved solutions. This method is applied to three different geometries and a corresponding number of classes of *exact* solutions are found, all being very flexible since they contain a minimum of three free functions. The solutions range from flows in flux tubes with a non-circular section in translational symmetry, to arcade type solutions in a stratified atmosphere with uniform gravity (suitable for magnetic structures in the solar corona), and finally to jet type, axisymmetric structures with a periodic, non-uniform section (suitable for models of astrophysical collimated outflows).

However, apart from direct physical applications of the solutions presented here, the importance of having non-linear, exact solutions to the set of stationary MHD equations is universally recognised. For example, these can provide a valuable basis for stability calculations or may be used as a test for numerical codes.

Chapter 3

Stationary flows in magnetic structures

3.1 Introduction

As discussed in Chapter 1, the solar atmosphere, which has a vertical stratification produced by the gravity, is by no means uniform in the horizontal direction and possesses a complex structure dominated by the magnetic field. X-ray and EUV observations, from the pioneering discoveries by Skylab in the seventies to the more recent, on-going missions such as Yohkoh and SOHO, have shown that the corona (outside coronal holes) consists largely of dense structured features, mainly in the form of loops and arcades. From the comparison with magnetograms it is rather apparent that these structures possess an intrinsic magnetic nature and can usually be described as magnetic flux tubes. Their general properties have been discussed, for example, by Priest (1978) and Chiuderi et al. (1981).

The first models for coronal loops were static and more concerned with finding a reasonable thermodynamic balance between heating, radiative losses and thermal conduction, rather than studying their mechanical equilibrium (Rosner et al. 1978; Hood & Priest 1979; Vesecki et al. 1979; Serio et al. 1981). Among other results, they have derived scaling laws relating the parameters of the model, namely the maximum temperature, pressure, loop length and the heating function, which is basically unknown and hence taken as a free parameter.

In particular, Serio et al. (1981) have modelled thermally isolated loops in hydrostatic equilibrium with a heating that declines exponentially with height; they found that loops

which are longer than a critical value, proportional to the characteristic scale height for the heat deposition, develop a temperature minimum at the summit, which may be relevant for prominence formation (see Chapter 4).

The next step in coronal loop modelling is the inclusion of a stationary siphon flow, driven by a sustained pressure difference at the two footpoints of the magnetic arch. These siphon flows were first studied by Meyer & Schmidt (1968) in the context of Evershed flows in sunspots. This flow occurs at photospheric level and was discovered at the beginning of this century (Evershed 1909) as a radial, horizontal motion outwards from the sunspot's umbra. The velocity is typically 6-7 km s^{-1}, that is comparable with the photospheric sound speed but less than the local Alfvén speed, usually accelerating until a maximum and then stopping rather abruptly at the penumbral outer boundary. The effect appears to decrease with altitude above the sunspot and eventually it even reverses its sign (radial inflow) at chromospheric level, with typical speeds of 10-20 km s^{-1}.

Apart from Evershed flows around sunspots, many other kinds of motions are observed in the solar atmosphere, such as chromospheric network downflows (up to 2 km s^{-1}), surges and spicules (20-30 km s^{-1}) and coronal rain (50-100 km s^{-1}). In particular, persistent red-shifts in emission lines are observed, very frequently on the Sun and sometimes also on other stars, thus suggesting the presence of steady, large scale downflows with speed of several km s^{-1} (Doschek et al. 1976; Lites et al. 1976; Gebbie et al. 1981; Dere 1982; Athay & Dere 1989; Hassler et al. 1991; Brekke 1993; Hansteen 1993; Linsky 1993), which could be an indirect proof of the descending siphon flows from coronal loop structures.

The inclusion of steady flows in coronal loop models is not only necessary for completeness from a theoretical point of view, but also plays an important role in explaining some observational results which seem to disagree with the predictions derived from static models. For example, from the fact that many transition region loops extend over heights much larger than predicted by models without flows (Foukal 1976), indicates that flows are important in determining their gross properties (the centrifugal force due to the flow circulation has an overall effect of lifting the structure). Moreover, Peres et al. (1992) compared the fitting of the intensities of some EUV transition region emission lines by loops with steady siphon flows relative to static loops and concluded that siphon flow models were in better agreement with the observations.

In the present chapter, a review of the different approaches to the theoretical study of stationary flows along closed magnetic structures in the solar atmosphere (with uni-

form gravity) will be presented. Usually, magnetised loops and arches are modelled as one-dimensional thin magnetic flux tubes embedded in an external vertically stratified atmosphere in uniform gravity.

Section 3.1 will be devoted to this approach and a further classification will be made, namely a separation between the *rigid flux tube* approximation (suitable for low β coronal loops), and the *thin flux tube* approximation, where the effect of the flow on the overall structure is taken into account (suitable for photospheric or low-lying chromospheric magnetic flux tubes, for which the plasma β is of order unity).

In Sect. 3.3 an interesting 2-D treatment for a magnetised, low β corona and sub-Alfvénic flows is presented. This approach may be derived from the theory of symmetric MHD flows discussed in Chapter 2 by means of of a linearisation in the magnetic field (or in the magnetic flux function A).

Section 3.4 will deal with a direct application of the non-linear theory of the previous chapter. This will be applied to the problem of symmetric MHD equilibria with flows in a planar, vertically stratified atmosphere in uniform gravity. By using Cartesian coordinates and assuming translational symmetry, a couple of ordinary differential equations will be derived from the two reduced equations, thanks to a self-similar separation for both the flux function A and the density ρ.

Finally, a brief discussion of the different theories presented will be given in Sect. 3.5.

3.2 Siphon flows in magnetic flux tubes

From a physical point of view, the basic features of siphon flows along magnetic flux tubes are easy to understand. If one starts with a static loop and switches on a pressure difference between the two footpoints, an accelerated flow will be driven from the high pressure footpoint. On the other hand, if a flow is already present in the loop and a small pressure difference is imposed in opposition to the flow, this can be decelerated.

There are several ways in which different footpoint pressures can be sustained. For example, the constancy of total base pressure (plasma plus magnetic) would imply that regions of high magnetic field strength possess a low plasma pressure, and *vice versa*. This is exactly the explanation given by Meyer & Schmidt (1968) (see also Spruit 1981) for the direct and inverse Evershed flows in the sunspot's penumbral flux tubes. A low-lying flux tube with one footpoint in the penumbra, with a field strength of say 1000 G, connecting

to a magnetic element in the surrounding photosphere with strength 1500 G will have a siphon flow directed radially outwards, producing the normal Evershed effect. A higher-arching flux tube originating in the umbra, where the field strength is say 2000 G, and connecting to a similar magnetic element outside the sunspot (which might even be another sunspot of intermediate field strength) will have a siphon flow directed inwards, producing the inverse Evershed effect in the chromosphere. One can then imagine a spatial array of flux tubes carrying siphon flows with a graduation between outward and inward direction with increasing height in the penumbra. Recent high resolution observations (Rimmele 1995a, 1995b) confirms this scenario.

Another possibility for sustaining a pressure difference at the two footpoints of a coronal loop could be due to converging (diverging) photospheric flows, which would enhance (reduce) the local pressure. Again, a supergranular flow could induce a downflow by viscous coupling in the intense tubes that make up the boundary of a supergranule cell. Finally, the pressure at a loop footpoint may be increased by enhancing the heating there.

Siphon flows in magnetic flux tubes will be studied here by considering the tube as essentially unidimensional, with a curvilinear coordinate s measuring the length of the tube. Section 3.2.1 is concerned with the low β assumption of tubes unperturbed by the flow, whereas Sect. 3.2.2 contains the treatment of the thin (or *slender* flux tube approximation for photospheric magnetic arch structures, in which the flow can affect the geometry of the tube.

3.2.1 Rigid flux tubes

In the rigid tube approximation the magnetic field strength is considered to be so high that the back reaction of the pressure and inertial forces is completely negligible ($\beta \ll 1$ and $M_A^2 \ll 1$). This is certainly valid in the solar corona and is a good approximation for chromospheric loops. Hence, the magnetic field just gives the shape of the arcade (always assumed to be a semi-circle of total length $2L$) but then does not enter in the physical equations, which are simply the 1-D hydrodynamic equations.

Treatments belonging to this category are the cited work by Meyer & Schmidt (1968) for Evershed flows (although in the photosphere $\beta \sim 1$) and models of coronal loop siphon flows (Glencross 1980; Cargill & Priest 1980, 1982; Priest 1981; Noci 1981; Borrini & Noci 1982; Noci et al. 1989; Spadaro et al. 1990; Spadaro 1991; Peres et al. 1992; Robb & Cally 1992; Orlando et al. 1995a, 1995b).

The simplest model of stationary siphon flows consists of a symmetric loop of uniform cross section with a polytropic energy equation. The 1-D set of equations is

$$\frac{\mathrm{d}}{\mathrm{d}s}(\rho v) = 0, \tag{3.1}$$

$$\rho v \frac{\mathrm{d}v}{\mathrm{d}s} = -\frac{\mathrm{d}p}{\mathrm{d}s} - \rho g \sin\theta, \tag{3.2}$$

$$\frac{\mathrm{d}}{\mathrm{d}s}\left(\frac{p}{\rho^\gamma}\right) = 0, \tag{3.3}$$

where θ is the inclination of the magnetic field with the horizontal plane, given by $\theta = \theta(s) = (\pi/2)(1 - s/L)$, where $2L$ is the total length of the loop ($s = L \Rightarrow \theta = 0$ is the summit).

Eliminating p and ρ between the three equations and using the sound speed $c_s(s) = \sqrt{\gamma p/\rho}$ yields

$$\left(v - \frac{c_s^2}{v}\right)\frac{\mathrm{d}v}{\mathrm{d}s} = -g\sin\theta, \tag{3.4}$$

which is similar in form to the solar wind equation (see Chapters 1 and 6) and possesses a critical point ($v = c_s \Rightarrow M = 1$) at the loop summit. This means that two kinds of physical solutions are allowed for given pressures p_0 and p_2 (and temperature T_0) at the footpoints: a subsonic solution ($M < 1$ everywhere) with a maximum ($\mathrm{d}v/\mathrm{d}s = 0$) at the summit when $p_2/p_0 = 1$ and a transonic solution, connecting through a shock to a lower branch in order to satisfy the condition $p = p_2$ at the second footpoint (see Fig. 3.1), when $p_2/p_0 < 1$.

For the shocked solutions, which are present whenever there is a pressure difference at the footpoints (in symmetric loops), the Rankine-Hugoniot relations are

$$\frac{v_+}{v_-} = \frac{2 + (\gamma - 1)M^2}{(\gamma + 1)M^2}, \tag{3.5}$$

$$\frac{\rho_+}{\rho_-} = \frac{(\gamma + 1)M^2}{2 + (\gamma - 1)M^2}, \tag{3.6}$$

$$\frac{T_+}{T_-} = \frac{[2\gamma M^2 - (\gamma - 1)][2 + (\gamma - 1)M^2]}{(\gamma + 1)^2 M^2}, \tag{3.7}$$

where the quantities with the $+$ ($-$) sign are downstream (upstream) at the shock position and $M > 1$ is the Mach number of the shock ($M = v_-/c_{s-}$).

Following Cargill & Priest (1980), the next step in the study of stationary siphon flows in rigid coronal loops is to introduce a variable cross sectional area $A = A(s)$. Choosing an appropriate functional form of $A(s)$ it is possible to study the behaviour of *asymmetric*

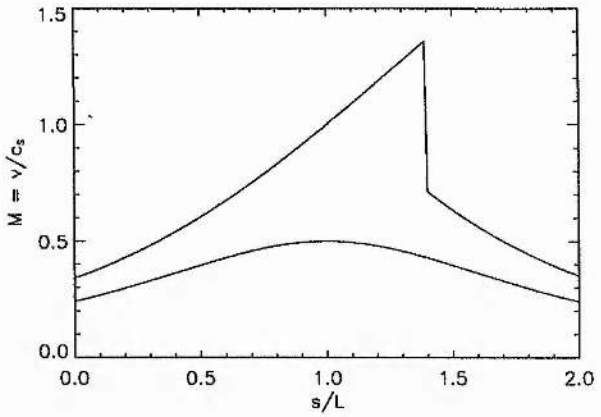

Figure 3.1: The Mach number v/c_s as a function of the position s/L along the loop (with a constant cross section). Both a symmetric, subsonic solution and a shocked, asymmetric solution are shown. Here the values of the parameters combine in such a way to yield $gL/c_s^2 = 1$, which is the right order of magnitude for a typical coronal loop.

loops: converging, when $\mathrm{d}A/\mathrm{d}s < 0$ and diverging when $\mathrm{d}A/\mathrm{d}s > 0$ (for a monotonic function A). The equation of continuity now reads

$$\frac{\mathrm{d}}{\mathrm{d}s}(\rho v A) = 0, \tag{3.8}$$

and the equation of motion becomes

$$\left(v - \frac{c_s^2}{v}\right)\frac{\mathrm{d}v}{\mathrm{d}s} = -g\sin\theta + \frac{c_s^2}{A}\frac{\mathrm{d}A}{\mathrm{d}s}, \tag{3.9}$$

where an extra term is present when comparing with Eq. (3.4). The first result of the introduction of the variable section is that the critical point position shifts in the downflowing (upflowing) leg of the loop for converging (diverging) loops. Moreover, the asymmetry caused by the introduction of a monotonic function $A(s)$ produces different results.

In particular, for converging loops a small pressure difference accelerates a subsonic flow from the high pressure footpoint to the low pressure one ($p_0 > p_2$), but when the pressure difference is large enough, a shocked flow results. For diverging loops a pressure decrease along the loop ($p_0 > p_2$) produces only shocked flows, with the pressure difference causing the flow to accelerate along the loop. However, a flow is also allowed along a diverging loop in the direction of an increasing pressure ($p_0 < p_2$); as the plasma moves along the loop the adverse pressure gradient decelerates it. For a certain range of pressure differences

there are two such decelerated flows, one subsonic and the other shocked, but it is not known whether both are stable and which would be preferred by the Sun.

From a physical point of view, it is more important to study in detail the energetics of the flow, rather than a variable cross section. The polytropic relation, Eq. (3.3), may be replaced by a complete energy equation, such as

$$\frac{1}{2}\left(5p\frac{\mathrm{d}v}{\mathrm{d}s}+3v\frac{\mathrm{d}p}{\mathrm{d}s}\right)-\frac{\mathrm{d}}{\mathrm{d}s}\left(\kappa\frac{\mathrm{d}T}{\mathrm{d}s}\right)=E_H-\frac{p^2}{4k_B^2T^2}\Lambda(T), \tag{3.10}$$

where $\kappa = 9.2\times10^{-7}T^{5/2}$ is the thermal conductivity given by Spitzer (1962), E_H is the volumetric power input in the solar atmosphere (heating) and $\Lambda(T)$ is the radiative loss function per unit emission measure (e.g. Raymond & Smith 1977). The equation of motion may be now be rewritten as

$$\left(v-\frac{c_s^2}{v}\right)\frac{\mathrm{d}v}{\mathrm{d}s}=-g\sin\theta-\frac{k_B}{\mu m_p}\frac{\mathrm{d}T}{\mathrm{d}s}, \tag{3.11}$$

where this time $c_s=\sqrt{k_BT/\mu m_p}=\sqrt{p/\rho}$ is the local, *isothermal* sound speed.

The system of coupled equations (3.10) and (3.11), together with the continuity equation (3.1) and the ideal gas law, have been solved by Orlando et al. (1995a, 1995b), who have explored thoroughly the possible families of solutions in the parameters space, especially near the critical points, both for regular and shocked solutions. Among other results, they derive scaling laws which relate the dynamic pressure $p+\rho v^2$ at the footpoints, the maximum loop temperature, the loop semi-length and the volumetric heating; such scaling laws extend those found by other authors for static loops.

3.2.2 Thin flux tubes

For low-lying chromospheric or photospheric loops, the plasma β is of order unity and the non-linear interaction between plasma and magnetic forces, resulting in a modification of shape and cross section of the tube, must be taken into account. The tube is considered to be still unidimensional and all the physical quantities still depend on the usual coordinate s along the loop, but now its geometry is no longer given *a priori*, that is the functions $\theta(s)$ and $A(s)$ are to be derived self-consistently from the equations.

The thin flux tube approximation means that the cross section radius is much smaller than both the loop length and the pressure scale height of the surrounding atmosphere, considered as static and non-magnetised (*isolated* magnetic flux tube). The fluid equations

along the flux tube are again

$$\frac{\mathrm{d}}{\mathrm{d}s}(\rho v A) = 0, \tag{3.12}$$

$$\rho v \frac{\mathrm{d}v}{\mathrm{d}s} = -\frac{\mathrm{d}p}{\mathrm{d}s} - \rho g \sin\theta, \tag{3.13}$$

to be completed by an energy equation and the gas law. The presence of the magnetic field enters through the flux conservation law

$$\frac{\mathrm{d}}{\mathrm{d}s}(BA) = 0, \tag{3.14}$$

and through the lateral pressure balance (which replaces the energy transfer between the tube and the surrounding, Parker 1979)

$$p + \frac{B^2}{8\pi} = p_e, \tag{3.15}$$

where p_e is the pressure in the external atmosphere. This is considered to be in hydrostatic equilibrium (vertically stratified), thus

$$\frac{\mathrm{d}p_e}{\mathrm{d}h} = -g\rho_e \Rightarrow \frac{\mathrm{d}p_e}{\mathrm{d}s} = -g\rho_e \sin\theta, \tag{3.16}$$

since $\mathrm{d}h/\mathrm{d}s = \sin\theta$.

The lateral pressure balance with a varying $B(s)$ has been first considered by Thomas (1984, 1988) and Montesinos & Thomas (1989), but the shape of the arch was still considered as fixed and semi-circular, that is $h(s)$, or $\theta(s)$, are specified functions. The most interesting result is the dependence of $A(s)$ on the flow speed, which results in a nozzle like shape of the tube at the shock position. Moreover, another critical velocity is found and, when the flow speed equals this new critical velocity, a *bulge point* appears in tube section.

Degenhardt (1989) dropped first the assumption of the shape and solved the equations for a given temperature profile, whereas Thomas & Montesinos (1990) considered the isothermal and adiabatic cases. The additional equation is the momentum balance *across* the fieldlines (with the same meaning of the transfield equation derived in Chapter 2), which reads

$$\left(\frac{B^2}{4\pi} - \rho v^2\right)\frac{\mathrm{d}\theta}{\mathrm{d}s} = -(\rho_e - \rho)g, \tag{3.17}$$

where x is the horizontal coordinate ($\mathrm{d}s/\mathrm{d}x = 1/\cos\theta$ and $\mathrm{d}h/\mathrm{d}x = \tan\theta$). Equation (3.17) describes a balance among the net force due to the magnetic tension, the inertial force due to the flow along curved stream-lines, and the transverse buoyancy.

An interesting integral of the equations has been discovered by Cheng (1992) (and generalised by Ferreira & Jardine (1996) to coronal loops of rapidly-rotating stars, thus including the effect of centrifugal forces), independently of the particular energy equation. One form of this integral is

$$(1 - M_A^2) B \cos\theta = \text{const}, \tag{3.18}$$

where $M_A = v/v_A = v/(B/\sqrt{4\pi\rho})$ is the Alfvénic Mach number. From this relation is clear that the flow must be either always sub-Alfvénic, or always super-Alfvénic.

Consider now an external isothermal atmosphere ($T = T_e = \text{const}$), for which

$$p_e \sim \rho_e \sim \exp(-h/H), \tag{3.19}$$

where $H = c_s^2/g$ is the isothermal scale height; for an isothermal siphon flow the following equation holds:

$$\left(1 - \frac{v^2}{v_t^2}\right) \frac{\mathrm{d}v}{v} = \left[1 - \left(\frac{\rho_e - \rho}{\rho}\right) \frac{c_s^2}{v_A^2}\right] \frac{\mathrm{d}h}{H}, \tag{3.20}$$

where ($v_A^2 = (2/\beta) c_s^2$)

$$v_t^2 = \frac{c_s^2 v_A^2}{c_s^2 + v_A^2} = \frac{c_s^2}{1 + \beta/2} \tag{3.21}$$

defines the characteristic *tube speed* (Roberts 1976; Defouw 1976). This tube speed, which actually coincides with the cusp speed defined in Sect. 2.3.3, replaces the sound speed as the critical velocity in the system. This is due to the non-linear coupling of the magnetic and plasma effects, neglected in the rigid tube case $\beta \ll 1$, where $v_t^2 \to c_s^2$. Also for this new critical point, shocked solutions are allowed. The correct jump relations for the supercritical siphon flows in the thin flux tube approximation have been discussed by Herbold et al. (1985) and by Ferriz-Mas & Moreno-Insertis (1987).

The simple example of isothermal flows in an isothermal external atmosphere briefly discussed above is useful for demonstrating the qualitative behaviour of siphon flows in flux tubes with $\beta \sim 1$, but is inadequate for a detailed modelling of actual siphon flows in the solar atmosphere. More realistic models have been developed which include a full treatment of the energetics of the temperature-stratified atmosphere (Degenhardt 1989; Thomas & Montesinos 1991) and the radiative transfer between the flux tube and the surroundings (Degenhardt 1991; Montesinos & Thomas 1993).

3.3 2-D, low β MHD flows in coronal loops

A very interesting generalisation of the rigid flux tube approximation is due to Surlantzis et al. (1994), in the case of a potential, 2-D, space filling magnetic field with a field aligned steady flow, in which the back reaction of the flow on the magnetic structure is taken into account as a first order perturbation. The formalism is taken from that of symmetric MHD equilibria, discussed in Chapter 2, but here a linearisation in the field is assumed, that is

$$\mathbf{B} = \mathbf{B}_0 + \mathbf{B}_1, \qquad |\mathbf{B}_1| \ll |\mathbf{B}_0|. \tag{3.22}$$

In a low β plasma ($\beta \ll 1$), pressure, gravity and inertial forces are considered as first order perturbations to the zeroth order, force free magnetic field

$$\nabla \cdot \mathbf{B}_0 = 0, \tag{3.23}$$

$$(\nabla \times \mathbf{B}_0) \times \mathbf{B}_0 = 0 \tag{3.24}$$

(in 2-D the field $\mathbf{B}_0$ is actually potential, thus $\nabla \times \mathbf{B}_0 = 0$). Now, the ideal, stationary MHD equations in the first order approximation read

$$\nabla \cdot \mathbf{B}_1 = 0, \tag{3.25}$$

$$\nabla \cdot (\rho \mathbf{V}) = 0, \tag{3.26}$$

$$\mathbf{V} \times \mathbf{B}_0 = 0, \tag{3.27}$$

$$\rho(\mathbf{V} \cdot \nabla)\mathbf{V} = -\nabla P + (1/4\pi)(\nabla \times \mathbf{B}_1) \times \mathbf{B}_0 - \rho \nabla \Phi. \tag{3.28}$$

The 2-D divergence-free vectors are given by

$$\mathbf{B}_0 = \frac{\nabla A_0}{h_3} \times \mathbf{e}_3, \quad \mathbf{B}_1 = \frac{\nabla A_1}{h_3} \times \mathbf{e}_3, \quad \mathbf{V} = \frac{\Psi}{4\pi\rho} \frac{\nabla A_0}{h_3} \times \mathbf{e}_3, \tag{3.29}$$

where $A = A_0 + A_1$, $A_1 \ll A_0$, is the magnetic flux function and $\Psi = \Psi(A_0)$ because of Eq. (3.27).

The linearised problem can be solved in three distinct steps.

1. The zeroth order magnetic field $\mathbf{B}_0$ is derived from A_0, which satisfies

$$\nabla \cdot \left(\frac{\nabla A_0}{h_3^2} \right) = 0, \tag{3.30}$$

that is simply the transfield equation for a 2-D force free field (potential).

2. The density ρ is derived from the Bernoulli equation

$$T\log\rho+\frac{1}{2}\left(\frac{\Psi}{4\pi\rho}\right)^2\frac{|\nabla A_0|^2}{h_3^2}+\Phi=E, \tag{3.31}$$

which is the momentum equation projected along the background field $\mathbf{B}_0$. An isothermal energy equation has been assumed, thus the new two integrals are $T=T(A_0)$ and $E=E(A_0)$.

3. The perturbations to the background field are derived from the first order transfield equation

$$\nabla\cdot\left(\frac{\nabla A_1}{h_3^2}\right)=\frac{\Psi}{4\pi\rho}\frac{\mathrm{d}\Psi}{\mathrm{d}A_0}\frac{|\nabla A_0|^2}{h_3^2}-\frac{\Psi^2}{4\pi\rho}\frac{\nabla\rho}{\rho}\cdot\frac{\nabla A_0}{h_3^2}-4\pi\rho\left[\frac{\mathrm{d}E}{\mathrm{d}A}+(1-\log\rho)\frac{\mathrm{d}T}{\mathrm{d}A}\right], \tag{3.32}$$

which is a linear, Poisson like PDE for $A_1(x_1,x_2)$.

Note that the main difficulty in deriving symmetric MHD equilibria, as discussed in the previous chapter, that was the coupling between the transfield and Bernoulli equations, is completely removed by means of the linearisation in $\mathbf{B}$. This is obviously a major advantage of the low β approximation, which makes it particularly attractive for the study of MHD properties of any coronal structure.

Equations (3.30)-(3.32) are solved by Surlantzis et al. (1994) both in Cartesian and cylindrical symmetry for closed magnetic structures in a uniform gravity field ($\Phi=gz$ in both cases), simulating respectively coronal arcades and arches around sunspots. The potential field configurations are chosen to be

$$A_0=A_\star\cos(kx)\mathrm{e}^{-kz}, \tag{3.33}$$

in Cartesian geometry, and

$$A_0=A_\star krJ_1(kr)\mathrm{e}^{-kz}, \tag{3.34}$$

in cylindrical coordinates, where $A_\star$ and k are dimensional constants and J_1 is the Bessel function of first kind of order 1.

In order to simulate coronal loops, the free functions $\Psi(A_0)$, $E(A_0)$ and $T(A_0)$ are chosen, so that for each fieldline the temperature, base density and initial velocity may be selected. Outside the loop the plasma is supposed to be static and with constant temperature and footpoint densities. Both subsonic and transonic solutions with shocks are considered for the siphon flows inside the loops, and the results discussed in Sect. 3.2.1 for rigid arcades are revisited in this 2-D treatment. Possibly, the most interesting result

is the modelling of loops with *cool cores*, which are essentially cool loops ($T \sim 8 \times 10^4$ K) surrounded by a hotter and denser material. Following the suggestion by Foukal (1976) they inject plasma with a sonic speed at the loop summit and then, by tuning the free functions along each fieldline, they manage to reproduce the desired structure, with the shock front profile somehow wrapping the cool core in the downflowing leg of the loop.

When solving Eq. (3.32) for the perturbation to the field, they always find an upward small displacement of the initial potential configuration, mainly due to centrifugal forces. For static loops this displacement is upward for fieldlines overlying the loop and downward under the loop, because of the unbalanced pressure gradients caused by the higher densities and temperatures inside the loop.

Finally, note that in their original work, Surlantzis et al. (1994) assumed an isothermal plasma

$$\mathbf{V} \cdot \nabla T = 0 \Rightarrow P = T(A_0)\rho, \tag{3.35}$$

but they forgot to include the term with $\mathrm{d}T/\mathrm{d}A_0$ in Eq. (3.32). This inconsistency has been pointed out by the author of the present thesis, leading to the writing of an *Erratum* (Surlantzis et al. 1996). In this paper they solve the correct equations and claim that the new results are essentially undistinguishable from the previous ones, with the same choices of the parameters. This happens because the presence of the forgotten term affects only the first order perturbation to the magnetic field, which must be naturally small in a low β treatment. However, since one of the original features in their work is precisely the calculation of the back reaction of inertial and pressure forces on the magnetic field, the correction cannot be neglected.

In Chapter 5 the method presented here for low β, 2-D equilibria will be applied in spherical coordinates for open field magnetic structures (coronal plumes), thus covering the complementary cases not considered here.

3.4 2-D MHD equilibria in an isothermal, vertically stratified atmosphere

When the plasma β is not small, like in the low chromosphere or in the photosphere, the treatment discussed in the previous section does not apply and the intrinsic non-linearity in the MHD equations due to the plasma and magnetic field interactions must be somehow preserved. In Chapter 2 the difficulties related to a 2-D treatment of the steady MHD

equations have been fully analysed and discussed; from that discussion it was apparent that a semi-analytical approach is possible only by means of some strong assumptions, since, apart from the relatively simple incompressible case, the coupling between the two reduced equations cannot be removed.

Recently, Tsinganos et al. (1993) presented a very interesting method for deriving new classes of exact solutions for 2-D MHD equilibria in an isothermal atmosphere with uniform gravity. Their main assumption is that both the magnetic flux function A and the density ρ can be factorised in a self-similar approach. By choosing appropriately this factorisation and the form of the free functions of A, they manage to derive a couple of two ordinary differential equations which have to be solved numerically but whose solutions topologies can be studied analytically.

This is done accurately in their paper and the topology of the solutions is found to be controlled by the classical sonic point and by a novel X type critical point, corresponding to the position of the slow separatrix surface (Tsinganos et al. 1996). With regard to solar applications, they find a subclass of low Alfvén numbers loop like solutions for a mildly stratified atmosphere; for stronger stratifications no solutions exist, while for moderate stratifications only periodic solutions are allowed. One of their conclusions is that an increase in the magnitude of the flow speed increases the height of the loops and reduces the footpoints separation, in agreement with the results by Surlantzis et al. (1994) for a low β plasma discussed in the previous section, while for stronger flows there are no equilibrium solutions (the loop may undergo a disruption).

In this section, the model by Tsinganos et al. (1993) will be discussed in some detail, since it provides the mathematical tools for the prominence model, that is the subject of the next chapter.

3.4.1 Governing equations

Consider a two dimensional atmosphere, described by the Cartesian coordinates x and z, with a uniform gravity field $\Phi = gz$, where g is the constant gravity acceleration. MHD dynamic equilibria in such an atmosphere, which will be considered isothermal with T constant everywhere, may be derived by the two coupled reduced equations for $\tilde{A}(x,z)$ and $\tilde{\rho}(x,z)$

$$\frac{\partial^2 \tilde{A}}{\partial x^2} + \frac{\partial^2 \tilde{A}}{\partial z^2} - \Psi \left[\frac{\partial}{\partial x} \left(\frac{\Psi}{4\pi\tilde{\rho}} \frac{\partial \tilde{A}}{\partial x} \right) + \frac{\partial}{\partial z} \left(\frac{\Psi}{4\pi\tilde{\rho}} \frac{\partial \tilde{A}}{\partial z} \right) \right] + 4\pi\tilde{\rho} \frac{\mathrm{d}E}{\mathrm{d}\tilde{A}} = 0, \qquad (3.36)$$

$$C_s^2 \log\left(\frac{\tilde{\rho}}{\tilde{\rho}_0}\right) + \frac{1}{2}\left(\frac{\Psi}{4\pi\tilde{\rho}}\right)^2 \left[\left(\frac{\partial \tilde{A}}{\partial x}\right)^2 + \left(\frac{\partial \tilde{A}}{\partial z}\right)^2\right] + gz = E, \quad (3.37)$$

where $C_s^2 = \tilde{P}/\tilde{\rho} = k_B T/\mu m_p$ is the square of the isothermal sound speed and $\tilde{\rho}_0$ is an arbitrary constant. Assume now the following self-similar factorisations:

$$\tilde{A}(x,z) = A(x)\mathrm{e}^{-\xi z/2H} \quad \Rightarrow \quad \tilde{\mathbf{B}}(x,z) = \mathbf{B}\mathrm{e}^{-\xi z/2H}, \quad (3.38)$$

$$\tilde{\rho}(x,z) = \rho(x)\mathrm{e}^{-\xi z/H} \quad \Rightarrow \quad \tilde{P}(x,z) = P(x)\mathrm{e}^{-\xi z/H}, \quad (3.39)$$

where H is the constant scale height, $H = C_s^2/g$, and $\xi > 0$ is a positive parameter which controls the strength of the stratification. In order to have these factorisations compatible with Eqs. (3.36) and (3.37), the following choices for the two integrals of $\tilde{A}$ must necessarily be considered:

$$\Psi(\tilde{A}) = 4\pi k\tilde{A}, \qquad E(\tilde{A}) = C_s^2 \log|\tilde{A}/\tilde{A}_0|^{2(\xi-1)/\xi}, \quad (3.40)$$

where k is a free parameter controlling the strength of the flow. With these assumptions, the velocity $\mathbf{V}$ is a function of x alone,

$$\mathbf{V} = k\frac{A}{\rho}\mathbf{B}, \quad (3.41)$$

and so are the Mach and Alfvén numbers

$$M^2 = M_x^2 + M_z^2 = 2\log\left[\frac{|A/\tilde{A}_0|^{2(\xi-1)/\xi}}{\rho/\tilde{\rho}_0}\right], \quad (3.42)$$

$$M_A^2 = \lambda M_x = 4\pi k^2 \frac{A^2}{\rho}, \quad (3.43)$$

with the parameter λ replacing k.

By differentiating the Bernoulli equation, Eq. (3.37), the two reduced equations are shown to give, after some lengthy algebra:

$$\frac{\rho}{A}\frac{\mathrm{d}A}{\mathrm{d}\rho} = \frac{M^2 + M_A^2 - M_A^6/\lambda^2 - 1}{M^2 - 2 + 2/\xi - 2M_A^6/\lambda^2}, \quad (3.44)$$

or, making use of Eqs. (3.42) and (3.43)

$$\frac{2}{M_A^2}\frac{\mathrm{d}M_A^2}{\mathrm{d}M^2} = \frac{[\xi(M^2/2 + M_A^2) - 1]}{[\xi(M^2/2 + M_A^2) - 1] - [M^2 + M_A^2 - M_A^6/\lambda^2 - 1]}. \quad (3.45)$$

The above equation allows one to study the solutions topologies analytically, without actually having to solve for the unknown functions of x. Once the parameters are chosen

in order to match with the desired class of solutions, the equations may be solved by using the two unknowns M^2 and M_A^2, instead of A and ρ. The governing equations read

$$\pm\frac{M_A^2}{2}\frac{\mathrm{d}M^2}{\mathrm{d}X} = 2\frac{[\xi(M^2/2+M_A^2)-1]-[M^2+M_A^2-M_A^6/\lambda^2-1]}{[M^2+M_A^2-M_A^6/\lambda^2-1]}\sqrt{\lambda^2M^2-M_A^2}, \quad (3.46)$$

$$\pm\frac{\mathrm{d}M_A^2}{\mathrm{d}X} = 2\frac{[\xi(M^2/2+M_A^2)-1]}{[M^2+M_A^2-M_A^6/\lambda^2-1]}\sqrt{\lambda^2M^2-M_A^2}, \quad (3.47)$$

where $X = x/H$ (note that the factor 2 was forgotten in the paper). Finally, the magnetic field geometry, as well as the density (and pressure), may be derived from a knowledge of M^2 and M_A^2. For example, the angle θ of the field with the horizontal plane is given by

$$\tan^2\theta = \left(\frac{B_z}{B_x}\right)^2 = \frac{\lambda^2M^2-M_A^4}{M_A^4}, \quad (3.48)$$

hence the quantity $\lambda^2M^2 - M_A^4$ has to be positive everywhere. Note that when this quantity vanishes the loop must either have a *summit* or a *valley* at that point.

3.4.2 Solutions topologies

Apart from the trivial case $M^2 = M_A^2 = 0$, two critical points are contained in the system of equations (3.45)-(3.47), namely the sonic point

$$M^2 = 1, \qquad M_A^2 = \lambda, \quad (3.49)$$

which lies on the curve $\lambda^2M^2 - M_A^4 = 0$, hence coinciding with a loop summit or valley, and a novel X point, given by the intersection of the two curves

$$M^2/2 + M_A^2 - 1/\xi = 0, \quad (3.50)$$

$$M^2 + M_A^2 - M_A^2/\lambda^2 - 1 = 0, \quad (3.51)$$

in the (M^2, M_A^2) plane, which yields a cubic equation for M_A^2

$$M_A^2 + M_A^6/\lambda^2 = (2-\xi)/\xi, \quad (3.52)$$

which is analytically solvable. The two critical points coincide when

$$\lambda = \lambda_{\mathrm{crit}} \equiv \frac{2-\xi}{2\xi}, \quad (3.53)$$

and thus also the novel X point is located at either a loop summit or valley.

It is possible to demonstrate that along the curve given by Eq. (3.51) the electric current and the vorticity diverge, with the exception of the two critical points, that means

that only trans-critical solutions are allowed to cross that curve in order to have physical solutions. In another brilliant paper, already cited in Sect. 2.3.3, Tsinganos et al. (1996) showed that Eq. (3.51) may be rewritten as

$$V_x^4 - (C_s^2 + V_A^2)V_x^2 + C_s^2 V_{Ax}^2 = 0, \tag{3.54}$$

which is the familiar condition for the slow separatrix critical surface with $V_p^2 = V_x^2$. The projection of the poloidal velocity along the coordinate x is a direct consequence of the assumed self-similarity in z, because the MHD waves can propagate only in the x direction, perpendicular to both the symmetry direction y and the self-similarity direction z. The critical curve defined by Eq. (3.54) hence lies in the hyperbolic regime $V_c^2 < V^2 < V_s^2$, according to the discussion in Sect. 2.3.3, and the slow separatrix is a surface normal to the x axis, along which one of the two families becomes tangent.

The topology of the various classes of solutions is studied in the plane (M^2, M_A^2) by varying the two parameters ξ and λ. It is found that the loop like solutions, with just one summit, say at $X = 0$, and no valleys, exist only for a *mild* stratification $1 \leq \xi \leq 2$. A further classification is made, depending whether $\lambda < \lambda_{\rm crit}$ or $\lambda > \lambda_{\rm crit}$. In the sub-critical case the solutions have a minimum density at the summits and are either always subsonic or always supersonic. In the super-critical case other classes of solutions are possible with a density minimum at the summit and a maximum M_A^2. In one of these two new classes there is a limiting value of $M_A(X = 0)$ for the existence of solutions. This result could be important in the study of erupting loops, in which the centrifugal force becomes so large that it cannot be sustained by the magnetic tension.

For $\xi > 2$, corresponding to a strong vertical stratification, physical solutions do not exist any more, at least for the particular self-similar factorisation assumed here. On the other hand, when $0 < \xi < 1$, loop like solutions are replaced by periodic solutions with a valley at $X = 0$. In particular, for a very low stratification parameter, $0 < \xi < 2/3$, like in prominences where the scale height is much smaller than in the corona (see Chapter 4), all periodic solutions have two points where the electric current diverges and therefore the range in X of validity of the solution must necessarily be limited, for instance by the prominence width.

3.4.3 The low β limit

The present analysis is valid whatever the value of the plasma β and it considers the full non-linear coupling between the magnetic and plasma interactions. In view of the usual practice to regard the solar corona as a low β plasma and in order to compare the results with the treatments presented in Sect. 3.2 and 3.3, consider now the limit

$$\beta \ll 1 \Rightarrow M_A^2 \ll M^2. \tag{3.55}$$

Equation (3.45) simplifies considerably

$$\frac{2}{M_A^2}\frac{\mathrm{d}M_A^2}{\mathrm{d}M^2} = \frac{\xi M^2/2 - 1}{(\xi/2-1)M^2}, \tag{3.56}$$

and admits the solution

$$\left(\frac{M_A}{M_{A0}}\right)^2 = \left(\frac{M}{M_0}\right)^{2/(2-\xi)} \exp\left[-\frac{\xi}{2(2-\xi)}(M^2 - M_0^2)\right]. \tag{3.57}$$

On the other hand, Eq. (3.46) becomes, after neglecting powers of M_A^2 relative to M^2 (but not relative to $\lambda^2 M^2$)

$$\pm\frac{\mathrm{d}M^2}{\mathrm{d}X} = \frac{(\xi/2-1)M^2}{M^2-1}\frac{\sqrt{\lambda^2 M^2 - M_A^2}}{M_A^2}. \tag{3.58}$$

By using the relations in Sect. 3.4.1, Eq. (3.58) is shown to have the solution

$$\left(\frac{M}{M_0}\right)^{\xi/(2-\xi)} \exp\left[-\frac{\xi}{2(2-\xi)}(M^2 - M_0^2)\right] = \cos\left(\frac{\xi X}{2}\right), \tag{3.59}$$

and the function $\tilde{A}(x,z)$ to be given by

$$\tilde{A} = \tilde{A}_0 \cos(\xi X/2)\mathrm{e}^{-\xi Z/2}, \tag{3.60}$$

representing a potential field ($Z = z/H$) with a field aligned, sub-Alfvénic flow, as expected. Note that the static magnetic configuration in Eq. (3.60) admits flows only for a mild stratification $\xi < 2$, as is clear from Eq. (3.59). Moreover, notice that the novel X point has disappeared in this low β analysis, and only the sonic critical point $M = 1$, $M_A^2 = \lambda \ll 1$ is present in Eq. (3.58), as was found in the case of rigid tubes and in the low β equilibria shown in Sect. 3.3.

3.5 Conclusions

In this section, a review of the different approaches to the study of MHD, stationary, siphon flows in the solar atmosphere has been presented. From the discussion it is clear that the fundamental parameter is the plasma β, that is the ratio of gas and magnetic pressures, which determines what the correct approximation is that can be employed in modelling solar flows.

This has been seen for magnetic flux tubes (Sect. 3.2), which may be regarded as *rigid pipes* in the corona, where the magnetic field is dominant, or for which the coupling with the plasma forces must be taken into account in lower atmospheric levels. In the first case the magnetic field is potential and provides only the shape of the arch, while along its structure there is a balance among pressure, inertial and gravity forces. In the second case, the shape and cross sectional area of the tube depend self-consistently on the non-linear interactions with the plasma.

In Sect. 3.3 an alternative view for 2-D, MHD equilibria in the low β approximation has been discussed for a space filling, force free magnetic field. In this 2-D approach, the formalism of symmetric equilibria has been revisited through a linearisation in the magnetic field, which allows one to remove the coupling between the Bernoulli and transfield equations. By making use of appropriate boundary conditions, loop like solutions can be found both in Cartesian and cylindrical geometry, modelling, respectively, coronal arcades and axisymmetric chromospheric arched structures above sunspots. The new feature of this approach is the calculation of the first order corrections to the potential magnetic field. This approach will be adopted also when discussing an MHD model for coronal plumes, in Chapter 5.

Finally, in Sect. 3.4, an exact method for finding semi-analytical 2-D equilibria in uniform gravity is presented and discussed in detail. This makes use of a self-similar factorisation for all the physical quantities, hence reducing the initial set of equations to just a couple of ODEs. The solutions topologies is studied analytically and a class of loop like solutions is found, which reduces to that of Sect. 3.3 when the limit $\beta \ll 1$ is employed. This method will be extended to a non-isothermal atmosphere and to symmetric 3-D structures in the next chapter, where an MHD model for quiescent prominences with steady flows is treated.

Chapter 4

A steady flow model for quiescent prominences

4.1 Introduction

An important class of steady siphon flows in closed magnetic structures is the flow circulation inside and around solar prominences (see Sect. 1.2.1 for their basic properties). In the present chapter a theoretical MHD model for quiescent prominences with field aligned steady flows will be discussed, following closely the contents of two published works (Del Zanna & Hood 1996a, 1996b).

Solar prominences have interested theorists and observers for many decades. There are several problems related to the formation, support and eventual eruption that have still to be fully resolved. Among them there is the question of the source of the prominence mass. Two models have been basically discussed in the literature: one is concerned with the condensation of material from the surrounding corona, whereas for the other the mass source is the below chromosphere, with the material being ejected or siphoned into the prominence. The former hypothesis seemed to be supported also by the observations of a *coronal cavity* in the surroundings of a prominence. However, Saito & Tandberg-Hanssen (1973) found that the missing mass of the cavity was insufficient to account for the prominence mass. Moreover, the fact that a small number of quiescent prominences contains as much mass as the entire corona (Athay 1976) must also be taken into account.

The siphon mechanism to transfer material from the solar surface into a prescribed gravitational dip in a magnetic coronal arcade, such as described in the classical static

model by Kippenhahn & Schlüter (1957), has been shown to be possible by several authors. The first model is due to Pikel'ner (1971), who studied the 1-D equations for a steady flow in a flux tube with a reasonable energy equation. Uchida (1979) and Ribes & Unno (1980) proposed also stationary models belonging to this class, but in the latter the thermodynamics of the system is not taken into account. Poland & Mariska (1986) showed, in a time dependent numerical model, that a sustained heat release in a loop may give raise to an evaporation from below followed by a thermal instability at the top of the loop and a similar result has been found also by Démoulin & Einaudi (1988). Possibly, both mechanisms are responsible for prominence formation. Wu et al. (1987) have investigated a chromospheric injection process, but have demonstrated, solving numerically the 2-D radiative-conductive MHD equations, that this mechanism alone cannot account for the observed mass. An et al. (1988) have incorporated into this injection model the effects of the shear in the magnetic field lines and of converging motions at the chromospheric level. Furthermore, Mok et al. (1990), Antiochos & Klimchuk (1991) and Mendoza & Hood (1996) have worked out models with fixed geometry and different forms of the heating along a coronal loop, all giving rise to an apex prominence with correct values for the density and temperature.

In the present chapter the problem of a steady supply of material from the solar surface into a quiescent prominence is treated, following the idea by Priest & Smith (1979) who suggested, in a cartoon, how a fully formed prominence could be supplied by material through a siphon mechanism with the prominence acting as a sink of material. They assumed that a Rayleigh-Taylor instability allows the plasma to dribble across the magnetic fieldlines resulting in a slow, but steady downflow. However, here the possibility of the presence of a steady flow along the fieldlines from the corona into the prominence will be fully demonstrated by solving the complete set of the ideal MHD equations. The structure of the magnetic arcade will result from the solution, that means that the flow plays an active role and is *not* just super-imposed over a static model, as done by the majority of the other authors.

The sign of the average vertical steady flow observed in prominences is still a controversial subject. Earlier observations reported downflows in the threads of prominences seen at the limb (Dunn 1960; Engvold 1976). When large prominences are observed on the disk as dark filaments, however, the Doppler signals indicate both upward and downward vertical motion with velocities of the order of ± 6 km s^{-1} in Hα (Kubota & Uesugi 1986;

Schmieder 1989; You & Engvold 1989), thus generating some confusion in the literature concerning the actual motions in the prominence fine structure. However, in a recent analysis of old, high resolution observations of limb prominences, Zirker et al. (1994) show that their measurements are in good agreement with the current Doppler measurements on the disk. Their conclusion is that the motions inside a prominence are rather turbulent and that forces other than gravitational seem to control the velocity field pattern.

Around filaments, the transition zone shows an ascending behaviour with persistent large scale motions of the order of $5 - 10$ km s^{-1} (Lites et al. 1976; Dere et al. 1986) and horizontal motions of the same order close to the prominence axis, with an inclination of $\simeq 20°$ and parallel to the magnetic field structure. Both these observational results will be taken into account in the present model for quiescent prominences with flows, since the latter will be considered to be field aligned and the magnetic field will be allowed to possess a component in the prominence direction.

The steady flow model for quiescent prominences proposed in the present chapter is a generalisation of the static model by Hood & Anzer (1990), which is itself a generalisation of the classical Kippenhahn & Schlüter (1957) model. Both these static models are discussed in some detail in Sect. 4.2. In Sect. 4.3 the equations for the dynamical model and the basic assumptions are presented. The formalism used is derived from the work by Tsinganos et al. (1993), discussed in Sect. 3.4, but this will be extended to a non-isothermal atmosphere and to allow for the presence of a field component along the invariance direction, both necessary improvements for a realistic prominence modelling. Section 4.4 is devoted to the discussion of the results from the numerical integration of the set of equations, for values of the parameters suitable for modelling flows in a realistic quiescent prominence. Finally Sect. 4.5 is concerned with a possible simple model for the actual replenishment of a prominence by means of the steady mass flow along the coronal arcade fieldlines, while Sect. 4.6 contains the conclusions to this work.

4.2 Static models for quiescent solar prominences with normal polarity

Models for solar prominences can be classified into two basic types. *Normal* polarity prominences have a magnetic field which passes across the prominence in the same sense as suggested by the underlying photospheric field and *inverse* polarity configurations if the

prominence magnetic field is in the opposite direction (Priest 1989). The classical normal polarity model is the Kippenhahn-Schlüter (KS) model (Kippenhahn & Schlüter 1957), whereas the typical inverse polarity model is due to Kuperus & Raadu (1974). Leroy et al. (1984) found that both types of configurations do occur on the Sun. In this chapter only the normal polarity approach will be used. For a review of inverse polarity models see Anzer (1989). Finally, a new, twisted flux tube model was presented by Priest et al. (1989).

Prominence modelling using magnetostatic support began in the fifties (Menzel 1951; Dungey 1953; Kippenhahn & Schlüter 1957; Brown 1958). Menzel (1951) obtained a solution to the magnetohydrostatic equations in which the fieldlines were periodic, with one period of this solution resembling the KS like dip in the fieldlines, although being 2-D. This solution was re-discovered as one of the arcade solutions obtained by Melville et al. (1984). Kippenhahn & Schlüter (1957) modelled the prominence by a vertical current sheet and found their classical analytical solution for its interior. This will be discussed in Sect. 4.2.1. Brown (1958), using the formalism by Dungey (1953), rewrote the previous static models in terms of the magnetic flux function A for 2-D equilibria in uniform gravity.

All these models are isothermal. In addition, they either ignore the magnetic field component along the prominence or it plays a completely passive role, including the non-isothermal extension by Poland & Anzer (1971). Observations, however, show that this component is very important, with the magnetic field making an angle of between 15° and 25° with the prominence (Leroy 1989) instead of 90° if this component were absent.

The most complete static model for normal polarity prominences is the Hood & Anzer (1990) model, from now on HA. In this model the cool prominence and the surrounding hot corona are treated in the same formalism and the classical dipped fieldlines inside the prominence are derived together with the overall coronal field solution, in a self-consistent approach. This extends also the work by Anzer (1972), which modelled the coronal field around a prominence, simply treated as a current sheet. Moreover, the presence of the field component along the prominence is considered and this is also shown to play a decisive role for the magnetostatic stability of the overall structure (Longbottom & Hood, 1994).

The HA model is presented here in Sect. 4.2.2. This will serve as the starting point for its dynamic extension to include steady flows along the fieldlines, as discussed in the remainder of this chapter.

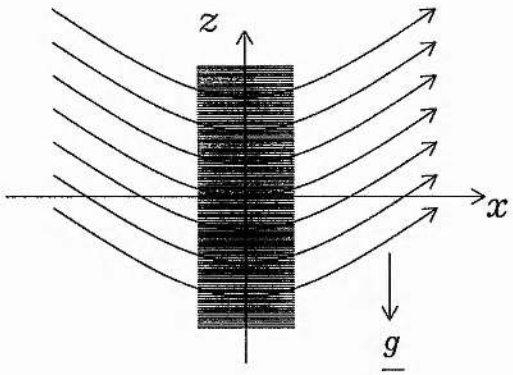

Figure 4.1: Sketch for the magnetostatic support of the dense prominence sheet against gravity.

4.2.1 The Kippenhahn-Schlüter solution

In the KS model the prominence is considered as a thin, isothermal sheet, which is one-dimensional in the sense that all the variables depend on the horizontal coordinate x alone. The magnetic fieldlines are bowed down by the dense prominence plasma, as shown in Fig. 4.1, and they play two roles. The magnetic tension provides an upward force to balance gravity and support the prominence, whereas the magnetic pressure increases with distance from the z-axis and so it provides a transverse force to compress the plasma and balance its pressure gradient.

The magnetohydrostatic equations, under the assumption of uniform field in the horizontal direction (B_x = const), uniform temperature and of vertical field and pressure depending on x only, are

$$\frac{\mathrm{d}}{\mathrm{d}x}\left(p+\frac{B_z^2}{8\pi}\right) = 0, \tag{4.1}$$

$$\frac{B_x}{4\pi}\frac{\mathrm{d}B_z}{\mathrm{d}x} - \rho g = 0. \tag{4.2}$$

Assuming $p \to 0$ and $B_z \to \pm B_0$ as boundary conditions for $|x| \to \infty$, Eq. (4.1) gives

$$p = \frac{B_0^2 - B_z^2}{8\pi}, \tag{4.3}$$

so the equation for B_z becomes

$$B_x\frac{\mathrm{d}B_z}{\mathrm{d}x} - \frac{B_0^2 - B_z^2}{2H} = 0, \tag{4.4}$$

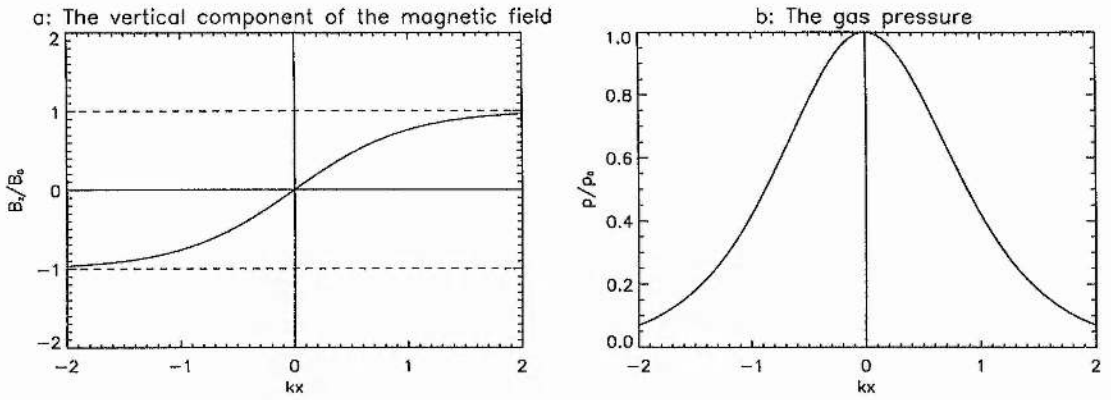

Figure 4.2: Solutions for the Kippenhahn-Schlüter model: **a** the vertical component of the magnetic field in units of B_0, **b** the gas pressure in units of $p_0 = B_0^2/8\pi$.

where $H = k_B T/\mu m_p g$ is the constant scale height. The solutions for B_z and p are, respectively

$$B_z(x) = B_0 \tanh kx, \tag{4.5}$$

$$p(x) = \frac{B_0^2}{8\pi} \mathrm{sech}^2 kx, \tag{4.6}$$

with $k = B_0/2HB_x$. The behaviour of the two analytical functions is plotted in Fig. 4.2, where the inversion in the sign of B_z and the enhanced pressure at the centre of the prominence are shown.

Obvious limitations of this model, apart from the isothermal assumption, are the complete passive role of the component of the field along the prominence (set to zero in the original paper), the pressure and density decaying to zero outside the prominence and the absence of a vertical stratification in the pressure, as expected for an isothermal atmosphere in uniform gravity. However, the basic physics of the prominence mass support by the magnetic field is fully contained in the model, which has inspired many other more sophisticated improvements, like the HA model which is presented in the next sub-section.

4.2.2 The Hood-Anzer model

The main assumption in the HA model is that the physical variables can be factorised in the following form

$$\mathbf{B} = B_0(X(kx), Y(kx), Z(kx))\, \mathrm{e}^{-kz}, \tag{4.7}$$

$$p = (B_0^2/4\pi)P(kx)\,\mathrm{e}^{-2kz}, \tag{4.8}$$

$$T = T(kx), \tag{4.9}$$

where k^{-1} is a characteristic length of the system and B_0 is a constant with the dimension of magnetic field. By substituting these expressions into the static MHD equations it is easily found that the y and z component are related to the x component of the field through

$$Y(kx) = \alpha X, \qquad Z(kx) = X', \tag{4.10}$$

where the prime indicates derivation with respect to kx and where $\alpha = \tan\theta$ is the (constant) angle between the field and the x-axis. The two resulting equations are

$$Z' = (\gamma P - X^2 - Y^2)/X, \tag{4.11}$$

$$P' = -\gamma P Z/X, \tag{4.12}$$

where

$$\gamma = 2\left[\frac{1}{2kH(kx)} - 1\right], \tag{4.13}$$

with H being the variable scale height, proportional to the temperature. An integral of the system is the total pressure in the horizontal direction:

$$2P + X^2 + Y^2 + Z^2 = 2P_{\mathrm{tot}}. \tag{4.14}$$

The equations derived so far hold whatever the function $T = T(x)$. In theory, this could be selected to model a typical prominence temperature profile and, by solving Eqs. (4.11) and (4.12), the resulting magnetic field and pressure could be deduced. However, since the prominence/corona transition region is very narrow, the two regions may be considered as isothermal with two different temperatures, namely T_{cool} and T_{hot}, with $T_{\mathrm{cool}} \ll T_{\mathrm{hot}}$. The scale height profile is then assumed to be (taking as plane of symmetry the $y-z$ plane and considering for simplicity only the region $x > 0$)

$$H(x) = \begin{cases} H_{\mathrm{cool}}, & 0 < x < x_{\mathrm{prom}}, \\ H_{\mathrm{hot}}, & x > x_{\mathrm{prom}}, \end{cases} \tag{4.15}$$

where x_{prom} is the prominence half width and where $H_{\mathrm{cool}} = \mathcal{R}T_{\mathrm{cool}}/\mu_{\mathrm{cool}}g$, $H_{\mathrm{hot}} = \mathcal{R}T_{\mathrm{hot}}/\mu_{\mathrm{hot}}g$.

In each of the two isothermal regions the function γ becomes a constant parameter, thus allowing an integral of Eq. (4.12) as

$$P = CX^{-\gamma}, \tag{4.16}$$

where C is a positive constant, and Eq. (4.11) yields

$$(X')^2 = 2P_{\rm tot} - (1+\alpha^2)X^2 - 2CX^{-\gamma}, \tag{4.17}$$

which is a phase plane relation for the function $X(kx)$. Whenever γ is positive, as in a cool prominence where $kH_{\rm cool}$ is small, the solution curves are closed contours. Hence, the prominence solutions will be periodic, with X oscillating between two values where X' vanishes. These periodic solutions are unphysical *unless* the temperature increases to a coronal value for which $\gamma \geq 0$ before one period is completed. Therefore, realistic prominence magnetic fields are allowed only for a non-isothermal atmosphere.

A free parameter that is left is the value of the constant k controlling the vertical stratification through the exponential factors in Eqs. (4.7) and (4.8). This will depend, in general, on the photospheric field distribution for a low β coronal plasma. In HA the value

$$k = \frac{1}{2H_{\rm hot}} \Rightarrow \gamma_{\rm hot} = 0 \tag{4.18}$$

is chosen, in order to have a constant pressure in the x direction, from Eq. (4.16), and the following analytical solution for a constant-α, force free field (e.g. Priest 1982):

$$X(kx) = X_{\rm m} \cos\left[\sqrt{1+\alpha^2}\, k\,(x - x_{\rm m})\right], \tag{4.19}$$

where $X_{\rm m}$ is the maximum value at the top of the arcade $x = x_{\rm m}$. The values of these constants are obtained by matching the (numerical) internal solution with the coronal analytic solution, through the continuity of the functions X, Y, Z and P at the prominence/corona interface.

The application of this model to realistic prominence values predicts reasonable values for the coronal plasma β and for the arcade width. The great improvement of the HA model with respect to previous static models is certainly the treatment of both the prominence and coronal region in the same mathematical frame. The prominence region is not treated like a simple current sheet, however, the electric current there is much stronger than in the corona and the current sheet approximation is retrieved when $kx_{\rm prom},\ kH_{\rm cool} \rightarrow 0$.

4.3 Basic model and governing equations

In this section the mathematical equations for the quiescent prominence model are derived. This will be done in two steps. In the first sub-section the general problem of dynamical

MHD equilibria in an isothermal and vertically stratified atmosphere with uniform gravity is discussed (generalising the 2-D treatment presented in Sect. 3.4), whereas the second sub-section is devoted to the actual prominence model and to the discussion of the correct jump conditions to be applied at the boundary between the prominence and the corona.

4.3.1 Field aligned, steady flows in an isothermal, stratified atmosphere

Consider an ideal, isothermal plasma in a uniform gravitational field (along the z axis) with a steady mass flow that, for sake of simplicity, is parallel to the fieldlines. Employing Cartesian coordinates, invariance along the y direction can be assumed. The theory exposed in Sect. 2.3 is then applied ($\Omega = 0$, $h_3 = 1$ and $\Phi = gz$), leading to the two reduced equations for $A(x,z)$ and $\rho(x,z)$:

$$\left(1 - \frac{\Psi^2}{4\pi\rho}\right)\nabla^2 A - \frac{\Psi}{4\pi\rho}\frac{\mathrm{d}\Psi}{\mathrm{d}A}|\nabla A|^2 + \frac{\Psi^2}{4\pi\rho}\frac{\nabla\rho}{\rho}\cdot\nabla A +$$

$$\frac{I}{1-\Psi^2/4\pi\rho}\left(\frac{\mathrm{d}I}{\mathrm{d}A} + \frac{I\Psi/4\pi\rho}{1-\Psi^2/4\pi\rho}\frac{\mathrm{d}\Psi}{\mathrm{d}A}\right) + 4\pi\rho\frac{\mathrm{d}E}{\mathrm{d}A} = 0, \tag{4.20}$$

$$c^2\log\rho + \frac{1}{2}\left(\frac{\Psi}{4\pi\rho}\right)^2\left[|\nabla A|^2 + \left(\frac{I}{1-\Psi^2/4\pi\rho}\right)^2\right] + gz = E, \tag{4.21}$$

where c is the isothermal sound speed. Once the functions A and ρ are known, the other variables are given by

$$B_x = -\frac{\partial A}{\partial z}, \quad B_y = \frac{I}{1-\Psi^2/4\pi\rho}, \quad B_z = \frac{\partial A}{\partial x} \tag{4.22}$$

$$p = c^2\rho, \quad \mathbf{V} = \frac{\Psi}{4\pi\rho}\mathbf{B}. \tag{4.23}$$

Assume now the following factorisations for A and ρ:

$$A(x,z) = (B_0/k)X(kx)\,\mathrm{e}^{-kz}, \tag{4.24}$$

$$\rho(x,z) = (B_0^2/4\pi c^2)P(kx)\,\mathrm{e}^{-2kz}, \tag{4.25}$$

and the following choices for the free functions of A:

$$\Psi(A) = \lambda(B_0/c)X(kx)\,\mathrm{e}^{-kz}, \tag{4.26}$$

$$I(A) = \alpha B_0 X(kx)\,\mathrm{e}^{-kz}, \tag{4.27}$$

$$E(A) = c^2\log\left[X(kx)\,\mathrm{e}^{-kz}\right]^{-\gamma}, \tag{4.28}$$

where B_0 is a constant, γ has been defined in Eq. (4.13) (where now $H = c^2/g$ is the *constant* scale height), and λ is a new parameter giving the strength of the flow.

Thanks to these assumptions, the magnetic field and the pressure are still given by Eqs. (4.7) and (4.8), but now

$$Y = \alpha X/(1 - \lambda^2 X^2/P), \tag{4.29}$$

while the relation $Z = X'$ still holds. The expression for the velocity field is

$$\mathbf{V} = c\,\lambda \frac{X}{P}(X, Y, Z), \tag{4.30}$$

which is independent from z in this model. After some lengthy but straightforward calculations, the two reduced equations may be written as

$$Z' = \frac{\gamma P - X^2 - Y^2 + (1+q)M_{\rm A}^2 Z^2}{X(1 - M_{\rm A}^2)}, \tag{4.31}$$

$$P' = -qPZ/X, \tag{4.32}$$

where the function q has been defined as

$$q = \frac{\gamma + M^2 - 2M_{\rm A}^6/\lambda^2}{1 - M^2 - M_{\rm A}^2 + M_{\rm A}^6/\lambda^2}. \tag{4.33}$$

In these equations, M and $M_{\rm A}$ are respectively the Mach and Alfvénic Mach numbers, given by

$$M^2 = \lambda^2 \frac{X^2}{P^2}(X^2 + Y^2 + Z^2), \tag{4.34}$$

$$M_{\rm A}^2 = \lambda^2 \frac{X^2}{P} = \frac{\beta}{2} M^2. \tag{4.35}$$

Here β is the plasma beta, defined as usual as the ratio of the kinetic and magnetic pressures p and $p_{\rm m} = |\mathbf{B}|^2/8\pi$, that is

$$\beta = \frac{2P}{X^2 + Y^2 + Z^2}. \tag{4.36}$$

Equation (4.33) simply reduces to $q = \gamma$ in the static case $\lambda = 0$ (the term $2M_{\rm A}^6/\lambda^2$ is proportional to λ^4), and Eqs. (4.31) and (4.32) become Eqs. (4.11) and (4.12), respectively. Note that this result is exactly the same as in Tsinganos et al. (1993) (see Sect. 3.4), but its validity has been extended here to the more general case $B_y \neq 0$ and $V_y \neq 0$. In particular, Eq. (4.32) reduces to Eq. (3.44) by letting $\xi = 2kH$. Here the analysis will be restricted to subsonic and sub-Alfvénic flows (for which q and Z' are always defined),

since the goal of the present study is the investigation of the corrections to the static case due to the introduction of a flow.

Needless to say, in the dynamic case $\lambda \neq 0$, Eqs. (4.31) and (4.32) must be solved numerically, whatever the value of γ. This is a simple initial value problem for the set of unknown functions $P(kx), X(kx)$ and $Z(kx)$, for any given values of the parameters γ, α and λ.

4.3.2 The jump conditions at the prominence/corona interface

Following closely the static HA model, the transition region between the prominence and the coronal environment is considered to be so narrow that the temperature profile is assumed to be a step function connecting the two isothermal regions. The function $H(kx)$ is again given by Eq. (4.15) and, as in HA, the value $2H_{\rm hot}$ is assumed for the characteristic length k^{-1}.

The presence of the flow modifies the matching conditions for the physical quantities at the interface $x = x_{\rm prom}$ as follows:

$$[B_x] = 0, \tag{4.37}$$

$$[\rho V_x] = 0, \tag{4.38}$$

$$\left[\rho V_x^2 + p + (1/8\pi)(B_y^2 + B_z^2 - B_x^2)\right] = 0, \tag{4.39}$$

$$[\rho V_x V_y - (1/4\pi) B_x B_y] = 0, \tag{4.40}$$

$$[\rho V_x V_z - (1/4\pi) B_x B_z] = 0, \tag{4.41}$$

where $[f]$ is the difference of the values of f in the two regions at the interface, that is

$$[f] = \lim_{\epsilon \to 0} [f(x_{\rm prom} + \epsilon) - f(x_{\rm prom} - \epsilon)]. \tag{4.42}$$

These are essentially the jump conditions for a MHD oblique shock with $\mathbf{v} \parallel \mathbf{B}$ (see, for example, Priest 1982). Assuming that the expressions for the physical quantities $p, \rho, \mathbf{B}$ and $\mathbf{V}$ given in the previous sub-section are the same in the two regions, Eqs. (4.37), (4.40) and (4.41) imply respectively

$$[X] = 0, \tag{4.43}$$

$$\left[(1 - \lambda^2 X^2/P) Y\right] = 0, \tag{4.44}$$

$$\left[(1 - \lambda^2 X^2/P) Z\right] = 0. \tag{4.45}$$

From Eqs. (4.38) and (4.44) the matching conditions for the parameters λ and α are derived, namely

$$\lambda_{\rm hot} = \lambda_{\rm cool}/\sqrt{2kH_{\rm cool}}, \quad \alpha_{\rm hot} = \alpha_{\rm cool}$$

where $2kH_{\rm cool} = H_{\rm cool}/H_{\rm hot} \ll 1$. The condition on the pressure function P can be obtained from Eq. (4.39) with the aid of Eqs. (4.43) – (4.45):

$$[P + \lambda^2 X^4/P] + a^2[(1 - \lambda^2 X^2/P)^{-2}] = 0, \tag{4.46}$$

where the factor $a^2 = (1 - \lambda^2 X^2/P)^2(Y^2 + Z^2)/2$ is continuous across the interface. This is a non-linear algebraic equation for the value of P after the discontinuity and it has to be solved numerically. As it will be shown in Sect. 4.4.1, there is a maximum value for λ beyond which no solution of Eq. (4.46) can be found. Note that in the static case $\lambda = 0$ the jump conditions (4.43) to (4.46) lead to the continuity of the four functions X, Y, Z and P, as expected.

It is worth noticing that the jump conditions for the prominence model at the boundary $x = x_{\rm prom}$, Eqs. (4.37), (4.38) and (4.40), yield directly the continuity of the integrals A, Ψ and I. However, note that the function E does *not* have to be continuous since the energy flux is not conserved at the boundary surface $x = x_{\rm prom}$ between the two isothermal regions. In fact, the last jump condition for the energy flux reads

$$[E] + \lim_{\epsilon \to 0} \int_{x_{\rm prom}-\epsilon}^{x_{\rm prom}+\epsilon} (1 - \log\rho)\frac{{\rm d}T}{{\rm d}x}{\rm d}x = 0. \tag{4.47}$$

It is clear that, since the derivative of the temperature behaves like a delta function for $x = x_{\rm prom}$, the free function E must be discontinuous at that point, according to its definition in Eq. (4.28). Therefore, the integral in Eq. (4.47) simply gives the input of energy necessary to balance the energy flux E and need not to be evaluated.

In the prominence and coronal isothermal regions the theory developed in the preceding sub-section is applied. Hence, the numerical integration starts from the centre of the prominence $x = 0$ and goes on with $H = H_{\rm cool}$ and $\gamma = 2(H_{\rm hot}/H_{\rm cool} - 1) \gg 1$ until $x_{\rm prom}$. Then the jump conditions (4.43) to (4.46) are applied and the new initial values and parameters are derived. In the corona $kH = 1/2$, $\gamma = 0$ and the integration is continued until $x_{\rm edge}$, the foot point of the arcade where $B_x = 0$ ($X = 0$). Note that in the dynamic case, even if $\gamma = 0$, the function q in Eqs. (4.31) and (4.32) is not zero and no analytic solution can be found. Hence, the solution (4.19) for a force free, constant α type coronal

field with constant pressure in the horizontal direction does not apply in the dynamic case. Deviations from this solution will be analysed in the next section.

The initial values for our model are $X(0) = X_0, Z(0) = Z_0$ and $P(0) = P_0$. In order to obtain a solution for which the fieldlines show a central dip, supporting the dense material of the prominence against gravity, the conditions $X(0) = 1, X'(0) = 0, X''(0) > 0$ are assumed, thus $X_0 = 1, Z_0 = 0$ and

$$\beta_0 \equiv 2P_0/(1+Y_0^2) > 2/\gamma_{\rm cool} \simeq H_{\rm cool}/H_{\rm hot}, \tag{4.48}$$

where $Y_0 \equiv Y(0) = \alpha_{\rm cool}/(1 - \lambda_{\rm cool}^2/P_0)$. This means that, given the scale heights ratio, the central pressure (or density) cannot be too small while the magnetic field component along the prominence cannot be too large in respect of the normal component. Moreover, other two quantities are required to derive the values of $\alpha_{\rm cool}$ and $\lambda_{\rm cool}$. Suitable choices are Y_0 and M_0, and the other parameters are given by:

$$\lambda_{\rm cool} = M_0 P_0/(1+Y_0^2)^{1/2}, \tag{4.49}$$

$$\alpha_{\rm cool} = Y_0[1 - M_0^2 P_0/(1+Y_0^2)]. \tag{4.50}$$

Concluding, the parameters that can be selected in the prominence model are five, namely the half scale heights ratio $kH_{\rm cool}$, which yields the value of γ, the dimensionless prominence half width $kx_{\rm prom}$, the central pressure P_0 in units of $B_0^2/4\pi$ (for $z = 0$), the magnetic field component Y_0 along the prominence calculated at the origin $x = 0, z = 0$ and finally the Mach number M_0 at the centre of prominence.

4.4 Results

The parameters of the model are chosen to be the same as in HA, so that the limit of the static case may be easily checked in order to compare the results. Therefore, for the prominence region, the temperature and the mean molecular weight are respectively $T_{\rm cool} = 6 \times 10^3\,{\rm K}$ and $\mu_{\rm cool} = 1$, giving a pressure scale height $H_{\rm cool} = 180\,{\rm km}$. The normal and longitudinal field components at $x = 0, z = 0$ as $B_x = 5\,{\rm G}$ and $B_y = 12\,{\rm G}$, yielding $B_0 = 5\,{\rm G}$ and $\alpha_{\rm cool} = 2.4$ (in the limit $\lambda_{\rm cool} = 0$), with a correspondent angle of $\theta \simeq 22.6°$ between the field and the prominence. The average number density is taken to be $\overline{n}_{\rm cool} = 2 \times 10^{17}\,{\rm m}^{-3}$; considering this value as half of the central density, the central pressure is $p(0,0) = 2k_{\rm B}T_{\rm cool}\overline{n}_{\rm cool} = 0.0332$ pascals, to be nondimensionalized against

$B_0^2/4\pi \simeq 0.2$ pascals. The width of the prominence is $2x_{\rm prom} = 3\,000$ km. In the corona $T_{\rm hot} = 10^6$ K and $\mu_{\rm hot} = 0.5$, with a corresponding scale height of $H_{\rm hot} = 6 \times 10^4$ km, so that $k^{-1} = 1.2 \times 10^5$ km.

The values of the parameters for the dynamical model are then

$$kH_{\rm cool} = 0.0015, \quad kx_{\rm prom} = 0.0125, \quad P_0 = 0.167, \quad Y_0 = 2.4,$$

that is exactly the same as in HA, to which a value for M_0 has to be added in order to fix the velocity field magnitude. The equations are integrated for four different values of M_0, namely

$$M_0 = (0.0,\ 0.5,\ 0.8,\ 1.0) \times 10^{-3},$$

and the results are shown in Figs. 4.3 and 4.4.

In Figs. 4.3a and 4.3b the projections of the magnetic and velocity fieldlines onto a vertical plane normal to the prominence are shown for a selection of equally spaced A-values, both inside the prominence and for the overall arcade (with different scales). Inside the prominence the fieldlines exhibit the classical KS structure with X almost constant. The general behaviour is of the classical support of the dense prominence against gravity provided by the magnetic tension due to the central dip. The half width of the coronal arcade is $x_{\rm edge} \simeq 1.4\ H_{\rm hot}$. Figures 4.3c and 4.3d show the behaviour of the function $Z(kx)$, again inside the prominence and for the overall arcade. The rapid turn round of B_z at $x = x_{\rm prom}$ indicates the presence of a strong current flowing inside the prominence, suggesting that the current sheet models are a reasonable approximation. In Fig. 4.3e the modulus of the magnetic field (in units of B_0 and for $z = 0$) inside the prominence is shown as a function of kx. In Fig. 4.3f the relative change in the same quantity, with respect to its static constant value, is shown for the four chosen values of the initial Mach number M_0 (in units of 10^{-3}).

In Fig. 4.4 the pressure P (in units $B_0^2/4\pi$ and for $z = 0$), the Mach number M and the Alfvénic Mach number $M_{\rm A}$ are plotted as functions of kx, both in the prominence and in the coronal regions. The prominence pressure (Fig. 4.4a) is unaffected by the flow, while in the corona (Fig. 4.4b) substantial percentage changes of $\approx 25\%$ can be found. It is easily seen that only in the static case the pressure is continuous at $x = x_{\rm prom}$, according to Eq. (4.46). Note that the final pressure at $x = x_{\rm edge}$ depends on the strength of the flow. The density ρ and the plasma β, as $|\mathbf{B}| \simeq$ const, behave like the pressure in the two regions but the density show a discontinuity of $(2kH_{\rm cool})^{-1} \ll 1$ at $x_{\rm prom}$, entering the corona,

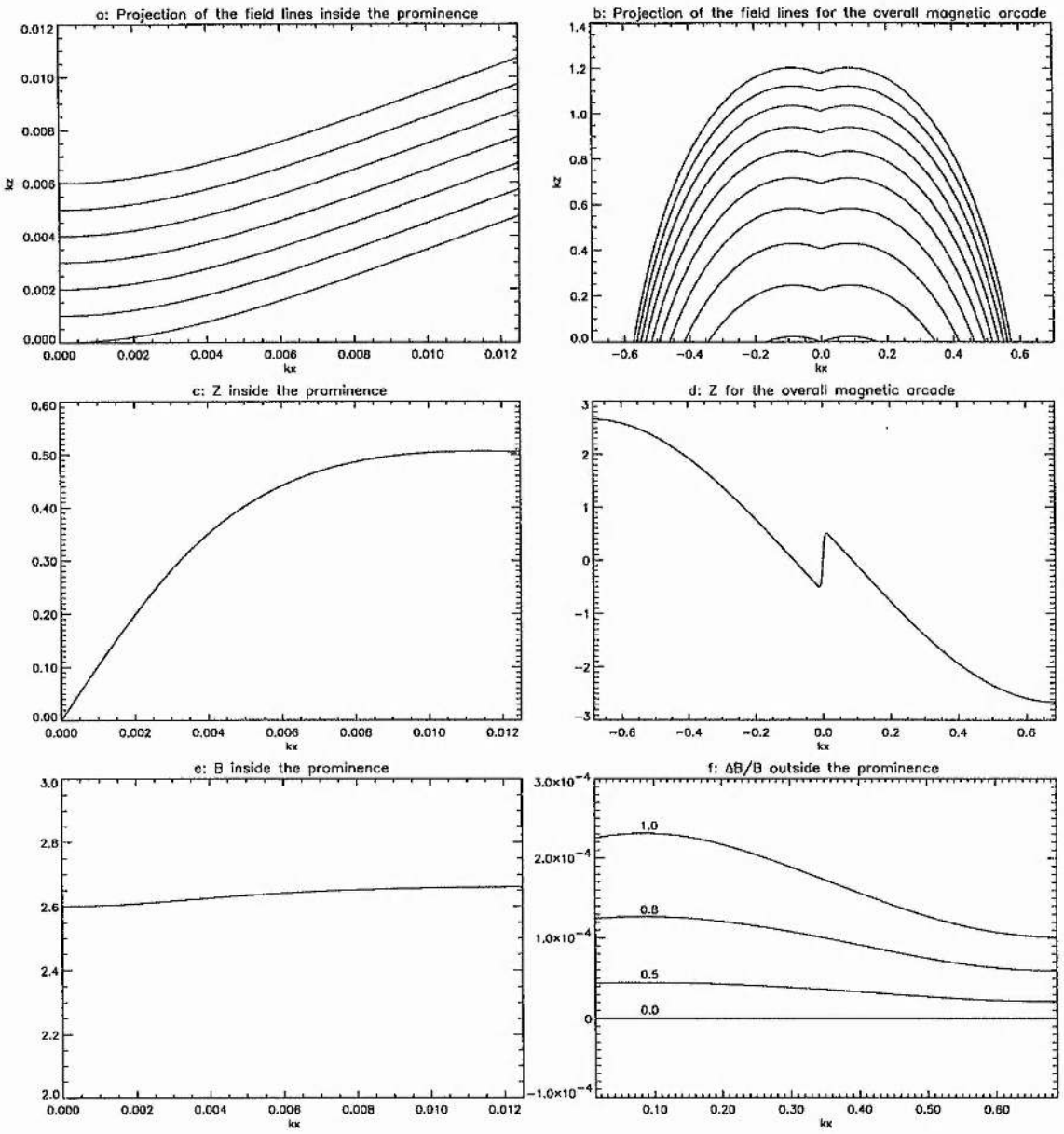

Figure 4.3: **a** Projection of the magnetic and velocity fieldlines inside the prominence on a plane normal to the prominence direction. A selection of equally spaced values of A is shown. **b** Projection of the overall arcade for equally spaced values of A, different from Fig. 4.3a. **c** The function $Z(kx)$ inside the prominence. **d** The function $Z(kx)$ for the overall arcade. **e** Modulus of the magnetic field in units of B_0 and for $z = 0$ inside the prominence. **f** Relative change in the modulus of the magnetic field, in respect to the static case, for $z = 0$. The reference numbers are the values of M_0 in units of 10^{-3}.

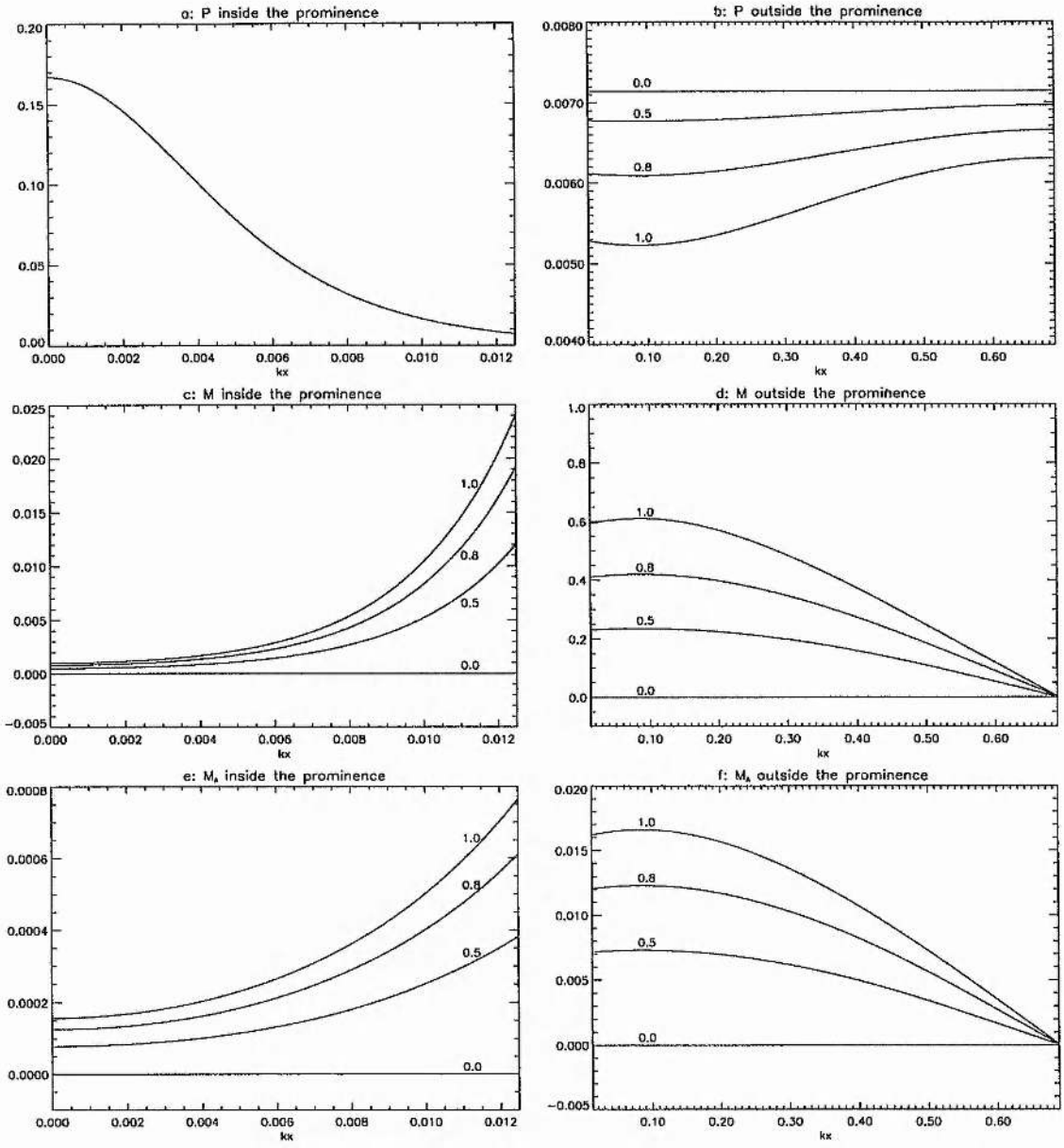

Figure 4.4: **a** The function $P(kx)$ inside the prominence, that is the pressure in units of $B_0^2/4\pi$ and for $z = 0$. **b** The function $P(kx)$ outside the prominence. The meaning of the reference numbers is the same as in Fig. 4.3f. **c** The Mach number $M(kx)$ inside the prominence. **d** The Mach number $M(kx)$ outside the prominence. **e** The Alfvénic Mach number $M_A(kx)$ inside the prominence. **f** The Alfvénic Mach number $M_A(kx)$ outside the prominence.

due to the jump in the sound speed c. Also the two Mach numbers are discontinuous functions of kx at $x = x_{\rm prom}$ and the flow is the strongest in the corona. Note that the flow is always subsonic and sub-Alfvénic, but in the corona velocities of the same order as the sound speed are allowed. For comparison, the sound speed in the prominence is $c_{\rm cool} = \sqrt{gH_{\rm cool}} \simeq 7\,{\rm km\ s^{-1}}$ and in the corona $c_{\rm hot} = \sqrt{gH_{\rm hot}} \simeq 130\,{\rm km\ s^{-1}}$. Therefore, if in the prominence region the magnitude of the flow is in the range $1 - 10^2\,{\rm m\ s^{-1}}$, that is essentially a static situation, in the corona velocities as high as $\simeq 100$ km s^{-1} can be reached. This is the reason why the pressure and the magnetic field are unaffected by the flow inside the prominence but may differ from the static case in the corona. This is even clearer in Figs. 4.4e and 4.4f, where the Alfvénic Mach number $M_{\rm A}$ is plotted for the two regions. Inside the prominence $M_{\rm A}^2 \simeq 10^{-7}$ and outside $M_{\rm A}^2 \simeq 10^{-4}$. This means that in both cases $M_{\rm A}^2 \ll 1$, so that the factor $1 - M_{\rm A}^2$ can be taken as 1 in all the relations where it appears, namely the definition of Y in Eq. (4.29), the equation (4.31) for Z' and the jump conditions (4.44) and (4.45) for Y and Z.

Concluding, the prominence region can be considered as static, as the magnetic field and the pressure are not modified by the flow because of the small Mach number and the negligible Alfvénic Mach number. In the corona, the magnetic field is again almost unperturbed by the flow, as the changes in its modulus $|\mathbf{B}|$ and in the angle $\theta = \cot^{-1}(Y/X)$ between the prominence and the horizontal magnetic field, as well as in the jumps of both the functions Y and Z at $x_{\rm prom}$, have a maximum magnitude of approximately 10^{-4}. On the contrary the presence of the flow substantially modifies the pressure. The result is that, in the corona, even if $\gamma = 0$, the pressure is no longer constant and hence the situation is no longer force free. Again, the pressure deficit shown in Fig. 4.4b does not result in a sensible deviation of the magnetic field from the static situation but, on the other hand, it balances a flow with $M \sim 1$, according to the Bernoulli equation with $\gamma = 0$.

4.4.1 The jump condition for the pressure and the limit on the initial velocity

As it has been anticipated in Sect. 4.3, the freedom in choosing the values of the initial Mach number M_0, that is the magnitude of the overall flow, is limited by Eq. (4.46) which

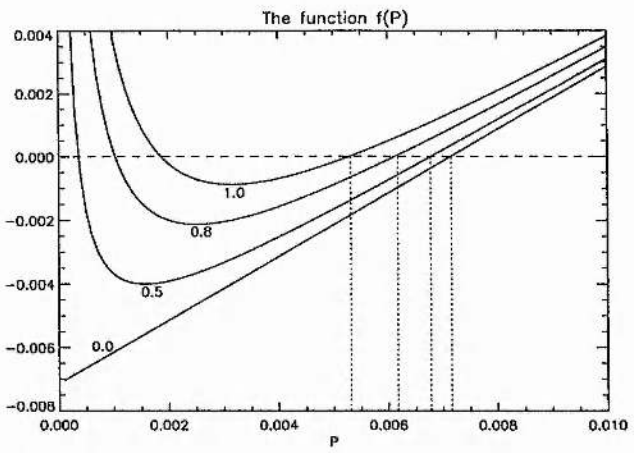

Figure 4.5: The function $f(\overline{P})$ defined in Eq. (4.51), for the usual values of the parameters and for the four chosen values of M_0 (in units of 10^{-3}). The roots of the equation $f(\overline{P}) = 0$ are given by the intersections of the curves with the dashed line and these are the values of the pressure $\overline{P}$ just after the interface $x = x_{\rm prom}$. Note that for too high values of M_0 no solution for $\overline{P}$ can be found.

is satisfied only if the flow is not too strong. Condition (4.46) may be rewritten as follows:

$$f(\overline{P}) \equiv \overline{P}+\lambda_{\rm hot}^2 X^4/\overline{P}+a^2(1-\lambda_{\rm hot}^2 X^2/\overline{P})^{-2}-(P+\lambda_{\rm cool}^2 X^4/P+a^2(1-\lambda_{\rm cool}^2 X^2/P)^{-2}) = 0, \tag{4.51}$$

where all the quantities are calculated at $x = x_{\rm prom}$, $\overline{P}$ in the corona just after the interface and P in the prominence just before it. In Fig. 4.5 the function $f(\overline{P})$ is plotted for the usual values of the parameters and for the four chosen values of M_0. It is clear that a maximum value of M_0 exists and that for higher values no solutions for the pressure satisfying the jump condition Eq. (4.51), given by the vertical dotted lines, can be found. The presence of a limiting strength of the flow is not due to our particular model nor to any magnetic effect, but it is a general hydrodynamic result when considering a flow through an interface between two isothermal regions, where the energy flux is not conserved (see Appendix B).

A very good approximation of this maximum value $M_0^{\rm max}$ of the initial velocity can be obtained easily through an analytic study of Eq. (4.51) using the approximation $M_{\rm A}^2 \ll 1$. After some straightforward algebra it is easy to see that the function $f(\overline{P})$ has a minimum for $\overline{P} = \lambda_{\rm hot} X\sqrt{X^2+Y^2+Z^2}$ and that this minimum must be negative. Then, replacing $\lambda_{\rm cool}$ by $M_0\beta_0/2$ and $\lambda_{\rm hot}$ by $(2kH_{\rm cool})^{-1/2}M_0\beta_0/2$, this condition can be written as a

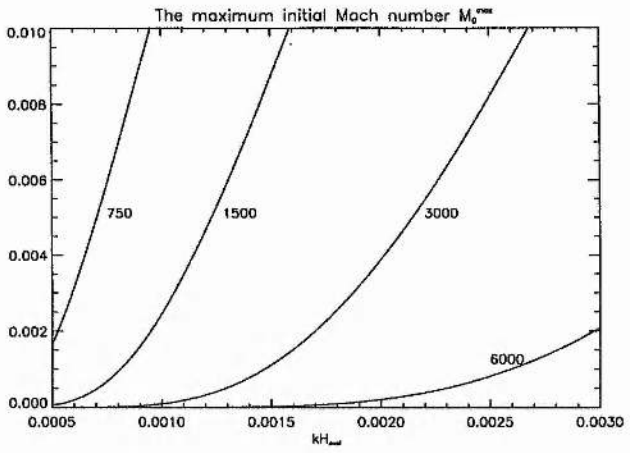

Figure 4.6: The dependence of the maximum initial Mach number $M_0^{\max}$, defined in Eq. (4.52), by $kH_{\rm cool}$ is shown for four values of the parameter $kx_{\rm prom}$, corresponding to the values of the total width of the prominence printed in the picture.

quadratic inequality for M_0. Finally, using the fact that $2kH_{\rm cool} \ll 1$, the solution is

$$M_0 \leq M_0^{\max} \equiv \sqrt{2kH_{\rm cool}}\,\frac{\beta/\beta_0}{2X}. \tag{4.52}$$

It is worth analysing in some detail the dependence of $M_0^{\max}$ on the different parameters of our model. Throughout the whole prominence, as in the classic KS model, $X \simeq X_0$. Therefore, the only factor that needs to be studied is β/β_0, taken at the edge of the prominence region. It is obvious that the influence of M_0 is negligible, as β/β_0 is calculated inside the prominence; besides, also the initial values P_0 and Y_0 do not affect the behaviour of $M_0^{\max}$ very much, as β is normalized against $\beta_0 \equiv 2P_0/(1+Y_0^2)$ ($M_0^{\max}(P_0)$ is a decreasing function while $M_0^{\max}(Y_0)$ is slowly increasing). Hence the two most important parameters are $kx_{\rm prom}$ and $kH_{\rm cool}$. The functional form of $\beta(kx_{\rm prom})$ is, as a matter of fact, the same as P shown in Fig. 4.4a, as the modulus of the magnetic field is almost constant towards the edge of the prominence (Fig. 4.3e). This means that β/β_0, as well as $M_0^{\max}$, must be a decreasing function of the width of the prominence. On the other hand, if the temperature difference between the two regions is enhanced, that means increasing $\gamma_{\rm cool}$ and decreasing $kH_{\rm cool}$, then again the plasma β decreases because gravity becomes more important inside the prominence and so the pressure falls off faster. The actual behaviour of $M_0^{\max}$ as a function of $kH_{\rm cool}$ and $kx_{\rm prom}$ is shown in Fig. 4.6.

4.4.2 An analytic solution for the low β corona

The results of the steady flow model agree with the observations of a low β coronal plasma, since its maximum value is $\beta \simeq 0.002$ for the chosen values of the parameters. Using the fact that $\beta \ll 1$ it is possible to derive a zeroth order analytic solution as it has been done in Sect. 3.4.3.

From Eq. (4.35) it is clear that $\beta \ll 1$ implies $M_{\rm A}^2 \ll M^2$, so that the function q defined in Eq. (4.33) reduces to $q = M^2/(1-M^2)$, as $\gamma = 0$. Using the relations in Sect. 4.3, the following expressions for the Mach numbers are found:

$$\frac{M}{M_{\rm m}} \mathrm{e}^{-(M^2-M_{\rm m}^2)/2} = \frac{X}{X_{\rm m}}, \tag{4.53}$$

$$\frac{M_{\rm A}^2}{M_{\rm A\,m}^2} = \frac{X}{X_{\rm m}} \frac{M}{M_{\rm m}}, \tag{4.54}$$

where $X_{\rm m}$, $M_{\rm m}$ and $M_{\rm A}$ are the maximum values of the respective functions assumed at the same point $kx_{\rm m}$.

Finally, combining the definitions of M^2 and $M_{\rm A}^2$ with Eq. (4.54) yields

$$X'^2 + (1+\alpha^2)X^2 = (1+\alpha^2)X_{\rm m}^2 \tag{4.55}$$

with the known solution (4.19) for a static, constant α type, force free field. Thus, the fact that in the corona the presence of a field aligned flow does not affect the shape of the magnetic arcade has been analytically demonstrated under the realistic assumptions of small β and Alfvénic Mach number values. However, the situation is still dynamic and the values of the Mach and Alfvénic Mach numbers are given by Eqs. (4.53) and (4.54) respectively, in perfect agreement with the plots in Figs. 4.4d and 4.4f.

4.5 A simple model for the prominence mass supply

The main purpose of this model is to demonstrate the actual possibility of the presence of a flow along the fieldlines of the whole magnetic arcade, both inside and outside the prominence, by studying in detail the jump conditions at the interfaces between the two regions. This has been achieved regardless of the actual direction of the flow. However, a symmetric converging flow into the prominence, as suggested in a simple cartoon by Priest & Smith (1979), may be considered as a possible explanation for the steady replenishment of the prominence mass. As neither the governing equations of the model nor the matching

conditions at the interfaces between the prominence and the corona depend on the actual direction of the flow, the only problem to solve is basically the question of the mass conservation inside the prominence. Again, following the idea by Priest & Smith, assume that the material sucked into the prominence neutralises cooling down and then dribbles across the fieldlines down to the solar surface.

Using the relations derived for the dynamic model, it is possible to calculate characteristic quantities like the time scale τ of the replenishment process and the downflow velocity, simply derived by imposing the conservation of the total mass of the prominence. Consider a prominence with a finite height extending from $z = 0$ to $z = z_{\rm prom} = 50\,000$ km. The total mass and the mass entering per unit time, as functions of z and per unit length, are respectively given by $2\int_0^{x_{\rm prom}}\int_0^z \rho\,{\rm d}x\,{\rm d}z$ and $2\int_0^z (\rho V_x)_{x_{\rm prom}}\,{\rm d}z$, yielding

$$m(z) \simeq \frac{B_0^2 P_0 x_{\rm prom}}{8\pi k c_{\rm cool}^2}(1 - {\rm e}^{-2kz}) \tag{4.56}$$

and

$$\dot{m}(z) \simeq \frac{B_0^2 M_0 P_0}{4\pi k c_{\rm cool}\sqrt{1+Y_0^2}}(1 - {\rm e}^{-2kz}), \tag{4.57}$$

where the approximation $\int_0^{x_{\rm prom}} P{\rm d}x \simeq (1/2)P_0 x_{\rm prom}$ and $X(kx_{\rm prom}) \simeq 1$ has been used. The characteristic time scale τ is independent of the height:

$$\tau = \frac{m}{\dot{m}} \simeq \frac{x_{\rm prom}\sqrt{1+Y_0^2}}{2c_{\rm cool}M_0}. \tag{4.58}$$

With the values of the parameters given in Sect. 4.4 and choosing $M_0 = 10^{-3}$, the result is $\tau \simeq 6.4$ days. Since the largest initial Mach number has been chosen, the time scale can be greater, in good agreement with the observed average life time of quiescent prominences ($\simeq$ 1 month). Therefore, this result leads to the suggestion that the existence of a quiescent prominence can be explained by a supply of chromospheric material siphoned into the prominence along the magnetic arcade fieldlines. Once this replenishment ends the prominence might disappear in a slow downflow towards the solar surface. Obviously, the possibility of a final eruption is not taken into account in this simple model.

The downflow speed $\dot{m}(z)/2\int_0^{x_{\rm prom}}\rho\,{\rm d}x$ is a function of z:

$$V_{\rm d}(z) \simeq \frac{c_{\rm cool}M_0}{kx_{\rm prom}\sqrt{1+Y_0^2}}[1 - {\rm e}^{-2k(z_{\rm prom}-z)}], \tag{4.59}$$

and the maximum velocity, at the bottom end of the prominence, is $V_{\rm d} \simeq 0.12$ km s^{-1}. This value is rather small and confirms the result of an almost static situation inside the

prominence region (v_d has the same order of magnitude of the entering velocity, as may be seen in Fig. 4.4c).

4.6 Conclusions

In this chapter the problem of steady flows in quiescent prominences has been treated. The prominence has been considered as a vertical cool sheet with finite length enbedded in the surrounding hot corona. The magnetic field and gas pressure have been assumed to be separable in the horizontal and vertical coordinates and an exponentially decaying behaviour has been chosen for the latter. These assumptions are the same as in the static HA model, so that the present treatment may be considered as a dynamical extension to the static case.

Both the prominence and coronal regions have been regarded as isothermal (with different temperatures) and, in each region, the generalised Grad-Shafranov equation for an isothermal, steady, MHD flow in uniform gravity has been solved. The method used is similar to that presented in Sect. 3.4, but here the vector fields retain all their components. The equations have been solved numerically and without the need of any approximation. The two solutions have been then matched solving the set of jump conditions at the boundary surfaces between the two isothermal regions. Since the energy flux is not conserved crossing these surfaces, a limiting strength for the flow has been found and this makes the flow always subsonic (and sub-Alfvénic as the plasma β is small everywhere).

The results are that the static magnetic configuration is slightly affected by the presence of the flow only in the coronal region, while the structure inside the prominence (that exhibits the classic KS dip for the magnetic support against gravity) can be still considered as static. On the other hand, the coronal pressure shows a deficit allowing the flow to occur and therefore the configuration is no longer force free as in the static case. The average velocities in the corona are of the order of 50 km s^{-1}, in good agreement with the observations, whereas inside the prominence $V \sim 0.1$ km s^{-1}.

Finally, the suggestion by Priest & Smith (1979) for the mechanism of the prominence mass supply has been revisited using the results of our model. The characteristic time scale of the mass replenishment is of the same order of magnitude as the observed average life time of quiescent prominences, suggesting that their existence is indeed connected to the mass supply from the below chromosphere.

Chapter 5

An MHD model for coronal plumes

5.1 Introduction

As an example of MHD modelling of steady flows in *open* magnetic structures in the solar atmosphere, coronal plumes are considered. The model treated here is essentially that of Del Zanna et al. (1997a). The observational properties of plumes have been reviewed in Sect. 1.2.2, here attention will be focused on their relationship with the solar wind and on their magnetic nature.

Together with macrospicules, short lived ($\sim$ 30 minutes) jets of cooler chromospheric material, coronal plumes are believed to trace the open fieldlines structure and they might play an important role for the physics of the solar wind. Possible remnants of the signature of these coronal hole fine structures have been discovered (Thieme et al. 1990) by analysing high speed streams data taken by the Helios probes in the range 0.3 – 1 AU. Their results show that plumes expand while retaining an overall pressure balance with the background, thus suggesting that the open magnetic fieldlines play an important role in confining the plume plasma even in the outer corona. This behaviour has been investigated by Velli et al. (1994), who proposed an interesting thin flux tube model in which the magnetic flux is conserved separately both in the plume and in the surrounding coronal hole and total pressure is balanced across the fieldlines (see Sect. 5.2.1). However, recent data by the Ulysses spacecraft, flying over the solar poles, does *not* seem to confirm the above scenario (Mc Comas et al. 1996; Poletto et al. 1996).

Another fundamental observational result, confirming the intrinsic magnetic nature of coronal plumes, is the connection between plumes and magnetic surface features related with flux concentrations, as briefly discussed in Sect. 1.2.2. Before the *Skylab* era, plumes were believed to be rooted in unipolar flux concentrations in relation with photospheric or chromospheric faculae, located at the vertices between supergranular cells (Newkirk & Harvey 1968). This picture was supported by the coincidence of the mean plume separation ($\approx 7 \times 10^4$ km) and the size of a typical supergranular cell. After the discovery of the presence of compact EUV enhancements at the base of the most bright plumes (Bohlin et al. 1975), which in turn correspond to X-ray bright points, the attention has shifted towards magnetic bipolar regions (Golub et al. 1974; Habbal 1992; Dowdy 1993). These observations have suggested a possible explanation for plume formation: one or more bipoles are pushed by photospheric motions towards an open flux region located at a supergranular junction; eventually reconnection occurs, fieldlines open up and the required energy for plume formation is released. This mechanism has been analysed in more detail by Wang & Sheeley (1995b), whereas a systematic analysis of the effect of heating of the inner corona at the plume base may be found in Wang (1994), who also investigated the solar wind implications by solving the full energy equation along the radial direction (although pressure balance across the fieldlines is not taken into account).

Although so far there is little direct evidence for the relationship between plumes and network activity (magnetograms are difficult to take at the limb, where the plumes are more easily observable), preliminary results from SOHO coordinated observational campaigns seem to suggest that it is reasonable to assume that plumes are rooted in open flux concentration regions. In support of this idea come also the observations of a super-radial expansion of plumes near their base, say in the range $1 - 1.2\, R_\odot$ (Saito 1965; Ahmad & Withbroe 1977; Ahmad & Webb 1978). What is observed is obviously a density behaviour, but if the plume is to be in equilibrium, then it must be threaded by diverging fieldlines with increasing height (Ahmad & Withbroe 1977). Potential field models trying to explain this behaviour were proposed by Newkirk & Harvey (1968) and by Suess (1982), but none of them include the plasma parameters in their analysis. Suess's model consists of an analytical, two dimensional field in Cartesian geometry with a given vertical field at the plume base. Since the idea of a dominant magnetic force at the plume base is retained in this chapter, Suess's model will be described in detail in Sect. 5.2.2.

The main goal of the present chapter is to present a self-consistent MHD model which

correctly reproduces the observed super-radial expansion near the plume base, assuming that magnetic effects are dominant in the inner corona but takes into account the pressure, inertial and gravity forces as well. This will be achieved by solving the steady, ideal, 2-D MHD equations, linearised with respect to the magnetic field under the assumption of a low β coronal plasma. The method of solution and the general equations are presented in Sect. 5.3, whereas the actual plume model is discussed in Sect. 5.4, first in the simple radial case. The effect of a flux concentration at the base of the plume is studied in Sect. 5.5 and the results are compared with the observations by Ahmad & Withbroe (1977). Finally, the conclusions are drawn in Sect. 5.6.

5.2 Previous stationary models of coronal plumes

In Chapter 3 it was shown that MHD models of closed magnetic structures in the solar atmosphere can be classified essentially according to two different approaches. The first is to assume that the structure is one-dimensional as a first approximation and that all the quantities depend on the coordinate along the flux tube only. The second is to study the 2-D equilibria for a space filling magnetic field. If the first method allows the inclusion of the non-linear effects of the interaction between the magnetic field and the plasma forces (and sometimes more realistic energy equations), the second requires either a linearisation in the magnetic field or very restrictive assumptions on the unknowns.

The same situation holds for open field configurations like coronal plumes. The rigid flux tube approximation, for which the plume has a radial structure with a varying, but given, cross sectional area can be applied for modelling a realistic energy balance (Wang 1994). For simpler energy equations, the thin flux tube approximation has been adopted by Velli et al. (1994) and the lateral pressure balance is taken into account by means of a numerical iterative method. This will be discussed in the next sub-section.

With regard to the 2-D approach, the only previous treatment is the above mentioned *potential field* model by Suess (1982), which will be here described in Sect. 5.2.2. The low β extension to this potential model is due to Del Zanna et al. (1997a), which is the subject of the remainder of the chapter.

5.2.1 A thin flux tube model (Velli et al. 1994)

The basic idea in this model is that coronal plumes expand into interplanetary space while retaining an overall pressure balance with the surrounding coronal hole, as *in situ* observations seem to suggest (Thieme et al. 1990). The coronal hole is divided in two different types of regions: the background coronal hole, with density ρ_1, temperature T_1, magnetic field B_1, covering an area A_1, and coronal plumes which are considered to have the same properties everywhere, namely density ρ_2, temperature T_2, magnetic field B_2 and area A_2. All these quantities are functions of the radial coordinate r alone and the two regions are supposed to be isothermal (here T will be actually identified with the square of the isothermal sound speed, so that $p = \rho T$).

If the filling factor of plumes at the coronal base is α_2, it is then possible to write

$$\alpha_1 A_1 + \alpha_2 A_2 = f(r), \qquad \alpha_1 + \alpha_2 = 1, \tag{5.1}$$

where $f(r)$ is the overall coronal hole expansion and the areas are normalised at the base $r = R_\odot$ to give $A_1 = A_2 = f(R_\odot) = 1$. The area is linked to the magnetic field by the conservation of the magnetic flux, which is supposed to hold separately for the two regions:

$$A_1 B_1 = \Phi_1, \qquad A_2 B_2 = \Phi_2, \tag{5.2}$$

where Φ_1 and Φ_2 are constants. In the thin flux tube approximation, curvature terms are neglected and the lateral pressure balance reads

$$\rho_1 T_1 + \frac{B_1^2}{8\pi} = \rho_2 T_2 + \frac{B_2^2}{8\pi}. \tag{5.3}$$

The stationary wind equations for the two regions are then

$$\left(M_1 - \frac{1}{M_1}\right) M_1' = \frac{a_1'}{a_1} + \frac{f'}{f} - \frac{g}{r^2}, \tag{5.4}$$

$$\left(\frac{M_2}{\delta} - \frac{1}{M_2}\right) M_2' = \frac{a_2'}{a_2} + \frac{f'}{f} - \frac{g}{\delta r^2}, \tag{5.5}$$

where $g = GM_\odot / T_1 R_\odot$ is the non-dimensional gravity factor (between 10 and 20 for typical coronal values) and the following relations have been assumed:

$$a_1 = A_1/f, \qquad a_2 = A_2/f, \qquad \delta = T_2/T_1. \tag{5.6}$$

When $\alpha_2 = 0$, the equations for the two regions are uncoupled and are solved in the standard way, with a_2 which can be derived from Eq. (5.3). When $\alpha_2 \neq 0$ the equations

are solved iteratively, starting from the $\alpha_2 = 0$ solution for M_2 to get M_1, imposing the total area constraint, and then updating the solution for M_2 with this guess for M_1 until convergence is achieved. The method works well for small values of the filling factor, for which the non-linear effects are small (Velli, private communication).

For a filling value of $\alpha_2 = 5\%$ and a plasma $\beta \sim 1\%$ at the coronal base, a plume which is hotter and denser undergoes a slight contraction within the first solar radii. This behaviour is due to the fact that initially the kinetic pressure decays exponentially while the magnetic pressure only decays algebraically: a pressure equilibrium at the base implies that regions with a stronger magnetic field will have a higher total pressure higher up and will therefore expand. After a few solar radii, however, the decay in the magnetic field begins to dominate and the plume begins to expand super-radially. These results will be confirmed by the 2-D, low β model described in the remainder of the chapter.

5.2.2 A 2-D potential model (Suess 1982)

If the magnetic field in coronal plumes is strong, say of the order of 10 G, the magnetic effects dominate in the low corona and the plume structure may be considered to be determined by a force free field. Suess (1982) applied a very simple 2-D potential solution to reproduce the observed super-radial expansion near the plume base. Since this expansion is very low down, say below $1.2\,R_\odot$, gravity and flow effects may be neglected and the geometry can be assumed as Cartesian.

For a 2-D field the magnetic field can be derived from a scalar potential Φ:

$$\mathbf{B} = \nabla\Phi, \tag{5.7}$$

where Φ satisfies the Laplace equation:

$$\nabla^2\Phi = 0. \tag{5.8}$$

Assuming a uniform, vertical, background field (normalised to unity), the solution for a symmetric structure in the strip $-a/2 \leq x \leq a/2$ is

$$\Phi(x,z) = \sum_{n=1}^{\infty} A_n \cos\left(\frac{n\pi x}{a}\right) \mathrm{e}^{-n\pi z/a} + z. \tag{5.9}$$

The values for the constants A_n are to be determined by the boundary conditions at $z = 0$. If the photospheric vertical field is taken to be

$$B_z(x,0) = b + c\left(\frac{m}{\pi}\right)^{1/2} \mathrm{e}^{-m\cos^2(\pi x/a)}, \tag{5.10}$$

which becomes a delta function for $m \to \infty$, the results are

$$c = (1-b)\left[\frac{1}{a}\left(\frac{m}{\pi}\right)^{1/2}\int_0^a \mathrm{e}^{-m\cos^2(\pi x/a)}\mathrm{d}x\right]^{-1}, \tag{5.11}$$

$$A_n = -\frac{2\pi}{n}\int_0^a \left[b + c\left(\frac{m}{\pi}\right)^{1/2}\mathrm{e}^{-m\cos^2(\pi x/a)}\right]\cos\left(\frac{n\pi x}{a}\right)\mathrm{d}x, \tag{5.12}$$

for n even and $A_n = 0$ for n odd. Finally, the magnetic field components are given by

$$B_x = \frac{\partial\Phi}{\partial x} = -\sum_{n\,\mathrm{even}}\frac{n\pi}{a}A_n\sin\left(\frac{n\pi x}{a}\right)\mathrm{e}^{-n\pi z/a}, \tag{5.13}$$

$$B_z = \frac{\partial\Phi}{\partial z} = 1 - \sum_{n\,\mathrm{even}}\frac{n\pi}{a}A_n\cos\left(\frac{n\pi x}{a}\right)\mathrm{e}^{-n\pi z/a}. \tag{5.14}$$

The three parameters of this potential models are a, b and m. However, a enters only as a scale factor and the value of m does not change things very much as long as it is large (say $m = 100$). Therefore, the geometry of the magnetic field is mainly controlled by the value of b, which is essentially the magnetic field on the axis of the plume at $z = 0$ normalised to the background field. By tuning this to an appropriate value, Suess found a shape which qualitatively reproduces the results of a super-radial expansion of the plume close to its base. This result confirms that this effect may be due only to the presence of a magnetic flux concentration at the base of the plume.

The main limitation of this model is certainly the total absence of the plasma effects, which makes it realistic only on a vertical scale comparable to the horizontal width of the plume, typically $a \approx 60\,000$ km, where the β is very small. Moreover, the whole analysis in the original paper is affected by a trivial mistake: the factor π was forgotten in the exponential in Eq. (5.9) and in the solution for the magnetic field components, resulting in a qualitatively different shape of the fieldlines.

5.3 Low β, 2-D equilibria: basic equations in spherical geometry

In this section, the formalism presented in Sect. 3.3 will be revisited under the assumptions of spherical geometry and azimuthal symmetry. The steady, ideal MHD equations may be written in the non-dimensional form:

$$\nabla\cdot\mathbf{B} = 0, \tag{5.15}$$

$$\nabla \cdot (\rho \mathbf{V}) = 0, \tag{5.16}$$

$$\nabla \times (\mathbf{V} \times \mathbf{B}) = 0, \tag{5.17}$$

$$(\nabla \times \mathbf{B}) \times \mathbf{B} = (\beta_\star/2)[M_\star^2 \rho (\mathbf{V} \cdot \nabla)\mathbf{V} + \nabla P + g_\star \rho r^{-2} \mathbf{e}_r], \tag{5.18}$$

where all the quantities have been non-dimensionalised against typical coronal values and where the values of the three parameters

$$\beta_\star = \frac{8\pi P_\star}{B_\star^2}, \quad M_\star = \frac{V_\star}{V_{s\star}}, \quad g_\star = \frac{GM_\odot m_p}{2k_B T_\star R_\odot} \tag{5.19}$$

indicate the relative importance of the various terms in Eq. (5.18) (here $V_{s\star} = \sqrt{2k_B T_\star / m_p}$ is a reference value of the isothermal sound speed and all the other symbols have their usual meaning).

As in Sect. 3.3, the main assumption in the model is that the magnetic forces are dominant over all the others, namely pressure gradients, gravity and inertial forces. In the low solar corona this is a good approximation and the coronal plasma is thus regarded as low β. Hence, in order to linearise the MHD equations with respect to the magnetic field, the following form for $\mathbf{B}$ is assumed:

$$\mathbf{B} = \mathbf{B}_0 + \frac{\beta_\star}{2}\mathbf{B}_1, \quad \beta_\star \ll 1, \tag{5.20}$$

where its zeroth order component $\mathbf{B}_0$ is necessarily force free (from Eq. (5.18)).

Consider now a purely 2-D spherical coordinate system in which all the quantities lie in the (r - θ) plane and do not depend upon the azimuthal coordinate ϕ (the plume axis will coincide with the symmetry axis $\theta = 0$). Using the formalism of the flux functions, Eqs. (5.15) to (5.17) give (see Sect. 3.3)

$$B_{0r} = \frac{1}{r^2 \sin\theta}\frac{\partial A_0}{\partial \theta}, \quad B_{0\theta} = -\frac{1}{r \sin\theta}\frac{\partial A_0}{\partial r}, \tag{5.21}$$

$$B_{1r} = \frac{1}{r^2 \sin\theta}\frac{\partial A_1}{\partial \theta}, \quad B_{1\theta} = -\frac{1}{r \sin\theta}\frac{\partial A_1}{\partial r}, \tag{5.22}$$

$$V_r = \frac{1}{r^2 \sin\theta}\frac{\Psi(A_0)}{\rho}\frac{\partial A_0}{\partial \theta}, \quad V_\theta = -\frac{1}{r \sin\theta}\frac{\Psi(A_0)}{\rho}\frac{\partial A_0}{\partial r}, \tag{5.23}$$

where the magnetic flux function is $A(r,\theta) = A_0 + (\beta_\star/2)A_1$ and Ψ is a free function of A_0 (note that the velocity and magnetic fields are parallel only at the zeroth order). In order to solve the equations a relation between pressure and density is needed. Here, like in Sect. 3.3, the isothermal case will be assumed, thus

$$\mathbf{V} \cdot \nabla T = 0 \Rightarrow P = T(A_0)\rho, \tag{5.24}$$

where the temperature T is another free function of A_0 (thus T is constant along the fieldlines). Making use of these assumptions, the component of Eq. (5.18) across $\mathbf{B}_0$ splits into the two transfield equations

$$\mathcal{L}(A_0) \equiv \frac{\partial^2 A_0}{\partial r^2} + \frac{\sin\theta}{r^2}\frac{\partial}{\partial\theta}\left(\frac{1}{\sin\theta}\frac{\partial A_0}{\partial\theta}\right) = 0, \tag{5.25}$$

$$\mathcal{L}(A_1) = M_\star^2\left[\frac{\Psi}{\rho}\frac{\mathrm{d}\Psi}{\mathrm{d}A_0}|\nabla A_0|^2 - \frac{\Psi^2}{\rho^2}\nabla A_0\cdot\nabla\rho\right] - \rho r^2\sin^2\theta\left[\frac{\mathrm{d}E}{\mathrm{d}A_0} + (1-\log\rho)\frac{\mathrm{d}T}{\mathrm{d}A_0}\right], \tag{5.26}$$

whereas the component along $\mathbf{B}_0$ yields the Bernoulli equation

$$\frac{M_\star^2}{2}\frac{\Psi^2}{\rho^2}\frac{|\nabla A_0|^2}{r^2\sin^2\theta} + T\log\rho - \frac{g_\star}{r} = E(A_0) \tag{5.27}$$

and E is the third free function of A_0.

The main result of the linearisation of the magnetic field is clearly the decoupling of the transfield and Bernoulli equations, which is the goal of the method. This allows one to solve the problem in three distinct steps:

1. Solve the transfield equation, Eq. (5.25), for the unperturbed field.

2. Solve the Bernoulli equation, Eq. (5.27), for the density.

3. Solve the transfield equation, Eq. (5.26), for the correction to the field.

Clearly, the corrections to the magnetic field must remain small and the condition for this is $A_1 \sim A_0$.

The first step is still solvable analytically. The general solution of Eq. (5.25) can be expressed in the form

$$A_0(r,\theta) = 1 - \cos\theta + \sum_{n=1}^{\infty}[a_n r^{-n} + b_n r^{n+1}]Q_n(\cos\theta), \tag{5.28}$$

where

$$Q_n(\cos\theta) = \frac{\sin^2\theta\, P_n'(\cos\theta)}{n(n+1)} = \frac{P_{n-1}(\cos\theta) - P_{n+1}(\cos\theta)}{2n+1} \tag{5.29}$$

and $P_n(\cos\theta)$ is the Legendre polynomial of order n. The components of the resulting current-free (potential) magnetic field are

$$B_{0r}(r,\theta) = r^{-2} + \sum_{n=1}^{\infty}[a_n r^{-(n+2)} + b_n r^{n-1}]P_n(\cos\theta), \tag{5.30}$$

$$B_{0\theta}(r,\theta) = \sum_{n=1}^{\infty}[n a_n r^{-(n+2)} - (n+1)b_n r^{n-1}]\frac{Q_n(\cos\theta)}{\sin\theta}. \tag{5.31}$$

Notice that the field has been chosen to be normalised against its radial component $\mathbf{B}_0 = r^{-2}\mathbf{e}_r$, while the series gives the deviation from the radial case. These corrections are only important on a vertical (radial) scale-height comparable with the horizontal width of the structure. For larger values of r the field tends to its radial background component.

In order to model an open coronal field, all the b_n coefficients must be set to zero to take the field finite at large distances, whereas the a_n coefficients may be derived by imposing a relation $B_{0r} = 1 + f(\theta)$ at the coronal base $r = 1$, yielding

$$a_n = \frac{2n+1}{2} \int_0^\pi f(\theta) P_n(\cos\theta) \sin\theta \mathrm{d}\theta. \tag{5.32}$$

This solution corresponds to Suess's model in Cartesian geometry, presented in the previous section. Clearly the same results could have been obtained making use of the magnetic scalar potential Φ ($\mathbf{B} = \nabla\Phi$); in this case the potential would have satisfied Laplace's equation $\nabla^2\Phi = 0$.

Given the analytical expression for the unperturbed field $\mathbf{B}_0$ and the three functions $\Psi(A_0)$, $T(A_0)$ and $E(A_0)$, the Bernoulli equation can be solved numerically, for example by using Newton's method. In general, Eq. (5.27) will provide two solutions for the density, corresponding to the subsonic and supersonic cases. Moreover, the transfield equation, Eq. (5.26), will be singular at the sonic points, whose position will depend on the choice of the free functions and on the shape of the unperturbed field. Thus, if the solution has to pass through the sonic point, or if a shocked solution is required, an extra condition must be imposed, hence limiting the freedom in the choice of the integrals of A_0.

5.4 The radial case

In order to investigate the basic physics involved in the plume model, consider first a simple background radial field

$$A_0(\theta) = 1 - \cos\theta \Rightarrow \mathbf{B}_0(r) = r^{-2}\mathbf{e}_r, \tag{5.33}$$

in a region around the plume axis $\theta = 0$ (where $A_0 \approx \theta^2/2$). This means that, at the moment, the problem of the super-radial expansion at the base is not treated and attention is focused on the global radial behaviour of the physical quantities.

Through the definition of the Mach number

$$M = \frac{V}{V_s} = \frac{M_* \Psi}{\sqrt{T}\rho r^2}, \tag{5.34}$$

and using the continuity equation to eliminate ρ, the radial derivative of the Bernoulli equation yields (the prime denotes a derivative in respect to r)

$$\left(M - \frac{1}{M}\right) M' = \frac{2}{r} - \frac{g_\star}{T r^2}. \tag{5.35}$$

This is simply the famous Parker equation for radial, isothermal winds (see Sect. 1.3.2). The only physically relevant solution for the solar wind problem is the one crossing the sonic point with $M' > 0$ (Parker or transonic solution) and eventually connecting via a shock to the interstellar medium (see also Chapter 6 for a detailed discussion on the problem of the boundary conditions).

In the present model the temperature is a function of the fieldlines, hence the sonic radius

$$r_{\rm sonic}(A_0) = \frac{g_\star}{2T(A_0)} \tag{5.36}$$

will be a function of the fieldlines too. This means that the flow becomes supersonic at different radii for different values of θ. Imposing the transonic condition, the equation for M can be integrated again to give

$$M \exp\left[-\frac{1}{2}(M^2 - 1)\right] = \left(\frac{r_{\rm sonic}}{r}\right)^2 \exp\left[2\left(1 - \frac{r_{\rm sonic}}{r}\right)\right], \tag{5.37}$$

Notice that, because of the transonic condition, the function $\Psi(A_0)$ must be now derived from Eq. (5.37) and hence it is no longer free.

The density is related to the Mach number through the Bernoulli equation, which yields

$$\rho = \rho_{\rm base} \exp\left[-\frac{g_\star}{T}\left(1 - \frac{1}{r}\right)\right] \exp\left(-\frac{M^2}{2}\right), \tag{5.38}$$

where the relationship $E = T \log \rho_{\rm base} - g_\star$ has been assumed and where $\rho_{\rm base}(A_0)$ gives the density profile at $r = 1$ in the static case (for solar values $M_{\rm base} \sim 10^{-3}$, hence the dynamic effects are actually negligible at the base of the corona). Note that for a constant temperature everywhere the Mach number does not depend upon θ (from Eq. (5.37)) and therefore the density profile across the fieldlines remains the same at all heights.

In order to investigate the behaviour of the physical quantities in our model, the shape of the two arbitrary functions $\rho_{\rm base}(A_0)$ and $T(A_0)$ has to be chosen. Here the following functional forms will be assumed:

$$\rho_{\rm base} = 1 + (\rho^0_{\rm base} - 1) \exp(-A_0/A_{0\rm w}), \tag{5.39}$$

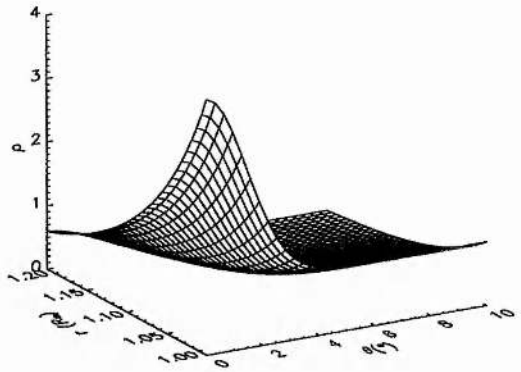

Figure 5.1: The density ρ, non-dimensionalised against its value at the base of the coronal hole, as a function of θ and r. The parameters are $\rho^0_{\rm base} = 4$, $T^0 = 1$, $\theta_{\rm w} = 2°$ and $g_\star = 11.5$. Here $\theta_{\rm w}$ is defined as the characteristic angular half width at which the density drops by a factor e^{-1} in respect to the corresponding axial value.

$$T = 1 + (T^0 - 1)\exp(-A_0/A_{0\rm w}), \tag{5.40}$$

where the density (temperature) is considered to be non-dimensionalised against its value in the inter-plume region at the coronal hole base, so that $\rho^0_{\rm base}$ (T^0) gives the ratio between the densities (temperatures) on the plume axis and in the background coronal hole. Observed values of $\rho^0_{\rm base}$ are in the range 3–5. Expression (5.39) has been chosen following Ahmad & Withbroe (1977), where a Gaussian like density profile is shown to provide the best fit to the observed EUV intensities when the temperature is constant (the same analysis has been applied in X-rays by Ahmad & Webb, 1978). An example of the resulting 2-D density structure near the plume base is shown in Fig. 5.1, in which the radial decaying behaviour and the conservation of the θ profile at all heights (for a constant temperature) are clearly visible.

As pointed out earlier, the main effect of a variable temperature is that the sonic point becomes a function of θ, thus affecting also the radial density decay. Assuming a background coronal hole temperature of $T_\star = 10^6\,K$ the resulting sound speed is $V_{s\star} \approx 130\,{\rm km\,s^{-1}}$ and $g_\star = 11.5$. In Fig. 5.2 the sonic point position, given by Eq. (5.36), is shown as a function of θ for different values of T^0.

The behaviour of the number densities and velocities, both on the plume axis (PL) and in the background coronal hole (CH), is given in Fig. 5.3, where the parameters used are

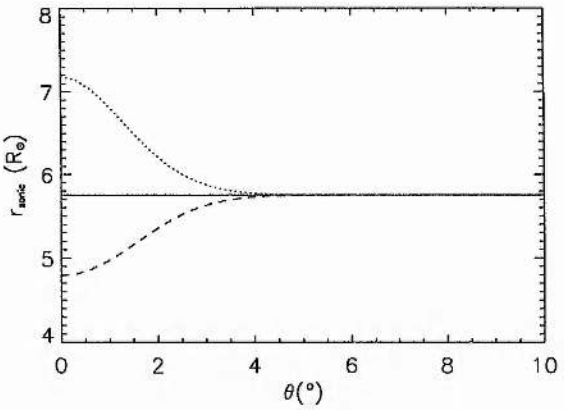

Figure 5.2: The position of the sonic point as a function of θ in units of $R_\odot$ (again $\theta_w = 2°$ and $g_\star = 11.5$). Three values of $r_{\rm sonic}$ are shown: for $T(\rm PL) = T(\rm CH)$ ($T^0 = 1.0$, solid line), for $T(\rm PL) > T(\rm CH)$ ($T^0 = 1.2$, dashed line) and for $T(\rm PL) < T(\rm CH)$ ($T^0 = 0.8$, dotted line). Note that the sonic point is closer to the Sun for a hot plume and further for a cold plume.

the same as in Fig. 5.2. Note that a hotter plume contains a higher speed solar wind but, despite this, the density contrast increases with r, thus implying that the factor containing $g_\star/T$ is dominant over the factor with $M^2/2$. On the other hand, when the plume is cooler than the surroundings, its wind speed is also lower and the plume to background density ratio decreases with r and the plume may become even less dense than the coronal hole after a few solar radii. Finally, as discussed before, when the temperature is constant the velocity in the plume is the same as in the coronal hole and the density ratio is constant for all the values of r.

From the above discussion it is apparent that the value of the temperature is a crucial parameter for the density and velocity behaviour at large distances. A plume to background temperature ratio as small as $T^0 = 1.2$ implies a variation of $\sim 1\, R_\odot$ in the sonic point position and a density ratio which increases quite rapidly with r. Unfortunately, as Habbal et al. (1993) pointed out in an interesting review of previous observations, temperature measurements in coronal holes are affected by so many unknown parameters (temperature values can only be inferred using some models, where it is usually supposed to be constant across the plume) and uncertain quantities (like element abundances), that the accuracy in the measurements cannot be better than 20%. Therefore, it is obvious that there is no way to deduce our temperature profile in Eq. (5.40) from observations

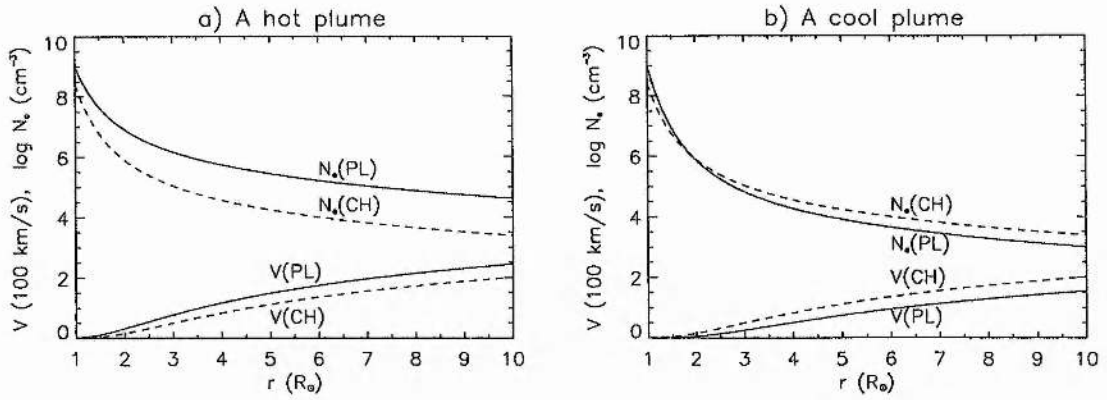

Figure 5.3: The number density N_e (in units of cm^{-3}) in logarithmic scale and the velocity V (in units of $100\,\mathrm{km\,s}^{-1}$). The solid lines refer to the plume axis (PL) whereas the dashed lines refer to the background coronal hole (CH). The parameters are $N_e(\mathrm{PL}) = 10^9\,\mathrm{cm}^{-3}$, $N_e(\mathrm{CH}) = 2.5 \times 10^8\,\mathrm{cm}^{-3}$ (at the coronal base), $T(\mathrm{CH}) = 10^6\,\mathrm{K}$, $\theta_w = 2°$ and $g_\star = 11.5$. **a** A hot plume with $T_0 = 1.2$, **b** A cool plume with $T_0 = 0.8$.

(there is not even an agreement whether a plume should be cooler or hotter than the surroundings), hence the comparison with observational data in the next sub-section will be done assuming $T = \mathrm{const}$. On the contrary, the present model could be used to calculate the expected emission, for given values of the parameters $T_\star$, T^0, $\rho_\star$, ρ^0_{base} and θ_w.

The results shown so far for the radial case may be considered as simple applications of the hydrodynamic theory of isothermal winds, since the magnetic effects have not been taken into account yet. The last step left in our radial case analysis is to calculate the modifications to the zeroth order radial magnetic field, due to the unbalanced pressure gradient across the fieldlines. In fact, as gravity and inertial forces act radially, Eq. (5.26) becomes simply

$$\mathcal{L}(A_1) = -r^2 \sin^2\theta \frac{\partial P}{\partial A_0}, \tag{5.41}$$

where $\mathcal{L}$ is the operator defined in Eq. (5.25) and the pressure P has been defined in Eq. (5.24). Making use of the expressions for ρ and M, the equation for A_1 may be written in the form

$$\mathcal{L}(A_1) = -r^2 \sin^2\theta\, \rho \left\{ \frac{T}{\rho_{\mathrm{base}}} \frac{\mathrm{d}\rho_{\mathrm{base}}}{\mathrm{d}A_0} + \left[\frac{g_\star}{T} - \frac{1}{2} + \frac{1}{1-M^2} \left(\log M + 2 \log \frac{r}{r_{\mathrm{sonic}}} \right) \right] \frac{\mathrm{d}T}{\mathrm{d}A_0} \right\}, \tag{5.42}$$

where the approximation $M^2_{\mathrm{base}} \ll 1$ has been used. Note that the sonic singularity is

removed from the right hand side thanks to the choice of the arbitrary function $\Psi(A_0)$ corresponding to the transonic solution.

Equation (5.42) has been integrated numerically on a square grid $0 \leq \theta \leq \theta_{\max}$, $1 \leq r \leq r_{\max}$ with the condition $A_1 = 0$ on all the boundaries. The solution automatically satisfies the symmetry condition $B_\theta = 0$ at $\theta = 0$. The numerical technique implemented is a linear multigrid solver using a V-cycle (see Appendix C). The scheme used here results in the expected multigrid behaviour over classical iterative schemes, that is the number of iterations to achieve convergence to round-off is independent of the number of grid points.

As expected, the modifications to the fieldlines are very small as long as the condition $\beta \ll 1$ holds, that also defines the range within which our model retains its validity. In Fig. 5.4 the plasma beta, both on the plume axis and in the inter-plume region, is plotted together with the angular displacement of the corrected fieldlines for a given colatitude θ_0, that is

$$\delta\theta(r,\theta_0) = -\frac{\beta_*}{2}\frac{A_1(r,\theta_0)}{(\partial A_0/\partial\theta)_{\theta_0}} = -\frac{\beta_*}{2}\frac{A_1(r,\theta_0)}{\sin\theta_0}. \tag{5.43}$$

The same behaviour is expected for the relative change in the area of the flux tube with colatitude θ_0:

$$a(r,\theta_0) = \pi(r\theta_0)^2 \Rightarrow \frac{\delta a}{a} = 2\frac{\delta\theta_0}{\theta_0} = -\beta_*\frac{A_1(r,\theta_0)}{\theta_0\sin\theta_0}. \tag{5.44}$$

It is interesting to notice that, apart from the line-tying effect at the coronal base (the fieldlines are supposed to be anchored in the sub-photospheric high β plasma), along each fieldline the behaviour of $\delta\theta$ follows exactly that of the plasma β. This may be seen from a simple dimensional analysis of the equation for A_1, since $A_1/r^2 \sim r^2 P$ and $B_0 = r^{-2}$, thus $\delta\theta \sim A_1 \sim \beta$. Therefore, the same result by Velli et al. (1994) has been retrieved: the plume contracts initially until the drop in the magnetic field definitely takes over and the plume expands super-radially in the lower pressure medium.

5.5 Flux concentration at the plume base

Although a background radial field is an excellent approximation at large distances, observations show evidence for a super-radial diverging field close to the plume base (see the introduction). As discussed in Sect. 5.3, the zeroth order potential field can be modelled by choosing a function $f(\theta)$ giving the non-radial contribution to B_{0r} at the coronal base.

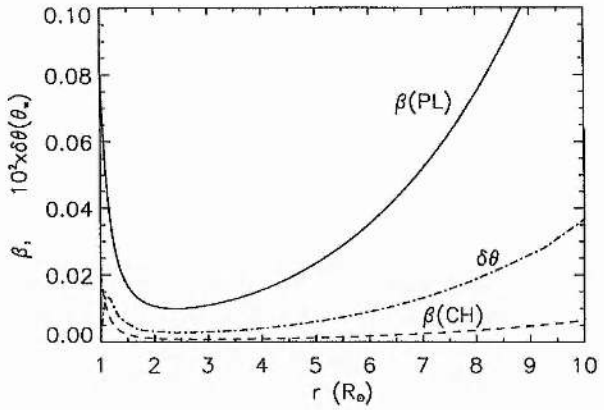

Figure 5.4: The plasma beta is shown at the plume axis (PL) and in the coronal hole region (CH) for $\beta_* = 0.02$. The fieldline displacement $\delta\theta$ is also shown as a function of r at the plume half width θ_w. The values of the other parameters are the same as in Fig. 5.3a.

A possible choice is

$$f = b(1-\omega)\exp(-\omega); \quad \omega = \frac{1-\cos\theta}{1-\cos\theta_w} \approx \frac{\theta^2}{\theta_w^2}, \tag{5.45}$$

where b is a free parameter ($b = 0$ gives the purely radial case) and where the angular width θ_w ($\theta = \theta_w \Rightarrow \omega = 1 \Rightarrow f = 0$) is chosen to be the same as in Eqs. (5.39) and (5.40) ($A_{0w} \propto 1 - \cos\theta_w$). Hence, the radial field component and the flux function at $r = 1$ are

$$B_{0r}(1,\theta) = 1 + b(1-\omega)e^{-\omega} \approx 1 + b(1-\theta^2/\theta_w^2)\exp(-\theta^2/\theta_w^2), \tag{5.46}$$

$$A_0(1,\theta) = (1-\cos\theta_w)\omega(1+be^{-\omega}) \approx (\theta^2/2)[1+b\exp(-\theta^2/\theta_w^2)], \tag{5.47}$$

giving a radial field outside the plume for $\theta \gg \theta_w$. A sketch of the function $f(\theta)$ is shown in Fig. 5.5 for typical values of the parameters b and θ_w. Since $f(\theta)$ has a negative minimum at $\theta \approx \sqrt{2}\theta_w$, where its value is $-b/e^2$, B_{0r} can be negative if $b > e^2$, thus giving a region of negative emerging flux around $\sqrt{2}\theta_w$.

In Fig. 5.6 an example of the resulting fieldlines is given for a large value of b to enhance the effect of the presence of the negative flux region. Note that this situation resembles strongly the proposed scenario for plume formation, with close loops interacting with a stronger open flux concentration located at a supergranular junction. The required heating might be provided in the X-point region above the bipole, where a current sheet could form in response to photospheric motions of the bipole.

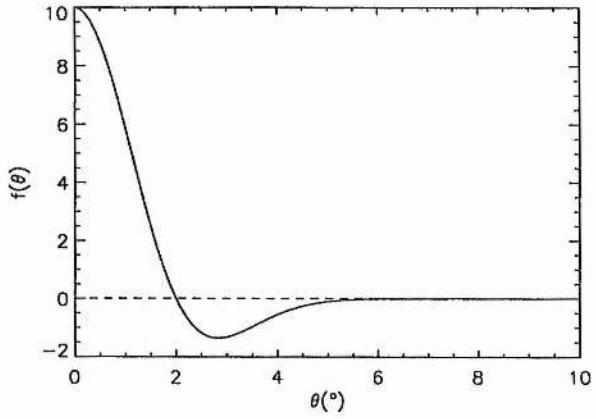

Figure 5.5: The function $f(\theta)$ defined in Eq. (5.45) for the values $b = 10$ and $\theta_w = 2.0°$. Note the presence of a (small) negative flux region ($f < 1$) around $\sqrt{2}\theta_w$ and the radial behaviour ($f = 0$) for large values of θ.

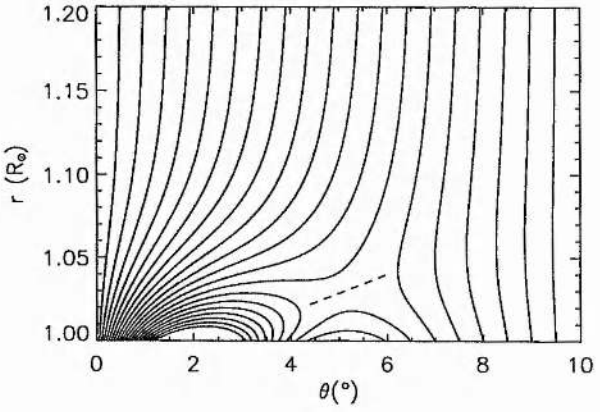

Figure 5.6: The fieldlines of the potential field calculated using Eq. (5.47) as lower boundary condition. The values of the parameters are $b = 100$ and $\theta_w = 2.0°$. Since $b > e^2$, closed structures are present (a large value of b has been chosen in order to enhance the effect). The dashed line indicates the X-point region where a current sheet might form in response to photospheric motions of the bipole.

The main feature of our solution, characteristic of a potential analysis, is that all the modifications to the radial field occur only at low heights, on a scale corresponding to that defined by the plume width: at larger distances the contribution by the higher order multipoles of the photospheric field decades away and the field assumes a radial configuration. This is the same result found by Suess (1982) and the conclusion that can be drawn is that the observed super-radial expansion is indeed due to a magnetic effect, rather than a pressure or inertial one. However, Suess's model does not include any relationship between the density and the magnetic field, necessary to compare the model with the observations, while this comes out quite naturally and in a self-consistent way from our model. Notice that similar results are found in coronal hole models, where the super-radial expansion occurs out to much greater distances (2–3 $R_\odot$, see, for example, Wang & Sheeley, 1990) than in plumes, but where the angular width of the structure is also larger by a corresponding factor.

The best values for the two parameters θ_w and b, which determine the shape of the non-radial potential field through Eqs. (5.46) and (5.47), may be obtained by fitting the density structure derived from the theoretical model with some observational data. In order to achieve this, the Bernoulli equation has to be solved numerically for the transonic flow making use of the non-radial, potential background field. However, since the non-radial behaviour is confined to the coronal base, the position of the sonic points remains unaltered, thus $r_{\rm sonic}$ is still given by Eq. (5.36). The equation for the Mach number, Eq. (5.37), becomes

$$M \exp\left[-\frac{1}{2}(M^2-1)\right] = \frac{B_0}{B_{0\rm sonic}} \exp\left[2\left(1-\frac{r_{\rm sonic}}{r}\right)\right], \tag{5.48}$$

with $B_{0\rm sonic} = 1/r_{\rm sonic}^2$. The changes due to the non-radial behaviour of the magnetic field occur where $B_{0r} \neq 1/r^2$.

The corresponding modifications to the velocity are shown in Fig. 5.7. These result in a slight enhancement of the flow due to the field concentration at the base, with a maximum effect on the axis of the plume while no changes occur at the boundary with the coronal hole, where the field is again purely radial. Note that the profile of the velocity on the axis suggests the presence of an additional critical point in the differential equation for the flow. This is clearly an O type point, as may be seen from the phase diagram in Fig. 5.8 relative to the axis of the plume, for the same values of the parameters.

The density distribution may be still derived from Eq. (5.38) and the results are shown

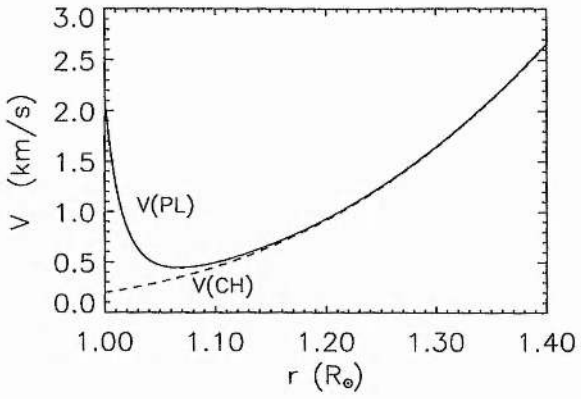

Figure 5.7: The flow speed on the axis (solid line) and in the background coronal hole, where the field is radial (dashed line). The modifications due to the non-radial potential field appear only very close to the coronal base, whereas after $\approx 1.2R_{\odot}$ the velocity follows exactly the behaviour expected for a purely radial field. The parameters used here are $\rho^0_{\rm base} = 4$, $T^0 = 1$, $b = 10$ and $\theta_{\rm w} = 2.0°$.

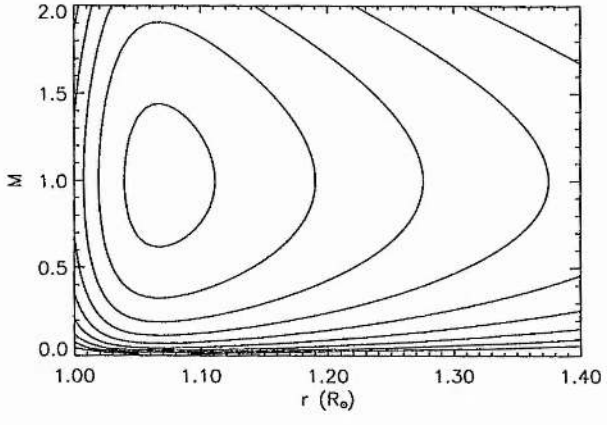

Figure 5.8: The phase diagram along the axis of the plume. This has been obtained by plotting the contours of equal values of the constant in the Bernoulli equation. Note the presence of an O type critical point, for which $M = 1$.

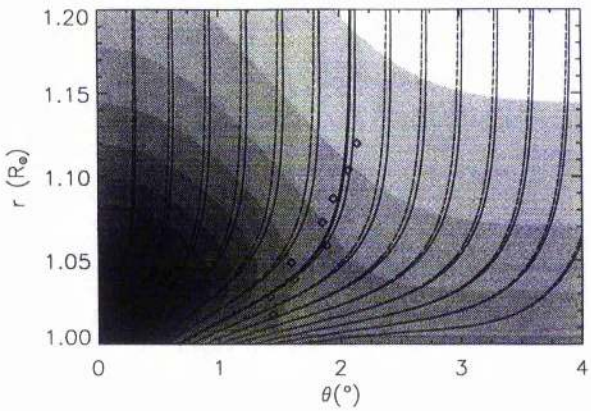

Figure 5.9: The corrected fieldlines (solid), the unperturbed fieldlines (dashed) and a gray scale density contour map (denser regions are darker). The thicker line corresponds to the theoretical plume width, defined as the angular distance at which the density drops by a factor e^{-1} with respect to the axial value at the same height, whereas the diamonds are taken from the EUV observations by Ahmad & Withbroe (1977) (the data refers to the NP1 plume in their paper). The parameters used are $\rho^0_{\rm base} = 4$, $T^0 = 1$, $\beta_\star = 0.1$, $b = 10$ and $\theta_{\rm w} = 2.1°$.

in Fig. 5.9, where a contour plot of the density is presented together with the unperturbed (dashed) and corrected (solid) fieldlines. The density contours are clearly distorted by the fieldline concentration through the function $\rho_{\rm base}(A_0)$. For a fully isothermal atmosphere ($T^0 = 1$) and neglecting the effects of the flow in the low corona, this function is proportional to the ratio of the density with its axial value at the same height r:

$$\rho(r,\theta)/\rho(r,0) \simeq \rho_{\rm base}[A_0(r,\theta)]/\rho^0_{\rm base},$$

thus providing a mean to compare density data with the magnetic field used in the model. In Fig. 5.9 the thicker solid line refers to a value e^{-1} in the density ratio, defined to be the half angular width of the plume, whereas the diamonds are the observed values taken from the analysis by Ahmad & Withbroe (1977). A good fit appears to be obtained for the values $\theta_{\rm w} = 2.1°$ and $b = 10$.

In spite of the impossibility of deriving with precision the shape of the field lines from the data (a straight line would appear to fit the data just as well!), it is important to remember that observations of plumes taken at larger distances yield a radial behaviour. For example, Fisher & Guhathakurta (1995) found that the density FWHM of polar plumes remains constant in angular width as a function of height extending from 1.16 to 5

solar radii. This observational evidence clearly indicates that the super-radial expansion vanishes on a scale comparable with the width of the plume, thus supporting our potential model.

The modification to the zeroth order field has been worked out by solving directly Eq. (5.26) and deriving the function Ψ from the knowledge of the two quantities M and ρ ($M_\star\Psi = \sqrt{T}M\rho/B_0$). Notice that, even for not very small values of the plasma beta ($\beta_\star = 0.1$ in Fig. 5.9), the corrections to the fieldlines remain extremely small, thus justifying our method of linearisation with respect to the magnetic field.

5.6 Conclusions

In this chapter an MHD model for solar coronal plumes has been presented. Coronal plumes have been treated as stationary, axisymmetric structures and spherical coordinates have been employed. Since both observational evidence and theoretical investigations seem to agree about the intrinsic magnetic nature of coronal plumes, a linearisation with respect to the magnetic field has been used by assuming a low β coronal plasma. This method allows one to decouple the momentum equation components along and across the fieldlines and to tackle the problem in three distinct steps:

1. The zeroth order potential field is calculated assuming a background radial field and superimposing a non-radial contribution due to a given flux distribution at the plume base.

2. A Bernoulli type equation is solved for the density along the zeroth order magnetic fieldlines in the isothermal case. The transonic solution is imposed for the flow along each fieldline.

3. The modification to the magnetic field, due to the unbalanced forces, is worked out by numerically solving a second order, Poisson like PDE for the magnetic flux function (transfield or generalised Grad-Shafranov equation).

The method allows for the presence of three free functions, namely the radial field component at the plume base, the density at the plume base and the (constant) temperature along each fieldline.

In the first part of the work, the plume structure has been considered to be purely radial in order to investigate easily the behaviour of the various physical quantities. The

results are obviously what is expected for an isothermal, radial solar wind but with different conditions along each fieldline. For example, a plume which is hotter than the surroundings shows an increasing ratio of axis to background densities and higher flow speeds (the sonic point occurs closer to the Sun). An original contribution to our radial model is the calculation of the fieldline displacement due to the unbalanced pressure gradients. This is shown to follow closely the plasma beta behaviour, that is the angular displacement decreases until 2–3 $R_\odot$ and then it increases at larger distances, the only difference being due to the line-tying constraints at $r = R_\odot$ and $r \to \infty$. Obviously, the model retains its validity only until the plasma beta becomes comparable with unity, that is between 10 and 100 $R_\odot$ for typical coronal values, well beyond observational limits.

In the second part the assumption of a purely radial background field has been relaxed by adding to it the contribution due to a flux concentration at the plume base. The resulting potential field shows similarities with that believed to lead to plume formation (closed bipolar loops interacting with a stronger open flux region). However, the main result of our non-radial analysis is the modelling of the observed super-radial expansion near the plume base, through a direct comparison with observational data. The good agreement between the theoretical model and the observations confirms that the plume structure is mainly determined by magnetic effects, whereas pressure and inertial forces only provide higher order perturbations. Another new feature is a slight enhancement in the flow speed (by a few kilometers per second) at the plume's axis and close to the coronal base, due to the concentration of the fieldlines; however this does not affect the flow at larger distances (the position of the sonic points remains the same as in the radial case).

Chapter 6

Numerical simulations of the solar wind and related flows

6.1 Introduction

For nearly vanishing values of the interstellar pressure, the only steady state solution for a spherically symmetric extended corona is a radial, supersonic outflow connecting, via a shock, to the interstellar medium (Parker 1958). The reason behind this supersonic expansion is that a static atmosphere, with a temperature profile that decays radially outwards less rapidly than $1/r$, requires a finite pressure (a kind of *lid*) to be confined. As discussed in Sect. 1.3.2, this is also true for subsonic *breezes*, since they possess a flow speed that goes to zero at large distances.

In this chapter, the problem of the reactions of an isothermal, spherically symmetric atmosphere to changes of the pressure at the outer boundary will be addressed. Following the guidelines of previous analytic work (Velli 1994), the evolution of the system will be studied by means of computer simulations, making use of a high order shock capturing scheme (see Appendix D), initially developed by Dr. P. Londrillo and then adapted in spherical geometry by the author of this thesis. When the external pressure is comparable to the corresponding static value, the changes in type of the steady state solutions for the flow are not straightforward but, on the contrary, follow a hysteresis type cycle with abrupt transitions from supersonic outflow to inflow and back. In particular, two catastrophe points are present: the value for a static atmosphere and that corresponding to the *critical* breeze, which is the breeze reaching the sonic speed as maximum velocity.

The reason for the hysteresis type behaviour is the instability of the breeze solutions. This has been studied by many authors (Velli 1994 and references therein), with different results which appear to depend not only on the particular energy equation chosen, but also, if not mainly, on the position of the outer boundary.

Even if it may seem unrealistic to consider external pressures of the same order of that corresponding to the static solution, the temperature necessary to confine an isothermal static corona is not so low (4×10^5 K for a base density of 10^9 cm^{-3} and a pressure of the ISM of the order 10^{-12} dyne cm^{-2}). Therefore, the present study could be useful for situations which may be found on stars with conditions different from those on the Sun, or also in the early phases of stars formation.

6.2 Isothermal flows: steady solutions and stability analysis

Isothermal flows are easier to treat analytically and do not introduce any special qualitative feature which distinguishes them from the more general polytropic flows. Therefore, following Parker's approach, they will be considered here first.

As discussed in Sect. 1.3.2, the equations of motion for an isothermal, spherically symmetric, stationary flow are:

$$\frac{1}{r^2}\frac{\mathrm{d}}{\mathrm{d}r}(r^2\rho v) = 0, \tag{6.1}$$

$$\rho v\frac{\mathrm{d}v}{\mathrm{d}r} = -\frac{\mathrm{d}p}{\mathrm{d}r} - \frac{GM_\odot}{r^2}\rho, \tag{6.2}$$

$$p = c^2\rho, \tag{6.3}$$

where $c^2 = 2k_BT/m_p$ is the square of the *isothermal* sound speed. By defining the non-dimensional quantities $M = v/c$, $g = GM_\odot/R_\odot c^2$ and $r/R_\odot \to r$, the Parker wind equation may be written as

$$\left(M - \frac{1}{M}\right)M' = \frac{2}{r} - \frac{g}{r^2}, \tag{6.4}$$

where the critical radius is $r_c = g/2$ and where M may be either positive (wind) or negative (accretion). Let $p = p_0$ and $M = M_0$ be the boundary conditions at $r = 1$, the coronal base, Eq. (6.4) can be integrated in two different ways

$$\frac{1}{2}(M^2 - M_0^2) - \log\left(\frac{M}{M_0}\right) = 2\log r + \frac{g}{r} - g, \tag{6.5}$$

$$\frac{M^2}{2} + \log p - \frac{g}{r} = \frac{M_0^2}{2} + \log p_0 - g. \tag{6.6}$$

The solutions topologies have been discussed in detail in Sect. 1.3.2. The allowed outflow solutions are either a *breeze* with $M \sim 1/r^2$ for $r \to \infty$ or a supersonic wind with M increasing with r. From Eq. (6.6) it is then easy to retrieve the main difference between breeze and wind solutions: the former have an asymptotic pressure p_∞ which is finite and slightly larger than the static asymptotic pressure $p^s_\infty = p_0 \exp(-g)$,

$$p_\infty = p_0 \exp(M_0^2/2 - g) = p^s_\infty \exp(M_0^2/2) > p^s_\infty, \tag{6.7}$$

whereas the wind solutions have a vanishing pressure at infinity. However, consider now a finite pressure at the outer boundary and study the dependence of the stationary outflow as a function of this p_∞. A supersonic solution can possess a finite pressure at infinity provided it is connected through a shock to the lower branch of the double valued solution of region II in Fig. 6.1 (the shocked solution is labelled with W).

The jump relations for an isothermal shock may be derived from Eqs. (3.5) and (3.6) by letting $\gamma = 1$, yielding

$$M_+ = \frac{1}{M_-}, \qquad p_+ = p_- M_-^2, \tag{6.8}$$

for the values downstream from the shock position $r = r_s$. Making use of Eq. (6.6) and of the jump relations Eq. (6.8), the pressure at infinity for a shocked wind may be written in terms of M_- and p_0 as ($M_\star$ is the base Mach number for the transonic solution):

$$p_\infty = p_0 \exp\left(\frac{M_\star^2}{2} - g\right) M_-^2 \exp\left[\frac{1}{2}\left(\frac{1}{M_-^2} - M_-^2\right)\right]. \tag{6.9}$$

Note that the position of the shock is uniquely determined by the value of p_∞. In particular, p_∞ is a monotonically *decreasing* function of $M_- > 1$, which is itself a monotonically *increasing* function of the shock position $r_s > r_c$, so that p_∞ decreases by increasing the shock position r_s beyond r_c. When p_∞ reaches the critical value

$$p^c_\infty = p_0 \exp(M_\star^2/2 - g) = p^s_\infty \exp(M_\star^2/2) > p^s_\infty, \tag{6.10}$$

the shock position coincides with the critical radius $r_c = g/2$ and the discontinuity in the flow velocity reduces to a discontinuity in the derivative of $M(r)$. This is the fastest possible, or critical, breeze. The value of p^c_∞ in Eq. (6.10) can be derived also from Eq. (6.7) by letting $M_0 \to M_\star$.

For a given base pressure p_0 and an asymptotic pressure p_∞ in the range

$$p^s_\infty \le p_\infty < p^c_\infty \Rightarrow 1 \le p_\infty/p^s_\infty < \exp(M_\star^2/2), \tag{6.11}$$

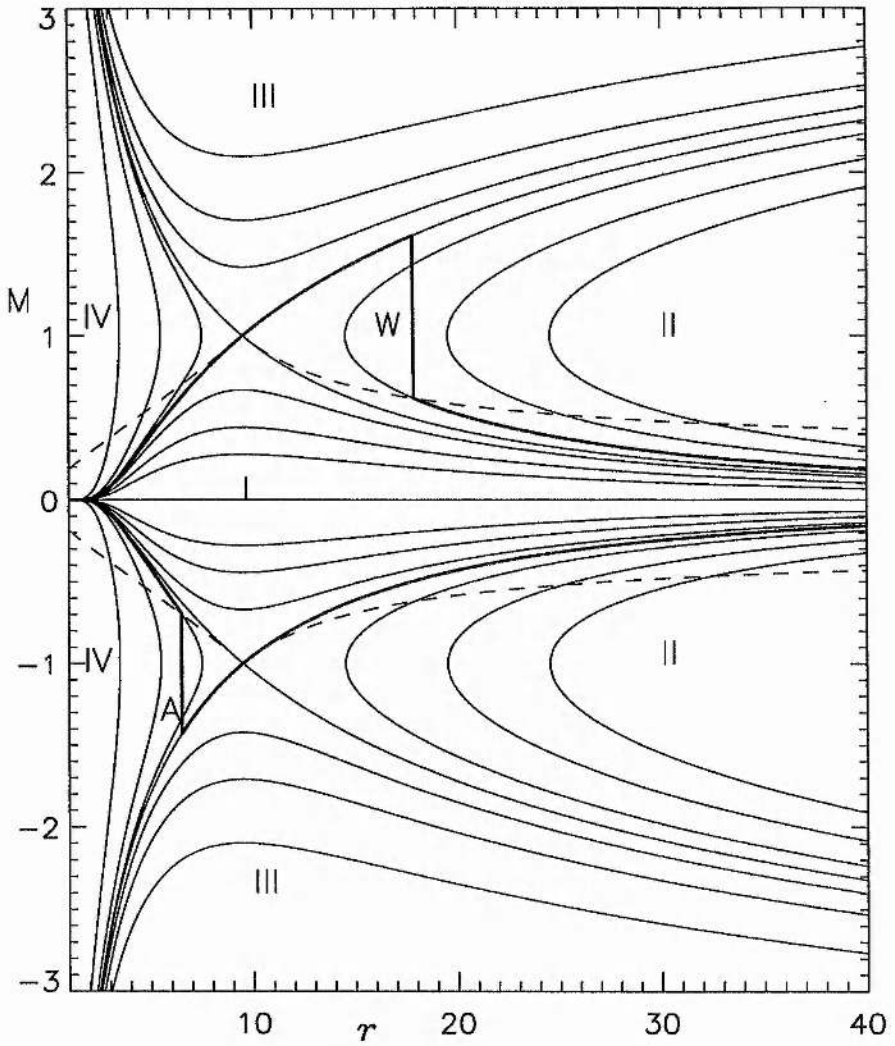

Figure 6.1: The phase plane (M, r), symmetric under a change of sign in M. Regions I contains the breeze, subsonic solutions. The dashed line intersection with double valued curves defines the shock position for winds (region II, curve W) and for accretion inflows (region IV, curve A). Here a large value of g has been chosen: $g = 20 \Rightarrow r_c = 10$ (courtesy of Dr. M. Velli).

two possible outflow solutions exist: a subsonic breeze and a supersonic shocked wind. Note that this range is quite narrow, since

$$M_\star \approx \frac{g^2}{4}\exp\left(\frac{3}{2}-g\right) \ll 1 \tag{6.12}$$

for realistic values of g. Finally, if a supersonic shocked outflow ($M > 0$, wind) is obtained for $p_\infty < p_\infty^c$, a supersonic shocked inflow ($M < 0$, accretion) is achieved when $p_\infty > p_\infty^c$. The equivalent expression of Eq. (6.9) is

$$p_\infty = p_0 \exp\left(\frac{M_\star^2}{2}-g\right)\frac{1}{M_-^2}\exp\left[\frac{1}{2}\left(M_-^2-\frac{1}{M_-^2}\right)\right], \tag{6.13}$$

where now $M_\star < 0$ and $M_- < -1$. This time p_∞ results to increase when the shock position r_s is pushed inwards beyond r_c. Again, the critical value at $r_s = r_c$ is p_∞^c.

6.2.1 The instability of breeze solutions

Despite breezes being allowed as stationary solutions, for values of the outer pressure in the range given in Eq. (6.11), Velli (1994) demonstrated analytically that these solutions are unstable to low frequency standing sound waves which leave the pressure (and density) unperturbed at the two boundaries. To prove this, consider the time dependent equations for a spherically symmetric, dynamic, extended corona:

$$\frac{\partial \rho}{\partial t} + \frac{1}{r^2}\frac{\partial}{\partial r}(r^2 \rho v) = 0, \tag{6.14}$$

$$\frac{\partial v}{\partial t} + v\frac{\partial v}{\partial r} + \frac{1}{\rho}\frac{\partial p}{\partial r} + \frac{GM_\odot}{r^2} = 0. \tag{6.15}$$

After the usual non-dimensionalisation of the quantities, the same employed for the stationary equations to which the relation $ct/R_\odot \to t$ must be added, the following linearised equations are found in the isothermal case:

$$\frac{\partial \hat{M}}{\partial t} + M\frac{\partial \hat{M}}{\partial r} + \frac{\partial \hat{p}}{\partial r} + M'\hat{M} = 0, \tag{6.16}$$

$$\frac{\partial \hat{p}}{\partial t} + M\frac{\partial \hat{p}}{\partial r} + \frac{\partial \hat{M}}{\partial r} - \frac{M'}{M}\hat{M} = 0, \tag{6.17}$$

where the relations $p \to p(1+\hat{p})$ and $M \to M + \hat{M}$ have been assumed, in which $p(r)$ and $M(r)$ are the values for a steady breeze solution, while $\hat{p}(r,t)$ and $\hat{M}(r,t)$ are the time dependent perturbations (note that the pressure perturbation is normalised to the stationary profile). It is now convenient to introduce the factorisation

$$\hat{M} \pm \hat{p} = y^{\pm}(r)\exp[-i(\omega + i\gamma)t], \tag{6.18}$$

where y^+ and y^- represent, in the homogeneous limit, sound waves propagating outwards and inwards, respectively. Thanks to Eq. (6.18), the two linearised equations may be written as

$$(M \pm 1)(y^\pm)' - i(\omega + i\gamma)y^\pm + \frac{1}{2}(y^\pm + y^\mp)\frac{M'}{M}(M \mp 1) = 0. \tag{6.19}$$

The next step is to derive an expression for the growth rate γ, which is assumed to be different from zero. This is achieved by multiplying Eq. (6.19) by $2(1 \pm 1/M)\overline{y}^\pm$ and then by taking the real part of the difference of the two resulting equations, yielding the *wave action* evolution equation:

$$\left[\frac{(1+M)^2}{M}|y^+|^2 - \frac{(1-M)^2}{M}|y^-|^2\right]' + \frac{2\gamma}{M}[(1+M)|y^+|^2 + (1-M)|y^-|^2] = 0. \tag{6.20}$$

Note that the second term in square brackets, which was erroneously multiplied by M^2 in Velli's paper (however leaving the results of the analysis unaffected), is always positive for breeze solutions ($|M| < 1$). If the condition of a vanishing pressure ($y^+ = y^-$) at the two boundaries r_0 and r_b is imposed, Eq. (6.20) can be integrated to give

$$\gamma = \frac{2(|y^+|_0^2 - |y^+|_{r_b}^2)}{\int_{r_0}^{r_b} M^{-1}[(1+M)|y^+|^2 + (1-M)|y^-|^2]\mathrm{d}r}. \tag{6.21}$$

It is clear that if the perturbation at r_0 is non-vanishing and goes to zero at large distances $r_b \to \infty$, the flow is unstable ($\gamma > 0$) for outflow breezes and stable ($\gamma < 0$) for inflow breezes.

For $\omega = 0$ and at large distances, where $|M| \sim r^{-2}$, Eqs. (6.19) become

$$(y^\pm)' \pm \gamma y^\pm + \frac{1}{r}(y^\pm + y^\mp) = 0, \tag{6.22}$$

whose *exact* solution is either

$$y^+ = \frac{A}{r}\mathrm{e}^{-\gamma r} + \frac{A}{2\gamma r^2}\mathrm{e}^{-\gamma r}, \qquad y^- = \frac{A}{2\gamma r^2}\mathrm{e}^{-\gamma r}, \tag{6.23}$$

or

$$y^- = \frac{B}{r}\mathrm{e}^{\gamma r} - \frac{B}{2\gamma r^2}\mathrm{e}^{\gamma r}, \qquad y^+ = -\frac{B}{2\gamma r^2}\mathrm{e}^{\gamma r}, \tag{6.24}$$

where A and B are arbitrary constants. The boundary conditions at $r = r_b$ are satisfied by the first solution when $\gamma > 0$ and by the second solution when $\gamma < 0$. In both cases the perturbation goes to zero at infinity and, for Eq. (6.21), the growth rate must actually be positive. Therefore, provided eigenmodes exist, this analysis shows that outflow breezes are unstable and inflow breezes are, instead, stable.

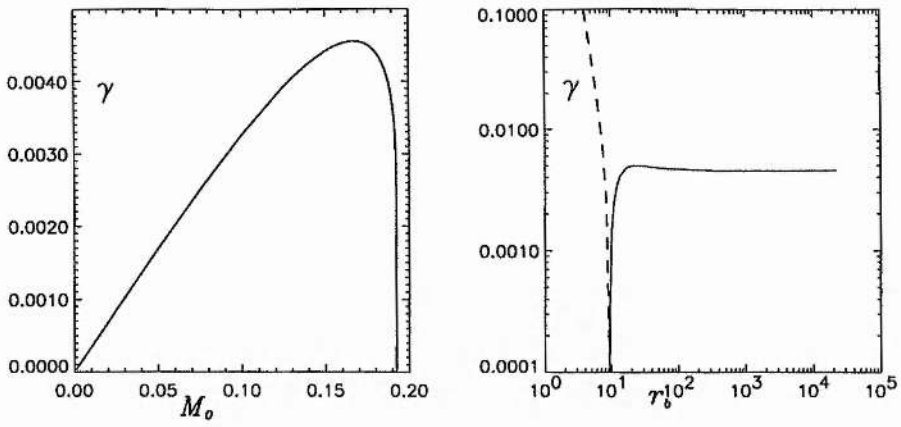

Figure 6.2: **a**: The non-dimensional growth rate of breeze instability, as a result of a perturbation due to standing sound waves, as a function of the base Mach number. Marginal stability is achieved in the static case and for the critical breeze. **b**: Maximal growth rate for outflow breezes (solid line) and for inflow breezes (dashed line), as a function of the outer boundary r_b, in logarithmic scale. The two lines join at $r_b = r_f$, where $\gamma = 0$. In both figures the value of the non-dimensional gravity constant has been taken to be $g = 5.0$ (courtesy of Dr. M. Velli).

The linearised equations, Eqs. (6.19), have been integrated numerically by Velli (1994) and the resulting growth rate of the (outflow) breeze instability is shown in Fig. 6.2a. This is the largest for high values of M_0, while marginal stability is achieved for both a static atmosphere ($M_0 = 0$) and the critical breeze ($M_0 = M_*$). In the latter case the perturbation equations become singular at the sonic point and an additional regularity condition must be imposed on the steady state equations, effectively isolating the region inside the sonic point from the region beyond it.

This is the mathematical reason behind the stability of flows with a continuous subsonic/supersonic transition. The physical interpretation of the breezes instability is simple, this is driven by the unfavourable stratification shown in Eq. (6.7): given a static atmosphere, an increase in p_∞ is clearly expected to result in an *inflow*, not in an outflow breeze (Velli 1994).

To summarise, for a given base pressure p_0, the possible classes of steady solutions for different values of the pressure at infinity p_∞ are the following:

1. $p_\infty < p_\infty^s$. Only a supersonic outflow with a shock beyond r_c is allowed. The position of the shock r_s moves outwards if p_∞ is decreased.

2. $p_\infty = p^s_\infty$. The static solution with $M(r) = 0$ everywhere is marginally stable. The supersonic shocked wind solution is again present.

3. $p^s_\infty < p_\infty < p^c_\infty$. Three different classes of solutions are allowed: an outflow breeze, an accretion breeze and still the supersonic shocked wind. However, the first class is ruled out because is unstable.

4. $p_\infty = p^c_\infty$. The shock position coincides with the critical radius $r_c = g/2$ and the shocked solutions, both outflow and inflow, collapse to the corresponding critical breezes. The outflow critical breeze is only marginally stable, whereas the inflow critical breeze is stable.

5. $p_\infty > p^c_\infty$. Only the accretion shocked solution is found, with r_s moving from r_c towards the coronal base as p_∞ increases.

The stratification produced by outflow breezes, though globally unstable, is not locally unstable everywhere. For example, below the critical point the pressure in breezes decreases with r more rapidly than in the static case, thus the pressure gradient is favourable in this case. An inspection of Eq. (6.6) actually shows that this is true out to a radius r_f where the Mach number has decreased to the same value as the base Mach number. By letting $M = M_0$ in Eq. (6.5), the radius r_f is defined through the relation

$$2\log r_f + g/r_f - g = 0 \Rightarrow r_f \approx \exp(g/2) - g/2, \tag{6.25}$$

where the approximation is valid for normal values of g.

The expression for r_f is independent of the base Mach number, which also means that at this radius r_f the pressure is the same for all breezes. When $r_b < r_f$ the critical outer pressure is less than the corresponding static value, which is the opposite of the situation in Eq. (6.10). Consider now Fig. 6.2b. As the boundary conditions are imposed at closer and closer distances r_b, the growth rate of the instability is reduced and marginal stability is obtained when $r_b = r_f$. Imposing boundary conditions below this radius stabilises the breezes, but consequently destabilises subsonic accretion.

6.3 Time dependent numerical simulations

In this section some results from time dependent simulations will be shown. The idea is to follow the time evolution of the system in response to perturbations of the pressure at

the outer boundary, with the aim to reproduce the results discussed in the steady state analysis. In order to achieve this, the hydrodynamic, one-dimensional version of the MHD code described in Chapter 7 has been used. The numerical method employed is a high order shock capturing scheme, which is particularly suitable for a study of the formation of supersonic shocked winds. This is presented in Appendix D.

The code requires that the equations are written in conservative form. By separating the fluxes derivatives from the geometrical and gravity terms (inhomogeneous terms), the time dependent fluid equations for a 1-D, spherically symmetric corona are

$$\frac{\partial \rho}{\partial t} = -\left[\frac{\partial}{\partial r}(\rho v) + \frac{2}{r}\rho v\right], \tag{6.26}$$

$$\frac{\partial}{\partial t}(\rho v) = -\left[\frac{\partial}{\partial r}(\rho v^2 + p) + \frac{2}{r}\rho v^2 + \frac{GM_\odot}{r^2}\rho\right], \tag{6.27}$$

and again isothermality will be assumed ($p = c^2\rho$).

At the two boundaries, $r = 1$ and $r = r_b$, great care should be used in imposing the proper conditions, in order to avoid spurious effects. Calling F_1' and F_2' the radial derivatives of the two fluxes ($F_1 = \rho v$ and $F_2 = \rho v^2 + p$), these may be decomposed through their two characteristics components as

$$F_1' = \mathcal{L}^+ + \mathcal{L}^-, \tag{6.28}$$

$$F_2' - vF_1' = c(\mathcal{L}^+ - \mathcal{L}^-), \tag{6.29}$$

where $\mathcal{L}^+$ is the characteristic sound wave propagating with velocity $\lambda^+ = v + c$ and $\mathcal{L}^-$ is the sound wave propagating with velocity $\lambda^- = v - c$ (see Sect. 7.4.2 for a general discussion on the characteristics for a full MHD system).

For subsonic inflow/outflow conditions, one wave is entering the domain (*incoming*) and the other is leaving (*outgoing*). The rule is that the contribution of outgoing waves must be taken into account by calculating the derivatives from interior points, while incoming waves are free (e.g. Poinsot & Lele 1992). The incoming wave is $\mathcal{L}^+$ ($\lambda^+ > 0$) and, in order to keep the pressure steady to its initial value, the choice to make is

$$r = 1: \qquad \mathcal{L}^+ = -\mathcal{L}^- - \frac{2}{r}\rho v. \tag{6.30}$$

The outgoing wave $\mathcal{L}^-$ ($\lambda^- < 0$) is instead derived from interior points through its definition

$$\mathcal{L}^- = \frac{1}{2}\left[F_1' - \frac{1}{c}(F_2' - vF_1')\right]. \tag{6.31}$$

At the outer boundary $r = r_b$, only the incoming wave $\mathcal{L}^-$ can be chosen. A way to impose an arbitrary time dependent behaviour for the pressure is to have

$$r = r_b : \qquad \mathcal{L}^- = -\mathcal{L}^+ - \frac{2}{r}\rho v - \frac{1}{c^2}\frac{\partial p}{\partial t}, \tag{6.32}$$

where now the quantity

$$\mathcal{L}^+ = \frac{1}{2}\left[F_1' + \frac{1}{c}(F_2' - vF_1')\right] \tag{6.33}$$

is calculated from interior points.

As a preliminary run, consider the effect of a small perturbation on the outer pressure for an initial subsonic breeze solution. According to the discussion of the previous section, for $r_b > r_f$, the breeze is unstable and must collapse to either a shocked wind, if the outer pressure is decreased, or to a subsonic accretion breeze, if the outer pressure is increased. The pressure at the external boundary is perturbed according to the function

$$r = r_b : \qquad p(t) = p(0) + \epsilon p^s f(t/\tau); \quad f(x) = x^2/(1+x^2), \tag{6.34}$$

so that for $t \gg \tau$ the outer pressure has increased of a factor ϵ, in units of the corresponding static value $p^s = p_0 \exp[-g(1 - 1/r_b)]$.

In Fig. 6.3 the time evolution of the velocity radial profile is shown as a shaded surface plot, with the time increasing towards the left along the y-axis. Here the value $g = 4.0$ will be assumed throughout, which leads to a critical radius located at $r_c = g/2 = 2.0$ and to a value for the critical outer radius $r_f \approx 5.39$, using Eq. (6.25). In order to show the outflow breezes instability, the value of r_b is taken to be $r_b = 10 > r_f$. The outer pressure is decreased by using Eq. (6.34) with $\epsilon = -0.01$ and $\tau = 1$. A variation as small as 1% in the outer pressure is enough to destabilise the breeze solution, which steepens into a steady supersonic shocked solution, even if the final value of the pressure at r_b still allows for a breeze stationary solution. The typical time-scale of the instability is, for this choice of the parameters, of the order of $100\, R_\odot/c$.

In the next series of runs the typical hysteresis type cycle is presented, demonstrating that the actual state chosen by the flow actually depends on its history, and that the transitions from inflow to outflow and back are necessarily catastrophic in nature. Let the initial situation be static (situation no. 2 in the scheme of the previous section). First, a supersonic shocked wind is created by lowering the external pressure (situation no. 1), and then the position of the shock is moved inwards by increasing the value of p_∞ in a way that its final value is in the range between the static and critical values

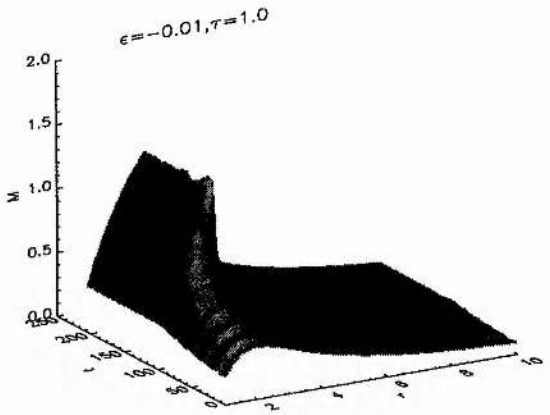

Figure 6.3: Instability of a breeze solution. The outer pressure is lowered from the initial value $p = 0.02782$ to $p = 0.02755$, corresponding to $\epsilon = -0.01$. Both the initial and the final pressure are in the range allowing for steady subsonic solution, since for $g = 4$ and $r_b = 10$ the static and critical pressures at $r = r_b$ are, respectively, $p^s = 0.02732$ and $p^c = 0.02897$ ($p_0 = 1$).

(situation no. 3). The corresponding time evolution may be followed in Figs. 6.4a and 6.4b, respectively. Note that, although subsonic outflows are present at certain stages, the final stationary solution is again a shocked wind. In the third run the outer pressure is increased even further, beyond the critical value, so that the only possible solution is a supersonic accretion inflow (situation no. 5). The catastrophic nature of the hysteresis cycle is especially apparent here, since a shocked outflow collapses directly to a shocked inflow, without passing through steady subsonic solutions (see Fig. 6.4c). Finally, in Fig. 6.4d, the evolution to an accretion breeze type solution is shown. This has been obtained by lowering the external pressure back to the value already reached at the end of the second run.

The situation is summarised in Fig. 6.5, where the four stationary, final states of the cycle are shown all together. Note that, if the pressure was further decreased below the static value, the accretion breeze would collapse back to a supersonic shocked wind solution (second catastrophe point).

Finally, it is interesting to verify that when the outer boundary is placed too near to the coronal base, that is when $r_b < r_f$, breeze outflows are actually stable steady state solutions. For example, consider an initial static atmosphere and allow the pressure at $r = r_b$ to decrease of a factor $\epsilon = -0.05$. This time, as it is shown in Fig. 6.6, the system

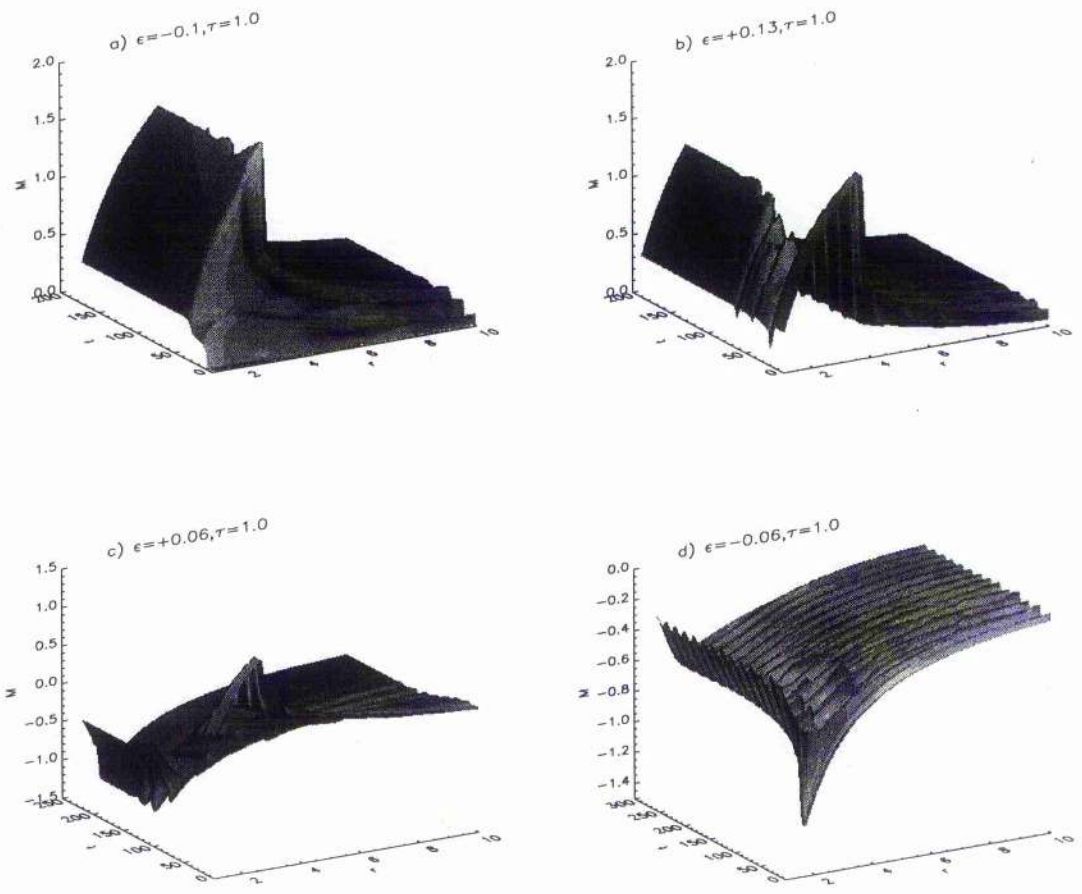

Figure 6.4: The hysteresis type cycle for the time evolution of the solar wind under the effect of a perturbation of the pressure at the external boundary. The values of the parameters are the same that in Fig. 6.3. **a** Creation of a shocked wind: the pressure is decreased from its static value, $p^s = 0.02732$, to a final value $p = 0.02459$, corresponding to $\epsilon = -0.1$. **b** The pressure is increased to a value inside the critical range ($\epsilon = 0.13 \Rightarrow p = 0.02815$): the steady final state is again a supersonic shocked wind. **c** The pressure is further increased out to a value larger than p^c_∞ ($\epsilon = 0.06 \Rightarrow p = 0.02978$): the wind reverses its direction collapsing to an accretion supersonic inflow. **d** The outer pressure is brought back to the value in the critical range ($\epsilon = -0.03$), but this time the final solution is a subsonic accretion breeze. Note that, in this last case, the oscillations at the final iteration are not damped yet.

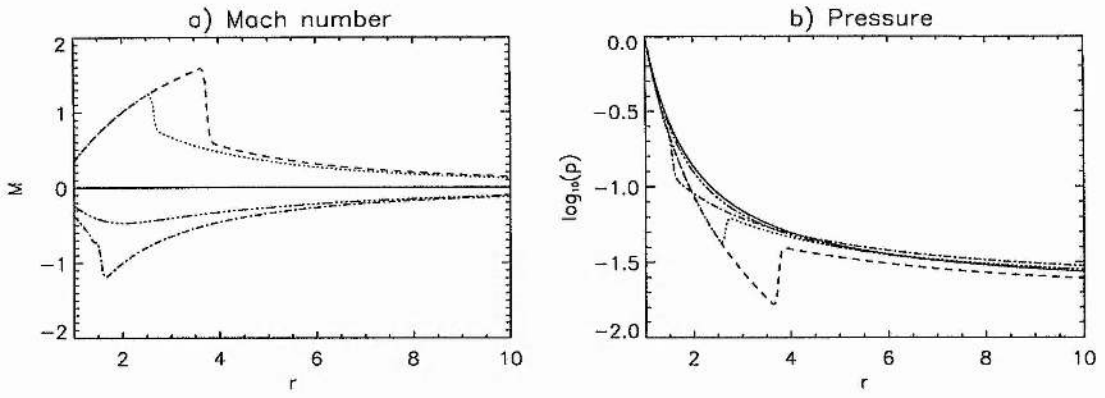

Figure 6.5: Steady state solutions resulting from the four runs of the cycle shown in Fig. 6.4. The solid line refers to the initial, static case. The dashed, dotted, dot-dashed and double dot-dashed lines refer to runs a, b, c and d, respectively.

slowly evolves towards a steady state breeze solution.

6.4 Conclusions

In this chapter, the analytical results found by Velli (1994) for the instability of breezes have been proved numerically. By perturbing the pressure at the outer boundary of an isothermal, spherically symmetric extended atmosphere in an initial steady state configuration, the time dependent evolution to the next final stationary state has been followed.

The main result is that the changes in the steady solutions, in response to a cyclical perturbation of the external pressure, have a catastrophic nature and follow a hysteresis type cycle, with the final state chosen by the system which depends upon the history of its previous evolution. This is due to the instability of breeze solutions: within a certain range of outer pressures (the two catastrophe points) both subsonic breezes and a supersonic shocked wind are allowed, but the system never develops a subsonic outflow as a final steady outflow. For this reason, the system may undergo an abrupt transition from a supersonic outflow to supersonic accretion, or from subsonic accretion (inflow breezes are stable) back to a supersonic outflow shocked wind.

Another important result which has been confirmed numerically here, is the dependence of breezes instability on the position of the outer boundary. When this is chosen too near to the coronal base (this limiting value is greater for larger values of the criti-

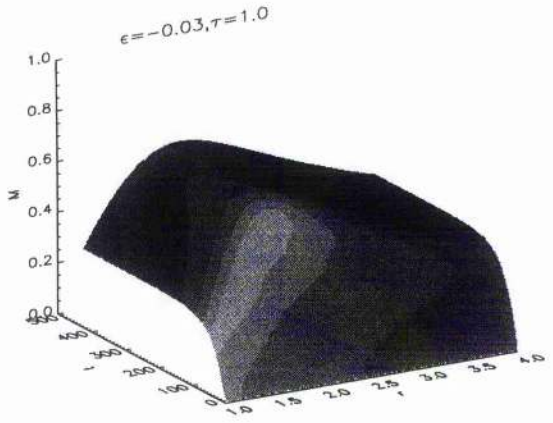

Figure 6.6: Stability of a breeze solution, for $r_b = 4 < r_f$. The outer pressure of a static atmosphere is lowered from its initial value $p = 0.04979$ to $p = 0.04829$, corresponding to $\epsilon = -0.03$. The system slowly evolves towards a steady state breeze solution.

cal radius $r_c = g/2$), the situation reverses, with outflow breezes being stable and inflow breezes being unstable. This point may explain some contradictory results found by other authors.

For example, some numerical simulations of the time evolution of stellar winds were performed by Korevaar (1989 and references therein), who used a complete energy equation, including thermal conduction, radiative losses and a distributed mechanical heating. When increasing the pressure at the outer edge, Korevaar found a smooth transition from supersonic shocked winds to breezes and then a *rapid onset* of supersonic shocked accretion: his result may be understood indeed in terms of the dimensions of the numerical box, since the external boundary conditions were imposed well below the marginal stability radius, as discussed above.

Concluding, even if this analysis has been carried out for an isothermal atmosphere, it is argued that its validity is retained also for more complex (and realistic) energy equations, with the condition of a positive total energy constant. This is certainly true for polytropic flows (with an index $1 \leq \gamma < 3/2$ to have a positive pressure everywhere in the static case) for which the hysteresis cycle has been shown to have exactly the same qualitative behaviour than for isothermal flows. Work is currently in progress to cover these more general cases (Del Zanna et al. 1997b).

Chapter 7

Conclusions and future work

7.1 Summary and discussion of the results obtained

In this thesis, different aspects of dynamic MHD equilibria in the solar atmosphere and extended corona have been analysed. In Chapter 1, the important role played by plasma flows inside coronal magnetic structures has been briefly discussed, with special attention being paid to the most important of all kinds of flows which may be found in the solar atmosphere: the solar wind. After some basic information about the physical properties of the phenomena under consideration, the appropriate mathematical equations have been introduced and discussed in detail.

These are the equations of magnetohydrodynamics, which are basically the fluid-dynamic equations modified by the presence of the magnetic field. Throughout the thesis, the MHD equations have been used in their ideal form, that is without the effects of viscosity and electrical resistivity, both being negligible in the solar corona when the spatial scale of the problem under consideration is large enough. Moreover, the energy equation has always been reduced to a simple relation between the thermodynamic quantities, since the aim of the thesis is to investigate the geometric and dynamic properties of the MHD equilibria, rather than to construct realistic models of the energetics of the plasma.

The actual thread which links together all the different works presented in this thesis is the search for solutions to the MHD equations. The order in which the various chapters are presented also reflects the chronological development of the research, with a progressive refinement of the mathematical tools in order to find physical solutions under more and more general (and realistic) assumptions.

The first approach used in this research was purely analytical (Chapter 2). In order to solve analytically the set of MHD equations, some drastic simplifications are obviously required. Attention has been therefore restricted initially to stationary equilibria with one ignorable coordinate (symmetric equilibria). These two assumptions allow one to reduce the initial MHD set of eight equations to a system of just two equations: a second order PDE for a magnetic flux function and an algebraic equation for the density. However, the non-linear coupling between these two equations still prevents analytic progress. The only way to proceed is to decouple the equations, and this is possible if one assumes incompressibility (the Bernoulli equation simply becomes an expression for the kinetic pressure while the density is a free function). Purely analytic solutions are finally found, for three different geometries, by assuming a self-consistent, regular nesting of the magnetic surfaces around the magnetic axis of the system under consideration.

The second approach has been semi-analytical. This time the coupling between the two reduced equations has been preserved, thus leading to the necessity of a numerical integration of the equations. The problem considered was the search of 2-D equilibria for field aligned flows in magnetic arcades embedded in an isothermal, vertically stratified atmosphere in uniform gravity. The method of solution follows Tsinganos et al. (1993), who reduced the initial 2-D problem to a couple of ODEs through a self-similar separation of variables in Cartesian coordinates. The formalism has been presented here in Chapter 3, while its use for the construction of a steady flow model for quiescent prominences has been discussed in Chapter 4.

A full two-dimensional treatment is recovered by relaxing the assumption of self-similarity, but some other simplifying assumptions are needed. In Chapter 2, a method of linearisation in the magnetic field, suitable in the low β corona, has been introduced following the work by Surlantzis et al. (1994). This method is based on a perturbation approach. The fundamental structure is given by a force free field, along whose fieldlines the fluid equations are solved (Bernoulli equation); the first order corrections to the initial field are found by solving the transfield equation across the fieldlines. The equation for the magnetic flux function is a linear elliptic PDE, which is homogeneous (Laplace like) at the zeroth order, and inhomogeneous (Poisson like) for the first order corrections. The equations have been solved here in spherical geometry for an MHD model of coronal plumes (Chapter 5), by imposing an isothermal, transonic wind along the open fieldlines. The numerical method employed to solve the PDEs is an iterative scheme which makes

use of a multigrid algorithm. This allows the enhancement of the efficiency of the scheme, at high resolutions, by several orders of magnitude (the computational time required to achieve a given accuracy depends only linearly on the total number of grid points). A detailed account of the numerical method was given in Appendix C.

The ultimate goal would be to solve the full 2-D, non-linear, stationary MHD equations for the interactions of the solar wind with the large scale coronal magnetic structures, but, as discussed in Sect. 2.3.2, one has to face the problem of the critical points, whose position depends on the solution itself. This is why, in the literature, only a very few examples of solutions can be found and these are valid only under very special restrictions (Pneumann & Kopp 1971; Sakurai 1985). Even from a numerical point of view, the problem is extremely hard to solve and it is more convenient to integrate the time dependent equations and eventually wait for the system to evolve towards a steady state solution. This problem is presently under consideration and a code that is being developed will be described in Sect. 7.4.

The hydrodynamic version of this code is, however, ready and functioning. As a test in 1-D, the problem of the instability of breeze solutions for the Parker wind equation has been investigated numerically in Chapter 6. By varying the pressure at the outer boundary, the time evolution of the system is followed, which depends upon its history in a hysteresis type behaviour. The system is shown to undergo abrupt transitions from supersonic outflow to accretion and back, confirming the presence of two catastrophe points in the hysteresis cycle, as predicted by Velli (1994).

In the remainder of this section, a detailed discussion of the novel and original contributions achieved in the three years of research which have led to this thesis will be given, separating the different topics in four short sub-sections.

7.1.1 A method for the analytic solution of the MHD equations

A new method to find *purely analytic* solutions to the system of ideal MHD equations has been proposed. This generalises a method, originally presented by Bacciotti & Chiuderi (1992) for axisymmetric field aligned flows to general non-aligned flows and to different geometries. The basic assumptions consist in neglecting the time dependence (stationary solutions) and in imposing a spatial symmetry (one ignorable coordinate). However, the equations are still non-linearly coupled together, hence an additional assumption must be made. This is to consider incompressible flows, for which the system of MHD equations

simply reduces to a single elliptic PDE for a magnetic flux function, where a number of integrals of this flux function are present.

The original contribution is the search for solutions which have magnetic surfaces regularly nested one inside the other around the magnetic axis of the system. In this way, singularities and physical discontinuities are avoided *a priori* and only well-behaved solutions are found. Mathematically, the above assumption translates into the flux function depending on a given self-similar factorisation with an unspecified function of one of the coordinates. After the substitution in the PDE, a number of *compatibility relations* for the free functions must be satisfied and finally an ODE for the shape of the magnetic surfaces is derived.

This approach has been followed in three different geometries. In cylindrical coordinates with translational symmetry along the vertical axis, a family of solutions with flows in magnetic flux tubes with a non-circular section was found. These exact solutions may be useful in stability calculations, since usually only flows in flux tubes with circular section are considered. The second case examined was MHD equilibria in uniform gravity, in Cartesian coordinates with invariance along one of the horizontal directions. Most of the solutions found are arch-shaped and may model coronal loops and arcades which are observed above the solar surface. Finally, the family of axisymmetric solutions in cylindrical geometry found by Bacciotti & Chiuderi (1992) was derived again under more general assumptions, namely the flow is no longer constrained to be parallel to the magnetic field and an extra free function is allowed.

The results of this work have been published (Del Zanna & Chiuderi 1996). However, apart from the direct application of the solutions for models of astrophysical structures (the main drawback being the assumption of incompressibility), the importance of having exact solutions to the system of stationary, ideal MHD equations is universally recognised. Above all, these may provide a valuable basis for stability calculations or may be used as a test for numeric MHD codes.

7.1.2 A steady flow model for quiescent prominences

The work described in Chapter 4, published in the literature as well (Del Zanna & Hood 1996a, 1996b), treats the problem of steady flows in solar prominences. The prominence was considered as a vertical cool sheet with finite width, embedded in the surrounding hot corona. The magnetic field, which provides the support against gravity, and the gas

pressure were assumed to be separable in the horizontal and vertical coordinates (the system is invariant along the third direction) and an exponentially decaying behaviour was chosen for the latter. Both the prominence and the coronal regions were assumed to be isothermal. These assumptions are the same as in the static model by Hood & Anzer (1990), so that this work may be considered as its dynamic extension.

As discussed above, the semi-analytic approach by Tsinganos et al. (1993) was used as mathematical formalism, but here its validity was extended to the presence of the third component of the magnetic and velocity fields, necessary for modelling prominences, whose magnetic field is nearly parallel to the direction of the structure. The correct jump relations are imposed at the prominence/corona interface and the interior and exterior solutions are then properly connected.

The results were that the static magnetic configuration is slightly affected by the presence of the (subsonic) flow only in the coronal region, while inside the prominence the pressure and the field are almost unperturbed by the flow. This happens because the flow speed is forced to decrease in a much denser region, therefore speeds as small as 0.1 km s^{-1} are found inside the prominence, while in the corona the average speeds are around 50 km s^{-1}, in good agreement with observations.

Finally, the idea of a steady replenishment of the mass of the prominence by means of siphon flows along the fieldlines of the arcade was revisited by using the results of the model. The characteristic time scale of the replenishment was shown to be of the same order of the average life time of quiescent prominences, thus suggesting that their existence may be indeed related to the mass supply from the below chromosphere.

7.1.3 An MHD model for coronal plumes

After an example of modelling steady flows in closed magnetic structures in the solar corona, using the formalism for MHD symmetric equilibria, attention was turned to open fieldlines structures, namely to coronal plumes. This time a low β assumption was used to decouple the reduced equations along and across the magnetic fieldlines. The formalism used was first introduced by Surlantzis et al. (1994), but the author of the present thesis discovered an inconsistency in their equations and this was acknowledged in an *erratum* (Surlantzis et al. 1996). After the extension of the correct equations to spherical geometry, the plume was modelled as an axisymmetric magnetic structure and the linearised equations (with respect to the magnetic field) are solved in three steps: first the under-

lying potential field is found (assumed to be radial at large distances both from the axis and from the coronal base), then the density, pressure and velocity are derived from the Bernoulli equation (assuming a transonic flow along each fieldline) and finally a Poisson like PDE gives the first order corrections to the potential field.

Free functions of the model are the radial magnetic field and the density at the base and the temperature on each fieldline. By tuning these parameters it was possible to obtain different radial behaviours for the plumes. For example, a plume which is hotter (and denser) than the surroundings has also a higher radial velocity and the density contrast increases indefinitely with height; on the other hand, a cooler plume (but still denser) has a slower velocity and, after a certain height, it becomes less dense than the background coronal hole.

In addition, it was possible to model, by a comparison with observational data, the super-radial expansion which occurs near the base of plumes, confirming their intrinsic magnetic nature. This also affects the flow speed inside the plume (an extra O type critical point appears, in addition to Parker's transonic X-point), but this effect decays rapidly with a scale-height comparable with the horizontal width of the plume. However, this is the first 2-D MHD model of coronal plumes in the literature (Del Zanna et al. 1997a), at least to our knowledge.

7.1.4 Time dependent evolution of the solar wind and related flows

In a thesis on flows in the solar atmosphere, it would have been impossible not to mention the solar wind. The original contribution given in this field, in addition to the mentioned plume model, consists of a series of time dependent simulations of the dynamic response of an extended, spherically symmetric, isothermal corona to perturbations of the pressure at the external boundary (Del Zanna et al. 1997b). This is to be seen as a numerical proof for the behaviour predicted analytically by Velli (1994).

Due to the instability of the so-called breeze outflows (subsonic everywhere), the reaction of the system to a time dependent perturbation of the outer pressure was shown to follow a hysteresis type cycle with two catastrophe points where the flow may reverse abruptly and change its sign. These two points correspond to the external pressure for the static solution and for the critical breeze (that with the same base Mach number as the transonic solution).

Although the real conditions for the Sun are far from those leading to a reverse in the

sign of the flow, this study may be important for understanding the possible conditions which can be found on other stars or during the early phases of star formation. Moreover, this simple treatment for an isothermal atmosphere provides a deeper understanding of the physics of the system, which may be lost, sometimes, when considering more realistic, and hence complicated, energy equations. For example, as discussed in Sect. 6.4, some contradictory results found in different models by other authors may be explained simply by an unsuitable choice of the dimensions of the numerical box.

7.2 Future work: extension of the plume model

Preliminary results from an observational campaign of plumes in the southern polar cap (March 1996, see De Forest et al. 1997), carried out simultaneously by five instruments on SOHO, show that plumes are indeed rooted in strong magnetic field concentrations (up to 200 G) and confirm the presence of neighbour bipoles of smaller strength. The super-radial expansion near the base, on a vertical scale comparable to the plumes width, is still observed and confirms once again the validity of the quasi-potential approximation for the field near the photosphere. Moreover, plumes are seen to expand super-radially also at larger distances, where the kinetic pressure begins to dominate over the magnetic pressure, in perfect agreement with the first order predictions from the MHD model. Therefore, the basic results and assumptions (especially the low β plasma) appear to be confirmed by these recent observations.

Great controversy is found in the estimation of plume temperatures. In the work cited above, plumes seem to be slightly cooler (maximum 30%) than the surrounding coronal hole, with temperatures in the range $1.0 - 1.5 \times 10^6$ K, while other observers instead find a constant temperature across the plume/interplume boundaries (Del Zanna G., private communication, working on SOHO-CDS data). Moreover, it seems that the velocity is high (≈ 100 km s^{-1}) even at altitudes as low as 2 solar radii.

Future work will certainly involve a detailed modelling of this new data from coordinated observations with different instruments. Hopefully, in the near future more precise data, and for a variety of radial distances, will be available for tuning of the model parameters. One of the improvements almost certainly needed in the plume model will be the relaxation of the assumption of an isothermal plasma along the fieldlines. This will be substituted by a more realistic energy equation, which includes thermal conduction

along the fieldlines, radiative losses and heating sources, possibly following the guide-lines of Wang (1994). In particular, it seems important to have a heating mechanism capable of enhancing the temperature above the plumes base and hence to accelerate the plasma there to the observed high speeds. This rise in temperature has been actually observed (Fisher & Guhathakurta 1995).

Another possible improvement is to try to reproduce the 3-D magnetic field distribution inside coronal holes. In this case, it will be impossible to use a scalar magnetic flux function. This could be achieved by a potential analysis and through a detailed confrontation with SOHO-MDI data. If this proves to be successful, it will also be possible to model the non-radial direction followed by plumes far from the solar poles (they appear to be slightly *tilted* with respect to the direction perpendicular to the surface).

7.3 Future work: further developments in the simulations of stellar radial flows

In order to compare the analysis of Chapter 6 with the results of the time evolution of the extended corona by other authors (e.g. Korevaar 1989), a more realistic energy equation is required. Many of the differences which are found may be understood in terms of the dimensions of the numerical box employed when compared to the marginal stability radius r_f. Examples of possible improvements are the following:

- As a first step, a polytropic relation could be assumed with an index in the range $1 \leq \gamma < 3/2$ (for larger values the transonic solution has no longer an increasing velocity profile). The physics is, however, the same as in the isothermal case and no qualitative changes are expected in the hysteresis cycle.

- A given momentum or energy input might be included in the equations. This should result in additional critical points in the wind equation. The same could be obtained by assigning a non-spherical geometry through a given variable cross section, in order to model the wind from a coronal hole or plume.

- The effect of dissipation by Alfvén waves could be included.

- A complete energy equation which takes into account heating, radiation and thermal conduction is required as a final step. Some, if not all, of the previous improvements

may be included in it.

- Finally, a two-fluid approach could be followed by solving simultaneously the fluid equations for the protons and the electrons.

These improvements could also be useful to the study of the formation of steady state standing shocks in the inner corona, especially in coronal holes. The presence of these shocks might modify greatly the predicted emission by the plasma. The first analysis, for polytropic flows, was made by Hasan & Venkatakrishnan (1982), who considered a coronal hole undergoing a time dependent evolution of its geometry, thus extending the analysis of Sect. 1.4.1 to the dynamical case. A complete treatment of this subject may be found in Habbal et al. (1994 and references therein), who included in their study the combined effects of mechanical momentum deposition, Alfvén waves energy and momentum dissipation (self-consistently), variable cross section, thermal conduction, in a two-fluid approach.

However, the final goal is to extend the 1-D code to a full MHD, 2.5-D code in spherical coordinates. This allows the study of the 2-D structure of the solar wind and its interactions with the large scale magnetic coronal structures and the results could be then compared with the observations of *in situ* plasma properties by the Ulysses spacecraft. The mathematical frame for the MHD code is described in the next section, whereas the numerical scheme employed is discussed in Appendix D.

7.4 Future work: a time dependent MHD code in spherical geometry

As it was discussed in Chapter 1, it is well known that the solar corona is far from homogeneous: large scale magnetic structures, like coronal holes and helmet streamers, interact continuously with the solar wind in a complex interplay of inertial, pressure, gravitational and magnetic forces. The purpose of this work is to construct a 2.5-D, full MHD, shock capturing code, which is able to simulate all the basic aspects of the observed steady coronal structures and to predict their time evolution when the conditions at their base are changed. To achieve this, great care must be used in treating the proper boundary conditions at the coronal base, which is a major feature of the code. This is employed through a spectral decomposition into the seven characteristic MHD eigenmodes, in order

to select the contribution of the waves entering the domain and to impose correctly the boundary conditions only upon them.

In the literature, many different codes have been proposed for the study of coronal dynamics. Time dependent MHD simulations of the extended solar corona were first made in 2-D, ignoring the azimuthal components of the fields (Steinolfson et al. 1982; Washimi et al. 1987; Wang et al. 1993), then the effects of these components and of solar rotation were included (Washimi 1990; Washimi & Sakurai 1993) and finally the full 3-D structure was simulated (Linker et al. 1990). All these works are concerned with the formation of a steady configuration resembling the equatorial helmet streamer, usually by starting from a dipolar magnetic field and a radial transonic wind and by letting the system evolve towards a steady solution. In other cases, the disruption of these magnetic configurations (coronal arcades or helmet streamers) is studied by means of applying shear motions at the coronal base (Mikić & Linker 1994; Linker & Mikić 1995).

However, in none of the works cited above there is a proper treatment of the boundary conditions at the coronal base, like that described in Sect. 7.4.2. Most of the times, some sort of numerical *tricks* are employed, in order to smooth the quantities near the boundary, or sometimes too many quantities are imposed at the boundary, thus allowing spurious effects to occur there. The only work in which there is an attempt to use the proper inflow/outflow boundary conditions, in the form given by Nakagawa (1981a, 1981b), is that by Wang et al. (1993). However, even there the induction equation is not treated correctly at the inner boundary. For all these reasons, these works are not suitable for a study of MHD wave propagation in the solar wind, which is the main purpose for the construction of the shock capturing code presented here.

7.4.1 Governing equations and basic assumptions

The equations for the time evolution of the large scale corona can be identified with the ideal MHD equations, where the viscous and resistive terms are neglected as they act on the small scales. Gravity is included. The energetics is simplified, as a starting approach, by the introduction of a constant polytropic index γ with possible values ranging from $\gamma = 1$ (isothermal case) to $\gamma = 5/3$ (adiabatic case). Thus, the equations are:

$$\frac{\partial \rho}{\partial t} + \nabla \cdot (\rho \mathbf{V}) = 0, \tag{7.1}$$

$$\rho \frac{\partial \mathbf{V}}{\partial t} + \rho(\mathbf{V} \cdot \nabla)\mathbf{V} = (\nabla \times \mathbf{B}) \times \mathbf{B} - \nabla P + \rho \mathbf{g}, \tag{7.2}$$

$$\frac{\partial \mathbf{B}}{\partial t} = \nabla \times (\mathbf{V} \times \mathbf{B}), \tag{7.3}$$

$$\frac{\partial P}{\partial t} + \mathbf{V} \cdot \nabla P + \gamma P \nabla \cdot \mathbf{V} = 0, \tag{7.4}$$

with the solenoidal relation

$$\nabla \cdot \mathbf{B} = 0 \tag{7.5}$$

as an additional constraint. Note that the normalisation $\mathbf{B}/\sqrt{4\pi} \rightarrow \mathbf{B}$ has been used.

The most logical choice for the coordinate system is certainly the spherical set, with radius r ($r = R_\odot$ is the coronal base), colatitude θ ($\theta = 0$ and $\theta = \pi$ are the poles) and azimuth ϕ. Although the vectors are fully three-dimensional, axisymmetry will be assumed, thus $\partial/\partial\phi = 0$ everywhere.

For the actual implementation in the code, a vectorial form of the equations and conservative variables are used. The equations now read

$$\frac{\partial U}{\partial t} = -\left[\frac{\partial}{\partial r}F(U) + \frac{\partial}{r\partial\theta}G(U) + H(U)\right], \tag{7.6}$$

where U, F, G, H are eight elements column vectors, given by:

$$U = \begin{pmatrix} \rho \\ \rho V_r \\ \rho V_\theta \\ \rho V_\phi \\ B_r \\ B_\theta \\ B_\phi \\ \rho s \end{pmatrix}, \quad F = \begin{pmatrix} \rho V_r \\ \rho V_r^2 - B_r^2 + \Pi \\ \rho V_r V_\theta - B_r B_\theta \\ \rho V_r V_\phi - B_r B_\phi \\ 0 \\ V_r B_\theta - V_\theta B_r \\ V_r B_\phi - V_\phi B_r \\ \rho s V_r \end{pmatrix}, \quad G = \begin{pmatrix} \rho V_\theta \\ \rho V_r V_\theta - B_r B_\theta \\ \rho V_\theta^2 - B_\theta^2 + \Pi \\ \rho V_\theta V_\phi - B_\theta B_\phi \\ V_\theta B_r - V_r B_\theta \\ 0 \\ V_\theta B_\phi - V_\phi B_\theta \\ \rho s V_\theta \end{pmatrix},$$

$$H = \begin{pmatrix} 2\rho V_r/r + \cot\theta \rho V_\theta/r \\ GM_\odot \rho/r^2 + [\rho(3V_r^2 - V^2) - (3B_r^2 - B^2)]/r + \cot\theta(\rho V_r V_\theta - B_r B_\theta)/r \\ 3(\rho V_r V_\theta - B_r B_\theta)/r + \cot\theta[\rho(V_\theta^2 - V_\phi^2) - (B_\theta^2 - B_\phi^2)]/r \\ 3(\rho V_r V_\phi - B_r B_\phi)/r + 2\cot\theta(\rho V_\theta V_\phi - B_\theta B_\phi)/r \\ \cot\theta(V_\theta B_r - V_r B_\theta)/r \\ (V_r B_\theta - V_\theta B_r)/r \\ (V_r B_\phi - V_\phi B_r)/r \\ 2\rho s V_r/r + \cot\theta \rho s V_\theta/r \end{pmatrix}$$

where $\Pi = P + B^2/2$ is the total pressure and $s = P/\rho^\gamma$. The vector U contains the conservative variables, $F(U)$ and $G(U)$ are the r and θ fluxes, whereas H(U) contains all the terms due to the non-Cartesian geometry and to external forces (gravity).

7.4.2 Boundary conditions

The physical domain is a rectangular box in the spherical coordinates $r - \theta$, with $r_{\min} \leq r \leq r_{\max}$ and $0 \leq \theta \leq \pi$. On the axis ($\theta = 0, \pi$) symmetry conditions are imposed (the θ and ϕ components must vanish) and these are, like periodic boundary conditions, trivial to be treated. On the other hand, great care has to be used for the conditions in the radial direction, where plasma flows cross the two boundaries (inflow/outflow boundary conditions, see Poinsot & Lele, 1992, for a general discussion applied to Euler and Navier-Stokes equations).

When situations of this kind occur, the MHD equations have to be decomposed into their characteristic modes and the conditions that can be imposed will be determined by the sign of the eigenvalues of the Jacobian matrix $A(U) = \partial F/\partial U$. Let us identify the radial direction with a generic coordinate x and write Eq. (7.6) in the form:

$$\left(\frac{\partial U}{\partial t}\right)_x + F' = 0; \quad F' = \frac{\partial}{\partial x}F(U) = A(U)\frac{\partial U}{\partial x}. \tag{7.7}$$

It is well known that this system is hyperbolic and admits 7 real eigenvalues (the equation for B_x is removed, since its corresponding flux is zero), which are (e.g., Jeffrey & Taniuti 1964):

$$\lambda_f^{\pm} = V_x \pm c_f \quad : \text{Fast magnetosonic modes} \tag{7.8}$$

$$\lambda_s^{\pm} = V_x \pm c_s \quad : \text{Slow magnetosonic modes} \tag{7.9}$$

$$\lambda_a^{\pm} = V_x \pm c_a \quad : \text{Alfvénic modes} \tag{7.10}$$

$$\lambda_0^{\pm} = V_x \quad : \text{Entropy mode} \tag{7.11}$$

and they represent the local speed for each characteristic MHD wave. The three velocities c_f, c_s, c_a are given by ($c_s \leq c_a \leq c_f$):

$$c_f^2 = 1/2[a^2 + B^2/\rho + \sqrt{(a^2 + B^2/\rho)^2 - 4a^2B_x^2/\rho}] \tag{7.12}$$

$$c_s^2 = 1/2[a^2 + B^2/\rho - \sqrt{(a^2 + B^2/\rho)^2 - 4a^2B_x^2/\rho}] \tag{7.13}$$

$$c_a^2 = B_x^2/\rho, \tag{7.14}$$

where $a^2 = \gamma P/\rho$ is square of the sound speed.

To impose inflow/outflow boundary conditions the quantities $F_i' = -(\partial U/\partial t)_x$ are projected into the space spanned by the right eigenvectors of $A(U)$ (see Ryu & Jones 1995, or Roe & Balsara 1996, for the correct normalisation):

$$F_1' = \mathcal{L}_0 + \alpha_f(\mathcal{L}_f^+ + \mathcal{L}_f^-) + \alpha_s(\mathcal{L}_s^+ + \mathcal{L}_s^-) \tag{7.15}$$

$$F_2' - V_x F_1' = \alpha_f c_f(\mathcal{L}_f^+ - \mathcal{L}_f^-) + \alpha_s c_s(\mathcal{L}_s^+ - \mathcal{L}_s^-) \tag{7.16}$$

$$F_3' - V_y F_1' = \sigma\beta_y[\alpha_f c_f(\mathcal{L}_s^+ - \mathcal{L}_s^-) - \alpha_s c_s(\mathcal{L}_f^+ - \mathcal{L}_f^-)] + \beta_z(\mathcal{L}_a^+ - \mathcal{L}_a^-) \tag{7.17}$$

$$F_4' - V_z F_1' = \sigma\beta_z[\alpha_f c_f(\mathcal{L}_s^+ - \mathcal{L}_s^-) - \alpha_s c_s(\mathcal{L}_f^+ - \mathcal{L}_f^-)] - \beta_y(\mathcal{L}_a^+ - \mathcal{L}_a^-) \tag{7.18}$$

$$\sqrt{\rho}F_5' = a\beta_y[\alpha_s(\mathcal{L}_f^+ + \mathcal{L}_f^-) - \alpha_f(\mathcal{L}_s^+ + \mathcal{L}_s^-)] - \sigma\beta_z(\mathcal{L}_a^+ + \mathcal{L}_a^-) \tag{7.19}$$

$$\sqrt{\rho}F_6' = a\beta_z[\alpha_s(\mathcal{L}_f^+ + \mathcal{L}_f^-) - \alpha_f(\mathcal{L}_s^+ + \mathcal{L}_s^-)] + \sigma\beta_y(\mathcal{L}_a^+ + \mathcal{L}_a^-) \tag{7.20}$$

$$F_7'/s - F_1' = -\gamma\mathcal{L}_0 \tag{7.21}$$

where $\sigma = \mathrm{sign}(B_x)$, with $\sigma = 1$ for $B_x = 0$, where

$$\alpha_s = \sqrt{\frac{c_f^2 - a^2}{c_f^2 - c_s^2}}, \quad \alpha_f = \sqrt{\frac{a^2 - c_s^2}{c_f^2 - c_s^2}}, \quad \alpha_s^2 + \alpha_f^2 = 1, \tag{7.22}$$

with $\alpha_s = \alpha_f = 1/\sqrt{2}$ when $c_f = c_a = c_s = a$, and where

$$\beta_y = B_y/B_\perp, \quad \beta_z = B_z/B_\perp, \quad \beta_y^2 + \beta_z^2 = 1, \tag{7.23}$$

with $\beta_y = \beta_z = 1/\sqrt{2}$ when $B_\perp = \sqrt{B_y^2 + B_z^2} \to 0$.

The quantities $\mathcal{L}$ represent the contribution given by the characteristic waves: if the wave is leaving the domain (outgoing) its corresponding $\mathcal{L}$ must be calculated by interpolating from interior points, otherwise $\mathcal{L}$ is free to be imposed (incoming wave). Possible choices are, for example, non-reflecting (or radiation) boundary conditions, where $\mathcal{L}$ is set to zero for incoming waves (see Thomson 1987 and Vanajakshi et al. 1989), so that the presence of the boundary does not introduce spurious perturbations, or stationary boundary conditions, in which the incoming waves combine in order to keep a corresponding number of physical quantities constant at the boundary. In this latter case, if n is the number of incoming waves, in the above system n equations can be inverted to find every incoming $\mathcal{L}$. In these equations each F_i' has to be replaced by the correspondent $-(\partial U/\partial t)_x$, which contains the time derivative (zero for stationary conditions), the θ derivative and the other geometrical terms.

In our specific case, logical choices are non-reflecting conditions at $r = r_{\max}$ and stationary conditions at $r = r_{\min}$. If the initial flow is a Parker type wind and the outer boundary is placed beyond all the critical points, the seven eigenvalues will be all positive and the behaviour at the boundary will depend only on interior points, with no other constraint to impose. On the other hand, at the coronal base the flow is subsonic, with typically four incoming waves ($\mathcal{L}_0, \mathcal{L}_s^+, \mathcal{L}_a^+, \mathcal{L}_f^+$) and three outgoing waves ($\mathcal{L}_s^-, \mathcal{L}_a^-, \mathcal{L}_f^-$).

To conclude, the rules for constructing the outgoing waves through left eigenvector composition are reported:

$$\mathcal{L}_0 = (F_1' - F_7'/s)/\gamma \tag{7.24}$$

$$\mathcal{L}_c^{\pm} = \frac{\mathcal{M}_c \pm \mathcal{N}_c}{2}, \quad c = c_f, c_s, c_a \tag{7.25}$$

with

$$\mathcal{M}_f = \alpha_f[(\gamma-1)F_1' + F_7'/s]/\gamma + \alpha_s\sqrt{\rho}/a(\beta_y F_5' + \beta_z F_6') \tag{7.26}$$

$$\mathcal{N}_f = \{\alpha_f c_f(F_2' - V_x F_1') - \sigma\alpha_s c_s[\beta_y(F_3' - V_y F_1') + \beta_z(F_4' - V_z F_1')]\}/a^2 \tag{7.27}$$

$$\mathcal{M}_s = \alpha_s[(\gamma-1)F_1' + F_7'/s]/\gamma - \alpha_f\sqrt{\rho}/a(\beta_y F_5' + \beta_z F_6') \tag{7.28}$$

$$\mathcal{N}_s = \{\alpha_s c_s(F_2' - V_x F_1') + \sigma\alpha_f c_f[\beta_y(F_3' - V_y F_1') + \beta_z(F_4' - V_z F_1')]\}/a^2 \tag{7.29}$$

$$\mathcal{M}_a = \sigma\sqrt{\rho}(\beta_y F_6' - \beta_z F_5') \tag{7.30}$$

$$\mathcal{N}_a = \beta_z(F_3' - V_y F_1') - \beta_y(F_4' - V_z F_1'), \tag{7.31}$$

where all the F_i' are interpolated from interior points.

7.4.3 Comments and preliminary results

The code described in this section has been tested in 2-D (letting V_ϕ and B_ϕ to zero) in two different ways. The first approach has consisted of assuming a Parker radial wind superimposed on a potential dipolar configuration for the coronal magnetic field as initial condition. Then the system has been allowed to evolve in time towards a steady state configuration. The flow is subsonic at the inner boundary and super-Alfvénic (actually $V_r > c_f$) at the outer boundary, where all the quantities can be extrapolated from interior points. As discussed above, four (three in 2-D) waves can be imposed at the inner boundary: one of the several choices which has been tested is to take $\mathcal{L}_0 = 0$, $\mathcal{L}_s^+ = -\mathcal{L}_s^-$, $\mathcal{L}_a^+ = -\mathcal{L}_a^- = 0$ and $\mathcal{L}_f^+ = -\mathcal{L}_f^-$, in order to keep the density, pressure and the tangential magnetic field components steady at the coronal base.

The initial evolution of the system is what may be expected and agrees with the results in the works cited at the beginning of this section. In the equatorial region the flow decreases drastically because the plasma is trapped by the closed magnetic fieldlines. At the same time, the presence of a supersonic flow at larger distances makes the fieldlines stretch outwards in a streamer like configuration. This behaviour is seen to depend strongly on the characteristic plasma β assumed. When the field is dominant ($\beta \ll 1$) the static *cavity* develops faster and the fieldlines are almost unaffected by the outflow, for a weaker field ($\beta \sim 1$) an outflow is still present in the equatorial region and the effect of stretching the fieldlines is stronger.

However, while the system evolves, at the coronal base some spurious *spikes* in the physical quantities begin to appear, especially in the velocity components. At the same time the solenoidal condition $\nabla \cdot \mathbf{B} = 0$ ceases to be fulfilled there. If the code is left to run further, it will invariably crash because of these numerical problems. At the moment, it is still not clear whether the problem is due to the numerical method, which fails to preserve the solenoidal condition because the field components evolve independently, or it is due to some ill posed boundary conditions. More likely, the problem is a combination of these two, that is the boundary conditions are not correctly imposed for the induction equation, which hence fails to advance in time the field components properly.

The second approach has been to start with a static atmosphere with a dipolar magnetic field and then to switch on a wind by lowering the pressure at the outer boundary, with the same technique explained in Chapter 6 and used for the hydrodynamic 1-D version of the code. In this case the incoming waves are set to their initial value. Also in this case, though, once the inward propagating fast magnetoacustic wave (which coincides with the sound wave where the field is weak, at large distances) has reached the inner boundary, the spurious effects begin to appear and the code eventually crashes. The same method, but without the magnetic field and with sound waves whose amplitude depends on the latitude, gives instead good results, thus confirming that the problem is certainly due to the magnetic field and to the treatment of the induction equation at the inner boundary. Research is presently in progress in order to solve this problem.

When the full MHD code finally works, it will be also interesting to use it to model the large scale field and plasma properties as measured *in situ* by the Ulysses spacecraft. For reviews of the preliminary results see Mardsen et al. (1996), Forsyth et al. (1996) and Goldstein et al. (1996), where the first paper is a general introduction to the mission, the

second deals with the interplanetary magnetic field and the third reviews the observations of the other plasma parameters.

The construction of the MHD code, its testing and the work described in Chapter 6 have been carried out by the author of this thesis during a six month visit to Florence, in collaboration with Dr. M. Velli and Dr. P. Londrillo.

7.5 Concluding remarks

Instead of focusing only on one particular topic in solar physics, the spirit of this thesis is different. Within the mathematical frame of MHD equilibria, the development of the thesis has followed the search for solutions to the corresponding equations. This has been achieved through a continuous refinement in the mathematical tools employed, starting with a pure analytic approach and ending up with a high order shock capturing code for time dependent simulations.

However, there is certainly a common background and this is provided by the physics of MHD flows in the solar atmosphere. The mathematical methods developed have been used to model these flows in some selected examples: steady flows in quiescent prominences, steady flows in coronal plumes and finally the time dependent evolution of the solar wind.

For the future, the ultimate hope is to be able to gain a deeper understanding of the physics of the sources of the solar wind, namely coronal holes and their fine scale structure (plumes). In particular, one would like to know how the solar wind is actually accelerated in these open fieldlines regions, which is one of the major open questions in this fascinating subject that is solar physics.

Appendix A: Vector calculus in orthogonal curvilinear coordinates

Consider a generic curvilinear system of orthogonal coordinates (x_1, x_2, x_3). The metric tensor of the system is diagonal and may be written as

$$g_{ij} = \begin{pmatrix} h_1^2 & 0 & 0 \\ 0 & h_2^2 & 0 \\ 0 & 0 & h_3^2 \end{pmatrix},$$

and the differential line element is given by

$$\mathrm{d}s = \sqrt{(h_1 \mathrm{d}x_1)^2 + (h_2 \mathrm{d}x_2)^2 + (h_3 \mathrm{d}x_3)^2}. \tag{A-1}$$

If $(\mathbf{e}_1, \mathbf{e}_2, \mathbf{e}_3)$ is the orthogonal base of unit vectors in the curvilinear coordinate system, a generic vector $\mathbf{B}$ can be decomposed as

$$\mathbf{B} = B_1 \mathbf{e}_1 + B_2 \mathbf{e}_2 + B_3 \mathbf{e}_3, \tag{A-2}$$

and the usual rules for scalar and vector products hold.

Consider now a scalar field $A(x_1, x_2, x_3)$. Its gradient in curvilinear orthogonal coordinates is

$$\nabla A = \frac{1}{h_1}\frac{\partial A}{\partial x_1}\mathbf{e}_1 + \frac{1}{h_2}\frac{\partial A}{\partial x_2}\mathbf{e}_2 + \frac{1}{h_3}\frac{\partial A}{\partial x_3}\mathbf{e}_3. \tag{A-3}$$

For a vector field $\mathbf{B}(x_1, x_2, x_3)$ the differential operators of divergence and curl are respectively given by

$$\nabla \cdot \mathbf{B} = \frac{1}{h_1 h_2 h_3}\left[\frac{\partial}{\partial x_1}(h_2 h_3 B_1) + \frac{\partial}{\partial x_2}(h_1 h_3 B_2) + \frac{\partial}{\partial x_3}(h_1 h_2 B_3)\right], \tag{A-4}$$

$$(\nabla \times \mathbf{B})_1 = \frac{1}{h_2 h_3}\left[\frac{\partial}{\partial x_1}(h_3 B_3) - \frac{\partial}{\partial x_3}(h_2 B_2)\right], \tag{A-5}$$

$$(\nabla \times \mathbf{B})_2 = \frac{1}{h_1 h_3}\left[\frac{\partial}{\partial x_2}(h_1 B_1) - \frac{\partial}{\partial x_1}(h_3 B_3)\right], \tag{A-6}$$

$$(\nabla \times \mathbf{B})_3 = \frac{1}{h_1 h_2}\left[\frac{\partial}{\partial x_3}(h_2 B_2) - \frac{\partial}{\partial x_2}(h_1 B_1)\right]. \tag{A-7}$$

By combining Eq. (A-3) and Eq. (A-4), the expression for the Laplacian of A can be obtained:

$$\nabla^2 A = \frac{1}{h_1 h_2 h_3}\left[\frac{\partial}{\partial x_1}\left(\frac{h_2 h_3}{h_1}\frac{\partial A}{\partial x_1}\right) + \frac{\partial}{\partial x_2}\left(\frac{h_1 h_3}{h_2}\frac{\partial A}{\partial x_2}\right) + \frac{\partial}{\partial x_3}\left(\frac{h_1 h_2}{h_3}\frac{\partial A}{\partial x_3}\right)\right]. \tag{A-8}$$

Another useful relation, especially for decomposing the Lorentz force in the MHD momentum equation, is

$$(\nabla \times \mathbf{B}) \times \mathbf{B} = (\mathbf{B} \cdot \nabla)\mathbf{B} - \nabla\left(\frac{B^2}{2}\right), \tag{A-9}$$

from which the expression for the operator $(\mathbf{B} \cdot \nabla)\mathbf{B}$ may be derived.

Finally, the line elements for the three most commonly used systems of orthogonal coordinates are shown in the table below ($R = r\sin\theta$).

Coordinate system	x_1	x_2	x_3	h_1	h_2	h_3
Cartesian	x	y	z	1	1	1
Cylindrical	R	ϕ	z	1	R	1
Spherical	r	θ	ϕ	1	r	$r\sin\theta$

Table A-1: The metric elements for the three main orthogonal coordinate systems.

Appendix B: One-dimensional flow through a discontinuity between two isothermal regions

Consider two isothermal regions with different temperatures separated by a discontinuity interface. Let c_1 and c_2 be the sound speed respectively in the regions before and after the discontinuity, according to the direction of the flow. Using the standard notation for the shock fronts, the two mechanical conservation laws are

$$\rho_1 v_1 = \rho_2 v_2 \tag{B-1}$$

and

$$\rho_1 v_1^2 + p_1 = \rho_2 v_2^2 + p_2, \tag{B-2}$$

from which, introducing the specific volume $V = 1/\rho$, the following relation can be obtained:

$$\frac{p_2 - p_1}{V_2 - V_1} = -\rho_1^2 v_1^2. \tag{B-3}$$

Given the values ρ_1, p_1 and v_1 before the discontinuity, Eq. (B-3) is a straight line in the (p, V) plane, starting from the point p_1, V_1 and reaching p_2, V_2, with a negative slope given by $-\rho_1^2 v_1^2$. The relation between p and ρ is simply given by the isothermal state equation $p = c^2\rho$, so at the interface the two relations $p_1 = c_1^2\rho_1, p_2 = c_2^2\rho_2$ hold, which in the (p, V) plane are two rectangular hyperbolae (the one corresponding to the hottest region above the other). Hence, the solutions to the problem are determined by the intersections of the upper hyperbola with the straight lines starting from p_1, V_1, for every value of the velocity v_1, as shown in Fig. B-1.

The locus of all these solutions is known as the *Hugoniot curve*. As the gradient of the straight line must be negative, each initial point p_1, V_1 determines two branches on the

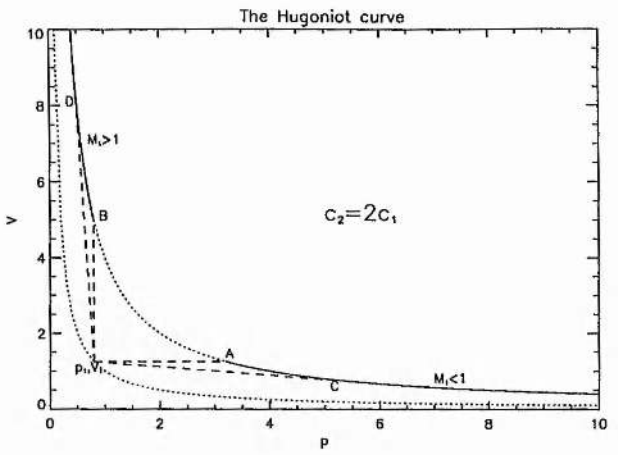

Figure B-1: The Hugoniot curve for a discontinuity between two isothermal regions for given initial values of p_1, V_1. The possible values of M_1 are determined by the (negative) value of the angular coefficient of the straight lines starting from p_1, V_1 and intersecting one of the two branches.

Hugoniot curve, one for subsonic initial velocities ($M_1 \equiv v_1/c_1 < 1$) and the other for supersonic velocities ($M_1 > 1$). It is also clear that two limiting values M_1^- and M_1^+ exist for the two branches, correspondent respectively to the tangential lines in C and D.

A very similar situation holds for the *detonation waves*, as described for example in Landau & Lifshitz (1959). In that case the energy equation is not isothermal but the Hugoniot curve shows the same properties. The similarity lies in the fact that the energy flux is not conserved because of the input of energy due to the combustion of the gas, that is a situation not so different from our condition (4.47) for the jump of the energy flux.

The values of M_1^- and M_1^+ may be found analytically. Rewrite Eq. (B-3) as an algebraic equation for p_2 (using the equation of state in order to eliminate V_2 and ρ_2):

$$f(p_2) \equiv p_2 - (1 + M_1^2)p_1 + (c_2/c_1)^2 p_1^2 M_1^2/p_2 = 0. \tag{B-4}$$

This function has a minimum for $p_2 = (c_2/c_1)p_1 M_1$ and its value must be negative (or zero) in order to obtain solutions of Eq. (B-4). This condition is equivalent to the second order inequality for M_1

$$M_1^2 - 2(c_2/c_1)M_1 + 1 \geq 0, \tag{B-5}$$

with the solutions

$$M_1 \leq M_1^- \equiv c_2/c_1 - \sqrt{(c_2/c_1)^2 - 1} < 1, \tag{B-6}$$

and

$$M_1 \geq M_1^+ \equiv c_2/c_1 + \sqrt{(c_2/c_1)^2 - 1} > 1, \tag{B-7}$$

respectively for the subsonic and supersonic branch. In the case $(c_2/c_1)^2 \gg 1$, like in the prominence model, the two limiting values assume the simple forms $M_1^- = c_1/2c_2$ and $M_1^+ = 2c_2/c_1$.

Appendix C: A linear multigrid Poisson solver

C-1 Introduction

Let the mathematical problem to solve be expressed by the following PDE:

$$\mathcal{L}(u) = f, \tag{C-1}$$

where $u(x_1, x_2)$ is the unknown function of the two spatial coordinates x_1 and x_2 in some 2-D orthogonal system. Consider, for simplicity, a *linear* problem, where $\mathcal{L}$ is a linear second order differential operator and $f(x_1, x_2)$ is a given function of the coordinates. Moreover, suppose that the operator $\mathcal{L}$ is elliptic and the function u is subject to Dirichlet boundary conditions, thus Eq. (C-1) is a Poisson like PDE, as in the physical application described in Chapter 5.

From a computational point of view, Eq. (C-1) is solved by means of a discretisation of the derivatives in the operator $\mathcal{L}$ over a numerical grid, which will be considered here to be square ($N \times N$ grid points in two dimensions) for practical reasons. The initial mathematical problem can be then reduced to the resolution of the *linear algebraic* system

$$AU = V, \tag{C-2}$$

where A is a square (sparse) matrix, U is the unknown column vector and V is a column vector of known quantities.

Methods of solution of Eq. (C-2) fall into two categories, the *direct* and *iterative* procedures. Direct methods, of which the inversion of a tridiagonal system is typical, are those which give the exact answer in a finite number of steps, if there were no round-off. However, these methods are often complicated and require large memory capacities for

storage of intermediate results of the calculations. Here the method of solution will be considered to be iterative, that means it consists of repeated applications of an often simple algorithm, for which the exact solution is reached only as the limit of a sequence (for a discussion of different methods for linear elliptic PDEs see Ames 1969).

Typical convergence properties of classical iterative methods sees a rapid initial fall in the error, due to the elimination of the short wavelength errors (those of the order of the grid spacing), but then this decay slows down and long wavelength errors may require a very long computational time to be eliminated (saturation). Moreover, the time necessary to sweep over the grid at each iteration goes like N^2 and the *equivalent time step* for the refinement of the solution at each iteration goes like N^2 as well, thus the global time per iteration goes like N^4. This means that when a high resolution is required, classical methods may be totally inadequate.

This is where multigrid algorithms come into play. Since classical iterative schemes are efficient only in eliminating short wavelength errors, if the grid could be somehow coarsened to an arbitrary size, all the errors would be considered as short wavelength. Therefore, the basic idea of multigrid algorithms is to eliminate different wavelength errors on grids with different mesh sizes, all at the same time at each iteration.

The problem is then how to link all the informations coming from the different grids and to obtain a final global error at each iteration. This is achieved by using two appropriate operators called *restrictor* and *prolongator*, which respectively pass the informations down to a coarser grid or up to a finer grid, thus allowing movement through the different mesh grids. The particular algorithm giving the *path* with which the different grids are visited for each iteration is called *multigrid schedule*.

The advantages in using multigrid methods over classical iterative schemes are twofold. Firstly, for a given number of grid points N, the convergence rate does not saturate for long wavelength errors, since all the wavelengths are considered to be short and treated at once, resulting in a often massive reduction of computational time in reaching the required accuracy. Secondly, the equivalent time step for the refinement of the solution is independent of the number of grid points (the *smoothing* of the errors is made principally on the coarsest grid, that is the same for all values of N), hence the time for each iteration only goes as N^2, thus allowing for much higher resolution than in classical iterative schemes.

Here the algorithm used in the code implemented for the work presented in Chapter 5 will be described briefly. For more general information the reader is referred to Wessel-

ing (1992), whereas for other applications to solar equilibrium magnetic structures see Longbottom et al. (1997) and references therein.

C-2 The multigrid algorithm

Let a sequence $\{G^k : k = 1, \ldots, K\}$ of increasingly finer grids be given. Let U^k be the set of grid functions $G^k \to \Re$ on G^k and be $L^k : U^k \to U^k$ the finite differences discretisation on G^k of the operator $\mathcal{L}$ in Eq. (C-1), $R^k : U^{k+1} \to U^k$ the *restrictor* operator and $P^k : U^{k-1} \to U^k$ the *prolongator* operator. Moreover, let

$$L^k(u^k) = f^k \tag{C-3}$$

be the equation to solve on G^k, with u^k, $f^k \in U^k$. The operation of *smoothing* of an initial guess $\tilde{u}^k$ into a new, improved guess u^k is achieved by an algorithm denoted by $\mathrm{S}(\tilde{u}, u, f, \nu, k)$, where ν_k is the number of iterations of a suitable smoothing scheme. Finally, let $\mathrm{S}(\tilde{u}, u, f, \cdot, 1)$ indicate the smoothing process on the coarsest grid until convergence to round-off is achieved.

The multigrid algorithm is basically a recursive subroutine which is able to work on a generic grid G^k and calls itself and the other subroutines (the smoother S) and operators (the differential operator L, the restrictor R and the prolongator R) with different values of k. The form given by Wesseling (1992) for the basic, linear multigrid algorithm is the following:

subroutine $\mathrm{LMG}(\tilde{u}, u, f, k)$
  if $(k = 1)$ **then**
(S) $\mathrm{S}(\tilde{u}, u, f, \cdot, 1)$
  else
(A) $\mathrm{S}(\tilde{u}, u, f, \nu, k)$
(A) $r^k = f^k - L^k(u^k)$
(A) $f^{k-1} = R^{k-1}(r^k)$
(A) $\tilde{u}^{k-1} = 0$
  for $i = 1$ **to** γ_k **do**
    $\mathrm{LMG}(\tilde{u}, u, f, k-1)$
    $\tilde{u}^{k-1} = u^{k-1}$
  end do

(B) $u^k = u^k + P^k(u^{k-1})$

(B) S(u, u, f, μ, k)

end if

end subroutine

Some comments are needed. At each iteration the recursive LMG subroutine is called with $k = K$ (the finest grid) from an outer loop, with f being the right hand side of Eq. (C-1) and $\tilde{u}$ an initial guess for the solution, with the only requirement to satisfy the boundary conditions. The first operation is that of *pre-smoothing*, to be repeated ν_k times. The resulting function u^k is an improved guess for the solution. Then, define the *residual* of this guess as $r^k = f^k - L^k(u^k)$. This is a measure of the error. In fact, if u^t is the *true* solution, then the error on G^k is $e^k = u^t - u^k$ and the relation

$$L^k(e^k) = L^k(u^t) - L^k(u^k) = f^k - L^k(u^k) = r^k \tag{C-4}$$

holds. The residual is then restricted to the next coarser grid and the result will provide the right hand side for the problem to be solved on G^{k-1}, thus to give e^{k-1} (in the linear case considered here the guess $\tilde{u}^{k-1}$ can be taken to be zero since its choice does not influence the final result). These operations are repeated until the coarsest grid is reached, where the smoothing to round-off is achieved. This should not take a long time, as the coarsest grid consists of just a few points (one plus the boundaries in the optimal case of a square grid and a centered, second order differencing scheme). The resulting function from this smoothing process is then *prolongated* upwards to the next finer grid and a *post-smoothing* operation is iterated μ_k times. In the code, both mu_k and ν_k have been taken as unity for all values of k.

Another set of parameters, giving the actual multigrid schedule, is $\gamma_k, k = 1, \ldots, K-1$. If these parameters are chosen in advance, the multigrid algorithm is said to be with *fixed schedule*; if γ_k depends on intermediate computational results it is said to be with *adaptive schedule*. In the code, the choice between three different kinds of fixed schedules is given, namely the so-called V-cycle ($\gamma_k = 1, k = 1, \ldots, K-1$), the W-cycle ($\gamma_k = 2, k = 1, \ldots, K-1$) and the F-cycle (an intermediate version of the previous two). For $K = 4$ the sequence of A, B and S processes for the three kinds of cycles is:

Cycle	Sequence ($K = 4$)
V	A–A–A–S–B–B–B
W	A–A–A–S–B–A–S–B–B–A–A–S–B–A–S–B–B–B
F	A–A–A–S–B–A–S–B–B–A–A–S–B–B–B

The following program carries out *nmg* multigrid iterations according to a V-, W-, or F-cycle:

```
program Multigrid
    Choose ũ^K
    if (cycle = V) then γ = 1 else γ = 2 end if
    for i = 1 to nmg do
        LMG2(ũ, u, f, K, γ)
        ũ^K = u^K
    end do
end program
```

The correspondent recursive multigrid algorithm is the following:

```
subroutine LMG2(ũ, u, f, k, γ)
  if (k = 1) then
    S
    if (cycle = F) then γ = 1 end if
  else
    A
    for i = 1 to γ do
        LMG2(ũ, u, f, k − 1, γ)
        ũ^{k−1} = u^{k−1}
    end do
    B
    if (k = K and cycle = F) then γ = 2 end if
  end if
end subroutine
```

The code has been written by the author of this thesis in FORTRAN 90, by translating and modifying a previous version in FORTRAN 77 due to Dr. A.W. Longbottom. In

FORTRAN 90 the multigrid algorithm is employed in a straightforward and very elegant way, by using recursion and matrix operators, both features which were absent in FORTRAN 77. In the following, the three operators L^k, R^k, P^k and the smoother subroutine S will be described in some detail.

C-2.1 The restrictor operator R^k

From now on the various grids will be considered to have a number of points per dimension which is the double of that of next coarser grid, with the coarsest being made up by one point alone plus the boundary points (four cells).

Let $u \in U^{k+1}$ be the input square matrix with $[2(n+1)+1]^2$ mesh points and $\tilde{u} \in U^k$, hence with $(2n+1)^2$ mesh points. A number of conditions must be fulfilled in this process of restriction to the coarser grid. One of these is the conservation of the integral of the residual over the two grids. One way to achieve this result is by using the method of *full weighting* (by area). Let i and j sweep the grids ($-2n \leq i \leq 2n$ and $-2n \leq j \leq 2n$, with step 2 in both directions), three different cases arise:

1. Interior points.

   When $-2n < i < 2n$ and $-2n < j < 2n$ the corresponding element at $i/2, j/2$ of the output matrix in the coarser grid is given by

   $$\tilde{u}_{i/2,j/2} = \frac{1}{16}[4u_{i,j} + 2(u_{i-1,j} + u_{i+1,j} + u_{i,j-1} + u_{i,j+1}) \quad \text{(C-5)}$$

   $$+u_{i-1,j-1} + u_{i-1,j+1} + u_{i+1,j-1} + u_{i+1,j+1}], \quad \text{(C-6)}$$

   from which is clear that points closer to the centre contribute more to the final result.

2. Edge points.

   At edges the previous formula may be used by assigning the values to the missing points to be equal to those in the correspondent specular positions. For example, at the edge $i = -2n$ the relations $u_{i-1,\ldots} = u_{i+1,\ldots}$, hence:

   $$\tilde{u}_{i/2,j/2} = \frac{1}{8}[2(u_{i,j} + u_{i+1,j}) + u_{i,j-1} + u_{i,j+1} + u_{i+1,j-1} + u_{i+1,j+1}]. \quad \text{(C-7)}$$

3. Corner points.

   A similar situation holds for corner points. Because of symmetry reasons, this time all the points have equal weight, thus ($i = -2n, j = -2n$):

   $$\tilde{u}_{i/2,j/2} = \frac{1}{4}[u_{i,j} + u_{i,j+1} + u_{i+1,j} + u_{i+1,j+1}]. \quad \text{(C-8)}$$

C-2.2 The prolongator operator P^k

This time the input matrix is $u \in U^{k-1}$ and the output matrix is $\tilde{u} \in U^k$. Bilinear interpolation is employed for the values of the matrix in the finer grid, that is coinciding points are simply *injected* from the coarser grid, those on an edge between other two points take the value of the average of the two points on that edge, whereas those at a cell centre of the coarser grid take the average of the four points on the corners of that cell. If $-n \leq i \leq n$, $-n \leq j \leq n$ are the indexes sweeping the finer grid, four different cases arise.

1. i and j even:

$$\tilde{u}_{i,j} = u_{i/2,j/2}, \tag{C-9}$$

2. i even and j odd:

$$\tilde{u}_{i,j} = \frac{1}{2}[u_{i/2,(j-1)/2} + u_{i/2,(j+1)/2}], \tag{C-10}$$

3. i odd and j even:

$$\tilde{u}_{i,j} = \frac{1}{2}[u_{(i-1)/2,j/2} + u_{(i+1)/2,j/2}], \tag{C-11}$$

4. i and j odd:

$$\tilde{u}_{i,j} = \frac{1}{2}[u_{(i-1)/2,(j-1)/2} + u_{(i-1)/2,(j+1)/2} + u_{(i+1)/2,(j-1)/2} + u_{(i+1)/2,(j+1)/2}]. \tag{C-12}$$

C-2.3 The differential operator L^k

Suppose that the differential operator $\mathcal{L}$ in Eq. (C-1) is linear and elliptic. Its most general form in curvilinear orthogonal coordinates is

$$\mathcal{L}(u) \equiv \frac{a}{h_1^2}\frac{\partial^2 u}{\partial x_1^2} + \frac{2b}{h_1 h_2}\frac{\partial^2 u}{\partial x_1 \partial x_2} + \frac{c}{h_2^2}\frac{\partial^2 u}{\partial x_2^2} + \frac{d}{h_1}\frac{\partial u}{\partial x_1} + \frac{e}{h_2}\frac{\partial u}{\partial x_2} + gu, \tag{C-13}$$

where $b^2 - ac < 0$ by hypothesis.

For interior points, a centered, second order differencing scheme is employed. Through Taylor expansions around the central point $u_{i,j}$ with steps Δ_1 and Δ_2 (the grid points separations, which are considered to be constant throughout the grid), the expressions for the various derivatives are easily found to be:

$$\frac{\partial^2 u}{\partial x_1^2} = \frac{u_{i+1,j} - 2u_{i,j} + u_{i-1,j}}{\Delta_1^2}, \tag{C-14}$$

$$\frac{\partial^2 u}{\partial x_1 \partial x_2} = \frac{u_{i+1,j+1} - u_{i+1,j-1} - u_{i-1,j+1} + u_{i-1,j-1}}{4\Delta_1\Delta_2}, \tag{C-15}$$

$$\frac{\partial^2 u}{\partial x_2^2} = \frac{u_{i,j+1} - 2u_{i,j} + u_{i,j-1}}{\Delta_2^2}, \tag{C-16}$$

$$\frac{\partial u}{\partial x_1} = \frac{u_{i+1,j} - u_{i-1,j}}{2\Delta_1}, \tag{C-17}$$

$$\frac{\partial u}{\partial x_2} = \frac{u_{i,j+1} - u_{i,j-1}}{2\Delta_2}. \tag{C-18}$$

For Dirichlet boundary conditions the operator L^k needs to be evaluated in interior points alone, while for Neumann boundary conditions the values in the points outside the domain are derived from the imposed values of the derivatives normal to the boundary. In the code only Dirichlet conditions are used.

C-3 A smoothing iterative scheme: Gauss-Seidel and SOR

The problem of the actual solution of Eq. (C-1) by means of an iterative scheme is addressed here. This is achieved by the smoother subroutine $S(\tilde{u}, u, f, \nu, k)$. After the discretisation of the differential operator $\mathcal{L}$, as discussed in the previous sub-section, and after ordering the elements of the matrices u and f into the column vectors U and V, respectively, the problem is turned in the inversion of the linear, algebraic system Eq. (C-2).

The Gauss–Seidel iterative method is based upon *immediate* use of the improved values. For an arbitrary but fixed ordering of the mesh points $i = 1, 2, \ldots, N$, the system in Eq. (C-2) can be inverted to yield an expression such as

$$U_i^{(n)} = \sum_{j=1}^{i-1} b_{ij} U_j^{(n)} + \sum_{j=i+1}^{N} b_{ij} U_j^{(n-1)} + c_i, \tag{C-19}$$

where the updated values $U_j^{(n)}$ are used to calculate $U_i^{(n)}$ for $1 \leq j \leq i-1$, that is for the points preceding i in the chosen ordering. For the points following i the updated values are not available yet, hence the values of the previous iteration $(n-1)$ are used instead. Obviously the grid scanning must follow the ordering. In vectorial form, let the matrix A be decomposed as

$$A = R + D + S, \tag{C-20}$$

where R, D and S are matrices having the same elements as A respectively below the main diagonal, on the main diagonal and above the main diagonal, and zeros elsewhere. The original equation (C-2) becomes

$$AU = (R + D)U^{(n)} + SU^{(n-1)} = V, \tag{C-21}$$

hence

$$U^{(n)} = -(R+D)^{-1}SU^{(n-1)} = (R+D)^{-1}V. \tag{C-22}$$

The convergence rate of the Gauss-Seidel method may be accelerated by means of the so-called *successive over-relaxation* (SOR). If $\bar{U}_i^{(n)}$ is the result of the Gauss-Seidel iteration at the point i, given by Eq. (C-19), the updated value is now written as

$$U_i^{(n)} = U_i^{(n-1)} + \omega[\bar{U}_i^{(n)} - U_i^{(n-1)}] = (1-\omega)U_i^{(n-1)} + \omega\bar{U}_i^{(n)}, \tag{C-23}$$

where $\omega \geq 1$ is a constant parameter ($\omega = 1$ returns the Gauss-Seidel scheme) called *relaxation parameter*. The algebraic form of SOR is, after using Eq. (C-19):

$$U_i^{(n)} = (1-\omega)U_i^{(n-1)} + \omega\left[\sum_{j=1}^{i-1} b_{ij}U_j^{(n)} + \sum_{j=i+1}^{N} b_{ij}U_j^{(n-1)} + c_i\right]. \tag{C-24}$$

In matrix notation this becomes

$$U^{(n)} = (1-\omega)U^{(n-1)} + \omega[-D^{-1}RU^{(n)} - D^{-1}SU^{(n-1)} + D^{-1}V], \tag{C-25}$$

and the solution is

$$U^{(n)} = (D+\omega R)^{-1}\{[(1-\omega)D - \omega S]U^{(n-1)} + \omega V\}, \tag{C-26}$$

which returns Eq. (C-22) for $\omega = 1$. A typical value for the relaxation parameter is $\omega = 1.5$.

Even if Eqs. (C-23)–(C-26) may appear complicated, their actual implementation in the code is straightforward. If $u(i,j)$ contains the initial guess for the solution, the updated guess is given by the following algorithm (take $b = d = e = g = 0$ for simplicity, thus $a > 0$, $c > 0$)

for $i = 1-n$ **to** $n-1$ **do**
  for $j = 1-n$ **to** $n-1$ **do**
    $\alpha = \omega\left[\frac{2a}{(h_1\Delta_1)^2} + \frac{2c}{(h_2\Delta_2)^2}\right]^{-1}$
    $L = \frac{a}{h_1^2}\frac{u_{i+1,j}-2u_{i,j}+u_{i-1,j}}{\Delta_1^2} + \frac{c}{h_2^2}\frac{u_{i,j+1}-2u_{i,j}+u_{i,j-1}}{\Delta_2^2}$
    $u_{i,j} = u_{i,j} + \alpha(L-f)$
  end do
end do

Note that L automatically takes the updated values for the points preceding (i, j) in the loops.

In the subroutine $S(\tilde{u}, u, f, \nu, k)$ this update is carried out for ν_k iterations on the grid G^k, starting with the guess $\tilde{u}^k$ and giving u^k as an output improved guess for the problem $L^k u^k = f^k$. When the bottom grid is reached ($k = 1$) the smoothing process is carried out until convergence to round-off is achieved, that is a certain *norm* of the residual satisfies $|f^k - L^k(u^k)| < \epsilon$, with ϵ being a given accuracy.

C-4 Numerical results

In this section, the convergence rate of the linear multigrid scheme implemented in the code (both for the homogeneous case $f = 0$ of Eq. (5.25) and the inhomogeneous case $f \neq 0$ of Eq. (5.26)) over the classical iterative Gauss-Seidel scheme is analysed. Define a *working unit* (WU) to be the computational time necessary to achieve one iteration on the top (finest) grid with the Gauss-Seidel classical method with SOR. In Fig. C-1 the convergence histories, given as some norm of the residuals (maximum or average) as a function of WU, are shown for various resolutions. Dashed curves are for the classical method (Gauss-Seidel with SOR: $\omega = 1.5$), whereas solid curves are for the linear multigrid implementation (V-cycle) of the same iterative scheme.

A number of features may be noticed. The classical method quickly saturates once short wavelength errors have been eliminated. Doubling the number of grid points in both directions results in four times the number of work units needed to reach a given level of convergence. The linear multigrid scheme not only converges quickly to round-off (smoothing all wavelength errors simultaneously), but the number of work units to reach a given accuracy is practically independent of the number of grid points in the computational domain. These are the typical (massive) advantages, anticipated in the introduction, which make multigrid methods essential for high resolution calculations.

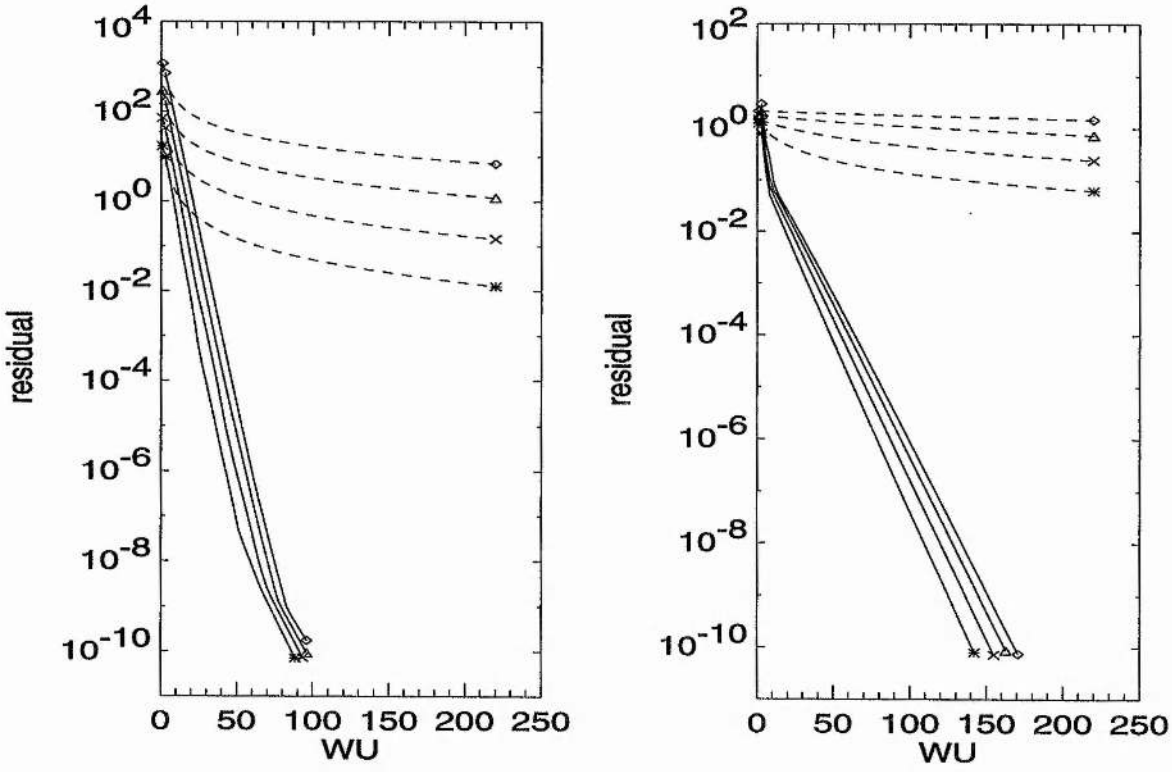

Figure C-1: Residual against WU for the homogeneous problem $f = 0$ (left hand side) and for the inhomogeneous problem $f \neq 0$ (right hand side). The resolutions used are 65^2 ($*$), 129^2 ($\times$), 257^2 (Δ) and 513^2 ($\diamond$). Dashed curves show the classical method, solid curves the linear multigrid (courtesy of Dr. A.W. Longbottom).

Appendix D: A high order weighted ENO differencing scheme

The numerical method employed in the MHD code described in Sect. 7.4, and in its 1-D hydrodynamic version of Chapter 6, is the WENO (Weighted Essentially Non Oscillatory) scheme proposed by Jiang & Shu (1996). This is probably the *state of the art* in the field of high order shock capturing schemes and performs particularly well on vector supercomputers. The idea is the following. Suppose that the spatial operator is discretised in the following conservative form (in the one-dimensional case):

$$L = (\hat{F}_{j+1/2} - \hat{F}_{j-1/2})/\Delta x. \tag{D-1}$$

First of all the fluxes on the grid points must be split into two parts, either globally or locally

$$F(U) = F^+(U) + F^-(U), \tag{D-2}$$

for which $\partial F^+/\partial U \geq 0$ and $\partial F^-/\partial U \leq 0$. For example one may adopt the Lax-Friedrichs (LF) flux splitting

$$F^{\pm}(U) = \frac{F(U) \pm \lambda_{\max} U}{2}, \tag{D-3}$$

where $\lambda_{\max} = V_x + c_f$.

The problem is how to find an approximate value for the numerical flux $\hat{F}_{j+1/2}$ (here the $\pm$ signs will be dropped, what follows actually refer to $\hat{F}^+_{j+1/2}$, the formulae for $\hat{F}^-_{j+1/2}$ being symmetrical) at the cell interface $x_{j+1/2}$. WENO schemes of order r use a weighted combination of r candidate stencils (each composed by r grid points) and the numerical flux is approximated by interpolation as

$$\hat{F}_{j+1/2} = \sum_{k=0}^{r-1} \omega_k q_k^r (F_{j+k-r+1}, F_{j+k-r+2}, \ldots, F_{j+k}), \tag{D-4}$$

where q_k^r is a linear function of its arguments, defined by some given constant coefficients, and ω_k is the weight for the stencil k.

To achieve the essentially non-oscillatory property, one then requires the weights to adapt freely to the relative *smoothness* of F on each candidate stencil such that any discontinuous stencil is effectively assigned a zero weight and the numerical flux in the shock region can be correctly computed. In smooth regions the contributions from all the r possible stencils combine together to give a high order ($2r-1$, the total number of grid points used) *upwind central scheme*, and these are known to be convergent when combined to a high order Runge-Kutta time integration method under appropriate CFL numbers.

In the code a WENO-LF scheme of order $r = 3$, which provides an accuracy of $F^{IV}(\Delta x)^5$ in smooth regions, has been employed. The radial and colatitudinal derivatives are computed separately, the contribution by the geometrical and gravitational terms is added and, at each time step, the right hand side, that we can call $-L(U)$ of Eq. (7.6) is calculated. The state variables are then updated through a third order TVD Runge-Kutta time stepping, developed by Shu & Osher (1988), where the equation

$$\frac{\partial U}{\partial t} = -L(U) \tag{D-5}$$

is integrated in three steps:

$$U^{(1)} = U^n - \Delta t L(U^n), \tag{D-6}$$

$$U^{(2)} = \frac{3}{4}U^n + \frac{1}{4}U^{(1)} - \frac{1}{4}\Delta t L(U^{(1)}), \tag{D-7}$$

$$U^{n+1} = \frac{1}{3}U^n + \frac{2}{3}U^{(2)} - \frac{2}{3}\Delta t L(U^{(2)}), \tag{D-8}$$

where the time step Δt is computed from

$$\Delta t = \mathrm{CFL}/\max\left[\frac{(V+c_f)_r}{\Delta r} + \frac{(V+c_f)_\theta}{r\Delta\theta}\right], \tag{D-9}$$

and $\mathrm{CFL} \leq 1$.

References

- Agim Y.Z., Tataronis J.A., 1985, J. Plasma Phys. 34(3), 337
- Ahmad I.A., Webb D.F., 1978, Sol. Phys. 58, 323
- Ahmad I.A., Withbroe G.L., 1977, Sol. Phys. 53, 397
- Ames W.F., 1969, *Numerical Methods for Partial Differential Equations*, Nelsen, London
- An C.-H., Wu S. T., Bao J. J., 1988, in: *Proc. Mallorca Workshop on Dynamics and Structure of Solar Prominences*, eds. J.L. Ballester, E.R. Priest
- Antiochos S.K., Klimchuk J.A., 1991, Astrophys. J. 378, 372
- Anzer U., 1972, Sol. Phys. 24, 324
- Anzer U., 1989, in: *Dynamics and Structure of Quiescent Solar Prominences*, ed. E.R. Priest, Kluwer Acad. Publ., Dordrecht, Holland
- Athay R.G., 1976, in: *The Solar Chromosphere and Corona: Quiet Sun*, D. Reidel Publ. Co., Dordrecht, Holland
- Athay R.G., Dere K.P., 1989, Astrophys. J. 364, 514
- Bacciotti F., Chiuderi C., 1992, Phys. Fluids B 4(1), 35
- Bardeen J.M., Berger B.K., 1978, Astrophys. J. 221, 105
- Belcher J.W., Davis L., Jr., 1971, J. Geophys. Res. 76, 3534
- Blandford R.D., Payne D.G., 1982, Monthly Notices Roy. Astron. Soc. 270, 721
- Bogovalov S.V., 1994, Monthly Notices Roy. Astron. Soc. 270, 721

- Bogovalov S.V., 1996, in: *Solar and Astrophysical Magnetohydrodynamic Flows*, Addison Wesley, Reading
- Bohlin J.D., Sheeley N.R., Tousey R., 1975, in: *Space Research XV*, ed. M.J. Rycroft, Akademie-Verlag, Berlin
- Borrini G., Noci G., 1982, Sol. Phys. 77, 153
- Boyd T.J.M., Sanderson J.J., 1969, *Plasma Dynamics*, Nelson, London
- Braginsky S.I., 1965, Rev. Plasma Phys. 1, 205
- Brekke P., 1993, Astrophys. J. 408, 735
- Brown A., 1958, Astrophys. J. 128, 646
- Cargill P.J., Priest E.R., 1980, Sol. Phys. 65, 251
- Cargill P.J., Priest E.R., 1982, Geophys. Astrophys. Fluid Dyn. 20, 277
- Chamberlain J.W., 1960, Astrophys. J. 131, 47
- Chandrasekhar S., 1956, Proc. Nat. Acad. Sci. 42, 273
- Chapman S., 1957, Smithsonian Contrib. Astrophys. 2, 14
- Cheng J., 1992, Astron. Astrophys. 259, 296
- Chiuderi C., Einaudi G., Torricelli-Ciamponi G., 1981, Astron. Astrophys. 97, 27
- Contopoulos J., 1996, Astrophys. J. 460, 185
- Contopoulos J., Lovelace R.V.E., 1994, Astrophys. J. 429, 139
- Defouw R.J., 1976, Astrophys. J. 209, 266
- Degenhardt D., 1989, Astron. Astrophys. 222, 297
- Degenhardt D., 1991, Astron. Astrophys. 248, 637
- De Forest C.E. et al., 1997, *in preparation*
- Del Zanna L., Chiuderi C., 1996, Astron. Astrophys. 310, 341

- Del Zanna L., Hood A.W., 1996, Astron. Astrophys. 309, 943
- Del Zanna L., Hood A.W., 1996, Astro. Lett. and Communications 34, 95
- Del Zanna L., Hood A.W., Longbottom A.W., 1997, Astron. Astrophys. 318, 963
- Del Zanna L., Velli M., Londrillo P., 1997, *in preparation*
- Démoulin P., Einaudi G., 1988, in: *Proc. Mallorca Workshop on Dynamics and Structure of Solar Prominences*, eds. J.L. Ballester, E.R. Priest
- Dere K.P., 1982, Sol. Phys. 77, 77
- Dere K.P., Bartoe J.-D.F., Brueckner G.E., 1986, Astrophys. J. 310, 456
- de Ville A., Priest E.R., 1989, Astrophys. J. 340, 529
- de Ville A., Priest E.R., 1989, Astrophys. J. 347, 1167
- de Ville A., Priest E.R., 1991, Astrophys. J. 359, 560
- Doschek G.A., Feldman U., Bohlin J.D., 1976, Astrophys. J. 205, L177
- Dowdy J.F. Jr., 1993, Astrophys. J. 411, 406
- Dungey J., 1953, Monthly Notices Roy. Astron. Soc. 113, 180
- Dunn, R.B., 1960, Ph.D. Thesis, Univ. Harvard
- Durney B.R., 1971, Astrophys. J. 166, 669
- Edenstrasser J.W., 1980, J. Plasma Phys. 24(2), 299
- Edenstrasser J.W., 1980, J. Plasma Phys. 24(3), 515
- Engvold O., 1976, Solar Phys. 49, 283
- Evershed J., 1909, Monthly Notices Roy. Astron. Soc. 69, 454
- Ferraro V.C.A., 1937, Monthly Notices Roy. Astron. Soc. 97, 458
- Ferreira J.M., Jardine M., 1996, Astron. Astrophys. 305, 265
- Ferreira J., Pelletier G., 1995, Astron. Astrophys. 295, 807

- Ferriz-Maz A., Moreno-Insertis F., 1987, Astron. Astrophys. 179, 268
- Fisher R., Guhathakurta M., 1995, Astrophys. J. 447, L139
- Forsyth R.J. et al., 1996, Astron. Astrophys. 316, 287
- Foukal P.V., 1976, Astrophys. J. 210, 575
- Gebbie et al., 1981, Astrophys. J. 251, L115
- Gebhardt U., Kiessling M., 1992, Phys. Fluids B 4(7), 1689
- Glencross W.M., 1980, Astron. Astrophys. 83, 65
- Goldstein B.E. et al., 1996, Astron. Astrophys. 316, 296
- Golub L., Krieger A.S., Vaiana G.S., Silk J.K., Timothy A.F., 1974, Astrophys. J. 189, L93
- Gopalswamy N., Schmahl E.J., Kundu M.R., 1992, in: *Proc. First SOHO Workshop*, ESA SP-348; Noordwijk: ESA
- Grad H., 1960, Rev. Modern Phys. 32, 830
- Guderley K.G., 1962, *The Theory of Transonic Flows*, Addison Wesley: Reading
- Habbal S.R., 1992, Ann. Geophys. 10, 34
- Habbal S.R., Esser R., Arndt M.B., 1993, Astrophys. J. 413, 435
- Habbal S.R., You Q.H., Esser R., 1994, J. Geophys. Res. 99, 8465
- Hansteen V., 1993, Astrophys. J. 402, 741
- Hartle R.E., Barnes A., 1970, J. Geophys. Res. 75, 6915
- Hartle R.E., Sturrock P.A., 1968, Astrophys. J. 151, 1155
- Hasan S.S., Venkatakrishnan P., 1982, Sol. Phys. 80, 385
- Hassler D.M., Rottman G.J., Orral F.Q., 1991, Astrophys. J. 372, 710
- Herbold G., Ulmschneider P., Spruit H.C., Rosner R., 1985, Astron. Astrophys. 145, 157

- Heyvaerts J., Norman C.A., 1989, Astrophys. J. 347, 1055
- Hood A.W., Anzer U., 1990, Solar Phys. 126, 117
- Hood A.W., Priest E.R., 1979, Astron. Astrophys. 77, 233
- Hundhausen A.J., 1972, *Coronal Expansion and Solar Wind*, Springer–Verlag, New York
- Jeffrey A., Taniuti A., 1964, *Nonlinear Wave Propagation*, Academic press, New York
- Jiang G-S., Shu C-W., 1996, J. Comput. Phys. 126, 202
- Kippenhahn R., Schlüter A., 1957, Z. Astrophys. 43, 36
- Kopp R.A., Holzer T.E., 1976, Sol. Phys. 49, 43
- Korevaar P., 1989, Astron. Astrophys. 226, 209
- Koutchmy S., 1977, Solar Phys. 51, 399
- Krieger A.S., Timothy A.F., Roelof E.C., 1973, Sol. Phys. 29, 505
- Kubota J. Uesugi A., 1986, Publ. Astron. Soc. Japan 38, 903
- Kuperus M., Raadu M., 1974, Astron. Astrophys. 31, 189
- Landau L. D., Lifshitz E. M., 1959, in: *Fluid Mechanics*, translated by J.B. Sykes, W.H. Reid, Oxford Pergamon Press
- Leroy J.L., 1989 in: *Dynamics and Structure of Quiescent Solar Prominences*, ed. E.R. Priest, Kluwer Acad. Publ., Dordrecht, Holland
- Leroy J.L., Bommier W., Sahal-Brechot S., 1984, Astron. Astrophys. 131, 33
- Lifschitz A., Hameiri E., 1991, Phys. Fluids B 11(3), 2644
- Lima J.J., Priest E.R., 1993, Astron. Astrophys. 268, 641
- Linker J.A., Mikić Z., 1995, Astrophys. J. 438, L45
- Linker J.A., Van Hoven G., Schnack D.D., 1990, Geophys. Res. Letters 17, 2281

- Linsky J.L., 1993, Proc. IAU Colloq. 144
- Lites B. W., Bruner E. C., Chipman E. G., Shine R. A., Rottman G. J., White O. R., Athay R. G., 1976, Astrophys. J. 210, L111
- Longbottom A.W., Fiedler R.A.S., Rickard G.J., 1997, Astron. Astrophys. suppl., *submitted*
- Longbottom A.W., Hood A.W., 1994, Sol. Phys. 155, 267
- Lovelace R.V.E. et al., 1986, Astrophys. J. Suppl. 62, 1
- Marsden R.G., Smith E.J., Cooper J.F., Tranquille C., 1996, Astron. Astrophys. 316, 279
- Maschke E.K., Perrin H., 1980, Plasma Phys. 22, 579
- Mc Comas D.J. et al., 1996, Astron. Astrophys. 316, 368
- Melville J.P., Hood A.W., Priest E.R., 1984, Sol. Phys. 92, 15
- Mendoza C.A., Hood A.W., 1996, Astro. Lett. and Communications 34, 107
- Menzel D., 1951, in: *Proc. Conf. on Dynamics of Ionised Media*, University College, London
- Meyer F., Schmidt H.U., 1968, Z. Angew. Math. Mech. 48, 218
- Mikić Z., Linker J.A., 1994, Astrophys. J. 430, 898
- Mok Y., Drake J.F., Schnack D.D., Van Hoven G., 1990, Astrophys. J. 359, 228
- Montesinos B., Thomas J.H., 1989, Astrophys. J. 337, 977
- Montesinos B., Thomas J.H., 1993, Astrophys. J. 402, 314
- Morozov A.I., Solov'ev L.S., 1963, Soviet Phys. 8, 243
- Munro R.H., Jackson B.V., 1977, Astrophys. J. 213, 874
- Nakagawa Y., 1981, Astrphys. J. 247, 707
- Nakagawa Y., 1981, Astrphys. J. 247, 719

- Neupert W.M., Pizzo V., 1974, J. Geophys. Res. 79, 3701
- Newkirk G. Jr., Harvey J., 1968, Solar Phys. 3, 321
- Noci G., 1981, Sol. Phys. 69, 63
- Noci G., Spadaro D., Zappalà R.A., Antiochos S.K., 1989, Astrophys. J. 338, 1131
- Nolte J.T. et al., 1977, Sol. Phys. 60, 143
- Orlando S., Peres G., Serio S., 1995, Astron. Astrophys. 294, 861
- Orlando S., Peres G., Serio S., 1995, Astron. Astrophys. 300, 549
- Parker E.N., 1958, Astrophys. J. 128, 664
- Parker E.N., 1960, Astrophys. J. 132, 175
- Parker E.N., 1960, Astrophys. J. 132, 821
- Parker E.N., 1961, Astrophys. J. 133, 1014
- Parker E.N., 1964, Astrophys. J. 139, 93
- Parker E.N., 1979, *Cosmical Magnetic Fields*, Clarendon Press, Oxford
- Peres G., Spadaro D., Noci G., 1992, Astrophys. J. 389, 777
- Pikel'ner S.B., 1971, Solar Phys. 17, 44
- Pneuman G.W., Kopp R.A., 1971, Sol. Phys. 18, 258
- Poinsot T.J., Lele S.K., 1992, J. Comput. Phys. 101, 104
- Poland A.I., Anzer U., 1971, Sol. Phys. 19, 401
- Poland A.I., Mariska J.T., 1986, Solar Phys. 104, 303
- Poletto G. et al., 1996, Astron. Astrophys. 316, 374
- Priest E.R., 1978, Sol. Phys. 58, 57
- Priest E.R., 1981, in: *Solar Active Regions*, ed. F.Q. Orrall, Colo. Ass. Univ. Press, Boulder

- Priest E.R., 1982, *Solar Magnetohydrodynamics*, D. Reidel Publ. Co., Dordrecht, Holland
- Priest E.R. (ed.), 1989, *Dynamics and Structure of Quiescent Solar Prominences*, Kluwer Acad. Publ., Dordrecht, Holland
- Priest E.R., Hood A.W., Anzer U., 1989, Astrophys. J. 344, 1010
- Priest E.R., Smith E.A., 1979, Solar Phys. 64, 217
- Raymond J.C., Smith B.W., 1977, Astrophys. J. Suppl. 35, 419
- Ribes E., Unno W., 1980, Astron. Astrophys. 91, 129
- Rimmele T.R., 1995, Astron. Astrophys. 298, 260
- Rimmele T.R., 1995, Astrophys. J. 445, 511
- Robb T.D., Cally P.S., 1992, Astrophys. J. 397, 329
- Roberts B., 1976, Astrophys. J. 204, 268
- Roe P.L., Balsara D.S., 1996, SIAM J. Appl. Math. 56(1), 55
- Rosner R., Tucker W.H., Vaiana G.S., 1978, Astrophys. J. 220, 643
- Ryu D., Jones T.W., 1995, Astrophys. J. 442, 228
- Saito K., 1965, PASJ 17, 1
- Saito K., Tandberg-Hanssen E., 1973, Solar Phys. 31, 105
- Sakurai T., 1985, Astron. Astrophys. 152, 121
- Sakurai T., 1990, Computer Phys. Report 12, 247
- Sauty C., 1994, Ann. Phys. Fr. 19, 459
- Sauty C., Tsinganos K.C., 1994, Astron. Astrophys. 287, 893
- Schmieder B., 1989, in: *Dynamics of Quiescent Prominences*, Lecture Notes in Physics, eds. V. Ruždjak, E. Tandberg-Hanssen
- Serio S., Peres G., Vaiana G.S., Golub L, Rosner R., 1981, Astrophys. J. 243, 288

- Shafranov V.D., 1957, JETP 33, 710
- Shu C-W., Osher S., 1988, J. Comput. Phys. 77, 439
- Solov'ev L.S., 1961, Zh. Tekh. Fiz. 31, 407
- Solov'ev L.S., 1967, Rev. Plasma Phys. 3, 277
- Spadaro D., 1991, Adv. Space Res. 11(1), 221
- Spadaro D. et al., 1990, Astrophys. J. 362, 370
- Spitzer L., 1962, *Physics of Fully Ionized Gases*, Interscience, New York
- Spruit H.C., 1981, in: *The Physics of Sunspots*, ed. L.E. Cram and J.H. Thomas, Sunspot, New Mexico
- Steinolfson R.S., Suess S.T., Wu S.T., 1982, Astrophys. J. 255, 730
- Sturrock P.A., Hartle R.E., 1966, Phys. Rev. Letters 16, 628
- Suess S.T., 1982, Solar Phys. 75, 145
- Suess S.T., Richter A.K., Winge C.R., Nerney S.F., 1977, Astrophys. J. 217, 296
- Surlantzis G., Démoulin P., Heyvaerts J., Sauty C., 1994, Astron. Astrophys. 284, 985
- Surlantzis G., Démoulin P., Heyvaerts J., Sauty C., 1996, Astron. Astrophys. 310, 351
- Tandberg-Hanssen E., 1974, *Solar Prominences*, Dordrecht, Reidel
- Thieme K.M., Marsch E., Schwenn R., 1990, Ann. Geophys. 8, 713
- Thomas J.H., 1984, in: *Small Scale Dynamical Processes in Quiet Stellar Atmospheres*, ed. S.L. Keil, Sunspot, New Mexico
- Thomas J.H., 1988, Astrophys. J. 333, 407
- Thomas J.H., Montesinos B., 1990, Astrophys. J. 359, 550
- Thomas J.H., Montesinos B., 1991, Astrophys. J. 375, 404

- Thomson K.W., 1987, J. Comput. Phys. 68, 1
- Tkalich V.S., 1959, Bull. Acad. Sci. USSR 4, 134
- Tkalich V.S., 1959, Bull. Acad. Sci. USSR 5, 122
- Tkalich V.S., 1962, Pis'ma Mat. Mekh. 26, 96
- Trussoni E., Tsinganos K.C., 1993, Astron. Astrophys. 269, 589
- Tsinganos K.C., 1981, Astrophys. J. 245, 764
- Tsinganos K.C., 1982, Astrophys. J. 252, 775
- Tsinganos K.C., 1982, Astrophys. J. 259, 820
- Tsinganos K., Sauty C., Surlantzis G., Trussoni E., Contopoulos J., 1996, Monthly Notices Roy. Astron. Soc. 283, 811
- Tsinganos K.C., Surlantzis G., Priest E.R., 1993, Astron. Astrophys. 275, 613
- Uchida Y., 1979, in: *Proc. of the Japan-France Seminar on Solar Phys.*, eds. J.C. Henoux
- Vanajakshi T.C., Thomson K.W., Black D.C., 1989, J. Comput. Phys. 84, 343
- Van de Hulst H.C., 1950, Bull. Astron. Soc. Neth. 11, 150
- Velli M., 1994, Astrophys. J. 432, L55
- Velli M., Habbal S.R., Esser R., 1994, Space Sci. Rev. 70, 391
- Vesecky J.F., Antiochos S.K., Underwood J.H., 1979, Astrophys. J. 233, 987
- Villata M., Ferrari A., 1994, Astron. Astrophys. 284, 663
- Villata M., Ferrari A., 1994, Phys. Plasmas 1(7), 2200
- Villata M., Ferrari A., 1995, Astron. Astrophys. 293, 626
- Villata M., Tsinganos K.C., 1993, Phys. Fluids B 5(7), 2153
- Wagner W.J., 1976, Astrophys. J. 206, 583

- Walker A.B.C. Jr., De Forest C.E., Hoover R.B., Barbee T.W. Jr., 1993, Solar Phys. 148, 239
- Wang A.-H., Wu S.T., Suess S.T., Poletto G., 1993, Sol. Phys. 147, 55
- Wang Y.-M., 1994, Astrophys. J. 435, L153
- Wang Y.-M., Sheeley N.R. Jr., 1990, Astrophys. J. 355, 726
- Wang Y.-M., Sheeley N.R. Jr., 1995, Astrophys. J. 446, L51
- Wang Y.-M., Sheeley N.R. Jr., 1995, Astrophys. J. 452, 457
- Washimi H., 1990, Geophys. Res. Letters 17, 33
- Washimi H., Sakurai T., 1993, Sol. Phys. 143, 173
- Washimi H., Yoshino Y., Ogino T., 1987, Geophys. Res. Letters 14, 487
- Weber E.J., Davis L., 1967, Astrophys. J. 148, 217
- Wesseling P., 1992, *An Introduction to Multigrid Methods*, John Wiley & Sons LTD
- Whang Y.C., Chang C.C., 1965, J. Geophys. Res. 70, 4175
- Widing K.G., Feldman U., 1992, Astrophys. J. 392, 715
- Woltjer L., 1959, Astrophys. J. 130, 400
- Woltjer L., 1959, Astrophys. J. 130, 405
- Wu S. T., Bao J. J., An C.-H., Tandberg-Hanssen E., 1988, in: *Proc. Mallorca Workshop on Dynamics and Structure of Solar Prominences*, eds. J.L. Ballester, E.R. Priest
- You Q.H., Engvold O., 1989, Hvar Obs. Bull. 13, 197
- Zehrfeld H.P., Green B.J., 1972, Nuclear Fusion 12, 579
- Zirker J.B., 1977, *Coronal Holes and High Speed Streams*, Colo. Ass. Univ. Press, Boulder
- Zirker J.B., Engvold O., Yi Z., 1994, Solar Phys. 150, 81